UNIVERSITÉ DE STRASBOURG

ÉCOLE DOCTORALE MSII

Laboratoire ICube - UMR 7357

THÈSE présentée par :

Anastasiia BOZHOK

soutenue le : **15 décembre 2020**

pour obtenir le grade de : **Docteur de l'université de Strasbourg**
Discipline/Spécialité : Signal, image, automatique, robotique

Microscopies ptychographique de Fourier et de polarisation : modèles, méthodes, comparaison

THÈSE dirigée par :

M. HEINRICH Christian	Professeur des Universités, Université de Strasbourg
M. ZALLAT Jihad	Professeur des Universités, Université de Strasbourg

RAPPORTEURS :

M. DEVLAMINCK Vincent	Professeur des Universités, Université de Lille
M. DAUL Christian	Professeur des Universités, Université de Lorraine

---

AUTRES MEMBRES DU JURY :

M. TAKAKURA Yoshitate	Maître de conférences, Laboratoire ICube
M. DELLINGER Jean	Maître de conférences, Laboratoire ICube
M. PIERANGELO Angelo	Ingénieur de recherche, École polytechnique / CNRS

Contents

Introduction 9

1 Optical microscopy **15**
1.1 Fundamentals of optical imaging 15
1.1.1 Light 15
1.1.2 Optical imaging techniques and their applications 19
1.2 Fundamentals of microscopy systems 21
1.2.1 Optical Components of a Microscope 21
1.2.2 Light source Components of a Microscope 22
1.3 Bright-field microscopy performance and limitations 23
1.3.1 Characteristics of the microscope system 24
1.3.2 Limitations of Conventional Microscopy and State of the Art Performance 27
1.4 Exceed the limits 29
1.4.1 Exceed the limits by hardware modifications 29
1.4.2 Exceed the limits by computational imaging 30

2 The phase problem and Fourier ptychography **33**
2.1 Phase retrieval applications and techniques 33
2.1.1 Examples of phase problems 33
2.1.2 Phase problem in optical imaging 35
2.1.3 Real-space ptychography 36
2.2 Fourier ptychographic microscopy 36
2.2.1 The phase problem (the forward model) in 1D 37
2.2.2 The principle of Fourier ptychographic microscopy 43
2.2.3 Assumptions, approximations and limitations 49
2.2.4 Patents 49
2.2.5 Conclusion 50
2.3 Numerical aspects of FPM phase retrieval 51
2.3.1 Overview of the state of the art 51
2.3.2 Optimization formulation 51
2.3.3 Inverse problem analysis 53
2.3.4 Sampling criteria for FP reconstruction process 54
2.3.5 Complex gradient 56
2.4 Reconstruction methods 56

2.4.1 Optimization algorithm . . . 58
2.4.2 Initial guess . . . 66
2.4.3 Cost function . . . 66
2.4.4 Comparison and choice of methods . . . 74
2.4.5 Conclusions . . . 83

3 Realization of the Fourier Ptychographic microscope 85
3.1 Instrument introduction . . . 85
3.1.1 System diagram . . . 86
3.1.2 Extension tube manufacture . . . 86
3.1.3 Device description . . . 87
3.1.4 Acquisition process and user control . . . 89
3.1.5 Pre-acquisition calibrations . . . 91
3.2 Device characterisation . . . 96
3.2.1 LED matrix characterisation . . . 97
3.2.2 Optical elements characterisation . . . 100
3.2.3 System characterisation . . . 104
3.2.4 Camera study . . . 107
3.3 Quality assessment . . . 113
3.4 Data pre-treatment . . . 113
3.4.1 Normalization, hot pixels and dark frame . . . 113
3.4.2 Offsets . . . 114
3.4.3 Results and discussion . . . 115
3.5 Numerical recovery of system parameters and aberrations . . . 117
3.5.1 Embedded pupil function recovery . . . 117
3.5.2 Modeling aberrations with Zernike polynomials . . . 118
3.5.3 System parameters estimation . . . 119
3.5.4 Angles misalignment correction . . . 120
3.5.5 LEDs intensities . . . 124
3.6 Importance of light coherence . . . 126
3.7 Whole field of view reconstruction . . . 127
3.7.1 Segment size choice . . . 127
3.7.2 Segments stitching . . . 128
3.7.3 Phase unwrapping . . . 129
3.8 More realistic simulations . . . 129
3.8.1 Noise generation procedure . . . 130
3.8.2 Plausible simulated data sets . . . 130
3.9 Results and conclusion . . . 131

4 Polarized light microscopy and multi-modal imaging 133
4.1 Quantitative phase imaging . . . 134
4.1.1 Inline holography introduction . . . 134
4.1.2 Transparent phase sample . . . 135
4.1.3 Lensless inline digital holographic microscope . . . 136
4.1.4 FPM phase retrieval results and comparison . . . 138

4.2 Polarized light microscopy . . . 141
4.2.1 Basics of polarization of light . . . 141
4.2.2 Applications of polarization microscopy . . . 144
4.2.3 Mueller matrix microscope . . . 144
4.3 Fourier Ptychographic and Mueller Matrix Microscopes: comparison . . . 147
4.3.1 Complementarity . . . 148
4.3.2 Discussion . . . 149
4.4 Extensions and improvements . . . 151
4.4.1 3D Fourier Ptychography . . . 151
4.4.2 Other modalities . . . 151
4.4.3 Better illumination design . . . 152
4.4.4 Reducing acquisition time . . . 153
4.4.5 Other improvements . . . 154
4.5 Conclusion . . . 154

5 Conclusion and Future Work **157**
5.1 General Conclusion . . . 157
5.1.1 Overview . . . 157
5.1.2 Contributions . . . 158
5.1.3 Authors contributions . . . 159
5.2 Future Work . . . 160

A Additional FPM reconstruction results **163**

Acknowledgements

Cette thèse n'aurait pas été possible sans le grand nombre de personnes qui m'ont aidée et soutenue.

Tout d'abord, je voudrais remercier les membres de jury, Christian Daul, Vincent Devlaminck , Angelo Pierangelo et Yoshitate Takakura pour avoir accepté de juger ce travail de thèse.

Je remercie bien sûr mes directeurs de thèse, Christian Heinrich et Jihad Zallat, pour m'avoir accueillie et encadrée. Un grand merci à Cemal Draman et Marc Torzynski pour leur investissement dans ce projet.

Je remercie Jean Dellinger pour m'avoir toujours fait sourire et rire. Et je le remercie d'avoir été mon ami malgré sa position dans ce projet.

Merci à Jennifer et Briséis, mes superbes collègues de bureau. J'oublierai peut-être les détails des heures de nos conversations, mais je me souviendrai toujours de votre soutien. Merci à Florian qui a tellement cru en moi que cela m'a même fait croire en moi aussi. J'adresse ma gratitude à Eléonore, qui a toujours été là pour moi et qui me comprenait parfois mieux que moi. Merci à Adrian, Jean R, Denis, Céline, Quentin, Alexi et beaucoup d'autres de m'avoir écoutée avec la plus grande patience mais aussi d'avoir rendu ces années joyeuses et enrichissantes. Cette thèse en valait le coup, rien que pour rencontrer toutes ces personnes merveilleuses.

Je voudrais également remercier mes parents qui, malgré la distance, ont été très proches de moi ces dernières années.

Et enfin, je tiens à exprimer ma profonde gratitude à Yoshi Takakura pour tout ce qu'il a fait pour cette thèse et pour moi.

Introduction

Optical microscopy is one of the oldest scientific methods of observation used today. A microscope can reveal information about the structure of materials and tissues that are too small to be visible to the naked eye. It is useful in many applications, including medicine, physics, materials science, and the study of biological processes. The basic mechanisms of microscopy have been known since the seventeenth century and progress in this field has never ceased since. Scientists and engineers around the world are constantly developing instruments and methods that offer innovative tools for tissue analysis.

Motivation and objectives

The fundamental operating principle of optical microscopy is the measurement of interactions between light and a sample of interest. However, some information on these interactions is inevitably lost due to the limitations imposed by both the laws of physics and the current capabilities of instruments.

A microscope system offering a good compromise between manufacturing cost and the amount of relevant information retrieved would be of great interest in many application areas. The objective of this thesis is to propose and develop such a measuring instrument and the corresponding data processing methods. The chosen field of application is biology and medicine, in order to provide original tools for the analysis of biological tissues.

To achieve this goal, the first objective is to build a microscope with high spatial resolution and wide field of view and to develop methods for reconstructing scenes of interest. To this end, we have chosen to implement Fourier ptychographic microscopy (FPM). In addition to improving the resolution of a captured intensity image, this technique also provides phase information.

The second objective is to confront the constructed microscope with another imaging modality, the Mueller matrix polarimetric microscopy. This step aims to give a comprehensive view of the interaction of light with the sample by complementing the phase and intensity information (from Fourier ptychography) with the polarization information.

The work of this thesis thus implies the elaboration of a general framework for the implementation of such an imaging system.

High resolution microscopy and phase imaging

The ideal optical microscope would allow us to observe an area of the desired size and have the required spatial resolution. At the same time, it would provide a complete description of the response of a medium to light excitation. Measurements would be performed instantaneously and without the need for expert training. Of course, it is not possible to build such a microscope. Moreover, the complexity of the manufacturing process and the cost of the system increase with the approach of this idealized version.

To avoid price increases while maintaining performance, the focus can be placed on computer imaging techniques rather than hardware advances. In this work, Fourier Ptychography is chosen to overcome some of the physical limitations of conventional light microscopy through digital processing. This technique therefore belongs to a group of computational imaging methods. One of the main reasons for this choice is the possibility of partially overcoming a compromise between the dimensions of the observed area and the desired resolution. In addition, this method also provides access to information on the optical phase of the sample.

This approach was initially proposed in 2013 [244] and has since attracted many theoretical and experimental developments [246]. We built our version of a Fourier ptychographic microscope from scratch.

Multi-modal imaging and polarimetric microscopy

We first demonstrate the super resolution capabilities of the constructed Fourier ptychographic microscope. We then conduct a study confirming the quantitative phase imaging capabilities of the device.

Pursuing the idea of developing a multimodal imaging system, we demonstrate the motivation to combine polarimetric microscopy with FPM. A part of the present study is therefore devoted to the confrontation of these two optical modalities.

Polarimetric imaging techniques, like quantitative phase imaging, have many applications, particularly in the analysis of biomedical tissues. We use a Mueller matrix microscope to access, as its name implies, a Mueller matrix of the sample. This provides the complete response of the specimen to polarized light. The recovered Mueller matrix is then used to calculate the physical parameters of the studied tissues, such as dichroism, retardance and depolarization.

We are particularly interested in the complementarity between the phase delays observed with the Fourier ptychographic microscope (optical phase) and the polarimetric microscope (retardance). We aim to show that the combination of the two gives richer information than their use in isolation.

Applications

Both FPM and polarimetric microscopy can be used in a wide range of applications.

Reported uses of FPM include counting white blood cells [36] and circulating tumor cells [220], monitoring the movement of dopaminergic neurons [98], distinguishing between healthy and cancerous cells [79], and many others. Photonic crystal imaging is an example of non-biomedical applications [171]. More broadly, any quantitative phase imaging technique can be used for digital staining of transparent tissue through deep learning [166].

Furthermore, the classic configuration of the FPM can be modified to allow numerous extensions, thus widening the possible field of use. In addition, the technique can be combined with other imaging modalities, such as fluorescence microscopy. In the current work, we discuss the prospects of merging Fourier ptychographic microscopy with polarimetric imaging.

Work scope

Research context of the team

This research work was carried out in the engineering, computer science and imaging laboratory ICube (UMR 7357). The project is part of a collaboration between two teams - IMAGeS and TRIO.

The TRIO team (Remote Sensing, Radiometry and Optical Imaging) is a multidisciplinary group that focuses on the extraction of physical information contained in the signal. One of its areas of research is the physics of optical imaging. In this field, several projects concerning the development of instruments for microscopy, holography and polarimetric imaging are underway.

Meanwhile, the IMAGeS team (IMages, leArning, Geometry and Statistics) works mainly on image modelling and processing as well as computer vision. Its research areas include approaches such as statistical analysis, probabilistic models, inverse problems and interpretation of digital image data.

The current project is the first in the field of computational microscopy for both teams. The instruments I worked on were built after my arrival at the laboratory. The expertise of the TRIO team proved particularly useful for the physics and engineering part of the current project, while the IMAGeS team contributed significantly to the development of the corresponding data processing methods.

A short overview of the state of the art

The technique that we use to achieve wide-field, high-resolution imaging – Fourier ptychographic microscopy (FPM) – was originally proposed by G. Zheng et al. [244] in 2013. It is a recent but highly active research topic

that has given rise to many theoretical and experimental developments. According to Web of Science Core Collection data at this date (22 September 2020), the original article has already been cited more than 600 times. More than 60% of these articles have been released between the beginning of my thesis and the current date.

Although there is a thorough theoretical description of the fundamental principles of the method provided by Zheng in his book Fourier Ptychographic Imaging [243], some aspects related to experimental conditions [25, 26, 27, 49, 149, 178, 202, 230] and numerical methods [26, 86, 94, 203, 218] are still under active development.

From an algorithmic point of view, this technique belongs to a set of problems called "Phase Retrieval", which dates back to the 1970s. Despite its age, this area of research is still active [121, 134, 212], indicating that the problem is not completely solved.

The graph in Figure 1(a) shows the number of articles citing Zheng's original paper published per year. The graph in Figure 1(b) shows the same characteristic for articles on the topic "Phase Retrieval". Both numbers increase each year. This trend is evident in the case of Fourier Ptychography and there is no indication that this tendency will reverse in the coming years.

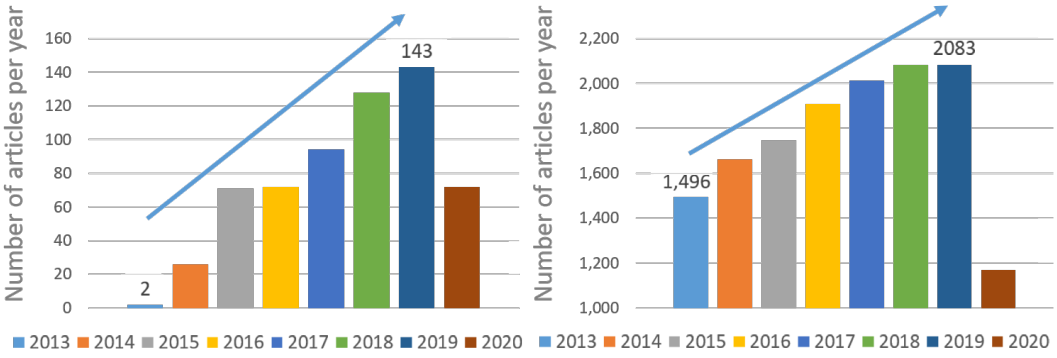

(a) (b)

Figure 1: Number of articles published per year. (a) Citing Zheng's original paper [244] (FPM). (b) On the topic "Phase Retrieval". According to data from the Web of Science Core Collection, September 22, 2020.

Contributions

The contributions of this thesis concern both the experimental developments related to the implementation of devices and the developments of the different parts of the data processing chain.

We particularly focused on the realization of the Fourier ptychographic microscope and on the corresponding processing methods. Although many sig-

nificant advances have been made in FPM over the last years, various sources of imaging noise and errors occurring in the actual experimental situation can still seriously distort the results of the recovery. We classified and compared several reconstruction algorithms and proposed system calibration schemes adapted to our microscope configuration. We demonstrated the super resolution and quantitative phase imaging capabilities of the device. As part of this demonstration, we conducted a study on a fabricated sample of large optical thickness. This research led to a publication in a peer-reviewed journal [110].

In a second step, we used a Mueller matrix microscope to access polarimetric properties of samples. We have experimentally validated the complementarity of the information extracted by the two constructed optical modalities. This part of the work has been the subject of an international communication with a published act [19].

Outline of thesis

The remainder of this work is outlined as follows. In the first chapter, the foundations and the limits of optical microscopy are laid out in order to highlight the contribution of Fourier ptychography. In the second chapter, we explain in detail the idea of the FPM method and its physical model. We continue by addressing the numerical aspects of the problem and investigating different reconstruction methods. The third chapter presents the experimental set-up of our Fourier ptychographic microscope. We then propose methods for its characterization and calibration. The fourth chapter introduces the quantitative phase imaging study performed. Next, the Mueller matrix microscope is presented, followed by a description of the comparative study. Finally, we draw conclusions and present the perspectives of the work accomplished.

Chapter 1

Optical microscopy

The general definition of an optical (or light) microscope is a device for obtaining enlarged images of objects invisible to the naked eye. Microscopes come in many different types and categories, however. The choice of a suitable device must be made according to the application and constraints such as budget, portability or the need for training.

One of the biggest differences in the design of any imaging system is the lighting mode. A distinction is made between reflection imaging (also called epi-illuminated) and transmission imaging (trans-illuminated). Everything in this chapter applies to both configurations, however, only transmission microscopy is employed in current work.

The operation principles and components of an optical microscope are summarized in this chapter, following an introduction to optical imaging methods and the properties of light.

1.1 Fundamentals of optical imaging

Optics is a branch of physics that studies light and its interactions with matter. As part of this work, we focus mainly on geometrical optics and wave optics [9].

Geometric optics, also called ray optics, is interested in light rays and treats them rather as an abstract entity with measurable position and direction. On the other hand, wave optics, sometimes called physical optics, express light in the form of waves and deal with all the consequences of such a representation.

1.1.1 Light

According to the most general definition given by physics, light is electromagnetic radiation. Depending on phenomena under consideration, the light can be studied using models with different levels of complexity.

In the second half of the 19th century, James Clerk Maxwell constructed the famous equations to describe the electromagnetic field and its disturbances

mathematically. One of the conclusions of his theory was the existence of synchronized oscillations propagating in space in coupled electric and magnetic fields in a wave-like pattern. A variable electric field is always associated with a variable magnetic field.

On the most fundamental level, light exhibits a so-called wave-particle duality. This principle holds fact that, from the point of view of quantum mechanics, light can not be considered only as a group of particles and can not be characterized solely as a wave. This duality is the characteristic of all quantum entities, including light particles called photons [44].

In the context of this work, unless otherwise indicated, by "light", we only refer to the wave properties of electromagnetic radiation.

Properties of light

Among the fundamental attributes of light to which we refer in this work are direction of propagation, amplitude, phase, frequency and polarization.

The definition of polarization is given later in Chapter 4.

The direction of propagation is simply a vector that indicates where the light wave is heading. Disturbances in electric and magnetic fields oscillate perpendicular to the direction of propagation and perpendicular to each other, which means that these waves are transverse. Electric and magnetic fields are vector fields. Their oscillations are described as changes in the amplitude and direction of a vector at each point in space.

Consider the simplest form of a one-dimensional wave signal which is a sinusoidal function $y(z,t)$ defined at the point z and the propagation time t. It is characterized by its amplitude A, angular frequency ω, phase constant δ and the wave number k [64]:

$$y(z,t) = A\cos[kz - \omega t + \delta] \tag{1.1}$$

The wavelength λ of such a wave can be expressed using the wave number k: $\lambda = 2\pi/k$. The angular frequency ω is the number of oscillations per unit time expressed in radians. The ordinary frequency ν of the wave, which is the inverse of the period (the duration of one full cycle) is related to the angular frequency ω as following : $\nu = \omega/2\pi$. It is measured in hertz. The wave described by the Eq. (1.1) is monochromatic, meaning that it is defined by a single frequency ω.

The intensity of light is defined as a square of the amplitude of the wave $I = A^2$.

A more practical way to represent the wave, avoiding working with the sinusoidal function, is to use the Euler formula and complex numbers. From the Euler's formula $z = r(\cos\phi + i\sin\phi) = re^{i\phi}$. The equation (1.1) can then be rewritten as :

$$y(z,t) = \mathrm{Re}[Ae^{i(kz-\omega t+\delta)}] \tag{1.2}$$

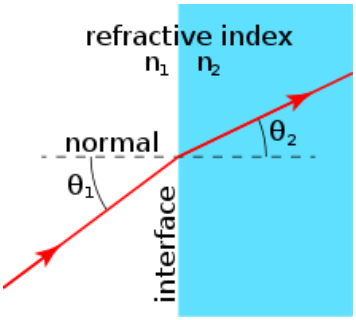

Figure 1.1: Refraction of a light beam. Reprinted from wikipedia.org.

Another definition, which will be used in the next chapter, is that of complex amplitude $\tilde{A}$.

$$\tilde{A} = Ae^{i\delta} \tag{1.3}$$

Finally, another type of wave that will be mentioned in Chapter 2 is the monochromatic plane wave. Such a wave is defined as a wave with a flat wavefront. In turn, the wavefront refers to the set of points that took the same time to propagate from the source. The electric and magnetic fields of such a plane wave can be written as follows:

$$\begin{aligned} E(z,t) &= \mathrm{Re}[\tilde{E}_0 e^{i(kz-\omega t)}], \\ B(z,t) &= \mathrm{Re}[\tilde{B}_0 e^{i(kz-\omega t)}] \end{aligned} \tag{1.4}$$

where $\tilde{E}_0$ and $\tilde{B}_0$ are the complex amplitudes.

The propagation of a plane wave is therefore described by a complex exponential.

Light-matter interactions

Light can interact with matter in a variety of ways. It can be reflected, absorbed, transmitted, refracted, diffracted, scattered and even emitted. All these interactions can modify the properties of the original light beam.

We will rely mainly on refraction, transmission, reflection, absorbance and diffraction to describe the functioning of the systems built. It is therefore useful to state these definitions here.

Refraction Refraction is the deviation of a light beam when its velocity changes as it passes between two media, see Fig. 1.1.

The refractive index n is a number that characterizes the speed of light propagation in the medium. More precisely, $n = c/v$, where c is a universal physical constant indicating the speed of light in vacuum and v is the phase velocity of light in the given medium. The value of the index depends on the composition of the medium and the wavelength of the light.

The refractive index of air is about n = 1.00028 for visible light frequencies. In the course of ongoing work, we will approximate this value to 1.

The amount of the deviation of the light beam angle is given by the Snell law :

$$\frac{\sin\theta_1}{\sin\theta_2} = \frac{v_1}{v_2} = \frac{n_1}{n_2} \tag{1.5}$$

The difference in propagation speed between two media with different optical properties leads to changes in the optical path of the light passing through them. It creates a phase shift with respect to a wave that has not changed the medium. This phenomenon can be quantified by a quantity called optical path length Λ, which is the refractive index of a material n multiplied by its physical thickness s: $\Lambda = ns$.

Another related descriptor of the optical properties of a material is the complex refractive index $n^* = n + ik$. It describes not only the delay in the phase velocity of wave propagation (which is a real index of refraction n) but also the amount of attenuation of the wave (the extinction coefficient k). In this work, we refer only to the real part of the refractive index.

Transmission, reflection and absorbance Transmission is simply the passage of light through a medium. The efficiency of transmission depends on the wavelength of the light used and the properties of the medium.

It is quantified by transmittance T, which is the ratio between the intensity of radiation transmitted through matter I and the incident intensity I_0 : $T = I/I_0$. For a totally transparent object, the transmittance is equal to 1, i.e. the amplitude of visible light is not attenuated.

At the atomic level, transmission, as well as reflection, occurs when the electrons of the atoms making up the medium do not vibrate at the same frequency as the incident light. If the frequencies match, absorption occurs.

Absorption is defined as a transition from the radiant power of incident light to another form of energy. In most cases it becomes thermal energy. The quantity directly related to transmission and absorption is called absorbance A. It describes the ability of the medium to attenuate light of a specific wavelength. It encompasses all the physical processes that could lead to the failure of electromagnetic radiation transmission, such as absorption, reflection and scattering. By definition, $A = -\log_{10} T$.

Diffraction Diffraction describes the behaviour of light when it passes through a slit or encounters an obstacle whose dimension is of the same order of magnitude as its wavelength. This encounter is accompanied by a bending and spreading of the wave propagation directions. Diffraction is an important element in understanding Fourier optics and the limit of resolution.

Transmission, reflection and refraction are the basic phenomena on which geometric optics is based, while diffraction is an essential part of wave optics.

It is important to note that some materials are sensitive to the polarization state of a wave. These materials are said to be optically anisotropic. This means that the refractive index, absorption coefficient, and other optical properties can vary depending on the polarization state of light. We will discuss the interactions of polarized light with anisotropic materials in Chapter 4.

Note also that the above definitions are given assuming that scattering (or diffusion), which is the process of deflecting a single beam of light into several beams, does not occur during refraction, reflection and transmission.

1.1.2 Optical imaging techniques and their applications

Human eye

The human eye is sensitive, up to a certain variation, to electromagnetic waves of wavelengths from 380 nm to 740 nm.

The structure of the eye is somewhat similar to that of a microscope with a camera. Light enters the eye through a hole of varying size in the iris called "pupil". It then passes through a lens and is projected onto the retina at the back of the eye. Some intermediate stages of this process have been deliberately left out.

The retina contains two types of photoreceptor cells: cones and rods. In low light conditions, only the rods are primarily activated, creating monochromatic vision. The cones function in high light conditions, allowing us to appreciate daytime vision. In humans, there are 3 types of cones, each type respond the most to one of the 3 possible frequencies, which results in colour perception.

The cons and rods are stimulated when enough photons of the specific wavelength are absorbed. Therefore, the human eye is sensitive to two properties of light: intensity and specific spectrum bands. Another piece of information that the brain can reconstruct using both eyes is the depth of a scene, that is, the interactions between light and the 3D world.

Common optical instruments

There are a wide variety of optical instruments, including devices that are used to create and manipulate light or to analyze and capture it. Only the instruments encountered in the course of the work in progress will be cited below.

Light emitters Among the light emitters used in this thesis are lasers, LEDs and lamps.

A word laser stands for "Light Amplification by Stimulated Emission of Radiation". It is a device that converts the energy of a source into a narrowly directed stream of light radiation that is coherent in space and time. The characteristics of a laser can be very different depending on the application.

Tungsten and xenon halogen lamps are the most commonly used light sources in optical microscopy. Both create incoherent electromagnetic radiation with a continuous spectrum. The voltage and thus the illumination power can usually be controlled. Depending on the type of lamp and the manufacturer, the spectrum range and the highest intensity band may differ. As an example, Thorlabs' Fiber-Coupled Xenon Light Source emits light from 240 nm to 1200 nm with intense lines in the spectral region of 600 to 1200 nm.

Recently, LEDs have become an important part of microscopic research, especially in fluorescence microscopy [120, 129]. LED is an acronym for "Light Emitting Diode". It is a device that generates electromagnetic radiation when an electric current flows through it (in the forward direction). Even if the illumination produced is not perfectly coherent, it can be considered monochromatic because the spectral band remains narrow. The advantages of LEDs over the light sources listed above include lower price, smaller size, lower power consumption and faster switching. Furthermore, some manufacturers offer LEDs with high luminous efficiency and in the ultraviolet and infrared wavelengths in addition to visible light.

Light analysers and light modification Different instruments are available to analyze the light, modify its properties or improve the image for visualization. Optical elements used in current work include: lenses, mirrors, optical filters, polarizers, optical retarders. Among the composite devices: microscopes and microscope objectives, spectrometer, refractometer, polarimeter.

Optical filters are used to select light in a desirable wavelength range. In the case of an absorbing filter, all light that does not fall within its spectrum is absorbed and the rest is transmitted through.

Polarizers, optical retarders or waveplates and other optical devices capable of changing the polarization state of light will be discussed in Chapter 4.

A spectrometer is a device used to measure the spectral components of incident light. It works by separating the radiation into individual narrow bands within certain wavelengths and measures the intensity of each band.

A Refractometer is capable of measuring the refractive index of a medium.

Lenses A lense is the basic and, until recently, the essential element of an optical microscope [17, 165]. Therefore, in order to understand imaging in microscopy and its performance limitations, it is useful to look at lenses from the point of view of geometric optics.

A lens uses the laws of refraction to deflect the light beam that has passed through the object. The simplest type of lens is a spherical lens whose axis is located at its physical centre. These lenses have two surfaces, each of which can be flat (does not deflect rays), convex (converges rays) or concave (diverges rays).

Lenses are generally characterized by their focusing points, focal length and optical power (reciprocal of focal length).

The focal point F is a point where the rays, coming from a point light source S on one side and passing through the lens on the other side, converge and form an image of the point S.

Focal length f is the distance from the center of the lens to its focal point F.

Light detectors Photodetectors, i.e. sensors for electromagnetic radiation, used in current work include a photon counter, a CCD (Charged Coupling Devices) camera and a CMOS (Complementary Metal Oxide Semiconductor) camera. Their sensors convert light signals into electrons.

Like the human eye, the sensors in digital cameras are only sensitive to the intensity of incoming light in a specific wavelength range. They are limited in terms of spatial and temporal resolution, frequency sensitivity and dynamic range.

The CCD sensor consists of a 2D array of light-sensitive photodiodes. When a photon in a given frequency band reaches a sensor pixel, it is absorbed and an electron charge is generated according to the photovoltaic effect [62]. After exposure, this charge is transported through the entire sensor field, from pixel to pixel, and is read at the output angle of the matrix.

On the contrary, in CMOS sensors, one or more transistors are attached to each pixel (a photodioid). This allows each pixel to be read out separately by moving the charge through wires attached to the transistors.

Conventional photodetectors can only detect variations in light intensity within a certain frequency range. Information about the change in polarization of the light and its phase is lost.

1.2 Fundamentals of microscopy systems

Figure 1.2 shows an example of a commercially available clinical microscope, Leica DM1000. This device will be used as a reference for a professionally designed microscope with which to compare the performance of our built system.

The main components of any optical microscope are an optical part and an illumination unit. Their composition is given below.

1.2.1 Optical Components of a Microscope

The objective of a microscope (Figure 1.2 b3) is one of the most important parts of a microscope that largely defines its final performance. It consists of a lens or a lens system constructed in such a way that the image produced is magnified [135]. An eyepiece (Figure 1.2 b1) is another component of a typical optical microscope. It works together with an objective to project a magnified image onto an eye or sensor. Like an objective, it consists of lenses.

Objectives may differ greatly in design, characteristics and applications. In order not to plunge into the internal design of objectives, we simply mention

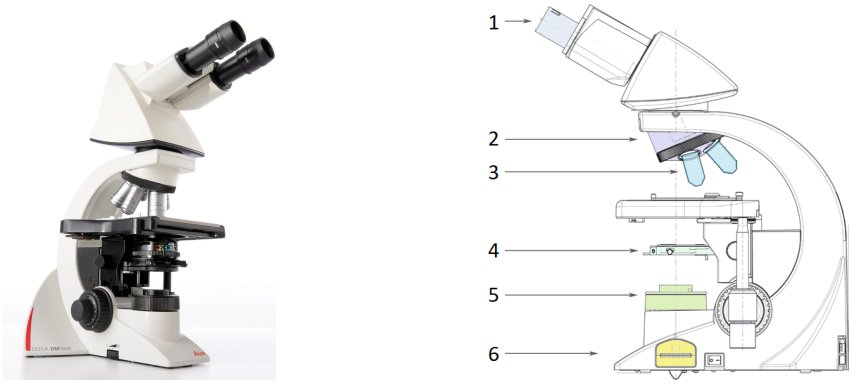

(a) Photo (b) Schema

Figure 1.2: Clinical microscope Leica DM1000. (1) – eyepiece, (2) – nosepiece, (3) – objectives, (4) – condenser, (5) – collector, (6) – lamp. Reprinted with modifications and annotations from leica-microsystems.com.

that only refractive (as opposed to reflective) objectives are used in this work. Objectives can also be classified as a finite conjugate and an infinite conjugate (corrected to infinity).

Early microscope objectives were all finite conjugate, meaning that the image was formed at a fixed distance from the objective lenses. The distance between the part of a microscope to which the objectives are attached (the nosepiece, Figure 1.2 b2) and the top of the eyepiece tubes is called the mechanical tube length. The standard has been set at a value of 160 millimetres for more than 100 years.

Infinity corrected objectives form an image at infinity. Their invention was particularly useful for applications involving a large distance between the objective lenses and the image plane, allowing the insertion of other optical elements between the two. Such objectives require a secondary lens to focus on a sample and produce the image.

1.2.2 Light source Components of a Microscope

The design and adjustment of illumination can be as critical to the overall performance of an imaging system as its optics [67]. Important characteristics of a light source component include its brightness, spectrum, uniformity of illumination in the field of view, illumination angles, presence of artifacts such as glare, etc.

Kohler illumination The most common illumination used in optical microscopy today is the Köhler illumination [131]. It was proposed in 1893 and practically replaced the critical illumination method used previously.

The main problem with critical illumination was the inhomogeneity of the brightness that led to the appearance of the light source in the observed image

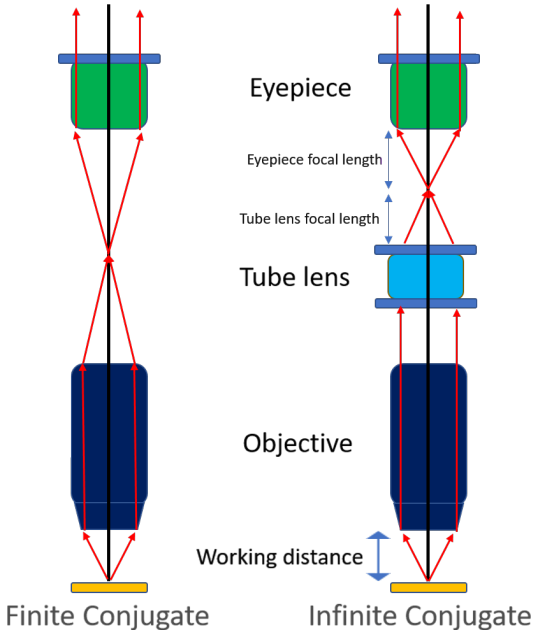

Figure 1.3: Finite conjugate and an infinite conjugate objectives. Reprinted from theonlinethoughts.com.

of the sample. The new technique solved this problem by providing a completely defocused light source image at the sample plane and thus uniform illumination.

Köhler illumination unit consists of a lamp (e.g. a halogen lamp, Figure 1.2 b6), a collector (Figure 1.2 b5) and a condenser (Figure 1.2 b4). The collector consists of a lens and a field diaphragm and is used to focus the incoming light at the plane of the condenser diaphragm. The condenser, in turn, diverges the light rays and projects them further through the plane of the sample. It also consists of a lens and a diaphragm. Its diaphragm defines the angle of the cone of light rays reaching the sample. The lighting produced is incoherent.

When the condenser diaphragm is adjusted so that the illumination angles (illumination NA) perfectly match the maximum accepted angles of the objective (collection NA), the final resolution of the system is optimized. Note, however, that this is only true for bright-field microscopy, the rules for the condenser diaphragm design are very different for dark-field and phase imaging [67].

1.3 Bright-field microscopy performance and limitations

A microscope in the example above (Fig. 1.2) is a bright-field microscope. This means that visible light is used to illuminate the sample in the range of angles collected by the optics. The image is then formed by contrasting the

amount of light transmitted/attenuated (or reflected/absorbed in the case of epi illumination) by the sample at different spatial positions.

The performance of a bright-field microscope is not evaluated by a single parameter, but rather is estimated as a combination of several important characteristics that will be discussed below.

1.3.1 Characteristics of the microscope system

Magnification The magnification of a microscope, or magnification power, can be defined as the ratio between the dimensions of the observed image and the dimensions of the object. The amount of enlargement is related to the optical power, or equivalently, the focal lengths, of its optical components (lenses).

Field of View The field of view (FoV) simply describes the size of the observed portion of the sample. It is mainly determined by the objective magnification and is inversely proportional to it.

When using a digital camera, the practical FoV is often limited by the size of the sensor. In this case, it can be calculated by dividing the camera sensor size by the lens magnification.

Numerical Aperture The numerical aperture (NA) is a dimensionless quantity describing the range of light angles that can pass through the system at a fixed distance, Eq. (1.6) [131].

$$\mathrm{NA} = n \sin\theta, \tag{1.6}$$

where
n is the refractive index of the medium between the sample and the lens,
θ is the aperture angle of a lens, it is half the maximum light angle accepted by the entrance lens.

The microscopes used in this work do not use immersion oil, so the medium is simply air with $n_{air} = 1$. Therefore, when we refer to NA in the consequent passages, we will emit the refractive index n in the Eq. 1.6. In the case of a simple thin lens (Fig. 1.4), the opening angle θ is related to the lens focal length f and the diameter of its entrance pupil D

$$\tan\theta = \frac{D}{2f} \tag{1.7}$$

The numerical aperture of the microscope largely defines the final resolution of the system. High NA objectives, accepting wide oblique angles, make it possible to distinguish smaller structures.

The effective numerical aperture of a classical bright-field microscope is defined as the sum of the cone of light delivered by the condenser and the maximum cone of light accepted by the objective: $\mathrm{NA} = \mathrm{NA}_{\mathrm{condenser}} + \mathrm{NA}_{\mathrm{objective}}$ [131].

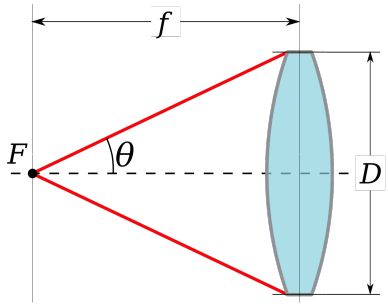

Figure 1.4: The numerical aperture of a thin lens working in air is defined by the angle θ. Reprinted from wikipedia.org.

Resolution Resolution, or resolving power, is one of the most important performance characteristics of a microscope system. In simple terms, it defines the system's ability to discriminate details.

Several phenomena can limit the resolution of an optical system [131], including fundamental physical limitations of imaging, such as diffraction introduced by the interaction of light with the sample, and system properties such as the ability of the lens to capture rays, lens aberration, various types of noise, and so on. The causes of these phenomena will be discussed in the next subsection, while only the definitions are given here.

Multiple associated descriptions can be used to quantify resolution, including angular resolution, spatial resolution, and Rayleigh criterion.

Angular resolution is the definition most often used in the context of optical microscopy and is described by the smallest angular distance $\delta\theta$ between two neighbouring points in space that can be clearly regarded as distinct.

The Rayleigh criterion mathematically defines this smallest distance. For the circular aperture, it is given by Eq. 1.8:

$$\delta\theta = \frac{1.22\lambda}{D}, \tag{1.8}$$

where
$\delta\theta$ is the minimum resolvable angle (in radians),
D is the diameter of the circular opening, see Fig. 1.4,
λ is the illumination wavelength, the wavelength is therefore part of the definition of resolution.

Another quantitative standard often used in microscopy is the spatial resolution r, which is based on the concept of numerical aperture.

$$r = \frac{1.22\lambda}{\mathrm{NA}_{\mathrm{condenser}} + \mathrm{NA}_{\mathrm{objective}}}, \tag{1.9}$$

where
r is the smallest resolvable distance between two objects,
$\mathrm{NA} = \mathrm{NA}_{\mathrm{condenser}} + \mathrm{NA}_{\mathrm{objective}}$ is the effective numerical aperture of the microscope.

Using the Eqs. (1.6-1.9), the angular resolution can be converted to spatial. Spatial resolution also indicates the maximum spatial frequency that the optical system can detect. The relationship between these two notions will be discussed in the next chapter, after introducing the concept of Fourier optics.

The resolution criteria mentioned above apply to the diffraction limit of optical microscopy. Another unrelated factor that decreases resolution in practice is lens aberration.

Aberrations An aberration is an error in the image produced by the actual system caused by the deviation of the beam from the direction predicted for the ideal system. These errors are mainly related to the interactions of the light with the lens material.

All aberrations can be considered as belonging to one of the following two categories: chromatic or monochromatic aberrations.

Chromatic aberrations are attributed to the dispersion that is caused by variations in the refractive index of the lens material for different wavelengths of light.

Monochromatic aberrations describe the deviation of light caused by the shape of the lenses and the alignment of the point source and its image with respect to the optical axis. Among the most common monochromatic aberrations are: spherical, coma, astigmatism, field curvature and distortion [131]. These aberrations will be discussed in more detail in Chapter 3 with respect to the constructed system.

Well-corrected lenses can offer larger numerical apertures and greater resolving power than uncorrected lenses of the same magnification.

Depth of Field The depth of field (DOF) Z describes the axial resolution of the system, measured parallel to the optical axis. It contrasts with the lateral resolution, measured in the plane of the sample perpendicular to the optical axis, to which we have referred when defining spatial or angular resolution above.

It is defined as the maximum distance between two slices in the object plane within which all points are in focus. In other words, DOF refers to the ability of the microscope to maintain focus while axially repositioning the object within a specified limit Z. One of the possible quantitative metrics for Z can be given by Eq. 1.10 [131]:

$$Z = \frac{\lambda}{\mathrm{NA}^2}, \tag{1.10}$$

As a result, low numerical aperture lenses have a greater depth of field.

The criterion above is sometimes referred to as wave optical depth of field. However, it is not sufficient in the context of low numerical aperture lenses where the geometrical optical depth of field also plays an important role. The

total depth of field is then defined as follows [41] :

$$Z_{tot} = \frac{\lambda}{\mathrm{NA}^2} + \frac{e}{m\mathrm{NA}}, \tag{1.11}$$

where m is a system magnification, e is the smallest resolvable distance in the intermediate image plane.

Depth of Focus The notion of depth of focus is linked to the notion of depth of field. It refers to the ability of the system to maintain focus while moving the sensor within a certain distance, as opposed to moving the object. Depth of field can be defined as the range in which the plane of a sensor must be in order for the image of an object in focus to be sharp [135].

Working distance The working distance is simply the distance between the lens and the object on which the object must be placed in order to obtain a sharp image. High-magnification lenses tend to have a small working distance.

Space-Bandwidth Product An important performance characteristic of optical systems is its space-bandwidth product (SBP) [132]. SBP is particularly relevant in the context of Fourier Ptychography and other computational imaging techniques.

This criterion comes from information theory and describes the amount of content transmitted by the system.

A common definition of SPB can be given [12] as a ratio between a total field of view A and a square of system resolution r, Eq. 1.12:

$$SPB = \frac{2A}{r^2} \tag{1.12}$$

Another possible definition uses the number of resolvable pixels. It defines the SPB as the number of effective pixels needed to image the given area A at full resolution.

Neither of these two definitions takes into account the signal-to-noise ratio (SNR), which is acceptable in the present work.

The design of a microscope is often optimized to obtain the highest SPB for the given price.

1.3.2 Limitations of Conventional Microscopy and State of the Art Performance

In order to understand the need for and benefits of computational imaging, the nature of the physical limitations as well as the state-of-the-art features of commercially available optical microscopes should be examined.

Space-Bandwidth Product limit

As mentioned above, the resolution of any optical system is intrinsically limited by the wave nature of light, see Eq. 1.9. According to Abbe's imaging theory [131], three main components contribute to this limitation: diffraction caused by the interaction of light with the internal structures of the sample, diffraction caused by the edges of the lens aperture, and constructive and destructive interference of light waves in the image plane.

Thus, an optical microscope is a diffraction-limited system. Moreover, the lens manufacturing process does not allow to build aberration-free objectives with an arbitrary large aperture.

The numerical aperture values in conventional optical microscopes range from 0.025 to about 1.35 [41, 136, 195]. Zeiss offers a 100x lens with NA = 1.57 [161]. Objectives with NA$>$ 1 are generally designed to operate in oil immersion mode.

The minimum value of the visible spectrum is 380 nm for violet light. Considering a system with numerical aperture of 0.6 (corresponds roughly to magnification of x40), the diffraction limit given by the Eq. 1.9 is about $\lambda/2 =$ 190 nm. Even taking into account the best available NA and oil immersion, the resolution of a bright field microscope still does not fall below 100 nm for any of the visible light frequencies.

Such resolution is acceptable for imaging biological cells (1 to 100 microns) and bacteria (500 nanometers to 5 micrometers), but is not sufficient for viruses (20 and 300 nanometres) and smaller structures.

Magnification and resolution cannot be directly deduced from each other. In practice, however, the lens manufacturer often ensures that the magnification is proportional to the numerical aperture, given the same level of optical aberration correction [41].

The objective magnification of commercially available light microscopes ranges from 1x to 150x [136, 161]. The final magnification of the system also depends on the eyepiece, which usually provides an additional factor of 10x, resulting in a maximum useful magnification of 1500x.

The magnification of a single lens is inversely proportional to its working distance and, therefore, the field of view of the lens is inversely proportional to the square of the magnification [63]. In addition, high NA lenses introduce a significant amount of geometrical aberrations, especially spherical aberrations, which also limits the area where image quality is acceptable.

This leads to the famous compromise between the observable area and the resolution of the system. Since the spatial bandwidth product describes both FOV and resolution, it is a good metric to describe the performance of the microscope with respect to this trade-off.

As analyzed in [12], a standard commercially available microscope objective has an SBP (as defined by Eq. 1.12) of the order of megapixels. And this holds true regardless of magnification, FOV or numerical aperture. Solutions to increase the SPB will be reviewed in the next subsection.

Loss of Information

Of all the interactions of the light with the specimen, the only possible information to be recorded is the intensity of the wavefront that reaches the camera sensor. This is due to the intrinsic limitations of digital cameras and will be discussed in more detail in Chapter 2. For transparent samples, this means that the information will simply not be captured by the system.

A common way to overcome this problem in the context of histological slides is tissue staining, which enhances contrast in samples by dyeing distinct cell structures. However, staining requires the intervention of a biologist and can damage the tissue. In addition, some staining is not compatible with cell life.

At the same time, the interactions of the light and the sample produce changes in the polarization state of the wave and also in its phase. Therefore, by using techniques that can reveal these changes, it is possible to shed light on lost information and/or avoid staining of the tissue.

The 3D information on the sample is also reduced to a single 2D image.

1.4 Exceed the limits

The race to increase the quantity and quality of information transmitted and to recover lost light-matter interactions has been going on since the very birth of microscopy. Many methods have been proposed to address some of these issues one by one or to find the optimal trade-offs.

1.4.1 Exceed the limits by hardware modifications

Increase Space-Bandwidth Product Motorized scanning systems are an obvious solution that offers high resolution with a wide field of view. An example of such a system would be a mechanical scanning microscope or a digital pathology scanner [160]. They rely primarily on the ability to scan a sample from one point to another within the area of interest. These systems are expensive, difficult to manufacture, require precise calibration, and take up a lot of space.

Increase contrast and recover lost information Conventional bright-field transmission microscopy depends primarily on the absorption of light by the non-transparent parts of the sample. Dark-field microscopy, on the other hand, aims to capture only those light beams that have been deflected rather than absorbed. The operation of a dark field microscope is based on eliminating the undeflected wave components by placing a stop under the sample and thus blocking direct illumination. This method allows the imaging of low-contrast samples, in particular the highlighting of edges and surface defects.

In the 1930s, a new method called phase-contrast microscopy was developed and virtually replaced dark-field microscopy. It allows the phase to be visualized by converting the underlying phase shifts produced by the sample into intensity differences. Phase-contrast microscopy requires a specialized objective with a phase plate and a condenser annular diaphragm. While a darkfield microscope tends to emphasize external details, a phase contrast microscope is equally excellent for revealing internal structures.

One disadvantage of phase contrast microscopy is the appearance of a bright diffraction halo around structures. Differential interference contrast microscopy aims to solve this problem. The configuration is very different from that of a brightfield, darkfield or phase contrast microscope. Imaging is based on polarization optics and double-beam interference, resulting in costly hardware modifications.

Finally, polarization microscopy is used to capture changes in the polarization state of the light lost by the detector. Its principles of operation will be explained in Chapter 4, after introducing the basics of polarization.

In addition, there is fluorescence microscopy, which is based on the emission of light in response to the excitation of a pre-prepared sample. An overview of other optical techniques, like modulation contrast microscopy or confocal laser scanning microscopy can be found in [131]

1.4.2 Exceed the limits by computational imaging

Computational imaging techniques seek to overcome the physical limitations of traditional imaging due to digital data processing. We are particularly interested here in improving resolution and phase retrieval.

In terms of improving resolution, a family of techniques called super-resolution is widely used. The objective is to increase resolution down to the nanometer scale. The first methods were based on fluorophores excitation. Examples include stimulated emission depletion (STED) microscopy, [74] photoactivated localization microscopy (PALM) [75] and structured illumination microscopy (SIM) [70], to name a few. However, sample preparation by application of fluorescence markers was required. Non-fluorescent analogues of some of these techniques were later proposed [32], but they still relied on the contrast present in the sample due to artificial or natural staining.

Phase imaging, on the other hand, can work with optically transparent samples without adding additional contrast. There are many different techniques for phase recovery using computational imaging [173, 175]. Many of them additionally improve the resolution of the system [128]. Examples include conventional ptychography [168], digital holography [23], quantitative phase structured illumination microscopy [33], quantitative interferometric microscopy [172] and many others.

However, Fourier ptychography, proposed by G. Zheng et al. in 2013 [244], has several important advantages. The most significant are cost effectiveness,

improved resolution without sacrificing the field of view (FOV), simplicity of hardware configuration, and recovery of both phase and intensity information.

Chapter 2

The phase problem and Fourier ptychography

Fourier Ptychography procedure seeks to reconstruct a complex, high-resolution signal from a set of low-resolution intensity images corrupted by noise. This complex signal can be decomposed into amplitude (square root of intensity) and phase.

This technique belongs to the family of information loss problems, called "phase problem". A procedure for solving the "phase problem", that is to say the phase reconstruction from intensity measurements of an object or, alternatively, its Fourier magnitudes, is called "phase retrieval".

On the other hand, the technique also belongs to the group of super-resolution methods.

2.1 Phase retrieval applications and techniques

Solutions to the phase problem are sought not only in optical imaging, but also in many other scientific fields [87, 175].

In general, this problem occurs during physical measurements of phenomena which can be described as waves. Most current measurement methods, such as detection using digital cameras, can only record the intensity of the wavefront. In addition, this phaseless data is, in real life, corrupted by noise. The exact reasons for the inaccessibility of the phase are specific to each field of application.

In this section, we give a brief overview of phase recovery techniques in optical imaging and other fields. We also describe conventional Ptychography, a forerunner of the Fourier Ptychography method.

2.1.1 Examples of phase problems

X-ray Crystallography X-ray crystallography is one of the first fields to highlight the benefits of phase retrieval. The idea of using phase information

to evaluate the atomic arrangements in crystal samples dates back to 1912 [169].

The initial objective of crystallography was to recover the structure of molecules arranged in a crystal lattice. Most approaches were based on the periodicity of such structures.

Indeed, such a periodicity is reflected in the Fourier domain of the object. The Fourier information is in turn obtained from measurements of diffracted waves in the far field. For the moment, we do not explain this phenomenon but we come back to it in Section 2.2.2.

The reconstruction algorithms still needed specific domain knowledge in order to correctly estimate the phase.

X-ray crystallography was then extended to more general non-crystalline samples, such as biological molecules in the end of 20th century [126].

Various techniques have been developed to solve the phase problem in crystallography, but we will limit ourselves to what has been said above and discuss in more detail the optical phase extraction at visible light frequencies.

X-ray Coherent Diffraction Imaging Coherent diffraction imaging is another phase recovery technique using X-ray light sources to image structures at the nanoscale. It can also be used to detect defects such as strain of materials [154]. Unlike the case of X-ray crystallography, the sample does not have to be crystalline and periodic.

The technique does not use lenses which make it possible to avoid significant aberrations in X-ray optics. The material and computer advances of recent years have alleviated some of the limits of conventional crystallography. We can thank the emergence of more powerful X-ray sources and detectors and the development of algorithmic approaches for the birth of coherent diffraction imaging [127]. Modern coherent diffraction imaging techniques are capable of reconstructing quantitative 3D images at the nanoscale using iterative inversion methods.

Astronomy As in many other imaging fields, phase information in optical astronomy is unavailable or very limited.

One of the most widely used methods for collecting spatial images are the techniques of radio interferometry. An astronomical interferometer consist of several telescopes working together. This intensity interferometric signals, combined, offer a higher resolution and the possibility to reconstruct the lost phase information [53].

Phase recovery algorithms are also used to align optics in space telescopes. In the case of the Hubble telescope, these algorithms have made it possible to determine the aberrations and to correct the distortion of the image [55]. In the James Webb space telescope, phase retrieval will be used to calculate the precise positions of the hexagonal mirror segments, and then adjust these segments using micro-motors [1].

2.1.2 Phase problem in optical imaging

As mentioned in the previous chapter, the wavelengths of visible light are between 400 and 700 nm, which corresponds to a frequency range of about 430 to 750 terahertz (THz). No measuring device can directly record oscillations of such a high frequency [175]. Modern digital cameras are only able to measure the amplitude squared of the light field.

In the context of optical imaging, the quantitative phase establishes a direct link between the reconstructed image and the delay of the electromagnetic output wave. This quantity in turn describes the product of the refractive index of the material and its thickness, which are among the important physical parameters of a sample.

As mentioned in Chapter 1, phase data can be visualized using optical techniques such as the phase contrast microscope or differential interference contrast microscopy. The phase images obtained do not give quantitative information, i.e. the intensity value of a pixel does not correspond directly to the amount of underlying phase shift. This is partly due to the mixing of the intensity differences introduced by the phase shifts with the intensity variations introduced by the transmittance of the sample.

Quantitative phase imaging, on the other hand, transforms the optical path difference of light passing through a sample into phase shifts in degrees. Such a phase image can be distinctly separated from the amplitude information. These techniques apply, in most cases, algorithmic approaches.

Systems providing phase contrast in the form of intensity variations rely mainly on hardware solutions, while quantitative phase imaging is mainly based on calculations.

Although there exist camera-like instruments for quantitative phase imaging [251], they also rely on algorithmic approaches via real-time computing and will not be discussed here.

There are numerous distinct techniques of retrieving the phase by computational imaging [173]. Some of these methods rely on recording the intensity of the interference patterns. Examples of such techniques include Scanning Diffraction Imaging (conventional Ptychography) [168] and Holography [23]. As in the case of X-ray crystallography and X-ray Coherent Diffraction Imaging, the recorded interference patterns represent the information on the spectrum of the sample. Other methods directly record intensity images in the conventional spatial domain, such as Fourier Ptychography or Structured Illumination Microscopy [33].

Digital holography Digital holography refers to a series of interferometric imaging techniques [193]. It captures holograms (interference patterns containing information about the diffracted wavefront of an object) using a digital camera. The intensity and the phase images are then reconstructed numerically. Among holographic microscopy methods mentioned in this work are phase-shifting digital holography and digital in-line holography. Both will be

discussed in more details in Section "Quantitative phase imaging" of Chapter 4.

2.1.3 Real-space ptychography

It is important to consider Conventional Ptychography because it is a direct precedent of the Fourier Ptychography imaging. Or, at least, we can say that this method has largely inspired the development of Fourier Ptychography. In addition, it has been shown that the developments in Conventional Ptychography, sometimes also called real-space Ptychography, can be directly applied in the context of Fourier Ptychography [69].

Although the idea of Ptychography was proposed around the 1970s, proof of principle and inversion methods were only developed after about 25 years [167].

Ptychography is a lenseless computational microscopic imaging technique, but lenses can and are often used in experimental set-ups.

There are many optical configurations for Ptychography. Most of them can be classified as a scanning imaging technique. In the simplest case of single aperture Ptychographic microscopy, the operating principle is as follows.

An object is lit with a known lighting function. This sample is then shifted several times by a known amount. The intensity of an interference pattern produced is recorded by the detector for each of these movements. Usually the interference pattern is in the form of a Fraunhofer diffraction which is obtained by placing the camera in the far field of the object. Fraunhofer diffraction will be described in more detail in the next section. A set of these patterns is then converted into high-resolution images of the phase and amplitude of the object. It is important to note that a strong overlap of the recorded diffraction patterns must be preserved when moving the object.

In recent years there has been a growing interest in the development of iterative phase recovery algorithms, which has contributed to the popularity of Ptychography.

Ptychography in real space is a distinct technique with its own advantages, and Fourier Ptychography does not replace it, but rather offers a different conceptual point of view. Despite the differences that will be discussed below, these techniques are closely related. More precisely, their datasets are linked by a linear transformation in the case of ideal illumination conditions [80].

2.2 Fourier ptychographic microscopy

The Fourier ptychographic microscopy (FPM) was originally proposed by G. Zheng et al. [244] to produce a wide-field, high-resolution image of the amplitude and phase of a sample. Like classical Ptychography, Fourier ptychographic microscopy is a computational imaging technique.

It allows to bypass some physical limits of a medium-quality microscope by adding a simple light-emitting diode (LED) matrix to the conventional setting and performing the digital processing. The cost efficiency of this solution has recently attracted extensive research interests.

Before discussing the details of this method and its relationship with the real-space Ptychography, let us first illustrate the phase problem with an example of a 1D signal.

2.2.1 The phase problem (the forward model) in 1D

In order to conveniently manipulate the phase and amplitude of the wave as a single value, complex numbers may be used. It is a common representation in signal processing, physics and other fields. In the case of optical imagery, the use of complex numbers reflects the wave property of electromagnetic radiation.

In addition to complex numbers, this section is largely based on two important notions: the frequency domain and signal filtering. The definition of these concepts will not be presented in this thesis as they can be easily found in any book on signal processing.

The signal To simplify, let us first consider a real 1D signal, that is to say that its phase is equal to zero. Such a signal $f(x) \in \Re$ is defined only by its amplitude values. In Figure 2.1a, we use as an example a profile of an image of a biological sample.

Fourier Domain Any signal can be represented in its frequency domain by calculating its Fourier transform, Eq. (2.1). In practice, we operate with discrete signals and apply a discrete Fourier transform using a fast Fourier transform algorithm.

$$\hat{f}(\xi) = \mathcal{FT}(f(x)) = \int_{-\infty}^{\infty} f(x) e^{-2\pi i x \xi} dx \tag{2.1}$$

where
x – the spatial coordinate;
ξ – the frequency coordinate in the Fourier plane;
$f(x)$ - the signal in the spatial domain;
$\hat{f}(\xi)$ – the 1D Fourier transform of the signal $f(x)$.

Even if the original signal $f(x)$ in this example contains only real values, the signal $\hat{f}(\xi)$ is complex in the Fourier domain and must still be defined by both the amplitude and the phase. To illustrate the importance of the phase part of the Fourier domain of the signal, we can perform an inverse Fourier transform operation only on the amplitude part, i.e. $g(x) = \mathcal{FT}^{-1}(|\hat{f}(\xi)|)$. The result of this operation is depicted in the Fig 2.2. As we can see, the inverted signal $g(x)$ does not look at all like the original one $f(x)$, which underlines the importance of phase information.

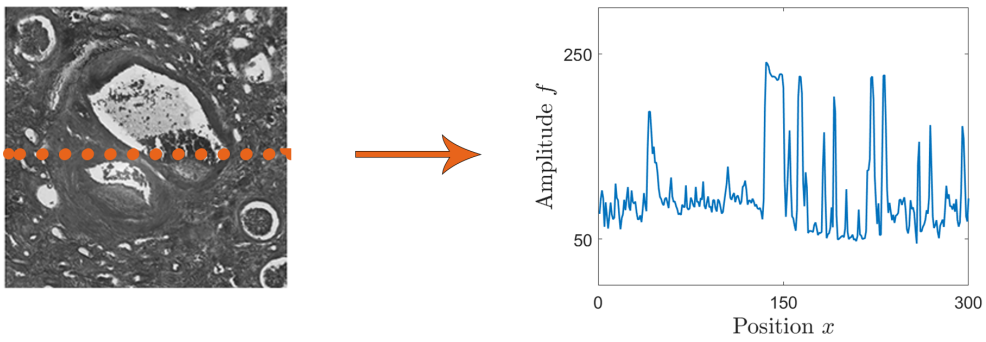

(a) 1D signal example $f(x)$ (a profile of an image of a biological sample)

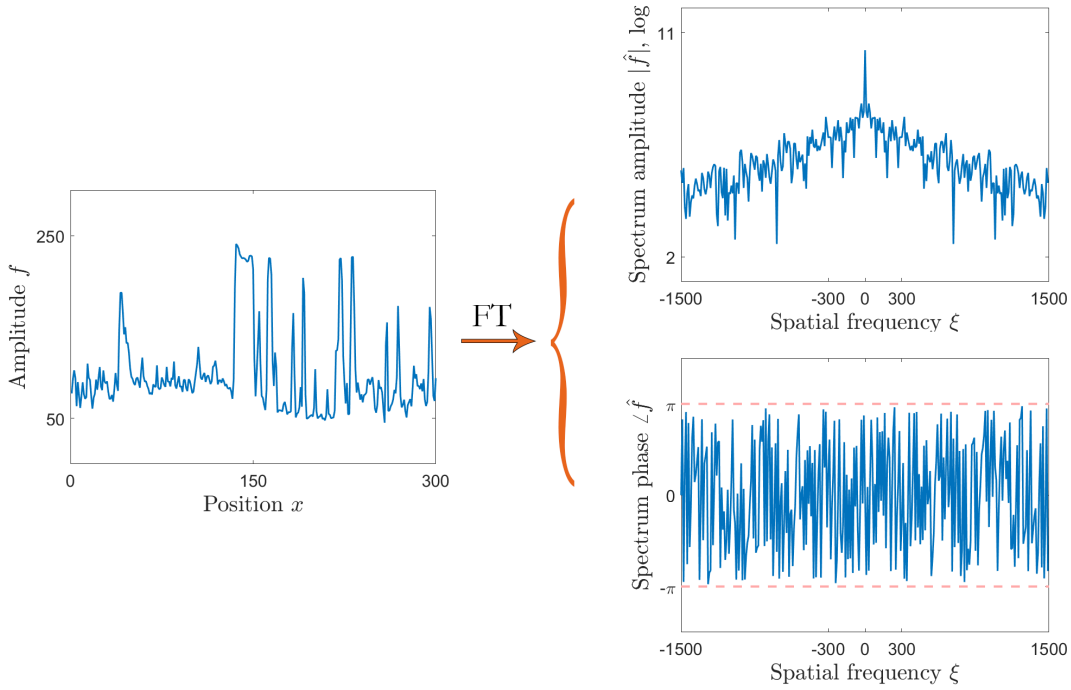

(b) Its Fourier transform $\hat{f}(\xi) = \mathcal{FT}(f(x))$

Figure 2.1: A 1D real signal $f(x) \in \Re$ in the spatial domain (left a) and its complex counterpart $\hat{f}(\xi) \in \mathbb{C}$ in the frequency domain (left b).

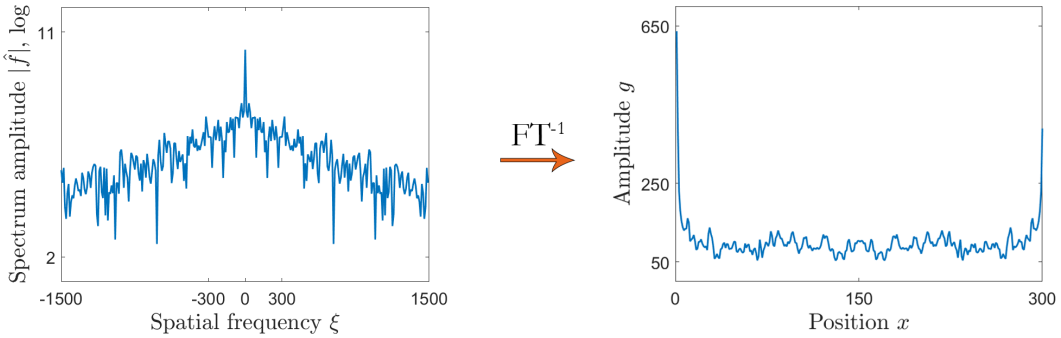

Figure 2.2: Inverse Fourier transform of the amplitude part of the signal in the frequency domain $g(x) = \mathcal{FT}^{-1}(|\hat{f}(\xi)|)$.

We discuss in the next section how the optical Fourier transform is effected by a pupil of the objective in a microscope system.

Low-pass filtering Before a signal can be recorded, most physical measurement systems apply some sort of filtering. In conventional optical microscopes, a low-pass filtering is carried out. In our 1D example, we use a boxcar function $P(\xi)$ to emulate such a filter in the frequency domain, Eq. (2.2).

$$P(\xi) = \begin{cases} 1, & \text{if } |\xi| \leq \xi_c \\ 0, & \text{if } |\xi| > \xi_c \end{cases} \tag{2.2}$$

where ξ_c is a cut-off frequency of the filter.

This cuts off the high frequencies, so the low frequencies only reach a recorder:

$$\hat{f}_c(\xi) = \hat{f}(\xi) \times P(\xi) \tag{2.3}$$

where $\hat{f}_c(\xi)$ is the filtered version of the original spectrum $\hat{f}(\xi)$, Figure 2.3.

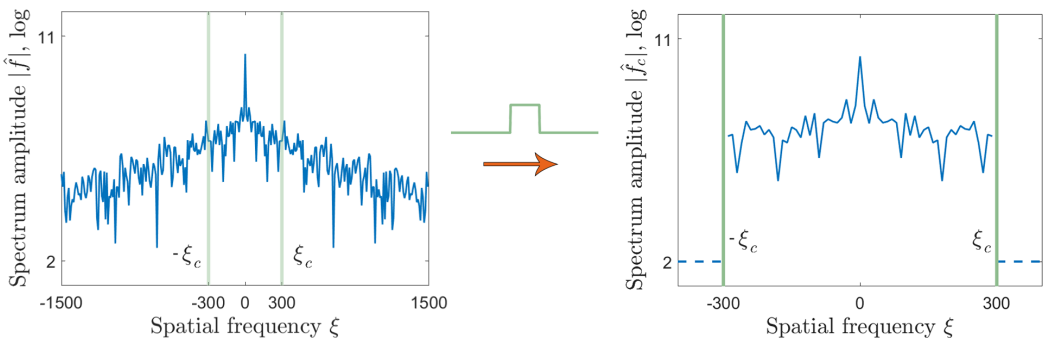

Figure 2.3: 1D low-pass filtering, only the amplitude part is shown.

In the case of conventional Ptychography, the intensity of this cut Fourier spectrum $|\hat{f}_c(\xi)|^2$ is recorded by the camera (as a 2D image of a diffraction pattern under real experimental conditions). However, in the case of conventional optical devices, the signal (an image) is captured in the spatial domain. Hence we need to perform the inverse Fourier transform on the filtered signal, Figure 2.4.

$$f_c(x) = \mathcal{FT}^{-1}(\hat{f}_c(\xi)) = \int_{-\infty}^{\infty} \hat{f}_c(\xi) e^{2\pi i x \xi} d\xi \tag{2.4}$$

where $f_c(x)$ is a low resolution version of the original signal $f(x)$, corresponding to the cut spectrum $\hat{f}_c(\xi)$.

Lost high frequencies cause signal blurring and loss of resolution. The cutoff frequency of the filter, or equivalently the width of the spectral band, defines the final resolution of the system.

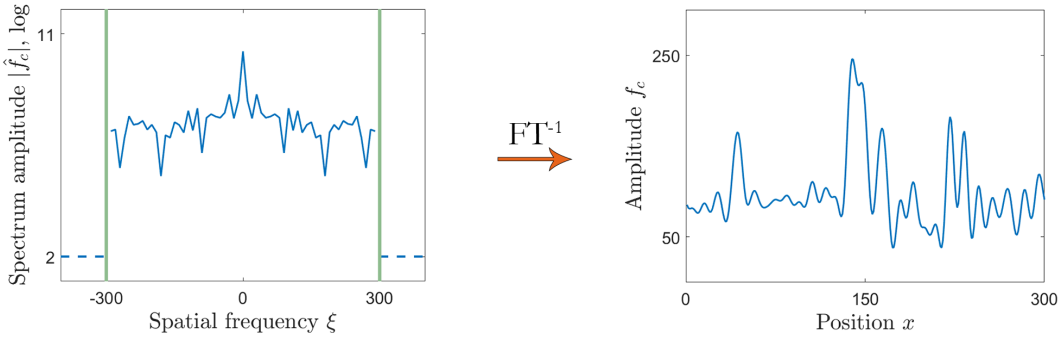

Figure 2.4: Inversion of the filtered signal $\hat{f}_c(\xi)$, only the amplitude part is shown.

Detection It is still not the filtered signal $f_c(x)$ that is measured in imaging, but its intensity, which is the amplitude squared $|f_c(x)|^2$. In the example given, there is no difference between measuring the signal strength rather than the signal itself because the original signal $f(x)$ is real and is entirely defined by its intensity.

On the other hand, an optical signal, which is an electromagnetic wave, is a complex signal, hence the phase is also necessary to fully define it. Two signals of the same intensity but of different phases might correspond to very different spectra, Fig. 2.5. Consequently, the loss of phase information makes it impossible to access the spectrum by a simple Fourier transformation.

Spectrum shift Without a doubt, we want any system to be able to record as much information as possible. In the example above, we would like to have access to the phase of the signal lost in the detection stage and to the high frequencies lost in the filtering stage. The width of the spectral band is intrinsic to the measurement system used and in many cases impossible to expand without compromising the other characteristics of the system. However, we can indirectly access those high frequencies by shifting the zero frequency component of the spectrum, or, equivalently, by shifting the spectral band, Fig. 2.6.

It follows from the properties of the Fourier transform that the frequency shift can be effected by multiplying the signal in the spatial domain by a complex exponential:

$$\mathcal{FT}(f(x)e^{2\pi i x\xi_0}) = \hat{f}(\xi - \xi_0) \tag{2.5}$$

.

The corresponding intensity signal $|f_{s_1}(x)|^2$ is still of low resolution, but this time it contains the high frequency information, Fig 2.7.

$$f_{s_1}(x) = \mathcal{FT}^{-1}(\hat{f}(\xi - \xi_0) \times P(\xi)) \tag{2.6}$$

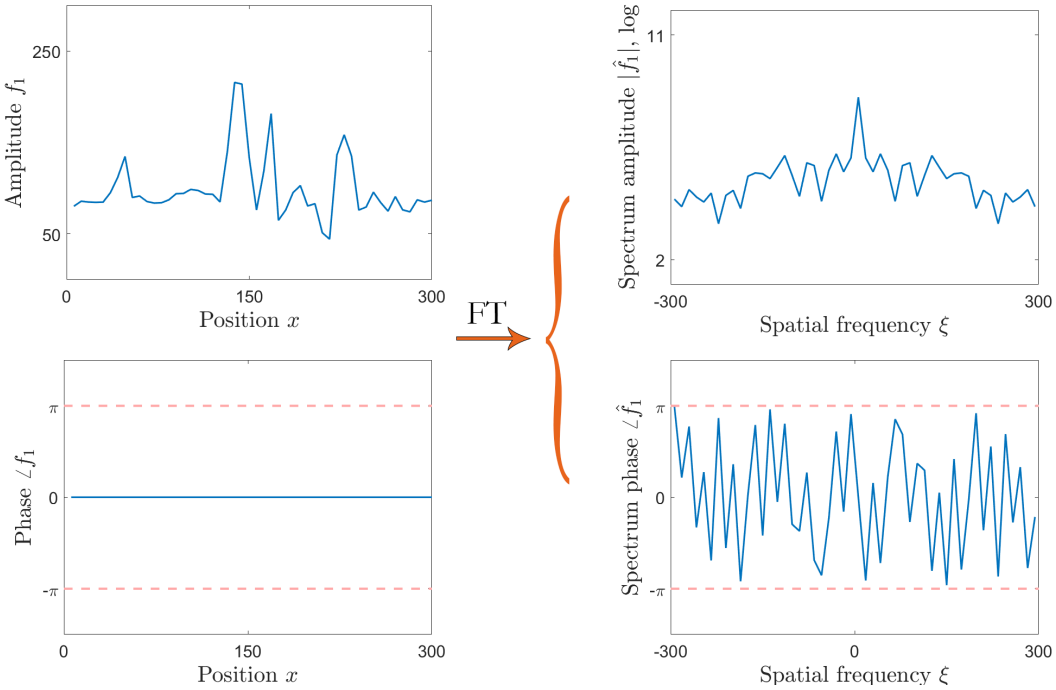

(a) Signal $f_1(x)$ and its spectrum $\hat{f}_1$ (ξ)

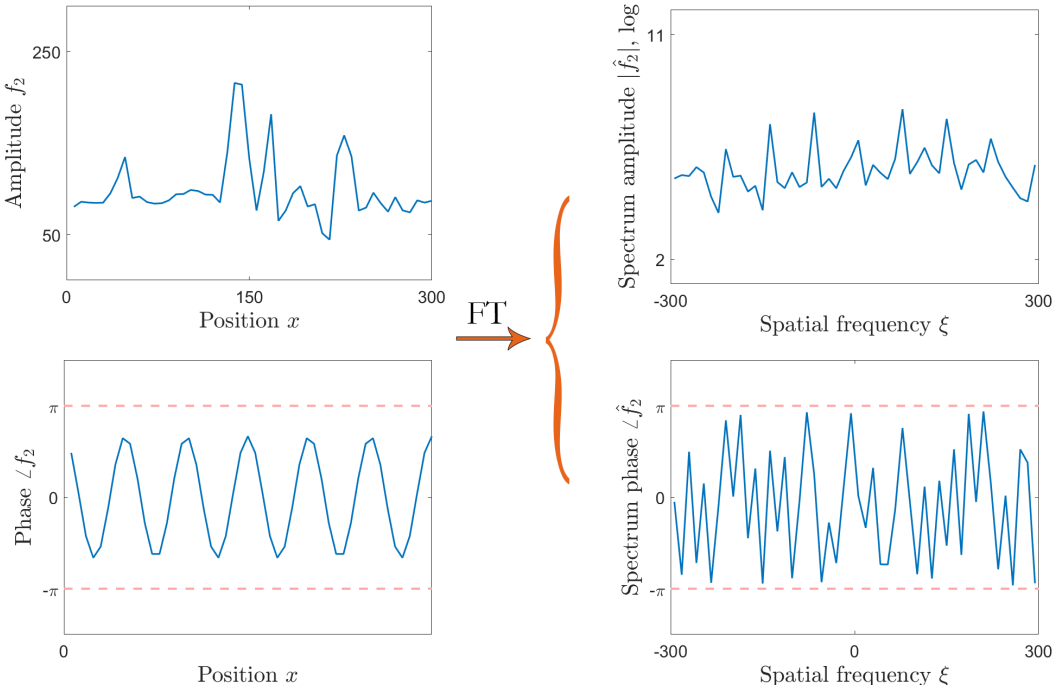

(b) Signal $f_2(x)$ and its spectrum $\hat{f}_2(\xi)$

Figure 2.5: Two signals $f_1(x)$ and $f_2(x)$ of the same amplitude $|f(x)|$ but of different phases might correspond to very different spectra.

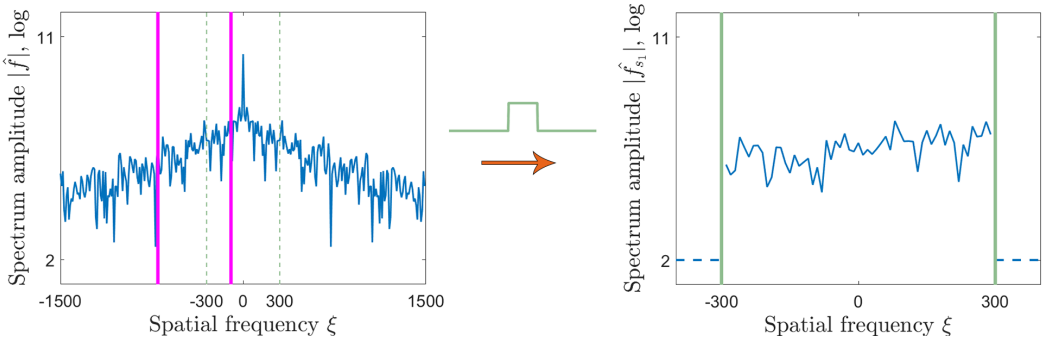

Figure 2.6: Part of the spectrum corresponding to the shifted spectral band, only the amplitude part is shown.

where $f_{s_1}(x)$ is a complex low resolution signal corresponding to the spectrum cut by a spectral band shifted to ξ_0.

The amplitude values of this signal $|f_{s_1}(x)|$ are lower than the values of the signal corresponding to the central spectral frequency band $|f_c(x)|$. This occurs due to the behavior of the power spectrum of this particular example (which is a profile of an image of a biological sample). Indeed, the signal $f(x)$ has a higher concentration of spectral energy at low frequencies.

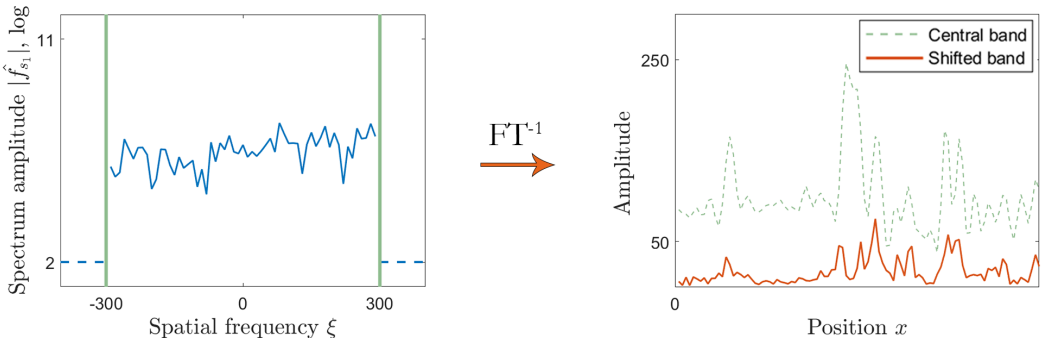

Figure 2.7: Amplitude of the signal $|f_{s_1}(x)|$ (on the right, the orange curve) corresponding to the shifted spectral band (on the left). Only the amplitude part of the spectrum is represented. The green dotted curve corresponds to the central spectral band.

Signal recovery Now, the two amplitude (or intensity) signals captured ($|f_{s_1}(x)|$ and $|f_c(x)|$) together represent an enlarged spectral bandwidth. Therefore, if we could have direct access to the corresponding parts of the spectrum, the final system resolution would be higher.

Unfortunately, the loss of phase information leads to inaccessibility of the spectrum. As we have shown above, two signals of the same amplitude but of different phases can correspond to very different spectra. This introduces ambiguity in phase recovery. Therefore, we need an overlap between two neigh-

boring parts of the "measured" spectrum to remove some of the ambiguity. This results in "redundancy" in the captured data set.

The same reasoning applies to the recovery of the signal only from the intensities of the spectrum, which is the case of real-space Ptychography, where the overlap between the recorded diffraction patterns is also necessary.

The process of capturing intensity signals corresponding to different frequency shifts is the basis of the idea of Fourier Ptychography. How to implement it using optics will be described in the next section.

Finally, we will have to apply an algorithm to perform the reconstruction of the high resolution complex signal. The inversion methods, as well as the data redundancy conditions will be discussed in Section 2.3.

2.2.2 The principle of Fourier ptychographic microscopy

The 1D model described above can be extended to the 2D variant of this problem, namely imaging systems.

The signal In transmission mode systems, a light wave emerging from an illumination source and passing through the sample is a complex object $o(x, y)$. It is defined at every point (x, y) of the sample by its amplitude and its phase.

The amplitude is directly related to the transmittance of the material. For the fully transparent object, the amplitude is constant at each point. Amplitude and phase can be two independent images, however, in real situations, some information often overlaps.

For illustration purposes, we take two classic images as an example, the USAF target for amplitude and the cameraman normalized from $-\pi$ to π for phase, Fig. 2.9. As in the case of the 1D signal, the phase information is a crucial part of the description of the object.

Fourier Domain and Fourier optics To understand the properties of the optical Fourier transform and the optical spectrum shift, it is important to first study the concept of Fourier optics.

Fourier optics considers light as a wave and studies it by spectral analysis. This means that the light passing through the object is considered as a sum of spatial sine waves at different frequencies [152]. Two common approximations to the scalar diffraction theory connects the diffraction patterns to the Fourier transform in Fourier optics [62]. These are Fresnel and Fraunhofer approximations, only the latter, also called the far field approximation, will be discussed here.

Consider an object illuminated by a plane wave with normal incidence. Fraunhofer's approximation is an approach to describe the field as observed at infinity with respect to an aperture of the system. In this condition, according to Fraunhofer's formula, the strength of the field is proportional to the two-dimensional Fourier transform of the object performed with respect to the

coordinates x and y in the plane of the object (up to a scaling constant and a change of coordinates).

Fraunhofer diffraction has also been shown to be observed in the focal plane of a positive (converging) lens. Indeed, one can place a lens at a focal distance from the sample and observe the Fraunhofer diffraction at a focal distance from the lens, which is, again, equivalent to the Fourier transform of the sample. The use of lenses then makes it possible to get rid of the condition of being placed at infinity.

In the same way, a lens can also be used to perform the inverse Fourier transform and obtain the image in the spatial domain. This is the principle of a 4-f system which is a two lens imaging system, Fig. 2.8. A classic Fourier Ptychographic microscope has optical configuration of the 4-f system.

It is important to note that Fourier optics remains true only for time invariant and linear imaging systems.

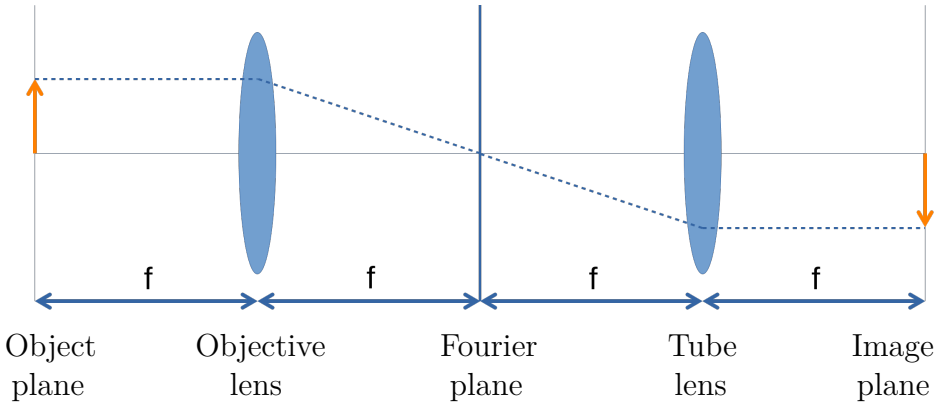

Figure 2.8: 4-f imaging system. The object plane is the front focal plane of the first lens. This is the objective lens in microscope systems. It performs a Fourier transform which forms in its back focal plane, this is where the Fourier plane of the object is located (also called the pupil plane). The inverse Fourier transform is performed by the second lens (in microscope systems, this is generally the tube lens). The image plane is in the back focal plane of this second lens.

In order to simulate the Fourier plane of the optical system, we apply a two-dimensional Fourier transform to the complex object using a fast Fourier transform algorithm. With the example images, we can observe that the phase of the Fourier domain seems almost random. However, just like in the case of a 1D signal, it stores a significant part of the information on the original object.

The two-dimensional Fourier transform:

$$O(k_x, k_y) = \mathcal{FT}(o(x, y)) = \int_{-\infty}^{\infty} \int_{-\infty}^{\infty} o(x, y) e^{-2\pi i (x k_x + y k_y)} dx dy \tag{2.7}$$

where
(x, y) – the spatial coordinates in the sample plane;

(k_x, k_y) – the spatial frequency coordinates in the Fourier plane;
$o(x, y)$ – the sample;
$O(k_x, k_y)$ – the 2D Fourier transform of the sample.

It might also be noted that a real object with a zero phase has a symmetrical Fourier transform. It is the phase differences at different points in the sample that cause changes in the direction of light propagation and result in asymmetries in the spectrum [201].

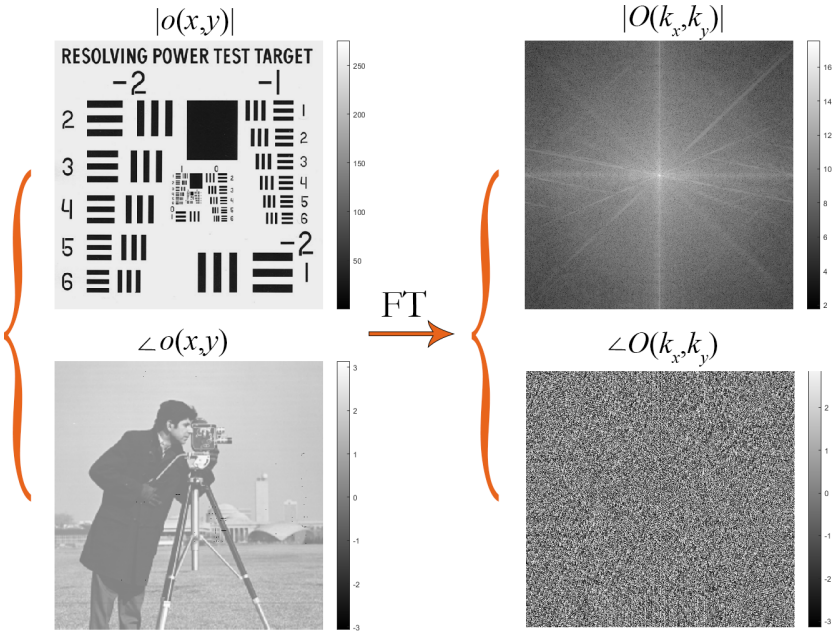

Figure 2.9: The complex 2D image $o(x, y)$ is defined by its amplitude $|o(x, y)|$ and phase $\angle o(x, y)$, on the right. On the left, its Fourier transform $O(k_x, k_y)$ is shown. The zero-frequency component is shifted to the centre of the output.

Low-pass filtering The classic Fourier ptychographic platform is a coherent microscopy imaging system, which means that the lighting is considered to be spatially coherent.

As has already been said in Chapter 1, any microscope has a resolution limit, imposed mainly by the objective lens. This resolution limit can also be explained using the concepts of Fourier optics and the frequency domain.

Consider a simple linear imaging system. Let the lighting to be a temporally and spatially coherent point source. We use a phasor (a complex amplitude) $o(x, y)$ to describe the light field created by this source and passed through the sample. A phasor is simply a complex number representation of a sinusoidal function whose amplitude, phase and frequency do not depend on time.

Let us also consider that an infinitely thin sample is placed at the working distance of the pupil, so that the sample is in focus. A complex amplitude of

the electric field transformed by the imaging system $o_{output}(x, y)$ is formed in the image plane.

It is known that for coherent systems, the output light field $o_{output}(x, y)$ is obtained in the form of convolution of the input field $o(x, y)$ with the spatial implulse response function of the imaging system $h(x, y)$, Eq. (2.8) [243]. The spatial impulse response function, also called in optics the point spread function (PSF), is a function that describes the response of an imaging system to a point source.

$$o_{output}(x, y) = h(x, y) \circledast o(x, y) \tag{2.8}$$

where $\circledast$ stands for the 2D convolution operation.

Convolution in Fourier domain becomes a multiplication:

$$O_{output}(k_x, k_y) = H(k_x, k_y) \times O(k_x, k_y) \tag{2.9}$$

where
$O_{output}(k_x, k_y) = \mathcal{FT}(o_{output}(x, y))$ – the spectrum of the complex amplitude of the output field,
$O(k_x, k_y) = \mathcal{FT}(o(x, y))$ – the complex amplitude of the input field in the Fourier plane of the system,
$H(k_x, k_y) = \mathcal{FT}(h(x, y))$ – the spectrum of the point spread function, we call it the coherent transfer function or the amplitude transfer function of the microscope.

In 4-f systems, the normalized coherent transfer function $H(k_x, k_y)$ is mathematically identical to the pupil function $P(k_x, k_y)$, scaled to the output coordinates. From now on, we will use the pupil function $P(k_x, k_y)$ instead of the transfer function $H(k_x, k_y)$ to describe the imaging model. The pupil function $P(k_x, k_y)$ describes the properties of light transmission through the lens and acts as a low-pass filter for spatial frequencies. For the moment, we assume the absence of aberrations and other imperfections in our optical system. Under these conditions, the pupil can be defined as a circular opening of radius R with unity inside and zero outside the aperture, Eq. (2.10).

$$P(k_x, k_y) = \begin{cases} 1, & \forall (k_x, k_y) : \sqrt{k_x^2 + k_y^2} \leq R^2 \\ 0, & \forall (k_x, k_y) : \sqrt{k_x^2 + k_y^2} > R^2 \end{cases} \tag{2.10}$$

However, it should be borne in mind that the pupil function is generally a complex object which indicates that the optical system can deviate not only the amplitude of the light, but also its phase.

The radius of the pupil function depends on the numerical aperture of the objective and the wavelength of the lighting: $R = 2\pi \frac{\mathrm{NA}}{\lambda}$. This value defines the system cutoff frequency of the system, the features defined by the frequencies outside the aperture are not resolved. Consequently, the spatial filtering is carried out, Fig. 2.10.

While the cutoff frequency defines the theoretical resolution of the system, the actual resolution is also affected by imperfections of the optical elements and other errors and noises.

As it was discussed above, after the high frequencies are cut, the tube lens gets back the image to the spatial domain by performing the inverse Fourier transform.

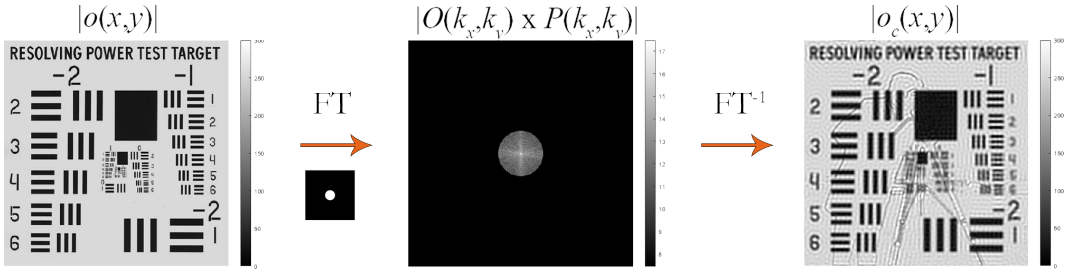

Figure 2.10: The complex 2D image $o(x, y)$ is filtered in the Fourier domain, only the low frequencies falling inside the aperture have passed through the system. The images (both the amplitude and the phase) in the spatial domain have fewer resolved features. Only the amplitude part is shown.

Detection A digital camera is only sensitive to the intensity of the light field, so the phase information is lost. Finally, a low-resolution intensity image I_c of the thin sample is captured. This process can be modelled as follows:

$$I_c(x, y) = |\mathcal{FT}^{-1}\{P(k_x, k_y)O(k_x, k_y)\}|^2 \tag{2.11}$$

where
(x, y) – the spatial coordinates in the sample plane;
$I_c(x, y)$ – the real-valued intensity measurement (the captured image, considered noiseless for the moment);
(k_x, k_y) – the spatial frequency coordinates in the Fourier plane;
$O(k_x, k_y)$ – the 2D Fourier transform of the sample's transmission function $o(x, y)$, i.e. $O(k_x, k_y) = \mathcal{FT}\{o(x, y)\}$;
$P(k_x, k_y)$ – the pupil function of the objective lens;
$\mathcal{FT}^{-1}$ – the inverse 2D Fourier transform operator.

Spectrum shift As suggested before, in the description of the 1D problem, it is possible to "capture" a part of the spectrum corresponding to a higher cut-off frequency by shifting the spectrum and combining the shifted images.

We know that multiplying a signal by a complex exponential produces a desired spectrum shift. It is also known that a plane light wave can be modelled as a complex exponential. Consequently, by illuminating a sample at an oblique angle of incidence with a wave whose front has a flat shape, the expected result is obtained.

For the light source to be validly approached by a plane wave, it must be far enough from the sample. We also want our lighting to be a coherent point source. These conditions are well approximated by a LED element placed at a sufficient distance below the object.

Hence, a LED element offset from the optical axis of the imaging system is used to produce a shift in the object's output Fourier spectrum, Fig. 2.11.

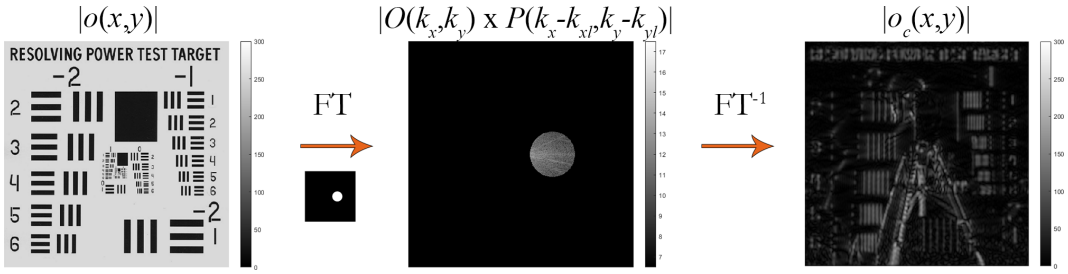

Figure 2.11: A shift in the output Fourier spectrum caused by oblique illumination.

As in the case of our 1D example, a natural image produced by a microscope tends to have a higher concentration of spectral energy at low frequencies [204]. This is at least the case for most biological samples. In addition, when the lighting angle is outside the pupil cut-off frequency, only the scattered light passes through the system, which gives a dark-field image. Such an image has values much lower than a bright-field image produced by direct lighting.

Complete forward problem in 2D To cover a large part of the spectrum by varying the lighting angles, we use a LED matrix.

The image acquisition process for the Fourier Ptychography can be described as follows. For each LED element, and correspondingly for each illumination angle, the low-resolution intensity image of the thin sample is captured by the camera.

An intensity image I_l, captured for the l-th LED is then modelled as below:

$$I_l(x,y) \approx |\mathcal{FT}^{-1}\{P(k_x,k_y)O(k_x-k_{x_l},k_y-k_{y_l})\}|^2, \quad l=1,...,L, \qquad (2.12)$$

where
$I_l(x,y)$ – on of the L real-valued noisy intensity measurements (a captured image);
(k_{x_l},k_{y_l}) – the spatial frequency corresponding to the illumination angle of the l-th LED;
$O(k_x-k_{x_l},k_y-k_{y_l})$ – the shifted version of the Fourier spectrum of the object.
The other variables are noted in the same way as for Eq. (2.11). The sign $\approx$ in the images formation equations (2.12) reflects the fact that the recorded intensities are always corrupted by at least a small amount of camera noise, pupil aberrations and other errors so that observed data are only approximated by the model.

2.2.3 Assumptions, approximations and limitations

Assumptions So far, we have made several assumptions both about the properties of the imaging system and the observed sample. In addition, the forward model described is of course only an approximation of a real physical process.

Among the approximations made on the properties of illumination, we assume that the LED element is an infinitely small point source emitting perfectly spatially coherent light. We also assume that when the light reaches the sample its wavefront is flat.

Regarding the optical elements, we considered that all the lenses were ideal and without aberration. However, we can change the model by introducing aberrations into the expression of pupil function. This point will be discussed in Chapter 3.

We also assume for the moment that the camera produces no noise and perfectly transforms the intensity of the light field into image intensity values at each pixel up to a scaling constant. The sampling criteria are assumed to be satisfied. The actual camera noise will be discussed and analysed in Chapter 3.

In addition, we assume that the system parameters necessary to calculate the spectrum shift are known precisely and that no misalignment is produced. This is of course not the case in real experimental environments. Uncertainties of parameters and system calibration methods will be discussed in Chapter 3.

Lastly, the sample itself is assumed to be infinitely thin. The limits of the thickness of the sample and its influence on the reconstruction will be discussed in Chapter 3.

Limitations The most obvious and perhaps the main limitation of the method is the long acquisition time. Combined with the processing time required for the reconstruction process and the large memory demands for data storage, real-time imaging becomes difficult [196].

Other constraints follow mostly from the assumptions discussed above.

For example, even if the condition of the coherent light is relaxed compared to conventional Pytychography, classical Fourier Ptychography still does not allow incoherent imaging techniques such as fluorescence.

The possible solutions for these limitations will be addressed in Section "Extensions and improvements" of Chapter 4.

2.2.4 Patents

Several patents related to different aspects of Fourier Ptychography were issued [34, 37, 81, 82, 99, 100, 138, 139, 142, 245, 246].

2.2.5 Conclusion

The Ptychographic Imaging Framework To summarize, the classic Fourier ptychographic platform is a coherent imaging system. It consists of an optical microscope with low numerical aperture (NA) lens and a CCD camera. The conventional light source is replaced by a matrix of LEDs that are lit sequentially one at a time, allowing different angle illumination.

Finally, FPM procedure seeks to reconstruct a high resolution complex signal from a set of phase-less corrupted by noise low-resolution images. To this end, digital processing in the form of a phase recovery algorithm is applied.

Comparison to the Conventional Ptychography We can now list the main differences between conventional Ptychography and Fourier Ptychography.

Conventional ptychography captures the intensity of the diffraction patterns which is equivalent to a Fourier transform of the light field. Fourier Ptychography, on the other hand, detects the intensities of the light field itself.

Then, conventional Ptychography mechanically moves the camera to produce the offset in the Fourier domain, while Fourier Ptychography achieves this by using variable angle lighting.

The final resolution is defined by the maximum lighting angles of a Fourier Ptychographic microscope and by the range of movement of the camera for conventional Ptychography.

As it has been analyzed in [243], Fourier Ptychography has a less strict requirement for the coherence of the illumination which allows the use of LED elements instead of a laser.

Despite the differences, the techniques are very similar, especially from the point of view of reconstruction; developments in one method can often be directly applied to another.

2.3 Numerical aspects of FPM phase retrieval

The FPM procedure is a non-convex non-linear inverse problem in which the data consists of several linear intensity measurements of the unknown complex signal. Hence, in general, there is no guarantee of reaching a global minimum [175]. In addition, the data has a wide dynamic range due to the presence of both dark-field and bright-field images and is corrupted by noise and aberrations. Moreover, misalignments and approximations of the observation model are inevitable in real experimental situations [16]. Furthermore, the measurements and the recovered signal are of a large size. In our experiments, 256 images of 2048 x 2048 pixels each are captured, from which a complex image of 8192 x 8192 pixels is reconstructed. Although the problem is solved for several smaller segments rather than for full field of view images, the size of the variables remains high even after this division.

2.3.1 Overview of the state of the art

Many phase recovery algorithms have been proposed to solve the reconstruction difficulties of FPM [226]. These includes projection-based algorithms [244, 252], various gradient [14, 22, 192, 237] or Hessian-based methods [111, 196, 226, 247], convex relaxation methods [21, 77] and, more recently, deep learning approaches [90, 95, 133, 174, 191]. In addition, these methods can be further differentiated by the choice of the cost function [104], the gradient truncation strategy [11, 30, 211], the step size calculation [252], the initialization procedure [22, 198], the use of a complete dataset versus a single image per iteration [102], the regularization constraints [14], etc.

2.3.2 Optimization formulation

We are looking for an object that, given our model, would have produced the images closest to our captured data.

It is convenient to reformulate the image formation model using linear algebra, Fig. 2.12. The equation (2.12) can be thus vectorized [225], [226]:

$$\mathbf{I}_l \approx |\mathbf{F}^{-1}\mathrm{diag}(\mathbf{P})\mathbf{Q}_l\mathbf{O}|^2 \equiv |\mathbf{g}_l|^2, \quad l = 1, ..., L, \tag{2.13}$$

where
$\mathbf{I}_l \in \mathbb{R}^{m^2 \times 1}$ – real-valued noisy intensity measurements obtained by rearranging each of the captured images $I_l(x, y)$ into a vector;
$\mathbf{O} \in \mathbb{C}^{n^2 \times 1}$ – the vectorized version of the Fourier space of the object to recover $O(k_x, k_y)$;
$\mathbf{Q}_l \in \mathbb{R}^{m^2 \times n^2}$ – a down-sampling matrix, it extracts a part of the spectrum vector corresponding to the LED l;
$\mathbf{P} \in \mathbb{C}^{m^2 \times 1}$ – the vectorized version of the pupil function;
$\mathrm{diag}(\boldsymbol{v})$ – an operator that produces a square matrix with the elements of the

vector $\boldsymbol{v}$ on the main diagonal;
$\mathbf{F}^{-1} \in \mathbb{C}^{m^2 \times m^2}$ – the inverse 2D Fourier transform operator;
$|(\cdot)|^2$ – the element-wise amplitude squared operator.

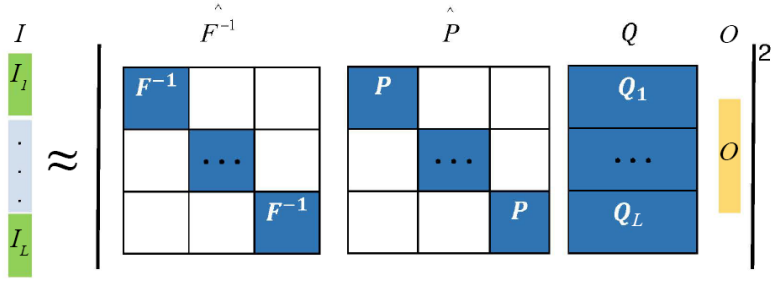

Figure 2.12: The forward imaging model expressed in a vector notation. Adapted from [241].

We can further simplify the notation and reformulate the forward problem (2.13) in a compact form. Let $\boldsymbol{I} = [\boldsymbol{I}_1, ..., \boldsymbol{I}_L]^T = [I_{1,1}, ..., I_{L,m^2}]^T \in \mathbb{R}^{Lm^2 \times 1}$, where $I_{l,j}$ accesses the j pixel of the vectorized version of a captured image $\boldsymbol{I}_l$.

$\boldsymbol{A} = [\boldsymbol{A}_1, ..., \boldsymbol{A}_L]^T \in \mathbb{C}^{Lm^2 \times n^2}$, where $\boldsymbol{A}_l = [\boldsymbol{a}_{l,1}^H, ..., \boldsymbol{a}_{l,m^2}^H]^T$ with $\boldsymbol{a}_{l,i} \in \mathbb{C}^{n^2 \times 1}$ a single row of the matrix $\boldsymbol{A}$.

$$\boldsymbol{I} \approx |\boldsymbol{AO}|^2 \tag{2.14}$$

$(\cdot)^T$ denotes transpose operation, $(\cdot)^H$ is a Hermitian transpose.

We call $\boldsymbol{A}$ a linear sampling matrix or a design matrix. It represents the model of image formation : $\boldsymbol{A} = \boldsymbol{F}^{-1} * diag(\boldsymbol{P}) * \boldsymbol{Q}$, where $\boldsymbol{Q} = [\boldsymbol{Q}_1, ..., \boldsymbol{Q}_L]^T \in \mathbb{R}^{Lm^2 \times n^2}$.

Many of the phase retrieval algorithms are described as an optimization problem. The FPM reconstruction procedure can be then formulated as follows in the general case:

$$\min_{\mathbf{O}} f(\boldsymbol{O}, \boldsymbol{A}, \boldsymbol{I}), \tag{2.15}$$

where f is a chosen cost function. We are looking for such an object $\mathbf{O}$ that would minimize the norm of the difference between the captured images $\boldsymbol{I}$ and the ones that would have been produced given the design matrix $\boldsymbol{A}$. The solution is sought in the Fourier space ($\mathbf{O}$ rather than $\mathbf{o}$) for convenience. One of the most intuitive formulation is a quadratic loss function :

$$\min_{\mathbf{O}} \left\| |\boldsymbol{AO}|^2 - \boldsymbol{I} \right\|^2, \tag{2.16}$$

where $\|A\| = \sqrt{\sum_i \sum_j |a_{i,j}|^2}$ is the Frobenius norm (sometimes also called the Euclidean norm).

2.3.3 Inverse problem analysis

The known data represent only the magnitude of several measurements of the unknown complex signal and are corrupted by noise. The FPM procedure seeks to uniquely recover the original signal. Due to the loss of phase information, the presence of noise, and the limiting nature of the pupil function, this problem is, in general, ill-posed.

It has been shown that for the 1D phase problem, there is no single solution [210] [175]. The uniqueness can nevertheless be achieved for the 2D variant of this problem. However, this requires a large number of measurements, much larger than the size of the original signal sought, i.e. $Lm^2 \gg n^2$. Shechtman, Eldar et al. have summarized in [175] the conditions for the uniqueness of the phase retrieval problem. Given a complex original signal, $4n^2 - 4$ random noiseless measurement are sufficient for bijectivity. For the noisy data, this number is estimated to be on the order of $n^2 \log(n^2)$. For the generic, non-random measurements, a lower limit is found to be $2n^2 - 1$. The trivial ambiguities inherent in any ptychographic imagery are not addressed by this analysis. These ambiguities are the operations preserving the amplitude of the Fourier spectrum: a global phase shift, a conjugate inversion and a spatial shift.

To better understand the issue of stability, we analyze the conditioning of the design matrix $\boldsymbol{A}$. Indeed, in the case of a linear inverse problem, described by an equation $\boldsymbol{I} = \boldsymbol{AO}$, the condition number can be calculated by performing a singular value decomposition (SVD) of $\boldsymbol{A}$. In our case, a non-linearity comes from the loss of phase : $\boldsymbol{I} = |\boldsymbol{AO}|^2$. However, we can still analyse the matrix $\boldsymbol{A}$ to get an overall assessment of the stability of the FPM problem. The condition number is defined as a ratio of the maximum singular value to the minimum singular value.

The matrix $\boldsymbol{A}$ in the particular case of $m = 30$, $n = 60$, $L = 64$ (only 8x8 LEDs are used) has a structure depicted in Fig. 2.13(a). The imaging parameters needed to construct the sampling matrix $\boldsymbol{Q}$ and the pupil function matrix $\boldsymbol{P}$ correspond to the final version of our system. The matrix $\boldsymbol{A}^H\boldsymbol{A}$ has most of its non-zero entries on and along the main diagonal, Fig. 2.13(b). An SVD decomposition $A = U\Sigma V^H$ yields the following images of orthonormal basis matrices U and V: Fig. 2.13(c,d). All of these matrices are highly structured and certainly do not correspond to random measurements. Yet, analysis based on the assumptions of random Gaussian measurements is sometimes used in the context of a more general case of ptychographic phase recovery algorithms [21, 87]. The condition number of a matrix $\boldsymbol{A}$ calculated for the FPM configuration above is 3.7e+17. For comparison, a design matrix $\boldsymbol{A}$ with random Gaussian complex entries has a condition number of 1.7 for one of the realizations, see Fig. 2.13(e-h).

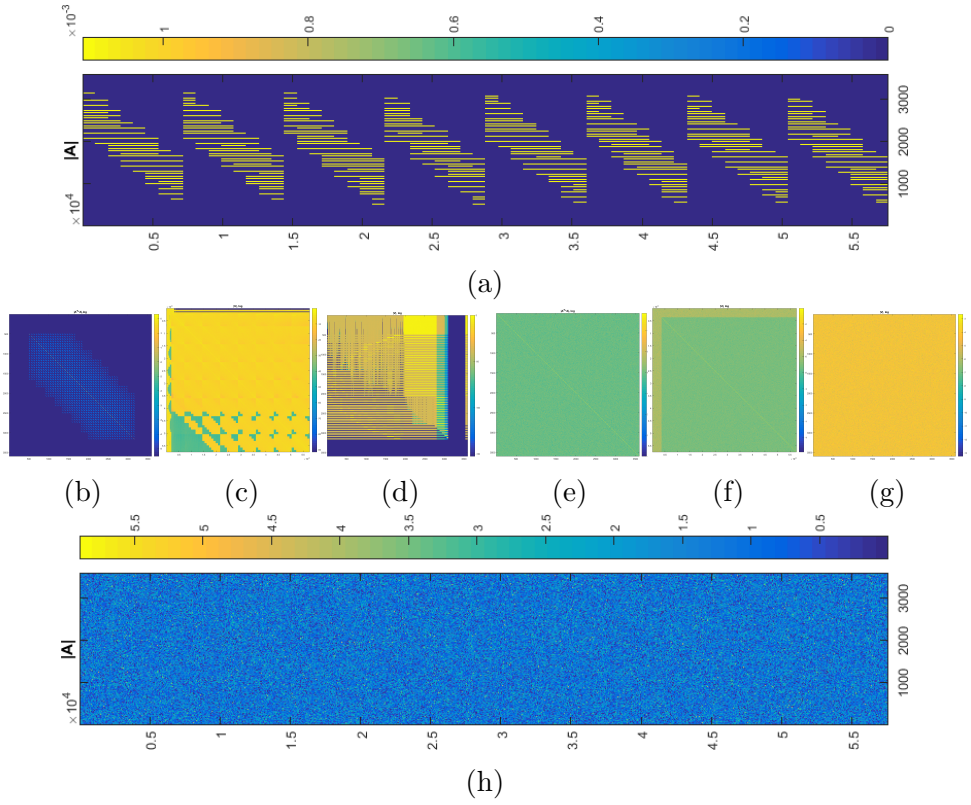

Figure 2.13: Analysis of an FPM design matrix $\boldsymbol{A}$ (a-d) and comparison with a random complex matrix of the same size (e-h). (a) The matrix $\boldsymbol{A} = \boldsymbol{F}^{-1} * diag(\boldsymbol{P}) * \boldsymbol{Q}$ (the axis aspect ratio x:y is 3:1, the image is rotated). (b) The matrix $\boldsymbol{A}^H * \boldsymbol{A}$, log scale. (c) The matrix U from $A = U\Sigma V^H$, log scale. (d) The matrix V from $A = U\Sigma V^H$, log scale. (h) The random matrix A. Its (e) $\boldsymbol{A}^H * \boldsymbol{A}$, (f) U and (g) V matrices from $A = U\Sigma V^H$, log scale. Only the absolute values of matrices are shown.

2.3.4 Sampling criteria for FP reconstruction process

The stability and quality of the reconstruction is highly dependent on the sampling chosen. Two categories of sampling issues need to be considered [243]. First, there is the potential for aliasing on low-resolution images. Second, the degree of overlap in the frequency domain influences the quality of the reconstructed image, especially in the presence of noise.

Spatial aliasing

The first question, concerning spatial aliasing, is defined by the Nyquist criterion. If the highest spatial frequency of the signal is equal to or greater than half the sampling frequency, the recorded signal will contain aliasing artifacts. This distortion will subsequently degrade the reconstruction quality. The maximum signal frequency is defined by the optical system and the illumination.

The sampling frequency is defined by the characteristics of the digital camera.

A common criterion for measuring aliasing in FPM is the spatial-sampling-ratio R_{cam}, introduced in [187]. It is defined as following :
* $R_{cam} = \frac{f_{cam}}{f_{obj}}$, where
* $f_{cam} = \frac{m}{2p}$ – the spatial cut-off frequency of the camera, where m – actual objective magnification, p – pixel size of the camera.
* $f_{obj} = \frac{\mathrm{NA}}{\lambda}$ – the spatial cut-off frequency defined by the objective lens NA and the LED wavelength λ.

The spatial-sampling-ratio R_{cam} should be more than 1 to satisfy the Nyquist criterion. A straightforward solution to overcome the problem of aliasing, should it occur, would be to increase the magnification factor m by changing the microscope objective. However, this would sacrifice the field of view. Instead, the violation of the Nyquist criterion can be overcome numerically in the case of FPM. One of such algorithms is referred to as "sub-sampled scheme" [243] [45]. The camera pixel pitch p is assumed to be halved. Only 1 sub-pixel out of 4 is then updated during the reconstruction. This algorithm has not been implemented in the current work.

Fourier space overlap requirement

In a conventional FPM, a LED matrix is rectangular and only one LED is lit for each captured image.

The requirement for spectrum overlap in the FPM is often expressed in two quantities [187]. The spectrum-sampling-ratio R_{LED} describes the density of Fourier space exploration :
* $R_{LED} = \frac{f_{obj}}{f_{LED}}$, where
* $f_{LED} = \frac{1}{\lambda}\frac{D_{LED}}{\sqrt{D_{LED}^2+h^2}}$ – the minimum angular difference between two LEDs, where D_{LED} is the gap between the LEDs, h is the distance from the center of the LED matrix to the sample.

In particular, the value $R_{LED} < 1/2$ identifies geometries that sample non-overlapping bands.

Another variable, called the aperture recovery rate $R_{overlap}$, quantifies the spectral redundancy between two adjacent spectral bands [187] :

$$R_{overlap} = \frac{1}{\pi}\left[2\arccos\left(\frac{1}{2R_{LED}}\right) - \frac{1}{R_{LED}}\sqrt{1-\left(\frac{1}{2R_{LED}}\right)^2}\right] \tag{2.17}$$

The $R_{overlap}$ is defined as 0 for $R_{LED} < 1/2$.

The minimum value of $R_{overlap}$ required for correct phase recovery varies depending on the phase retrieval technique, i.e. the mode of ptychography and the reconstruction algorithm. For a general sequential algorithm applied to a classical ptychography (ptychographic iterative engine), the overlapping optimal condition in terms of reconstructed image quality is $R_{overlap} \in (60, 85)\%$

[20]. The algorithm can still converge with as little overlap as $R_{overlap} = 30\%$, but the reconstruction error would be significantly higher.

A similar analysis was also made for a more specific case of Fourier Ptychography [117, 187, 213]. Regardless of the technique it is agreed that a minimum of $R_{overlap} = 32\%$ is required for correct phase retrieval. Reconstruction error decreases as the percentage of overlap increases. The value of $R_{overlap} = 60\%$ is considered an optimal value in terms of the trade-off between image quality and convergence speed. The reconstruction error decreases to a value of approximately $R_{overlap} = 80\%$, after which the error tends to increase. It is also noted that the optimal overlap value for FPM moves as a function of noise level, wavelength mixing, but also the presence of aliasing.

The above requirements are for a uniform, rectangular LED pattern, with one LED lit at a time. However, it is possible to use a more efficient sampling scheme or LED matrix geometry. It is also possible to significantly reduce the overlap requirement by using deep learning methods. Those questions will be addressed in Section 4.4.

2.3.5 Complex gradient

The design matrix and the object sought in the optimization problem Eq. (2.15) have complex values. This means that the general non-convex optimization methods have to be adapted to the case of a function with a complex value variable. One of the frameworks for doing this is called the Wirtinger calculus.

A Wirtinger derivative relaxes the definition of an ordinary derivative [2]. It allows complex-variable functions to be treated in almost the same way as a differential function with real variables. Optimization based on the Wirtinger gradient is widely used to solve the phase retrieval problem [11, 14, 22, 26, 93, 102, 115, 222, 227, 228].

A Wirtinger gradient $\boldsymbol{g}$ of a scalar-valued function $f(\boldsymbol{O})$ of a complex variable $\mathbf{O} \in \mathbb{C}^{N\times 1}$ is defined as follows [22]:

$$\boldsymbol{g} = \frac{\delta f(\boldsymbol{O})}{\delta \boldsymbol{O}^*} = \left[\frac{\delta f}{\delta O_1^*}, ..., \frac{\delta f}{\delta O_N^*}\right]^T \tag{2.18}$$

with

$$\frac{\delta f(\boldsymbol{O})}{\delta O_n^*} = \frac{1}{2}\left(\frac{\delta f}{\delta \Re(O_n^*)} + j\frac{\delta f}{\delta \Im(O_n^*)}\right), \quad n = 1, ..., N \tag{2.19}$$

where $\Re(\cdot)$ and $\Im(\cdot)$ designate respectively a real and imaginary part of a complex number.

2.4 Reconstruction methods

Many phase recovery algorithms have been proposed to solve this non-convex problem [226].

The initial solution of the Fourier Ptychography problem proposed by G. Zheng et al. [244] is an alternating projections algorithm which is a sequential approach based on ptychographical iterative engine (PIE) [123]. Modifications to the original alternative projections have since been proposed. One of the suggestions is to adjust the step size of the update if the error is not reduced enough [252].

Another widely used sequential algorithm is the Newton's method [196, 247]. This is a second-order method, which means that it uses the second derivative, a Hessian matrix during the update. In practice, it is implemented as a quasi-Newton method with a Hessian matrix approximation.

The term "sequential" refers to the mode of operation of the algorithm, where an update step is performed for each image, one at a time. In contrast to "global" algorithms where an update uses the complete set of images for each iteration.

Many of the non-projections algorithms are global and described as an optimization problem with a certain cost-function. In 2015, a solution to the phase retrieval problem based on Wirtinger calculus and termed Wirtinger flow was proposed [22] and then adapted to the FPM framework [14].

Various other algorithms based on a gradient have also been proposed, different in particular in the optimization algorithm, the cost function, the initialization method, the step size of the update, the regularization constraints and others settings.

Another group of solvers are convex-based methods. They promise to reach the global minimum at the expense of reformulating the problem in higher dimensions. The PhaseLift method [21] was first proposed for a general phase retrieval problem. Its adapted version was then applied to the FPM recovery [77]. However, in practice, the solution is calculated using the L-BFGS method [226].

Lastly, methods based on neural networks are increasingly used in the recent years [90, 95, 133, 174, 191].

Finally, it is important to note that Fourier Ptychography is closely linked to conventional Ptychography. The many algorithmic developments underway in conventional Ptychography can often be directly applied to its Fourier counterpart [80, 121]. The methods of the more general problem of phase recovery can also be adapted for the FPM framework [66, 87, 88, 214]. In addition, in theory, any optimization algorithm for a non-convex problem could potentially be suitable. Research in this area is ongoing and new procedures are constantly being proposed.

There are several important aspects to keep in mind when choosing a reconstruction method. The first and most obvious is the quality of the reconstructed images of phase and amplitude. This can be measured by various criteria and parameters, including visual validation. Another crucial issue is the speed of convergence in terms of iterations and also in terms of computing time. Depending on the machine used, calculation memory requirements can

also become a limiting factor. Stability in the presence of noise and errors is essential. As well as the predictability of the behaviour of the algorithm given different data sets.

Furthermore, there are different possible configurations of FPM. The question arises whether we want the algorithm to be adapted to our specific case, or even to the type of datasets, or whether we want it to be as universal as possible. The amount of spectrum overlap, the NA of the objective, the number of bright field images, the error levels and other factors can influence the choice of the optimal reconstruction method. The reproducibility of results must also be taken into account. This includes the number of parameters to be tuned, the need for additional prior information but also the widespread use of the chosen algorithm.

Finally, as part of the work in progress, it was important for us to be able to easily integrate modifications and physically interpret the stages of the reconstructions. Overall, there is no simple and universal answer to the question of which algorithm is the best choice.

From the results of the literature review, it was possible to deduce different bricks which, in combination, constitute existing algorithms (in most cases). The main components that characterize the methods are as follows:

– optimization engine algorithm,
– the incremental versus global approach,
– step size selection strategy,
– initialization method,
– underlying assumptions of the noise model,
– gradient regularization by truncation,
– presence of regularization term in the cost function,
– processing of optical aberrations and other errors.

Most of these bricks have been implemented to some extent. This makes it possible to compare and combine different approaches in order to choose an optimal algorithm for the given device.

2.4.1 Optimization algorithm

Existing optimization algorithms can be categorized according to different characteristics. One of the biggest differences can be attributed to the explicit calculation of a gradient of a cost function versus the use of non-gradient methods. We will first discuss the latter type of approaches.

Alternating projection algorithm

The initial solution of the Fourier Ptychography problem proposed by G. Zheng et al. [244] is an alternating projection algorithm. It is often referred to as the Gerchberg-Saxton phase retrieval approach. Another name "ptychographical iterative engine" indicates its original adaptation of classical ptychography.

The workflow The main workflow of the algorithm is illustrated in Fig. 2.14. The idea can be summarized as follows [243]. The Fourier transform of an enlarged version of the central LED captured amplitude image is used as the first estimate of the object spectrum $O^{(0)}(k_x, k_y)$. Then, two nested loops take effect.

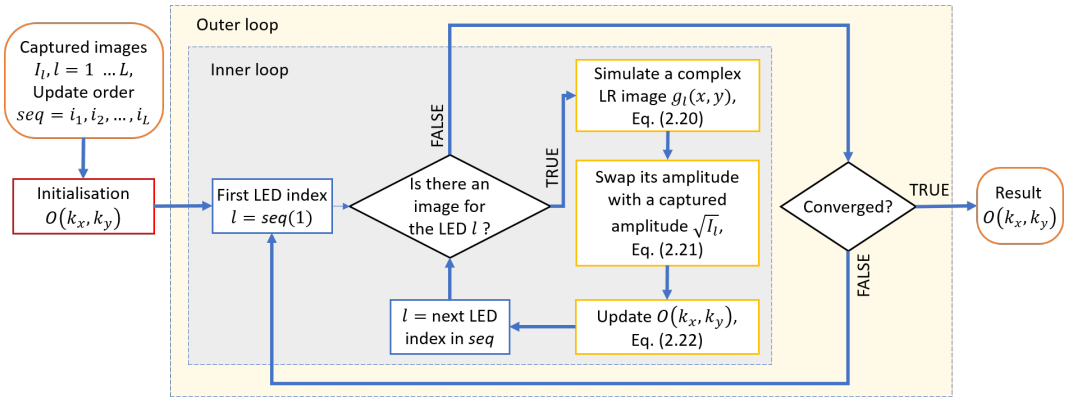

Figure 2.14: A flowchart of the basic PIE algorithm for FPM reconstruction.

The internal loop is traversed for each of the L LED angles. The image update sequence seq is chosen in advance and will be discussed below. A complex low-resolution image $g_l^{(t)}(x, y)$ is computed at each step l according to the observation model given by Eq. (2.20):

$$g_l^{(t)}(x, y) = |\mathcal{FT}^{-1}\left\{P(k_x, k_y)O^{(t)}(k_x - k_{x_l}, k_y - k_{y_l})\right\}|^2. \tag{2.20}$$

The notations are the same as for Eq. (2.12). The $(\cdot)^{(t)}$ notation indicates an iteration t of the outer loop. The amplitude $|g_l(x, y)|$ of the generated object is then swapped with the amplitude $\sqrt{I_l(x, y)}$ of the corresponding captured image:

$$\tilde{g}_l(x, y) = \sqrt{I_l(x, y)}e^{i\phi_l(x,y)}, \quad \text{where} \quad \phi_l(x, y) = \arg(g_l(x, y)). \tag{2.21}$$

The Fourier transform of the resulting object $\tilde{g}_l(x, y)$ is then used to update the corresponding band of the previous spectrum estimate $O(k_x, k_y)$ according to the Eq. 2.22:

$$O_l^{(t+1)}(k_x, k_y) = O_l^{(t)}(k_x, k_y) + \nabla O_l^{(t)}(k_x, k_y) \tag{2.22}$$

where we note
$O_l^{(t)}(k_x, k_y) = O^{(t)}(k_x - k_{x_l}, k_y - k_{y_l})$;
$\nabla O_l^{(t)}(k_x, k_y) = \tilde{G}_l^{(t)}(x, y) - P(k_x, k_y)O_l^{(t)}(k_x, k_y)$ and
$\tilde{G}_l^{(t)}(x, y) = \mathcal{FT}\left\{\tilde{g}_l^{(t)}(x, y)\right\}$.

Another proposal for the update step reflects at the same time a better step size and the fact that the pupil function may contain aberrations [196].

The aberrations themselves and the ways to address them will be discussed in the next chapter. The update becomes:

$$O_l^{(t+1)}(k_x, k_y) = O_l^{(t)}(k_x, k_y) + \frac{P^*(k_x, k_y)}{(|P^*(k_x, k_y)|^2)_{\max}} \nabla O_l^{(t)}(k_x, k_y) \tag{2.23}$$

The outer loop executes the inner loop until convergence is achieved.

Recovery sequence An important parameter to consider in the PIE algorithm is the images update sequence during the internal loop. The sequence of recovery is not only important for the speed and quality of reconstruction, but may even be entirely detrimental to convergence due to stagnation in local minima. Several options are proposed in the literature, including the ordering based on the Hilbert fractal curve [27]. However, we stick to the original, classic proposal [243]. It consists in arranging the images according to spiral lines starting from the LED closest to the center of the optical axis and going outwards.

The traditional Gerchberg-Saxton algorithm above and its variations is probably the most commonly used method in Fourier ptychography research. It is not posed as a minimization procedure (2.15) with a specific cost function. However, it can be shown that the algorithm can also be obtained by optimizing the amplitude-based cost function via the majorization-minimization framework [163, 226].

Several important advantages contribute to its popularity. First of all, it is computationally efficient. Only one low-resolution image is processed at a time and the number of calculations performed is the minimum of what can be expected from a phased retrieval method. Second, this approach is highly flexible; changes in the forward model can be easily incorporated into the reconstruction process [252]. There are also a number of extensions that make the basic algorithm more efficient and more stable in the presence of noise [121, 134, 252].

Instructions for implementing the alternating projection algorithm in Matlab can be found in the book "Fourier Ptychographic Imaging, Matlab Tutorial" [243].

Adaptive step size strategy

One of these extensions improves noise and misalignment tolerance by simply modifying the step size of the update. Indeed, the problem of non-convergence and local optima can be decreased through an adaptive step size approach. [252]. The idea is to adjust the step if the error is not sufficiently reduced.

The classical version, described above, adds an updated part of the spectrum to the previously estimated object:

$$O_l^{(t+1)}(k_x, k_y) = O_l^{(t)}(k_x, k_y) + \alpha^{(t)} \frac{P^*(k_x, k_y)}{(|P^*(k_x, k_y)|^2)_{\max}} \nabla O_l^{(t)}(k_x, k_y) \tag{2.24}$$

with a unitary constant step size $\alpha^k = 1$.

The adaptive strategy, on the other hand, calculates the step size α^k at the beginning of each outer loop by evaluating the quality of the descent using a previous estimate.

$$\alpha^{(t+1)} = \begin{cases} \frac{\alpha^{(t)}}{2} \text{ if } \frac{E^{(t-1)}-E^{(t)}}{E^{(t-1)}} < 0.1 \\ \alpha^{(t)} \text{ otherwise} \end{cases} \tag{2.25}$$

where $E^{(t)} = \left\| |g_l^{(t)}(x,y)|^2 - I(x,y) \right\|^2$ is a quadratic loss function at iteration t.

Note that other error metrics for (Eq 2.25) are also possible. Unlike what is proposed in the original work, our criterion uses an amplitude-based cost function instead: $E^{(t)} = \left\| |g_l^{(t)}(x,y)| - \sqrt{I(x,y)} \right\|^2$. The reason is that this measure is consistent with the cost function implicitly minimized by the PIE algorithm. It was also used in [148]. Another option would be a convergence index, which will be presented later.

Other non-gradient-based algorithms

Many other improvements to the PIE core have since been proposed to solve the problem of ptychographic phase recovery [65, 121, 214]. Not all of them have been tested for the FPM configuration, but they are expected to be adaptable to the case of Fourier ptychography.

Another type of a non-gradient-based phase retrieval is a hybrid input-output (HIO) algorithm [54]. A combination of HIO with an error reduction method can also be cited [130]. However, these methods are less commonly used and will not be addressed in the current work.

Wirtinger flow

The Wirtinger calculus enables the problem of phase retrieval to be approached from the perspective of classical gradient-based optimization. One of the first algorithms to solve a ptychography in this framework was called "Wirtinger flow" [22]. It was soon adapted to a more specific case of FPM reconstruction [14].

It is essentially a classic gradient descent algorithm with a specific step size and a relaxed definition of a gradient [14, 22]. A steepest descent looks for a minimum of a function $f(\boldsymbol{O})$ starting with an initial guess $\boldsymbol{O}^0$ and updating the estimate $\boldsymbol{O}^t$ at each step t according to :

$$\boldsymbol{O}^{(t+1)} = \boldsymbol{O}^{(t)} - \gamma^t \boldsymbol{g}^{(t)} \tag{2.26}$$

where $\boldsymbol{g}^{(t)} = \nabla f(\boldsymbol{O}^{(t)})$.
In early versions of the Wirtinger flow algorithm, the quadratic loss function,

also called "intensity-based" cost, was used. It aims to minimize the difference between measured intensity images and estimated intensities.

$$f_I(\boldsymbol{O}, \boldsymbol{A}, \boldsymbol{I}) = \left\| |\boldsymbol{AO}|^2 - \boldsymbol{I} \right\|^2. \tag{2.27}$$

For the purpose of this discussion, we omit the noise relaxation constraints present in some literature. Note that $|\boldsymbol{AO}|^2 = (\boldsymbol{AO})^H \odot (\boldsymbol{AO})$, where $\odot$ is a dot product. The Wirtinger gradient with respect to $\boldsymbol{O}$ for such a cost function is then calculated as follows:

$$\nabla f_I(\boldsymbol{O}) = 2\boldsymbol{A}^H \left[\left(|\boldsymbol{AO}|^2 - \boldsymbol{I} \right) \odot (\boldsymbol{AO}) \right]. \tag{2.28}$$

A method for estimating the initial guess $O^{(0)}(k_x, k_y)$ has also been proposed as part of the Wirtinger Flow algorithm. However, this will be discussed in a later section.

Different proposals for γ^t exist, but the original works propose to use the following scheme:

$$\gamma^t = \frac{\min\left(1 - e^{-t/t_0}, \gamma_{max}\right)}{\left\| O^{(0)}(k_x, k_y) \right\|^2}, \tag{2.29}$$

the authors suggest to use $t_0 = 330$ and $\gamma_{max} = 0.4$ [14, 22]. The idea is to use small steps at the beginning, since the noise is too high, and to gradually increase the step value as the global minimum is expected to be approached. The proposed constant parameters are chosen experimentally.

Other gradient-based global optimization

Wirtinger derivatives can be used not only with a classical gradient descent method, but also with many other gradient based optimization methods.

For example, the nonlinear conjugate gradient algorithm is sometimes used in the context of phase retrieval problem [111, 162, 218, 219, 222, 237]. The steepest descent type update, used in the Wirtinger flow, takes a negative gradient direction that is always perpendicular to the previously calculated trajectory. Conjugate gradient descent, on the other hand, constructs its route in such a way that the new direction is conjugated with all the previously calculated paths [159], Eq. (2.30).

$$\boldsymbol{O}^{(t+1)} = \boldsymbol{O}^{(t)} + \gamma^t \boldsymbol{d}^{(t)}, \tag{2.30}$$

where γ^t is a step size, often defined by a line search method and $\boldsymbol{d}^{(t)}$ is the conjugate search direction. The next direction $\boldsymbol{d}^{(t+1)}$ is determined using the previously calculated path $\boldsymbol{d}^{(t)}$ as follows:

$$\boldsymbol{d}^{(t+1)} = \boldsymbol{\beta}^{(t)} \boldsymbol{d}^{(t)} - \boldsymbol{g}^{(t)}, \qquad \boldsymbol{d}^{(0)} = -\boldsymbol{g}^{(0)}. \tag{2.31}$$

Several options are possible for the coefficient $\boldsymbol{\beta}$. Two commonly used in the context of ptychography are the coefficient of Hestenes-Stiefel [111]:

$$\boldsymbol{\beta}^{(t)} = \frac{\Re\left(\boldsymbol{g}^{H(t)}(\boldsymbol{g}^{(t)} - \boldsymbol{g}^{(t-1)})\right)}{\Re\left(\boldsymbol{d}^{H(t-1)}(\boldsymbol{g}^{(t)} - \boldsymbol{g}^{(t-1)})\right)} \tag{2.32}$$

and the coefficient of Polak-Ribière [219]:

$$\boldsymbol{\beta}^{(t)} = \frac{\Re\left(\boldsymbol{g}^{H(t)}(\boldsymbol{g}^{(t)} - \boldsymbol{g}^{(t-1)})\right)}{\left\|\boldsymbol{g}^{(t-1)}\right\|^2}. \tag{2.33}$$

The conjugate gradient algorithm has also been employed to treat angular misalignments in the FPM [206].

Another common method to achieve greater robustness and convergence is to use a second order gradient method. This involves calculating the Hessian matrix of a function in addition to the gradient of the function. Wiritinger calculus is likewise used to derive an analytical expression of a Hessian. Global Newton algorithm is used by some authors [226]. However, the cost of calculation becomes too high for this method to be used in a practical context. For this reason, second-order methods have not been implemented in the current work.

At the same time, a group of quasi-Newton methods can provide an alternative solution to Newton method. Indeed, these algorithms seek to approximate a Hessian matrix or an inverse of the Hessian matrix in order to avoid its direct calculation at each iteration. One of these methods is the L-BFGS (memory limited Broyden-Fletcher-Goldfarb-Shanno) algorithm. Implementation details of L-BFGS for the broader problem of phase retrieval can be found in [111]. Gauss-Newton method or its variations are also popular [196, 226].

Gradient-based sequential optimization

For the projection-based algorithms, only one image is taken into account at each upgrade. They belong to the family of sequential algorithms. Global approaches, on the other hand, refer to optimization procedures where all data are used for each upgrade process. It is implicit in Gerchberg-Saxton type algorithms that an underlying optimization problem iteratively uses only one component of the gradient of a global cost function [226]. On the other hand, global methods calculating an entire gradient are more expensive in terms of computation. At the same time, a number of results show that sequential algorithms could perform as well as global algorithms while offering additional advantages. [225, 226].

In theory, a global gradient descent algorithm with any explicit cost function can be transformed into a sequential one [102, 226]. A sequential version

of a global Wirtinger flow is often referred to as an incremental Wirtinger flow [102]. In addition to reducing computational requirements, sequential algorithms allow greater flexibility in introducing adjustments to the model. It has also been shown that sequential algorithms could be more effective in avoiding the stagnation of local minima [121, 134]. At the same time, sequential algorithms are expected to be less robust against noise and model misalignments [226].

Finally, it is noteworthy that a majorization-minimization (MM) framework offers yet another perspective on sequential optimization [163]. Indeed, it is a procedure for constructing an iterative optimization problem so that an original non-convex model is divided into a set of simpler surrogate functions. A sequential algorithm called "PRIME-Power" is proposed using this approach [163].

In the current work, however, we have not implemented gradient-based sequential optimization for an explicit cost function. Nor have we implemented methods derived by the MM technique.

Other methods

Two other major groups of solvers available for the FPM problem are convex optimization approaches and deep learning methods.

Convex lift The greatest advantage of convex programming is the theoretical guarantee of reaching a global minimum. The biggest disadvantage is a huge computational requirement. Indeed, the algorithms proposed for ptychography, such as PhaseLift and PhaseCut, involve raising a problem in a higher dimension [21, 77, 82]. Given the already large size of the variables in an FPM, this raises a real question about the suitability of these methods for any practical application. This is why proposals for actual implementation are usually only an approximation of the convex version of the problem, which discards global minimum guarantees [226].

Deep learning Following a growing trend in neural network research, a number of solutions have also been proposed for Fourier ptychographic reconstruction [90, 95, 133, 174, 191, 232]. All the methods described in the previous sections are based on modelling the underlying physical process. Machine learning methods, on the other hand, have historically taken a different approach based on statistics and data training. The physics-based methods offer an interpretability and robustness. On the other hand, deep learning can offer faster reconstruction at the cost of a large set of training data and no theoretical guarantee of the physical accuracy of the result. Some algorithms for ptychography successfully combine the two approaches to propose an optimal compromise. Without going into detail, we only note that deep learning approaches to FPM are applied to both the design of the acquisition process

as well as the reconstruction procedure. These algorithms also often result in a reduction in the spectrum sampling requirement.

A number of other strategies have also been proposed and are still being actively researched. These include an alternate direction method of multipliers [86], an acceleration of the Wirtinger flow algorith based on Nesterov acceleration [222], methods designed for graphical processing unit computing [233] and many more.

The approaches in this subsection are quite different from those using alternative projection or gradient-based optimization. It was decided not to implement in the current work all the available solvers for phase retrieval.

Step size

This subsection deals only with the step size γ^t of gradient-based optimization procedures. The step size of an alternative projection algorithm has already been discussed in Subsection 2.4.1. The appropriate choice of step size is particularly important when the data is noisy or the model is imperfect. Many different strategies have been proposed, ranging from a simple constant value to an empirically chosen value and line search methods.

The basic form is a constant step: $\gamma^t = \gamma$ for all t. Despite its simplicity, this method can give descent results when the selected value is small enough to avoid divergence [104].

The Wirtinger Flow approach introduced a heuristic scheme with an increasing step size, given by Eq. (2.29). The two constants t_0 and γ_{max} must however be chosen experimentally. Other formulas for the ascending step are also proposed in the literature, but are not implemented in current work.

Another widely used approach is line search methods [30, 206, 227, 241]. In the case of a gradient descent alorithm, a line search looks for such a step γ^t that minimizes the objective $h(\gamma^t) = f(\boldsymbol{O}^{(t)} - \gamma^t \boldsymbol{g}^{(t)})$, where $f(\boldsymbol{O})$ is a cost function of the reconstruction procedure, Eq. (2.15). This problem can be solved in several ways. The most common proposals are a backtracking line search [227] (not implemented), Wolfe conditions [111, 180] and a Golden-section search [159].

While line search methods have the potential to perform better and to reduce the number of iterations to achieve convergence, they are expensive to use in the case of the FPM. Indeed, a cost function must be calculated at each update stage. This involves, among other things, an expensive Fourier transform operation applied to every captured image.

We use codes provided by Sorber et al. [180] to implement a congujate gradient algorithm and a Strong Wolfe line search method.

In addition, some of the proposed modifications to the original Wirtinger Flow algorithm take advantage of an analytically derived optimal step size [93, 222]. This step size must be calculated for a given cost function. This strategy is not implemented in the current work.

2.4.2 Initial guess

Several methods for generating an initial object guess have been proposed in the literature. As a general ruse, only the amplitude image is estimated while the phase is defined as a matrix of zeros.

The simplest proposal is to simply upscale a low-resolution amplitude image corresponding to the smallest LED angle $I_c(x, y)$ [243]. Most interpolation methods would provide a solution. We use a bicubic interpolation provided by Matlab libraries. As the object $O(k_x, k_y)$ is estimated in Fourier space, a Fourier transformation of the generated image is necessary. Alternatively, the Fourier transform of a central amplitude image $\mathcal{FT}\{I_c(x, y)\}$ can be directly placed at the center of a high-resolution spectrum estimate $O(k_x, k_y)$.

The next often used procedure is called a spectral method [22]. It is based on the eigenvectors of a carefully constructed matrix formed by measurements, a design matrix and its inverse [163]. It was not implemented in the current work.

Instead, we use an initialization by a central amplitude image $I_c(x, y)$ followed by several iterations of the basic PIE algorithm. Indeed, alternate projection methods are arguably more robust against the stagnation of local minima than global algorithms when the solution is too far away. We therefore adopt this scheme to compare the reconstruction algorithms.

A quite different approach focuses on the estimation of the initial phase. Indeed, depending on the type of specimen, it may be desirable to obtain a correct initial phase image evaluation. For mainly transparent samples, the information is contained in the phase part rather than the amplitude part of the signal. As noted in [202], it may be more problematic for the FPM procedure to reconstruct the low frequencies of the phase rather than the high frequencies. Although the spectral method also attempts to generate a phase estimate, it is fundamentally similar to the reconstruction procedure. A proposal has been made by Tian et al. [198, 202] to use a LED array as a means of calculating low phase frequencies by the differential phase contrast (DPC) deconvolution. Four additional measurements of the semi-squares of the LED matrix (left, right, top, and bottom) are needed to estimate the DPC phase, Fig. 2.15(a). However, in the case of sequential acquisition (one image corresponds to one LED), these images can be simply generated by adding up the captured images of the corresponding LEDs, Fig. 2.15(b). The details of the DPC initialization procedure can be found in [200]. The source code is provided by Laura Waller computational imaging lab.

2.4.3 Cost function

The optimization algorithms described above could produce their own reconstruction artifacts. However, the quality of the reconstruction depends even stronger on the underlying noise model and thus on the choice of a cost function. The optimization problem 2.15 can be solved based on a number of

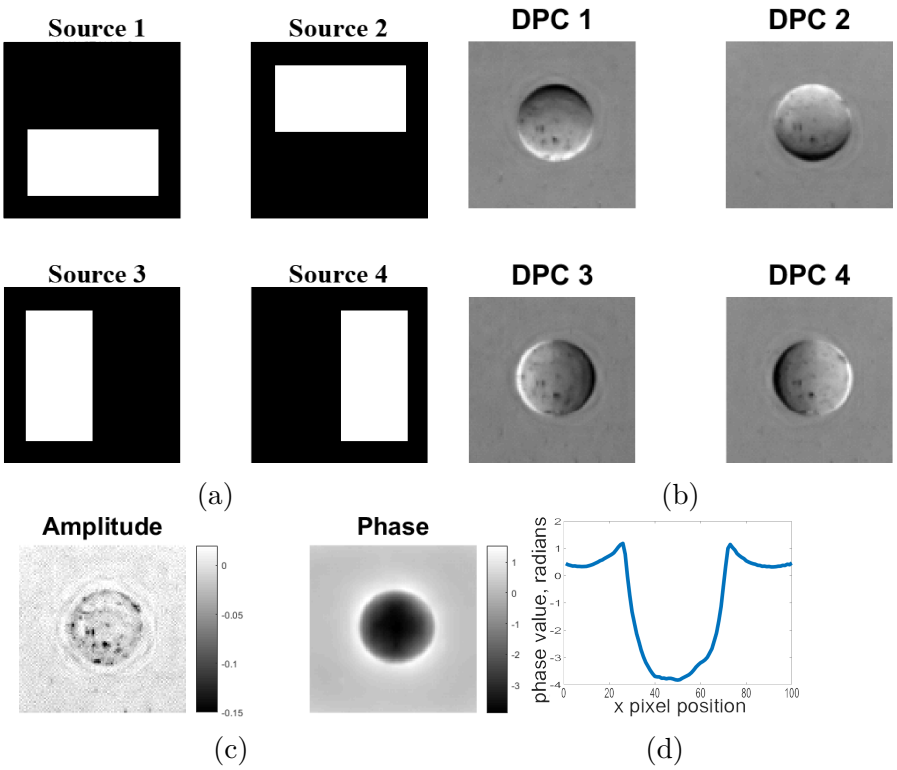

Figure 2.15: (a) LED source masks. The images corresponding to the masks are added together to simulate the images captured when the half squares of the LED array are lit. (b) The generated images corresponding to the half-squares. The sample is a glass microsphere that will be presented in Section 4.1. (c) DPC deconvolution estimation of low-resolution amplitude and phase images. (d) The estimated phase profile.

possible objective functions $f(\boldsymbol{O})$.

The most often used cost functions [104] are the intensity-based [14], the amplitude-based, the Poisson-likelihood-based [11, 226] and mixed Poisson-Gaussian-likelihood-based approximated by a variance stabilizing transform [241]. They are based on noise assumptions with different statistics. An adaptive cost function has been proposed to mitigate the need for noise statistics [105]. Gradient truncation in various forms is also often applied [11, 30, 102, 211, 227] to prevent the reconstruction divergence, which in some sense indirectly alters the initial cost function.

As we will see in detail in the next chapter, the appropriate noise model for the FPM measurements is a mixed Poisson-Gaussian noise with a significant Poisson component. With this in mind, it is worth considering how this may influence the choice of a cost function.

Intensity-based cost function

The most straightforward approach consists of minimizing the difference between intensity measurements and estimated intensities.

$$f_I(\boldsymbol{O}) = \left\| |\boldsymbol{AO}|^2 - \boldsymbol{I} \right\|^2 . \tag{2.34}$$

It has already been introduced above as a quadratic cost function, Eq. (2.16). The cost $f_I(x)$ is known as the intensity-based cost function. This is a good choice under the assumption that the measurements are corrupted by additive Gaussian noise $\boldsymbol{n}_\sigma$ only, i.e. $\boldsymbol{I} = |\boldsymbol{AO}^*|^2 + \boldsymbol{n}_\sigma$, where $\boldsymbol{O}^*$ is a true object spectrum.

The solution of the optimization problem based on $f_I(\boldsymbol{O})$ is addressed in the literature by different approaches such as Wirtinger Flow [22, 93], MM [163] and convex relaxation [77]. Its gradient has already been presented in Eq. (2.28). Several modifications to the intensity-based cost function have been proposed, including the incorporation of noise relaxation [14] and background subtraction [196].

Amplitude-based cost function

The amplitude-based cost function $f_A(\boldsymbol{O})$ is one of the most widely used objectives [163, 252]. It aims at minimizing the difference between the measured amplitude (the square root of the intensity of the captured images) and the estimated amplitude:

$$f_A(\boldsymbol{O}) = \left\| |\boldsymbol{AO}| - \sqrt{\boldsymbol{I}} \right\|^2 . \tag{2.35}$$

This formulation is standard in the context of coherent imaging systems.

Its gradient is calculated as follows:

$$\nabla f_A(\boldsymbol{O}) = \boldsymbol{A}^H \left(\boldsymbol{AO} - \sqrt{\boldsymbol{I}} \odot \frac{\boldsymbol{AO}}{|\boldsymbol{AO}|} \right) . \tag{2.36}$$

Such a cost function does not explicitly assume any noise statistics. However, its gradient was compared to the gradient of the Poisson likelihood-based cost function (see next subsection) in [226]. Significant similarities between the two were found. At the same time, it was also shown that the amplitude cost can be considered as a special case of a variance stabilizing transform for Poisson distributed measurements [104]. It can therefore be concluded that the amplitude-based cost function is well suited to handle intensity images corrupted by Poisson noise.

As it was already noted above, the classical PIE (Gerchberg-Saxton) algorithm for FPM indirectly optimizes the amplitude-based cost function. Indeed, each step of an internal loop of the algorithm is somewhat analogous to a step of a sequential gradient descent optimization minimizing an amplitude cost.

Given the strong Poisson component of noise in FPM measurements, an amplitude-based cost function $f_A(\boldsymbol{O})$ is more appropriate than an intensity one $f_I(\boldsymbol{O})$ [11].

Poisson-likelihood-based cost function

In order to directly take into account the Poisson-statistics hypothesis of the FPM data, a proposal has been made by Yeh et al. to use a maximum likelihood framework [226]. The assumption here is that each pixel $I_{l,j}$ of a captured image $\boldsymbol{I}_l$ can be modelled as independent random variable following the Poisson distribution with parameter $|\langle \boldsymbol{a}_{l,j}, \boldsymbol{O}^* \rangle|^2$:

$$\boldsymbol{I} \sim \text{Pois}\left(|\boldsymbol{A}\boldsymbol{O}^*|^2\right). \tag{2.37}$$

where Pois$(\cdot)$ indicates that each element of a vector follows the Poisson distribution.

We note $p[I_{l,j}|\boldsymbol{O}]$ the probability to measure a pixel $I_{l,j}$, $l = 1...L$, $j = 1...m^2$ given the estimated signal $\boldsymbol{O}$. The corresponding cost function then comes from a negative log-likelihood of this probability:

$$f_{Poisson}(\boldsymbol{O}) = \sum_{l=1}^{L}\sum_{j=1}^{m^2}\left[|\langle \boldsymbol{a_{l,j}}, \boldsymbol{O}\rangle|^2 - I_{l,j}\log\left(|\langle \boldsymbol{a_{l,j}}, \boldsymbol{O}\rangle|^2\right)\right]. \tag{2.38}$$

And its gradient:

$$\nabla f_{Poisson}(\boldsymbol{O}) = 2\boldsymbol{A}^H\left(\frac{|\boldsymbol{A}\boldsymbol{O}|^2 - \boldsymbol{I}}{\boldsymbol{A}\boldsymbol{O}}\right). \tag{2.39}$$

Details of its derivation can be found in [30] or [226].

This cost function is actively used recently [11, 30, 226, 228] due to the fact that, in general, the noise statistics in experimental data of FPM is more consistent with a Poisson model rather than with a Gaussian model. Unfortunately, solving the optimization problem directly based on the cost $f_{Poisson}(\boldsymbol{O})$ could lead to the divergence [104]. One way to prevent it is to truncate the gradient of the function. This issue will be addressed in Subsection 2.4.3.

Mixed Poisson-Gaussian-likelihood-based cost function

As we will show in the next chapter, our FPM measurements are not corrupted by a single type of noise, but rather by a mixture of noises. Indeed, the camera introduces noise of Poisson-Gaussian statistics.

Each pixel of an observed image $\boldsymbol{I}_l$ can then be seen as an independent random Poisson variable $\boldsymbol{p}_l$, scaled by $\alpha_l > 0$ and distorted by additive Gaussian noise $\boldsymbol{n}_{\mu_l,\sigma_l}$ of mean μ_l and standard deviation σ_l^2:

$$\boldsymbol{I}_l = \frac{1}{\alpha_l}\boldsymbol{p}_l + \boldsymbol{n}_{\sigma_l}, \quad l = 1, ..., L, \tag{2.40}$$

where $\boldsymbol{p}_l \sim \text{Pois}\left(\alpha_l \left|\langle \boldsymbol{A_l}, \boldsymbol{O}^* \rangle\right|^2\right)$ and $\boldsymbol{n}_{\sigma_l} \sim N(\mu_l, \sigma_l^2)$.

The number of photons received by a pixel of a camera's sensor follows the Poisson distribution. This number is then transformed into an intensity value of a captured image, which is linearly proportional but not necessarily equal to the photon count. A scale factor α_l represents the coefficient of this transformation [10]. It could also vary for different images if the acquisition times were not the same. Therefore, the actual pixel value might follow the Poisson distribution of a different "power". It is likewise not obvious that all captured images suffer from the same amount of additive noise, especially in the case of uneven acquisition times. Therefore, σ_i could potentially be different for dark and bright field images. To our knowledge, this question is not addressed in the literature on Fourier ptychography.

An attempt was made to derive and test cost functions considering a possible non-unitary Poisson scale α_l and σ_l variations. The experimental identification of these two parameters will be discussed in the next chapter. However, no promising results in terms of reconstruction quality were observed during the first trials. It was decided that this issue would not be fully explored in the ongoing work. However, it may be interesting to investigate this point in future work, particularly in the case of variable acquisition times.

We therefore assume that $\alpha_l = 1$, $\sigma_l = \sigma$ and $\mu_l = 0$ for all L captured images, which leads to the following model:

$$\boldsymbol{I}_l = \boldsymbol{p}_l + \boldsymbol{n}_\sigma, \quad l = 1, ..., L. \tag{2.41}$$

This is the model first presented for FPM by Zhang et al. in [240].

As the authors have shown, the log-likelihood corresponding to such a distribution would be difficult to handle directly. Instead, a generalized Anscombe transformation (GAT) is used to approximate the model (2.41):

$$\widetilde{\boldsymbol{I}}_l = \sqrt{\boldsymbol{I}_l + 3/8 + \sigma^2}, \quad l = 1, ..., L. \tag{2.42}$$

Using this approximation, the Poisson-Gaussian-likelihood-based cost function is derived by a log-likelihood approach:

$$f_{GAT}(\boldsymbol{O}) = -2 \sum_{l=1}^{L} \sum_{j=1}^{m^2} \left[\widetilde{I}_{l,j} \sqrt{\left|\langle \boldsymbol{a_{l,j}}, \boldsymbol{O} \rangle\right|^2 + 3/8 + \sigma^2} - \left(\left|\langle \boldsymbol{a_{l,j}}, \boldsymbol{O} \rangle\right|^2 + 3/8 + \sigma^2 \right) \right]. \tag{2.43}$$

As in the case of the Poisson-likelihood-based cost function, the gradient truncation is proposed as a part of an optimization algorithm.

We note that other variance-stabilized cost functions are also proposed in the literature [104].

Gradient truncation

The Poisson-based cost functional takes into account a noise statistic of the data. However, there is a challenge with the derived optimization problem.

As many papers have pointed out, the gradient $\nabla f_{Poisson}(\boldsymbol{O})$ of this function is uncontrollable [11, 30, 115, 241]. This can lead to the degeneration of the solution by outliers. The same problem has also been observed for the Gaussian-Poisson-based cost [240] and the amplitude cost [211].

Gradient truncation in the form of a pixel-wise thresholding operation is adopted as a classic strategy for dealing with outliers in the phase retrieval problem. Several formulations have been proposed in the literature. Each cost function is usually associated with its own outliers.

The classical truncated gradient proposed for the Poisson optimization problem has the following form:

$$\nabla_{\mathcal{T}} f_{Poisson}(\boldsymbol{O}) = A^H \boldsymbol{v}, \qquad v_i = \begin{cases} 2\frac{|\langle \boldsymbol{a}_i, \boldsymbol{O}\rangle|^2 - I_i}{\langle \boldsymbol{a}_i, \boldsymbol{O}\rangle}, & i \in \mathcal{T}(\boldsymbol{O}) \\ 0, & \text{otherwise} \end{cases}, \tag{2.44}$$

where the notation I_i and $\boldsymbol{a_i}$ with $i = 1...Lm^2$ is used instead of $I_{l,j}$ and $\boldsymbol{a}_{l,j}$ with $l = 1...L$, $j = 1...m^2$.

The key point here is to update only those pixels of the object that belong to a subset $\mathcal{T}(\boldsymbol{O})$ of non-aberrant directions [30]. The decision whether or not to update the pixel is made on the basis of the data and the current estimate. One of the most common formulas for defining these acceptable gradient components is:

$$\mathcal{T}(\boldsymbol{O}) = \xi_1^i(\boldsymbol{O}) \cap \xi_2^i(\boldsymbol{O}) \tag{2.45}$$

with

$$\xi_1^i(\boldsymbol{O}) = \left\{ a^{lb} \leq \frac{|\langle \boldsymbol{a}_i, \boldsymbol{O}\rangle|}{\|\boldsymbol{O}\|^2} \leq a^{ub} \right\}, \tag{2.46}$$

$$\xi_2^i(\boldsymbol{O}) = \left\{ \left| I_i - |\langle \boldsymbol{a}_i, \boldsymbol{O}\rangle|^2 \right| \leq a^h \left\| \boldsymbol{I} - |\boldsymbol{AO}|^2 \right\|_1 \frac{|\langle \boldsymbol{a}_i, \boldsymbol{O}\rangle|}{\|\boldsymbol{O}\|^2} \right\}, \tag{2.47}$$

where a^{lb}, a^{ub} and a^h are experimentally chosen parameters. Moreover, these constants must be chosen differently depending on the step size strategy and, of course, on a minimized cost function.

The truncation procedure, Eq. (2.45), is based on the law of large numbers, a detailed explanation of the underlying principles of this method can be found in [30]. Another common version [11] does not take into account the subset $\xi_1^i(\boldsymbol{O})$. Note, that other rules for $\mathcal{T}(\boldsymbol{O})$ exist [102, 115, 211, 228], but we have only implemented the one given by Eq. (2.45). In addition, a similar approach can in theory be applied to any cost function.

To illustrate the importance of this truncation in the case of Poisson-based cost function optimization, we can examine the percentage of truncated pixels in the vector $\boldsymbol{v}$, Eq. (2.44). A set of simulated image data presented at the beginning of this chapter is used for demonstration purposes. In the first step, with a basic initialization strategy (a low-resolution resized image), up to 20% of the pixels can be truncated. This figure decreases significantly

for subsequent iterations, as the estimate becomes better, and varies around 0.3% and 2%, see Fig. 2.16(a). Fig. 2.16(b) shows a distribution of truncated pixels as a function of the position of a LED. Each square represents the percentage of truncated pixels for an image $l = 1...L$ of the corresponding gradient component. By one component here we understand a part of the vector $\boldsymbol{v}$ that corresponds to one illumination angle. While some components are completely intact, others suffer from up to 20% truncated pixels. The most affected components correspond to the LEDs at the edge of the bright/dark field area. These edge LEDs also produce images with a high value variance. As an example, Fig. 2.16(c) shows a gradient component with a highest number of outliers. Fig. 2.16(d) shows its truncated pixels. And the Fig. 2.16(e) shows the same gradient component after the application of truncation. Outliers could be expected to be random pixels corrupted by noise in the original captured images. But this is not the case, and the truncated values rather correspond to structures in the signal.

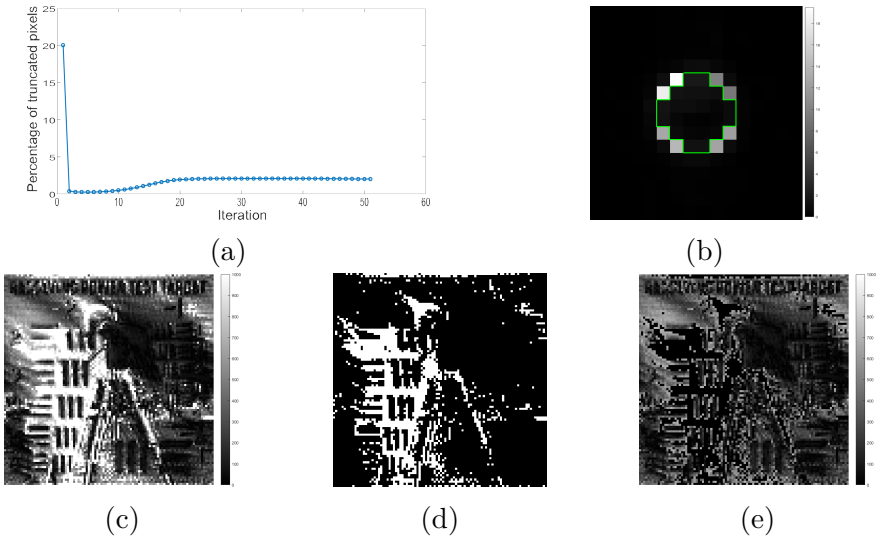

(a) (b)

(c) (d) (e)

Figure 2.16: Gradient truncation. The ground source object for the simulated data set is a USAF target image for amplitude and the cameraman for phase. The optimization procedure is a Wirtinger flow algorithm with a Poisson cost function and an increasing step size. (a) The percent of truncated pixels in the vector $\boldsymbol{v}$ at each iteration. (b) The distribution of truncated pixels as a function of the position of a LED, calculated at the 10th iteration. The squares inside the green outline correspond to simulated bright field images. (c) A calculated gradient component with a highest number of outliers (at the 10th iteration). (d) Its truncated pixels mask. (e) The gradient component after the application of truncation. The colormap limits are the same for the image (c) and (e).

We have also considered an alternative idea of using a weighted truncation instead of the binary one. The proposed procedure is mainly based on

the assumption that the outlier search directions within the components have been computed correctly, but their values are too elevated relative to the surrounding pixels. For this reason, we suggest reducing the influence of these components instead of inactivating them completely. This translates into the following rule, which simply implies setting a threshold for all pixels considered abnormally high :

$$\nabla_{\mathcal{T}} f_{Poisson}(\boldsymbol{O}) = A^H < \boldsymbol{v}, \boldsymbol{w} >, \qquad w_i = \begin{cases} 1, & i \in \mathcal{T}(\boldsymbol{O}) \\ \frac{a^h \left\| \boldsymbol{I} - |\boldsymbol{A}\boldsymbol{O}|^2 \right\|_1 |\langle \boldsymbol{a}_i, \boldsymbol{O} \rangle|}{|I_i - |\langle \boldsymbol{a}_i, \boldsymbol{O} \rangle|^2 |\|\boldsymbol{O}\|^2}, & \text{otherwise} \end{cases}, \tag{2.48}$$

In this way, a criterion ξ_2, Eq. 2.47, is always satisfied, but the modified gradient components do not contain abrupt fluctuations in values.

We also note that an analogous gradient reweighting procedure has been proposed for a Wirtinger flow algorithm with a cost function based on the amplitude [212, 227]. However, the rules for calculating the weights are different. The weights would also be applied to the cost function. These rules have not been implemented in the current work.

The effects of those gradient truncation will be explored in Section 2.4.4. While the gradient truncation approach works well in practice, it has obvious drawbacks. First of all, it is necessary to choose the parameters experimentally. Second, such a procedure indirectly alters the minimized cost function. Therefore, strictly speaking, we no longer optimize the cost function based on the Poisson noise statistics (or another cost), but a version of it that we do not have access to.

Denoising and regularization

A number of constraints and regularizations could improve the robustness of the algorithms to noise and increase performance. We give a brief overview of the possible modifications of the cost functions. However, none of them are implemented in the current work, so they will not be discussed in detail.

Re-weighting The re-weighting of the updates for the alternate projection algorithm is somewhat similar to the re-weighting of the gradient in the case of gradient-based optimization. Several studies have been proposed in this direction [92, 179, 214].

Other studies propose to re-weight directly the cost functions. For example, a much higher weight could be set for the components of a cost function corresponding to bright-field images and a lower weight for dark-field entries [94]. Another method involves giving greater weight to regions of captured images having a high SNR [237].

Noise relaxation Several works have proposed to introduce an additive noise relaxation constraint [14, 26]. Such a constraint is most often a form of l_2 regularization of a noise model term that is optimized for.

De-noising Zhixin Li et al. have adapted a framework called "regularization by denoising" to FPM. Their regularizer is constructed using a BM3D denoiser engine. [114]. A method based on the BM3D denoiser has also shown promising results in the context of compression phase retrieval with a limited number of measurements [125]. David Ren et al. use total variation regularization on both amplitude and phase of the object in the spatial domain [164]. This translates into two additional terms in the cost function.

Sequential algorithms The above approaches are intended for global gradient algorithms. Several denoising and regularization methods have also been developed for alternating projections like sequential algorithms. For example, a noise discrimination factor can be introduced as an additional step in a PIE algorithm [51]. Another approach is proposed by Laura Waller et al. [196] by adding a regularization constant in a denominator of a spectrum update step. This is essentially equivalent to a l_2 regularization. Yongbing Zhang et al. introduced a regularization term based on a sparse constraint [236].

To conclude, the regularization of a cost function is a fairly common solution in the FPM reconstruction. It would be worthwhile to adopt some of these methods in future work.

2.4.4 Comparison and choice of methods

Simulated data

We use 3 data sets of numerically simulated images to compare the methods.

The first set $S_1 : \boldsymbol{I} = |\boldsymbol{AO}^*|^2$, $l = 1...L$ is a noiseless simulation with perfect model parameters, given by the Eq. (2.12). This scenario is, of course, never observed in practice.

The second set S_2 is corrupted by Poisson noise and Gaussian additive noise, $S_2 : \boldsymbol{I}_l = \boldsymbol{p}_l + \boldsymbol{n}_{\sigma_l}, \quad l = 1, ..., L$. The notations is defined by the Eq. 2.40. In order to be consistent with other works, we set $\alpha_l = 1$, $\mu_l = 0$ and $\sigma_l = \sigma$ for all $l = 1...L$. Although many studies use Poisson noise and Gaussian noise as separate cases for model analysis, we argue that this is not consistent with experimental data. Indeed, the actual noise in the case of FPM measurements is a mixture of the two, as we illustrate in the next chapter. We set $\sigma = 2.2$ which results in around 10% noise corruption according to the formula $\sum \frac{|\mathbf{I}_{noisy} - \mathbf{I}_{perfect}|}{\mathbf{I}_{perfect}}$.

The third data set S_3 is what we define as being close to the observed data. The data are corrupted by scaled camera noise ($\alpha_l \neq 1$) and model

misalignments. The set is defined as

$$S_3 : \boldsymbol{I}_l = c_l \left(\frac{1}{\alpha_l} \boldsymbol{p}_l + \boldsymbol{n}_{\sigma_l} \right), \quad l = 1, ..., L, \tag{2.49}$$

with $\boldsymbol{p}_l \sim \text{Pois}\left(\alpha_l \left| \left\langle \tilde{\boldsymbol{A}}_{\boldsymbol{l}}, \boldsymbol{O}^* \right\rangle \right|^2 \right)$, where $\tilde{\boldsymbol{A}}_{\boldsymbol{l}}$ is a component of a design matrix with misalignments. All model deviations and errors, as well as an intensity variation coefficient c_l, will be presented in detail in the next chapter after the characterization of the constructed instrument.

We use the USAF target and the cameraman images as the amplitude and the phase of the ground truth object. The system parameters correspond to the configuration of our microscope. More precisely, a pixel size is 6.5 µm x 6.5 µm, the NA is 0.07, the magnification is 2.03, the wavelength is 629 nm. The centre of the LED matrix is located between 4 LEDs. The segment size is 100 x 100 pixels. The pixel size ratio is fixed at 3.5 as 16x16 central LEDs are used for this analysis.

Error metrics

Several error metrics have been proposed in the literature to assess the quality of reconstruction. Here we present only those measures that take into account the ground truth. Quality assessment for experimental data will be discussed in Section 3.3.

A common measure for the phase retrieval problem is the Euclidean distance metric [22]:

$$\text{dist}(\boldsymbol{O}, \boldsymbol{O}^*) = \min_{[0,2\pi)} \left\| \boldsymbol{O} e^{-j\phi} - \boldsymbol{O}^* \right\|, \tag{2.50}$$

where $\boldsymbol{O}$ is an estimated complex solution, and $\boldsymbol{O}^*$ is the ground truth. The term $e^{-j\phi}$ reflects one of the trivial ambiguities of phase recovery. Indeed, the solutions $\boldsymbol{O}$ and $\boldsymbol{O}e^{-j\phi}$ are equivalent.

For the FPM, the most widely adapted metric is perhaps the relative error [226]:

$$RE(O, O^*) = \frac{\|\boldsymbol{O} - \boldsymbol{O}^*\|^2}{\|\boldsymbol{O}^*\|^2}, \tag{2.51}$$

Or its more correct variant, taking into account the global phase recovery ambiguity [11]:

$$RE_\phi(O, O^*) = \frac{\min_{[0,2\pi)} \left\| \boldsymbol{O} e^{-j\phi} - \boldsymbol{O}^* \right\|^2}{\|\boldsymbol{O}^*\|^2}, \tag{2.52}$$

Alternatively, these errors could also be calculated in the spatial domain. Other metrics, such as the normalized invariant field root mean square error [92, 237] are also used.

Method comparison

In this section, we study the performance of the implemented algorithms under different error levels by means of simulation. All our programs are written in Matlab. Separate aspects of methods are tested against each other, as opposed to a mixture of methods. For the data sets with errors (S_3), we focus on assessing the quality of the reconstruction rather than the convergence behaviour.

First, we compare the convergence of methods for a noise-free data set (S_1) and for a data sets with only Poisson-Gaussian noise (S_2). The relative error given by the Eq. (2.52) is plotted as a function of the number of iterations. Then we compare the approaches one-by-one under noise and error conditions (S_3). For this, we generate 100 realizations of the noise and plot the relative error as a function of the realization. A maximum of 100 iterations are performed.

The influence of the following algorithmic features is reported here: the choice of the spectrum update step (the optimization algorithm), the size of the update step, the initialization strategy, the cost function and the gradient truncation rule.

The computer used has 64 GB of RAM and 2 processors with a 2.10 GHz base frequency.

Optimization algorithm The following optimization algorithms are compared:

a) the PIE (alternating projections) with a constant update step given by Eq. (2.23);

b) the PIE with an adaptive step size;

c) the steepest gradient descent;

d) the conjugate gradient descent with a coefficient of Polak-Ribière;

e) the conjugate gradient descent with a coefficient of Hestenes-Stiefel;

f) the L-BFGS.

We use the same initialization and the same cost function (amplitude-based) without truncation. The step size is also the same, it increases according to the rule given by Eq. (2.29). The exception is alternative projection algorithms which, strictly speaking, should not be directly compared in the same way to global gradient-based algorithms. Essentially, a comparison between gradient-based algorithms only looks at the direction of descent.

The results for the noiseless case are shown in the Fig. 2.17 (a,b) The relative error is plotted against the iteration number. The same metric evaluated on a reconstruction from the data corrupted by Poisson-Gaussian noise is shown in Fig. 2.17 (c,d).

The Fig. 2.18 shows objects reconstructed by different algorithms from the data set S_2. The visual quality of reconstruction corresponds well to the relative error metric. For example, the images (b) and (f) corresponding to the PIE with an adaptive step size and the L-BFGS algorithms are practically visually indistinguishable and have close final error. The image (e) showing the result of the conjugate gradient descent with a coefficient of Hestenes-Stiefel contains the most artifacts and has the biggest error.

And lastly, we simulate 100 different realizations of a data set S_3 with noise and errors. The relative error calculated at the final stage of the reconstruction procedure is plotted as a function of the noise realization, Fig. 2.19. The PIE with an adaptive step and the L-BFGS outperform on average the other schemes tested. However, there are some instances where this is not the case. These realizations correspond to datasets where misalignments result in abnormally high levels of generated model error.

The runtime for a reconstruction on $S2$ data is measured at 53 s, 39 s, 104 s, 104 s, 105 s and 109 s in the respected order of the algorithms listed above. We note that adaptive step PIE has a different convergence metric and has converged faster than conventional PIE. Otherwise, it takes a little longer to perform an iteration because the step size reduction descision has to be computed. It should also be noted that additional resources are used because we save the data at each iteration and display intermediate results. In addition, there is room for improvement regarding code optimization, which could further reduce computation time.

Simulation results suggest that, given our FPM configuration, the PIE algorithm with adaptive step size is superior to all other optimization algorithms tested and under all noise conditions tested. Both in terms of reconstruction quality (i.e. the smallest relative error $RE_\phi(O, O^*)$) and in terms of computing time. However, this comparison is not entirely fair due to the different nature of the algorithms (sequential vs. global) and the choice of step size for global algorithms.

The conjugate gradient descent performs better with the coefficient of Polak-Ribière rather then the coefficient of Hestenes-Stiefel in our simulations. However, as we can see, the Polak-Ribière conjugate gradient produces results almost equivalent to those of the steepest descent, assuming that the coefficient may simply be too small for the conjugate direction to be taken into account. The Hestenes-Stiefel conjugate gradient diverges in the case of perfect data, but the problem is mitigated for noisy conditions. That being said, conjugate gradient algorithms are supposed to be used with a line search strategy. It would be interesting to test the different $\boldsymbol{\beta}^{(t)}$ coefficients with another step size implementation.

Among the gradient based methods, the L-BFGS algorithm is the most powerful, which is not surprising. Indeed, it is based on the approximation of a Hessian matrix which yields better search directions.

We note that we build our implementation of conjugate gradient and L-

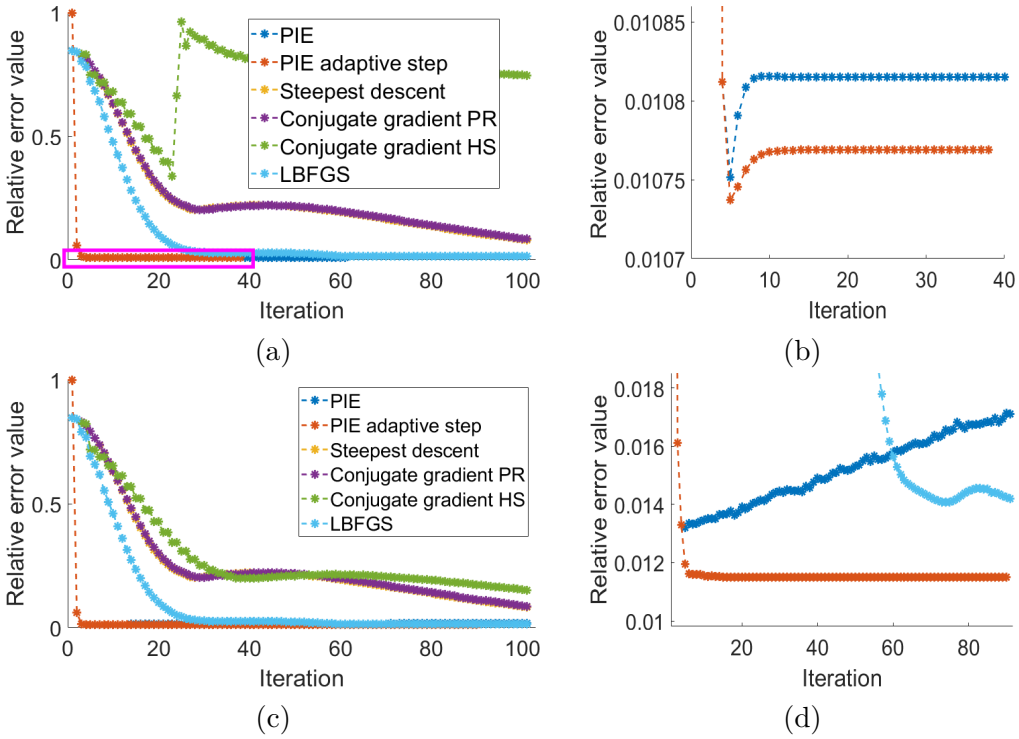

Figure 2.17: The relative error plotted as a function of the number of iterations. (a) The results for the noiseless case S_1. (b) A zoom on the magenta zone to highlight the differences between PIE and PIE with the adaptive step methods. (c) Evaluation on a reconstruction from the data corrupted by Poisson-Gaussian noise S_2. (d) A zoom on the PIE and PIE with the adaptive step methods.

BFGS methods on the basis of the open-source project "Unconstrained optimization of real functions in complex variables" by Sorber et al. [180]. The basic algorithm of alternate projections for FPM is given in the book "Fourier Ptychographic Imaging" by Guoan Zheng [243]. We have also adapted codes for the quasi-Newton method provided by Laura Waller's team [196]. However, we do not test it against our methods because the proposed algorithm has too many additional components such as regularization, pupil reconstruction, background noise removal, etc. The comparison would therefore not be fair.

Step size The step sizes are tested under the steepest gradient descent algorithm. The cost function is amplitude-based. We have studied the following rules:

a) the constant step size $\mu = 1$;

b) the constant step size $\mu = 0.1$;

c) the increasing step given by Eq. (2.29), $t_0 = 330$ and $\gamma_{max} = 0.4$;

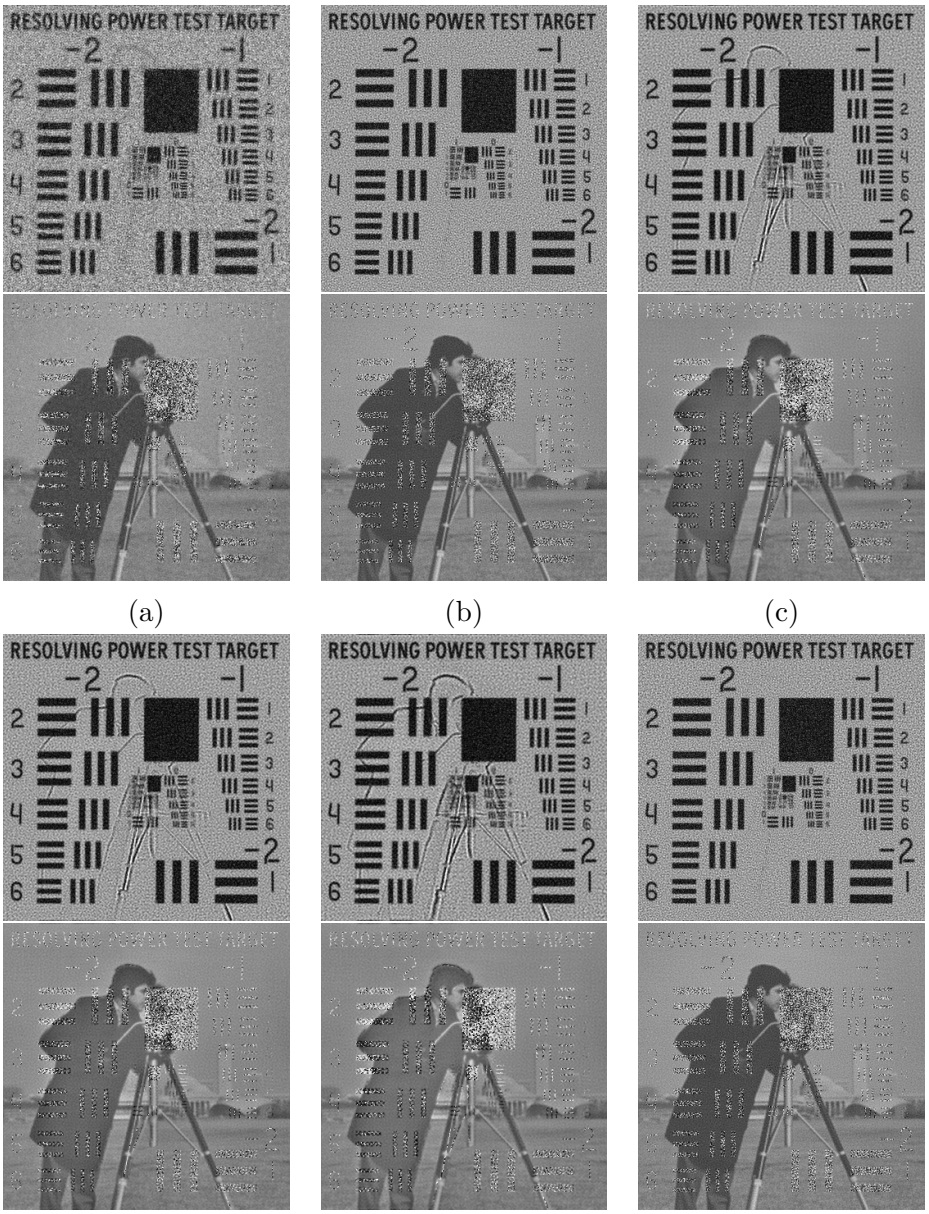

Figure 2.18: Examples of images reconstructed from the simulated set S_2. The top image of each sub-figure is the reconstructed amplitude, the bottom image is the phase. The order of the methods corresponds to the list given above (2.4.4).

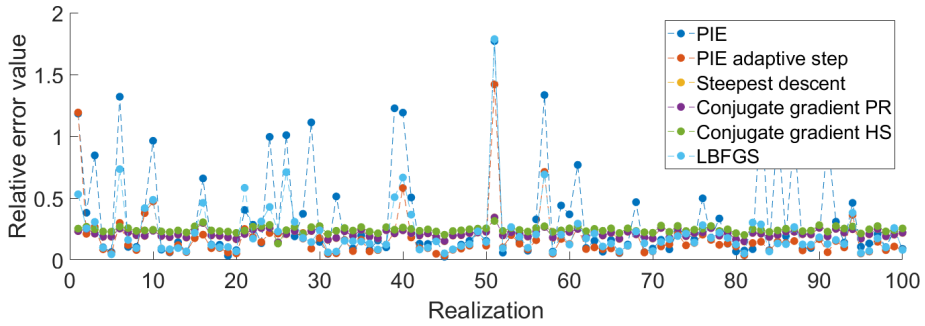

Figure 2.19: The relative error plotted for different realizations of a simulated set S_3 with noise and errors.

d) the Golden-section line search.

The results for the S_2 mixed camera noise dataset are presented in figure 2.20(a). The figures are very similar for the noiseless case S_1 and are therefore not presented here. An evaluation on a S_3 set with camera noise and model error is shown in Fig. 2.20(b).

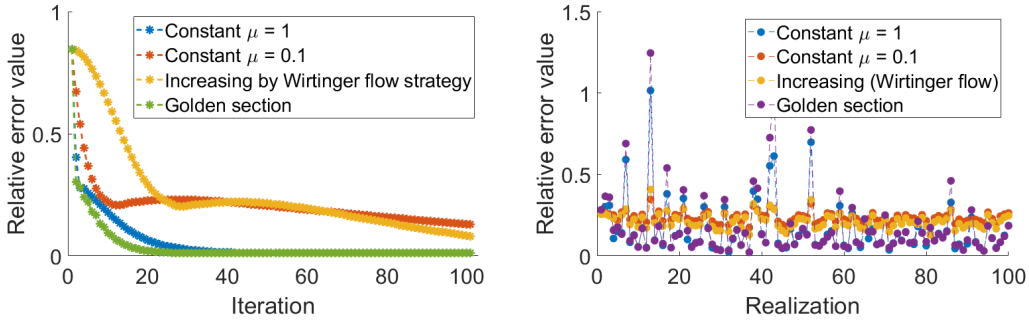

(a) (b)

Figure 2.20: Step size strategies evaluation. (a) The relative error plotted as a function of the number of iterations, based on the data corrupted by Poisson-Gaussian noise S_2. (b) The relative error plotted for different realizations of a simulated set S_3 with noise and errors.

The results indicate that the choice of the step size is indeed an important parameter to take into account when choosing a reconstruction approach. However, even a simple constant step could be a good choice if the chosen size is appropriate. A line search method (here the golden section) produces the fastest convergence in terms of number of iterations and the best quality of reconstruction but on the extent of costly additional calculations. It slows down the reconstruction by a factor of 6 in our experiments.

Cost function The cost functions are tested under the steepest gradient descent algorithm with an increasing step size. The cost functions considered are:

a) the intensity-based, Eq. (2.34);

b) the amplitude-based, Eq. (2.35);

c) the Poisson-likelihood-based, Eq. (2.38);

d) the mixed Poisson-Gaussian-likelihood-based, Eq. (2.43).

We used a classical parameter of $t_0 = 330$ for the step size with all cost functions except a cost based on intensity. Indeed, such a step is too small for the intensity-based cost. The parameter $t_0 = 10$ is used instead. The comparison results are shown in the Fig. 2.21. As we see, the final errors are quite close for all four cost functions, Fig. 2.21(a). The Poisson-based reconstruction deviates for some realizations of the set S_3, Fig. 2.21(b).

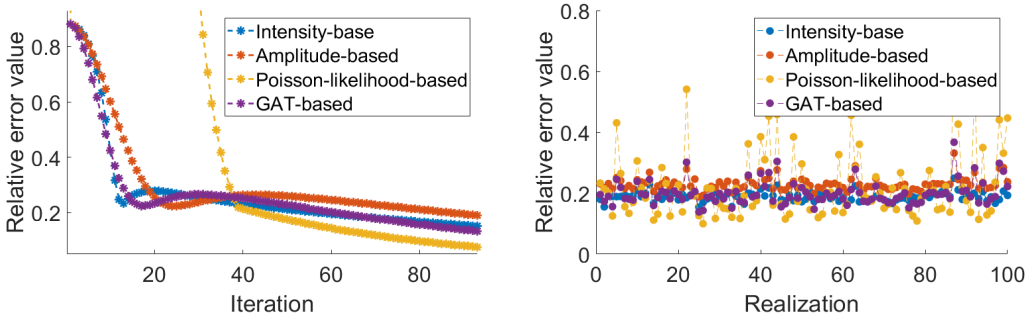

(a) (b)

Figure 2.21: Cost function choice evaluation. (a) The relative error plotted as a function of the number of iterations, based on the data corrupted by Poisson-Gaussian noise S_2. (b) The relative error plotted for different realizations of a simulated set S_3 with noise and errors.

In future work, a relationship between the cost function and the optimization procedure, in particular the step size strategy, should be examined in detail.

Gradient truncation The gradient truncation strategy was originally proposed for the Poisson cost function as it suffers the most from possible outliers. We therefore test this strategy for the Poisson functional. The algorithm is once again the steepest gradient descent with an increasing step size. The truncation rules tested are the following:

a) no truncation applied;

b) the classical truncation for the Poisson cost function, Eq. (2.44), the parameters are $a^{lb} = 0.3$, $a^{ub} = 25$ and $a^h = 25$;

c) its modified weighted version, Eq. (2.48).

The results for the simulated set S_2 are shown in the Fig. 2.22. The efficiency of the truncation was also evaluated on 100 different realizations of a data set S_3 with noise and errors. The relative error calculated at the final stage of the reconstruction procedure is plotted as a function of the noise realization. Figure 2.22(b) shows the error taking into account a global shift ambiguity $RE_\phi(O, O^*)$. Figure 2.22(c) shows the simple relative error $RE(O, O^*)$. If we consider only the first formula $RE_\phi(O, O^*)$, we could conclude that a pure Poisson cost function performs better than the classical truncation strategy. However, looking at the relative error calculated with the basic formula $RE(O, O^*)$, the situation is reversed. Visual validation clearly indicates that the application of truncation strategies is beneficial, see Figure 2.23. This example shows that the choice of the error measure is not obvious, even in the case of a known ground truth. The choice of a correct error metric can influence the interpretation of the quality of the reconstruction.

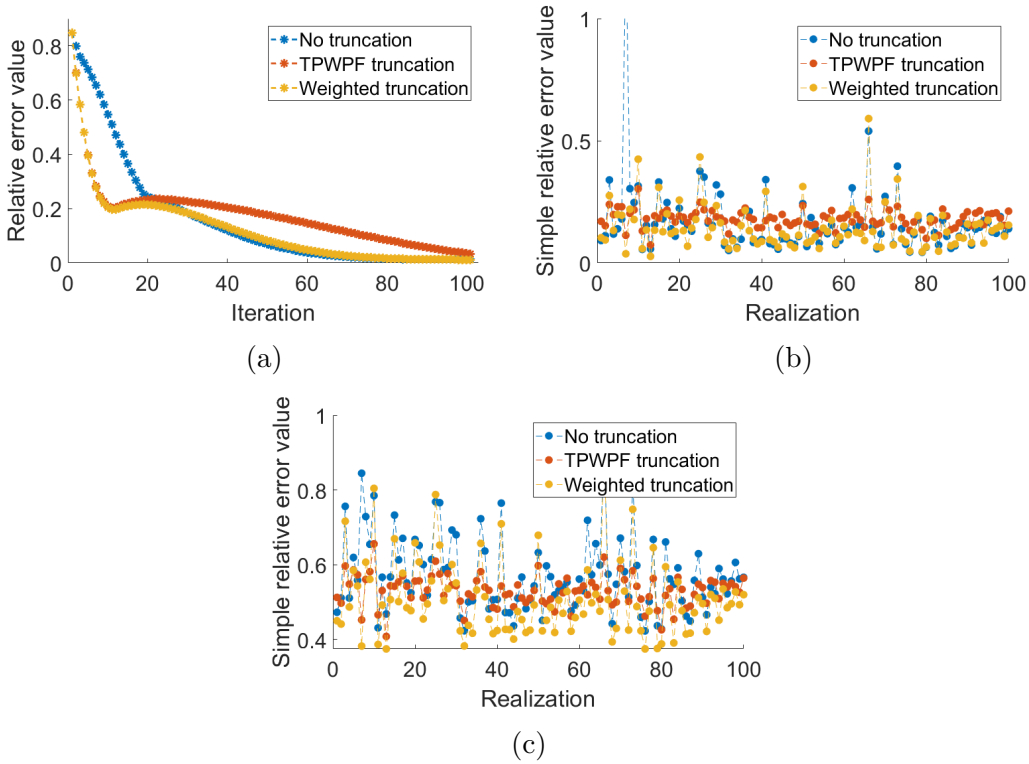

Figure 2.22: Truncation strategies evaluation. (a) The relative error plotted as a function of the number of iterations, based on the data corrupted by Poisson-Gaussian noise S_2. (b) The relative error accounting for a global shift ambiguity $RE_\phi(O, O^*)$ plotted for different realizations of a simulated set S_3 with noise and errors. (c) The simple relative error $RE(O, O^*)$ plotted for different realizations of a simulated set S_3 with noise and errors.

The steepest descent with increasing step size, Poisson cost function and gradient truncation is know under the name "truncated Poisson Wirtinger

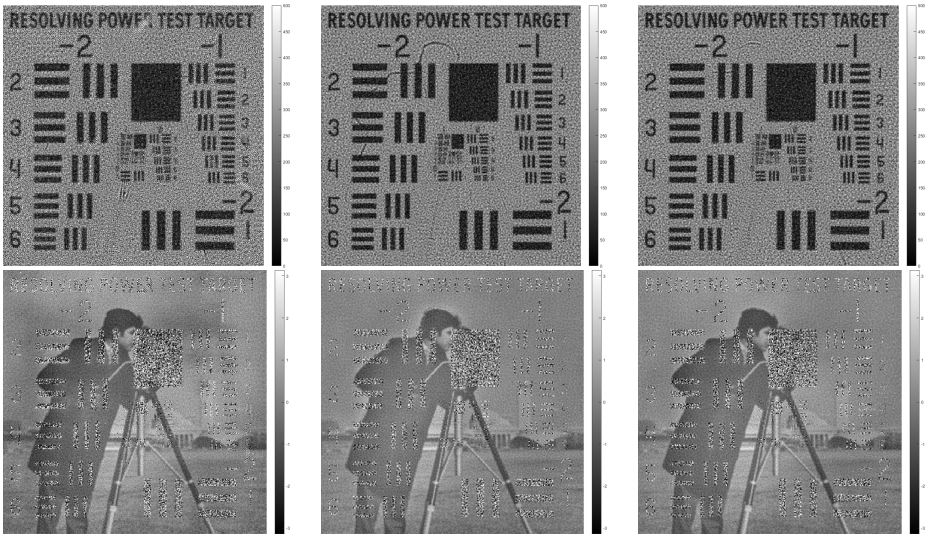

Figure 2.23: Examples of images reconstructed with a Poisson cost function from the simulated set S_3. The top image of each sub-figure is the reconstructed amplitude, the bottom image is the phase. (a) No truncation is applied, $RE_\phi = 0,14$, $RE = 0,57$. (b) The classical truncation, Eq. (2.44), $RE_\phi = 0,21$, $RE = 0,56$. (c) The weighted truncation, Eq. (2.48), $RE_\phi = 0,15$, $RE = 0,52$.

Fourier ptychographic reconstruction" [11]. Its code is provided for free access by Liheng Bian et al. It is a little bit different from our implementation, having only ξ_2^i subset considered for the truncation, Eq. (2.47).

2.4.5 Conclusions

We have implemented several approaches, some of which could be combined with each other. There is no single clear and obvious answer as to which algorithm or aspect of an algorithm is the best choice under all possible conditions and constraints. For the present thesis, the decision was made to use a PIE (alternating projections) method with an adaptive step size strategy.

Several reasons contributed to this choice. First, it is one of the most robust methods. It reconstructs consistently and with satisfactory results most of the data sets we have tested, including the experimental ones. Secondly, it is the fastest of our implemented methods, with rapid convergence and low memory requirements. Given the number of pixels to be treated and reconstructed, this becomes a significant advantage. Third, alternative projection algorithms are used extensively in FPM research. Fourth, it implicitly minimizes an amplitude-like cost function, which proves to be a good choice for data corrupted by Poisson noise. Finally, the PIE framework allows great flexibility and a more intuitive interpretation of iteration results. It is easy to incorporate modifications and test the effects directly at the update stage. While this is not considered an advantage for the final application of the instrument, it was important for us to have a visual representation of each sub

iteration in order to identify potential problems. On the other hand, global methods are more sensitive to initialization and can get stuck in global minima. As the whole data set is processed at each iteration, it requires more calculations than an iterative method. In addition, most algorithms require fine tuning of the parameters. Moreover, the number of options to be taken into account, such as the cost function, the truncation of the gradient, the size of the update step, makes it difficult to justify all these small choices.

We note that the reason we found the PIE algorithm so successful may be related to the amount of spectrum overlap in our FPM configuration. Indeed, it has been suggested that sequential methods may perform better when there is considerable data redundancy.

The relationship between algorithms performance and spectrum overlap need to be further investigated. Numerous other aspects must also be assessed in order to confirm with certainty the choice of a reconstruction method. Different combinations of elements examined separately in Section 2.4.4 should be tested against other combinations. That is, a more in-depth analysis would be required with a mixture of parameters and configurations. Other data sets should be additionally tested. These include different types of ground truths, such phase-only objects or objects simulating biological tissues. In addition, as shown in the simulations with 100 noise realizations, the algorithms behave differently depending on errors and noise levels and conditions. This needs to be carefully examined and explained. We also stress the importance of the choice of the error metric used during validation, even when the ground truth is known. It is possible to misinterpret the results when no visual confirmation is additionally used. And, of course, similar tests should also be conducted with experimental data sets and with data that are available on internet. Furthermore, popular algorithms such as a quasi-Newton sequential method should be implemented as they are often used for comparison in FPM research [196]. It would also be worth implementing a sequential version of the global algorithms, especially for second-order methods. Indeed, some studies have shown that this could be beneficial for FPM [104].

Undoubtedly, all these aspects of numerical methods deserve further study. However, in the context of the time constraints of this thesis, it was decided to stick to a single optimization strategy and to further develop the experimental part and multimodal imaging capabilities. Especially since a number of studies comparing reconstruction procedure have already been carried out, both for the general phase retrieval problem [221] and for the more specific case of FPM [104, 226].

Chapter 3

Realization of the Fourier Ptychographic microscope

Upon my arrival to the laboratory, there was no device in the team to perform Fourier Ptychography or any other phase recovery technique. The following specifications and constraints for the design of the device have been adopted:

– It should make it possible to implement a classic Fourier Ptychography technology;

– The device must have the fewest components and be as simple as possible in order to obtain better knowledge and better control of the experimental conditions;

– It should have a low price, at least in its simplest original configuration;

– The working distance shall be long enough to ensure a wide field of view and a place to insert additional optical elements;

– It should allow interchangeability of components and be easy to maintain.

Based on these constraints and the experience of the TRIO team in the development of optical devices, it was decided to build the microscope from scratch instead of buying and modifying an existing microscope.

Consequently, the following design steps must be implemented: the system diagram must be proposed, the equipment must be ordered and the mechanical parts manufactured, the device must be correctly assembled, calibrated and characterized.

3.1 Instrument introduction

The hardware components of the device and the acquisition process will be described in this section. As well as the calibrations that are performed outside the reconstruction algorithm.

3.1.1 System diagram

Following the proposal of the classical configuration of FPM, the basic components of the system should include: a matrix of LED elements, a microscope objective, an extension tube, a camera, as well as mechanical parts to hold a specimen and optical components. To this end, the diagram of the mechanical parts was designed in the SolidWorks software by the members of the TRIO team, Fig. 3.1.

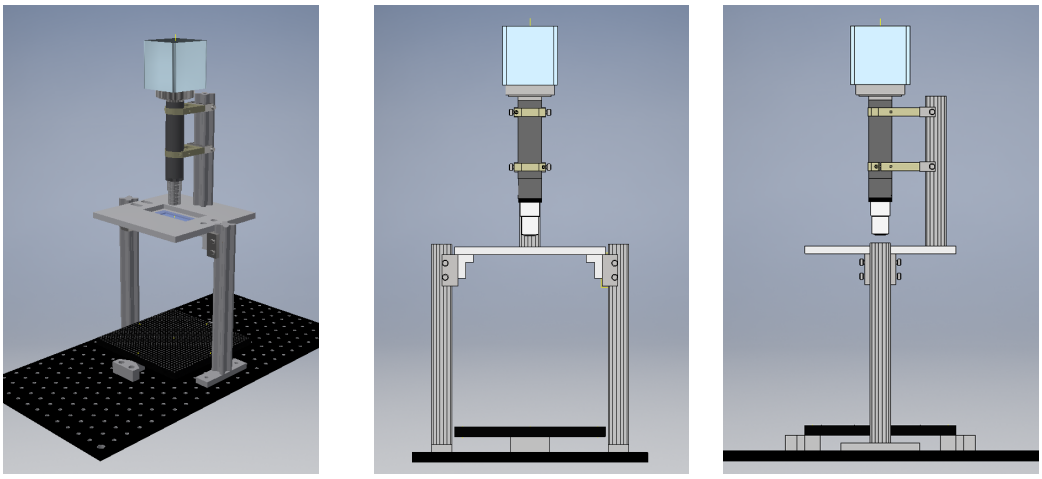

(a) 45° view (b) Front view (c) Side view

Figure 3.1: The diagram of the mechanical parts of the device.

3.1.2 Extension tube manufacture

The length of the extension tube can be calculated theoretically given the specification of the objective and the lens tube. However, any small deviation in the distance between the optical elements or in the actual lens focal lengths may cause the focal point to shift. The purpose of this part is to manufacture an extension tube of fixed length that allows a projection of the focused image exactly at the level of the camera sensor plane. To this end, the work is divided into two stages. Firstly, the working distance of the objective A is defined. Secondly, flange focal distance of the camera B is measured for the lens tube used.

The first part is used to find the actual working distance at which the lens forms an image at infinity. This is crucial for correct measurements in the second step. Our set-up is based on a classical autocollimation method, Fig. 3.2(a). First, a point source is generated using a laser (1), a 20x microscope objective (2) and a 30 µm pinhole (3). We place the microscope 2x objective (4) on a moving rail. The mirror (5) is used to reflect back the beam of light. The exact working distance is then defined by analysing the light reflected on

the pinhole screen. The measurements are consistent with the manufacturer's data and give a value of $A = 34$ mm.

The second stage, Fig. 3.2(b), involves a tube lens (2) a an adapter ring (3), a variable length extension tube (4) and the camera (5). A focal length of 200 mm of the tube lens suggest that the distance C between the centre of that lens (2) and the camera sensor (6) should be exactly 200 mm. Given that we could deduce theoretically the flange distance B from the edge of the adaptor ring to the camera tube adapter. However, there may be a small discrepancy in measurements or an error in the manufacturer's specifications of components (2), (3) or (6). We therefore decided to confirm the distance B on an experimental basis. To do this, the length of the extension tube is modified (4) until the finest point is formed on the camera image. The extension tube length deducted is $B = 174$ mm.

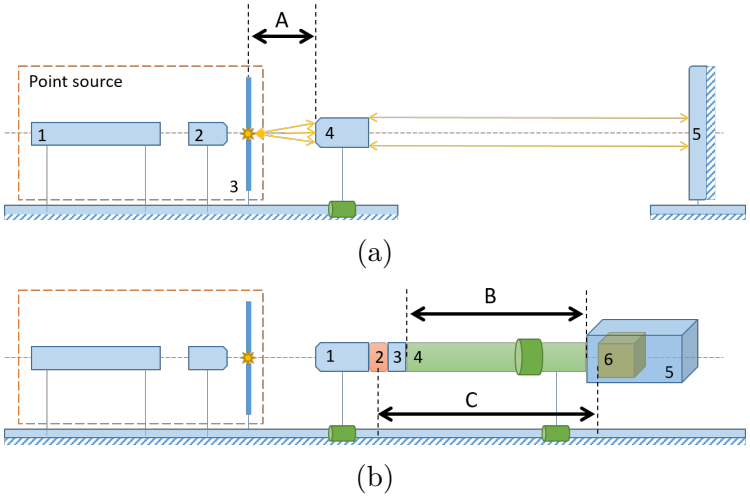

Figure 3.2: Diagram of the set-up used to calibrate the length of the extension tube. The components are described in the text. (a) The definition of the working distance A of the objective. (b) The definition of the flange-to-flange distance B.

3.1.3 Device description

Fig. 3.3 shows and annotates the parts of the assembled experimental setup. The choice and characteristics of the components are described below.

The camera used in the initial configuration is the Prosilica GE2040 from Allied Vision. It has a 12-bit CCD sensor of 2048 x 2048 pixels with a pixel size of 7.4 µm x 7.4 µm. The other cameras studied will be presented in Section 3.2.4.

A wide FOV is ensured by a 2x long working distance objective from Edmunds Optics (2X Mitutoyo Plan Apo Infinity Corrected Long WD Objective, EO 59875). It is infinity corrected and combined with an $f = 200$ mm lens

(1) – Camera

(2) – Extension tube

(3) – Tube lens

(4) – Microscope objective

(5) – Sample

(6) – LED array

Figure 3.3: Our first configuration of the FPM platform. It consists of a CCD camera (1), an extension tube (2), a tube lens (3), an optical microscope objective with low NA lens (4) and a matrix of LED elements used as a light source (6).

tube (AC254-200-A-ML). The objective is apochromatic and the tube lens is achromatic doublet. Which means that the effects of chromatic and spherical aberration are partially corrected. The long working distance (34 mm) allows additional optical elements to be inserted between the sample and the observation head. In addition, the small aperture and high correction for optical aberrations ensure that specimen-induced angular deviations are not exaggerated by the lens. The depth of focus provided by the manufacturer is 91 µm.

We use a 32x32 RGB LED matrix panel from Adafruit. The LEDs are arranged in a grid with a spacing of 6 mm. Each element of the matrix consists of a triplet of 3 diodes.

The numerical aperture (NA) value given by the manufacturer is 0.055. However, the experimentally induced value is greater, around 0.07. The details of its estimation will be given in the next section. The use of a low NA lens means that the high frequencies are cut off, resulting in low spatial resolution. At the same time, however, it allows a wide field of view to be obtained.

A sample is positioned on a stage that is $h = 245$ mm above the LEDs. The distance h is chosen so as to favour the overlap in Fourier space. The parallel position of the sample holder plane with respect to the plane of the LED matrix is controlled using the level instrument, as suggested in [249].

According to our observations, only 22 x 22 LEDs can provide sufficient light on the sample in this configuration.

The final version of the system is shown in Figure 3.4. The CCD camera is replaced by a sCMOS pco.edge 4.2. It is equipped with a sCMOS (Scientific complementary metal-oxide-semiconductor) sensor of 2048 x 2048 elements, a pixel size of 6.5 µm x 6.5 µm and a 16-bit converter. All figures for this work will be given taking into account the final congiguration, unless otherwise specified. The light scattered by the rails of the specimen holder platform is reduced by a non-reflective fabric. The camera support and focus distance control are stabilized by the incorporation of additional mechanical elements, see Fig. 3.4(b). It should be noted that there is some instability in the position of the optical axis in relation to the centre of the LED array. This is different from FPM platforms built by modifying a professional microscope system. The optical axis calibration is discussed in Section 3.1.5.

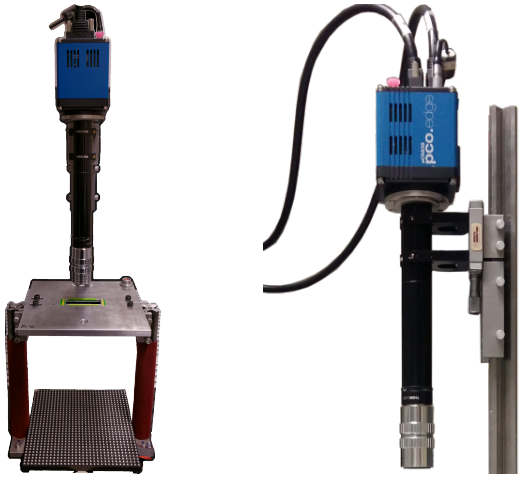

(a) (b)

Figure 3.4: Final version of the system. (a) Front view. (b) Side view, only the upper part is shown. A micro-metric screw allowing micro-displacements of the objective and a lower fixing block have been added.

3.1.4 Acquisition process and user control

The camera and the LED matrix are controlled by an image acquisition program written in LabVIEW by members of the TRIO team. Fig. 3.5 shows the user interface of the first version of the program.

The LED matrix has been programmed in such a way that it has 2 brightness modes. Normal intensity provided by the manufacturer and modified high intensity. Only the default brightness was available in the first system configuration.

Given the dynamic range of some cameras, it might be necessary to adjust the acquisition times to account for differences in signal intensity. This is the case of the 12-bit GE2040 camera used for the initial configuration. The

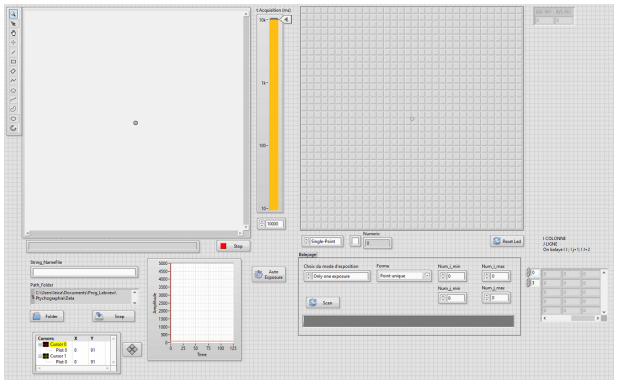

Figure 3.5: The first version of the user interface of the image acquisition program.

PCO.edge camera has a dynamic range of 16 bits and allows data acquisition with the same exposure time for all LEDs.

Exposure times can either be calculated by the image acquisition program or pre-calculated in advance. In the first case, images are captured as bright as possible while avoiding saturated pixels. In the latter case, an assumption is made about the similarity of the brightness distribution of the spectrum of different biological specimens. For most biological samples examined and normal LEDs brightness, this translates into exposure times ranging from 200 ms to 10 seconds.

Another way to reduce acquisition time is to increase the camera gain. However, after several experiments, this idea was abandoned. The reason is that a significant decrease in the signal-to-noise ratio (SNR) of the captured images was observed.

We generally capture a total of 20x20 grayscale images under sequential red light illumination. The acquisition time depends on the sample and the system configuration. For the GE2040 camera and the default LED brightness mode, it is on average 4 hours for a typical semi-transparent biological sample. This time also includes the search for the correct exposure value for each image, while only 30 to 40 minutes are spent on the acquisition process itself. For the PCO.edge camera, this figure is about 20 minutes . Thanks to the high-intensity LED mode, the acquisition time can be further reduced by a factor of 5.

The captured images can be divided into two categories: high intensity "bright-field" data; and "dark-field" images produced primarily by the scattered light [243]. Some images, however, contain a transition area. They can be classified as bright-field or dark-field depending on the segment selected, see Fig. 3.6. In the final configuration of the instrument, the bright-field angle is about 4°. This gives 26 bright-field images for the central segment of 100x100 pixels.

It is also important to acknowledge that, the presence of "semi-dark", "semi-

bright" images is not taken into account in the classic FPM model. Moreover, as demonstrated by Pan et al. in [150], these transition images have a vignetting effect. This could be particularly significant when using a low-power objective, as in our case. They proposed a modified imaging model to overcome this issue. However, this model is not implemented in the current work.

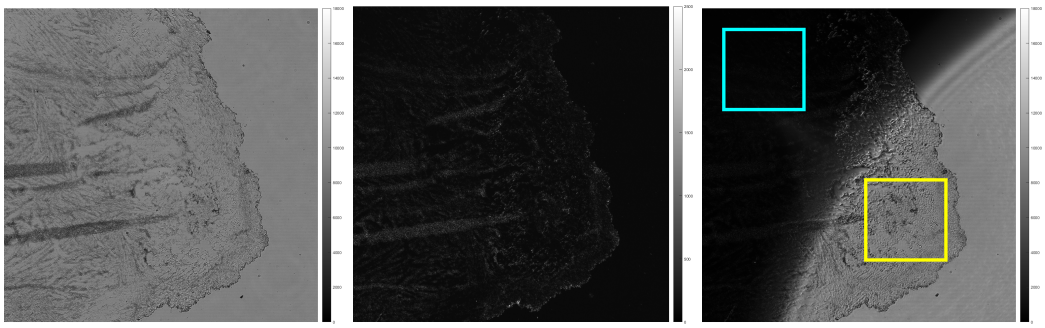

(a) (b) (c)

Figure 3.6: Examples of captured images. The sample is a stained histological slide of mouse breast tissue. Red illumination is used. (a) A bright-field image. (b) A dark-field image. (c) An images with a transition area. The segment delimited by a cyan square is dark-field, the segment delimited by a yellow square is bright-field. The size of the images is 2048 x 2048 pixels, which corresponds to 7.4 mm x 7.4 mm at the object plane.

3.1.5 Pre-acquisition calibrations

Adjusting the focus distance

In microscopy, it is essential to set the focal distance correctly. The system can introduce blurring, aberrations and other errors when the sample is refocused. This is particularly important in the context of computational imaging if correction of the focus error is not performed during the reconstruction procedure. Fortunately, the FPM platform offers a way to control the focus prior to acquisitions.

Indeed, defocusing generates geometric shifts in bright field images when the sample is illuminated by an oblique wave. The structures of the focused sample do not move with the change in illumination angle, see Fig. 3.7 (a-d). If the structures of the specimen are below the focal plane, there is a positive movement in the direction of the angle inclination. For example, if the sample is placed 130 µm below the focal plane and illuminated by a LED located above the central LED, the structures will move downward relative to their position in the central illuminated image, see Fig. 3.7 (e). They move upwards when the lighting on the opposite side is used, see Fig. 3.7 (g, h). The movement of the structures changes direction when the sample is above the focus plane.

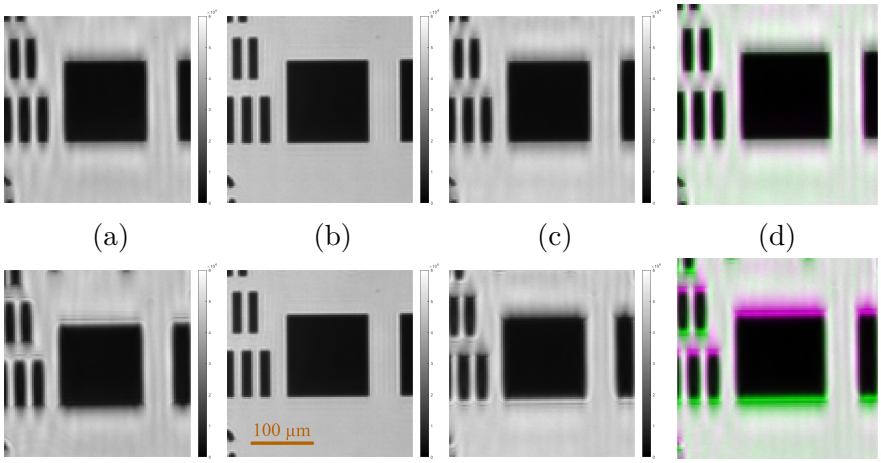

(a) (b) (c) (d)

(e) (f) (g) (h)

Figure 3.7: A small area of the USAF target sample captured under different lighting angles. In the first line (a-d), the sample is located in the focal plane. The second row (e-f), the sample is located 130 µm above the focal plane. The first column (a, e) corresponds to the images captured by the LED (17, 14) which is a central upper LED in a bright field. The images in the second column (b, f) are captured by a central LED (17, 17). The third column (c, g) corresponds to the images captured by the LED (17, 19) which is a lower central LED in a bright field. The last column (d,h) shows the differences between the images in the first and third columns to highlight the displacement of structures.

Based on this observation, a displacement criterion can be used to physically adjust the focus prior to acquisitions. For this, at least 2 images must be captured for each focus position tested by LEDs corresponding to the opposite edges of the bright field. An image registration procedure is used to calculate the displacement between this two images. This can be done, for example, by means of the Matlab image registration optimizers. In this case, the procedure must be set to the "monomodal" mode. The transformation sought is translation. The adjustment is then guided by the minimization of a criterion. This criterion can be a norm of translation distance over x and y calculated for each focus position.

In practice, however, we no longer apply the method described above to its full extent. Indeed, we still examine the 2 opposite images in the bright field for rough adjustments of the focus distance. However, we no longer calculate the displacement metric. The reason for this is that digital defocus compensation is used instead. This avoids the need for time-consuming physical focus adjustment.

Optical axis calibration

As mentioned above, our system has a certain degree of instability with respect to the optical axis. By optical axis, we mean here a line passing through the center of the LED matrix and perpendicular to it, see Fig. 3.8. We call an optical axis pixel an intersection of the camera sensor plane with the optical axis.

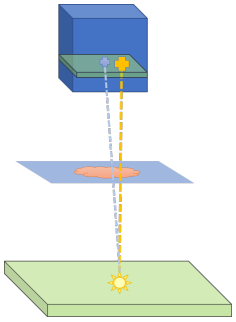

Figure 3.8: The pixel corresponding to the optical axis of the system is indicated by the orange cross. In the ideal system, the blue cross, indicating the centre of the camera sensor, would coincide with the orange cross.

By touching the camera or the objective, the optical axis can be accidentally tilted. It is assumed that the camera plane, the lens planes and the plane of the LED matrix are perfectly parallel to each other. However, the LED array can also be installed with a slight tilt or displacement. None of this is the case in systems where all components are rigidly connected and fixed. Since most research in this field obtains the FPM platform by modifying a professional optical microscope, this issue is rarely addressed.

In addition to mechanical misalignments of the system itself, a sample, not infinitely thin in real life, also introduces angular deviations. This results in an extra shift of the optical axis.

The main idea of the calibration procedure is based on the transition between bright-field and dark-field areas in the captured images. Indeed, as noted above, LEDs can produce bright-field, dark-field, or transition images, see Fig. 3.6. The pixel limit of the light field is determined by the maximum light angle accepted by the lens. This transition curve is symmetrical about the optical axis.

Fig. 3.9 (a) shows an image, $I_{stitched}$, formed by stitching together captured full-FOV raw images. Only 8x8 LEDs are used to produce this example. Each red square corresponds to an image captured by a single LED. The position of a square reflects the index of its LED in the plane of the LED matrix. In this example, the optical axis pixel coincides with the center pixel of the camera and the system is aligned. Figure 3.9 (b) shows the case of the system with a displaced optical axis.

The idea is to calculate the position of the optical axis pixel by a precise

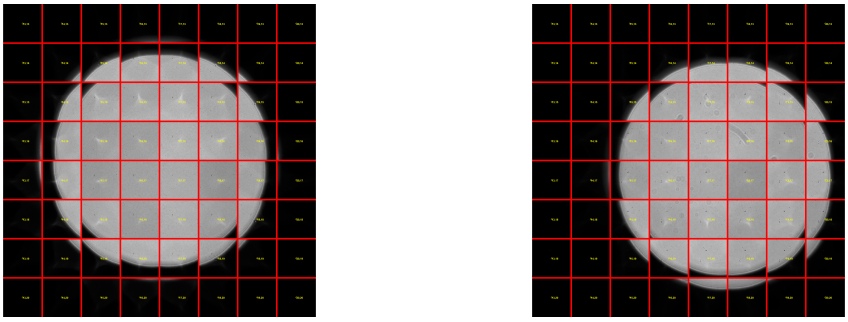

(a) (b)

Figure 3.9: 8x8 raw images stitched together. (a) The optical axis of the system is correctly aligned. (b) The optical axis is displaced.

localization of the center of the bright-field area. However, it is quite problematic to analyze this area directly from the images shown in Fig. 3.9 because of its irregular shape. This shape depends on the size of the captured image, the system sampling and the pupil cut-off frequency.

The full FOV is 2048x2048 pixels for the camera PCO.edge. For this case, a detection of the bright-field contour is bothered by disconnected parts. Fig. 3.10(c) shows a binary version of the image $I_{stitched}$. The binarization threshold is an average over all pixels. When the images used to produce $I_{stitched}$ are cropped in a central region of 100x100 pixels, the transition images almost disappear and the detection of the edge of the brigh field is no longer accurate enough, (a). However, by increasing the size of a segment, the area becomes almost perfectly circular for a segment of 1200x1200 pixels, (b). A circle can be easily fitted to this shape and its center coordinate can later on be converted into a pixel shift of the optical axis.

In order to determine the optimal segment size (l_s) to be used for bright field center detection, a circularity criterion $L_{circularity}$ is minimized :

$$L_{circularity}(l_s) = \|1 - \frac{P(l_s)^2}{4\pi A(l_s)}\| \tag{3.1}$$

where $A(l_s)$ - area of the bright-field zone; $P(l_s)$ - its perimeter. The binarized image is used to determine the perimeter and the area.

Figure 3.10 (d) shows the circularity criterion on a logarithmic scale as a function of segment size on a logarithmic scale. The optimal segment size for centre detection is then 1200x1200 pixels. The studied configuration is the one with the PCO.edge camera.

The following observations allow the subsequent detection of the optical axis pixel. When the original images are cut not at the center but at a corner, the circular area moves. When the optical axis is aligned, the circular area is located in the center of the stitched images $I_{stitched}$. The area moves when the optical axis is not perfect. The method proposed is based on the estimation of the centres of the bright field area $I_{stitched}$ for image segments cropped in

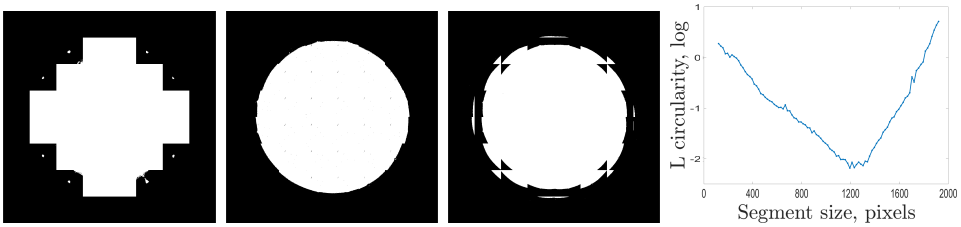

(a) 100x100 (b) 1200x1200 (c) 2048x2048 (d) $L_{circularity}, log$

Figure 3.10: (a-c) Binary version of images $I_{stitched}$ stitched from segments of different sizes cropped in a central region. (d) The circularity criterion used to define the optimal crop size.

different parts of a complete FOV image. See Fig. 3.11. The size of a crop corresponds to the optimal size $l_s = 1200$ pixels defined above. The cutting coordinates of the segments are evenly spaced from the upper left corner (1,1) to the position (2048 - l_s, 2048 - l_s). A line is then placed on the displacement of the found centers as a function of the center position of the cut segment. The intersection of this line with a zero gives the optical axis pixel sought.

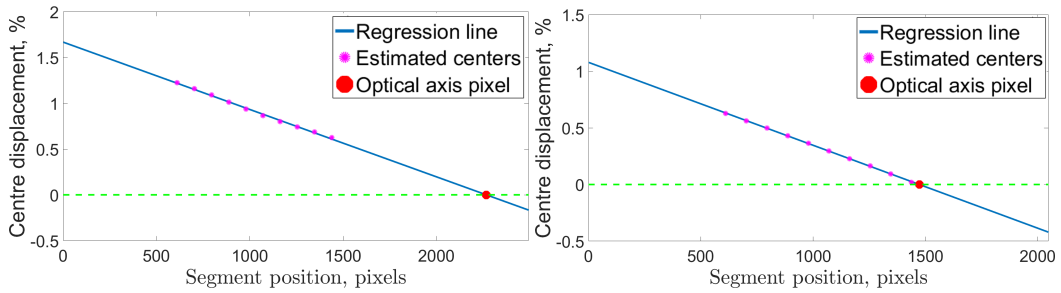

(a) x coordinate (b) y coordinate

Figure 3.11: Estimation of the optical axis pixel. The example data set is the same as in Fig. 3.9 (b).

A few other works propose to use a bright-filed border localization to estimate the alignment of the system.

A somewhat related calibration procedure has been proposed by Zhou et al. in [249]. It is based on four-point detection. These locations correspond to the points furthest from the edge of the light field along x and y. It has been used to perform an approximate mechanical alignment of the position of the LED array. However, it is less robust than our circular adjustment combined with linear regression. Besides, our system does not have an xy translation stage for the LED array.

Another procedure, also based on detecting the bright-field area on the sample plane, was proposed in [231]. In our case, 12 images are classified as bright-field for the whole FOV and the circular area on $I_{stitched}$ is formed at about half the size of the sensor. Only 4 bright-field images are available in the

case of the paper in question. Our method would be rather difficult to apply on such a data set. Instead, the authors use particle swarm optimization and random sample consensus algorithms.

The global shift of the optical axis can also be retrieved as 2 additional parameters (x and y sifts) during reconstruction [150, 186, 249].

Our method estimates the optical axis pixel during the calibration stage, before the phase retrieval procedure. It is robust and fast given the configuration of our system. We use it to mechanically align the optical axis by physically tilting the camera support rail. This is not a perfect procedure as it is rather cumbersome and time-consuming. Building a system with rigidly attached components could partly solve this problem. This is planned for the next version of our microscope.

All alignments are made for the red LED, but the centers in this case appear to be shifted for the other 2 wavelengths, see Fig. 3.12. In addition, deviations caused by a sample can also be estimated by the same method. In all cases, knowing the position of the optical axis shift allows the displacement to be corrected numerically.

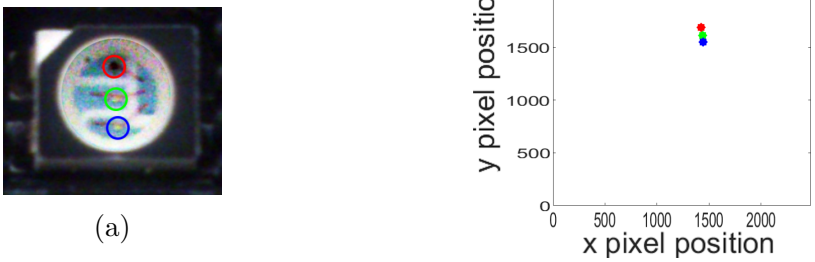

(a) (b)

Figure 3.12: Diodes layout. (a) An image of a LED matrix element. (b)An example of estimated optical axis pixel position for 3 wavelengths used.

3.2 Device characterisation

The built system consists of three main components: the lighting unit, the optical part and the digital camera. Each of these components must be carefully characterized in order to obtain the correct imaging model and reduce the influence of errors.

Errors in any experimental system can be divided into systematic and random non-systematic [226]. In FPM, differences in LED irradiance, optical aberrations and dark current noise can be classified as systematic. Fluctuations in LED brightness and camera noise, with the exception of dark current and hot pixels, are non-systematic errors. Angular misalignments can be classified as both systematic and non-systematic. Indeed, a part of the deviations

is due to mechanical imperfections of the constructed system and an error in estimating the parameters, and another part is due to deviations caused by a sample. The same reasoning can be applied to the NA misalignments attached to each LED. On the one hand, the NA depends on the applied illumination and optics, and on the other hand, it seems that a thick specimen can also influence the aperture variations. Some of these errors can probably be reduced by modifying and adjusting the instrument mechanically, but this would increase the cost of installation.

3.2.1 LED matrix characterisation

Relative irradiance The geometry of the LED matrix used is a simple rectangle. As a result, the amount of light arriving at the sample from a distant LED is different from that arriving from a LED close to the optical axis. This difference can be partially explained by a radiation pattern of a LED. Fig. 3.13 shows the normalized light intensity as a function of the emission angle. This data is provided by the manufacturer of the LED matrix.

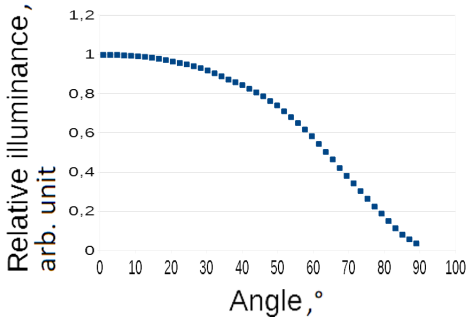

Figure 3.13: Radiation pattern of a LED.

In the imaging model (2.12), it is assumed that the sample receives the same quantity of light regardless the LED position. In order to get around this assumption, the captured images must be normalized to account for the difference in light energy.

The radiometric units concerned [64] will be briefly presented here before the normalization coefficient is calculated. Radiant power, or radiant flux, describes the amount of radiant energy Q received per unit of time δt : $\Phi = \delta Q/\delta t$ (Watt). This quantity is proportional to a photon flux Φ_{ph} which is a number of photons per unit of time. Radiant intensity I_e, referred to above as light intensity, is the radiant power Φ emitted or received per unit of solid angle Ω : $I_e = \delta\Phi/\delta\Omega$. Irradiance is a density of the radiant power received by a surface per unit area δS : $E = \delta\Phi/\delta S$ (Watt/m^2).

We first calculate the relative irradiance level E on a sample for each lighting angle. In the current section, we note θ being the angle between the direction of the emitted beam and its normal, Fig. 3.14. The relative irradiance $E(\theta)/E(\theta_0 = 0)$ is then converted into a normalization coefficient $c(\theta)$ to

adjust intensity images captured by a camera.

In addition to the angular dependence, the intensity of the light is also a function of the distance r from the source. The energy emitted by a light source will be distributed over an increasingly large area. The irradiance of the surface will therefore be inversely proportional to the square of the distance to the source r and will depend on its radiation pattern, Eq. (3.2).

$$E(\theta) = \delta\Phi(\theta)/\delta S = I_e(\theta)\frac{\cos\theta}{r^2} \tag{3.2}$$

Given the system configuration, $r = h/\cos\theta$, see Fig. 3.14. Therefore, the irradiance for the angle θ become $E(\theta) = I_e(\theta)\cos^3\theta/h^2$, where $I_e(\theta)$ is defined by the radiation pattern of a LED, see Fig. 3.13. The relative irradiance for the system is then defined by the following ratio :

$$\frac{E(\theta)}{E(\theta_0 = 0)} = I_e(\theta)\cos^3\theta \tag{3.3}$$

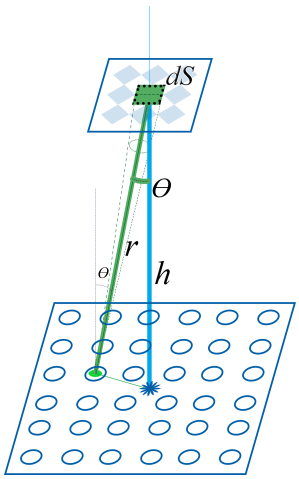

Figure 3.14: LED angle notations.

A photodiode is used for experimental validation of the dependence of the amount of light received by the sample on the illumination angle. The photodiode is placed on the sample holder. The voltage V is generated in the diode by the light reaching its surface from the LED matrix. It is measured in volts. In a simple photodiode model, the photocurrent, and thus also the voltage, is linearly proportional to the irradiance [71]. This holds true within a specific wavelength range and is valid in our case. Therefore, the measured relative voltage can be meaningfully compared with the calculated relative irradiance.

Fig. 3.15(a) shows a measured relative voltage map $V(\theta)/V(\theta_0 = 0)$ measured for red LEDs. The result is averaged over 100 realizations. The LED matrix is placed at the usual distance $h = 245$ mm and works in the "normal intensity" mode. Fig. 3.15(b) shows the voltage profiles for the red, green and

blue LEDs. The voltage value for the central line of the LED matrix is understood by profile here. Measured relative voltage profile for red LEDs (dash-dot line) is plotted against relative irradiance profile simulated by Eq. (3.3) (solid line), Fig. 3.15(c).

As can be seen, the simulated relative irradiance is underestimated compared to the measured relative voltage. This may be due to a incorrect radiation pattern $I_e(\theta)$ provided by the LED matrix manufacturer. The dark current of the measuring photodiode could also influence the observed deviation. Nevertheless, we decided to keep the calculations with the radiation diagram provided. Another thing to note is the inhomogeneity of the brightness of the LEDs. This issue will be addressed in Section 3.5.5. The asymmetry of the profiles results from the imperfect positioning of the photodiode in relation to the centre of the LED matrix.

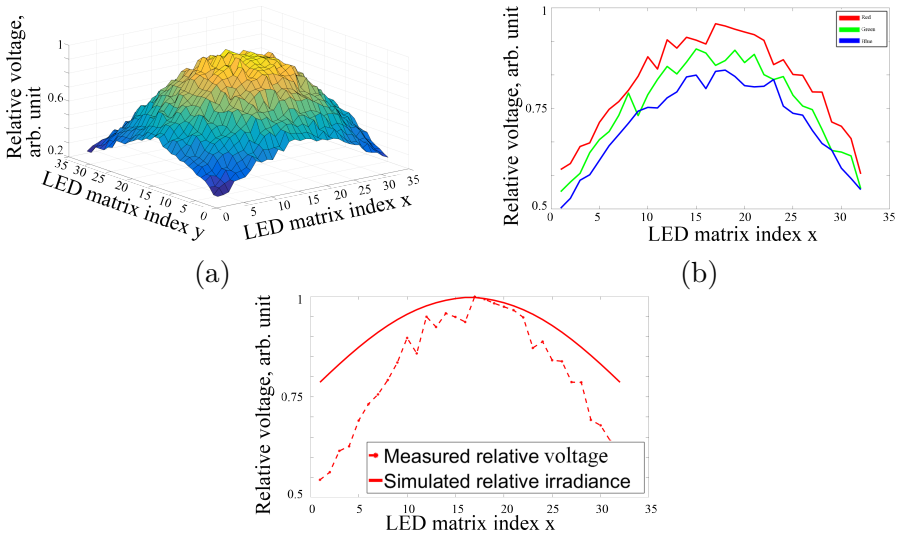

Figure 3.15: (a) Relative voltage measured as a function of LED position, for red LEDs. (b) Voltage profiles measured as a function of LED position, for red, green and blue LEDs. (c) Measured relative voltage profile (dash-dot line) plotted against simulated relative irradiance profile (solid line), for red LEDs.

Finally, the relative irradiance is used to determine the normalization coefficients $c_1, ..., c_L$ for captured images $I_1, ..., I_L$. The intensity recorded by the camera is proportional to the square of the amplitude of the electromagnetic field which, in turn, is proportional to the irradiance, thus :

$$\widetilde{I}_l = I_l * c_l = I_l \left(\frac{E(\theta_0 = 0)}{E(\theta_l)} \right)^2 = \frac{I_l}{I_e^2(\theta_l) \cos^6 \theta_l}, \quad l = 1, ..., L, \tag{3.4}$$

where θ_l is the angle corresponding to the LED l; $\widetilde{I}_l$, $l = 1, ..., L$, are corrected images that will be used for the reconstruction procedure. In practice, this correction should be applied after the background noise pre-treatment.

LEDs spectre A portable spectrometer was used to measure the center frequency and assess the coherence of the LEDs. Fig. 3.16 plots the measured values.

The full width at half maximum method is used to determine the spectral band. Amplitude of spectrum curves $f(\lambda)$ are first normalized to one. Next, a profile is traced at half the maximum height (at 1/2). The width of the spectral band is then defined by the difference between the maximum and minimum argument of this profile. The wavelengths measured give values of 621-636 nm for red, 494-533 nm for green and 454-476 nm for blue with peaks at 632, 515 and 465 nm respectively. These numbers are different from the specification given by the manufacturer of the LED matrix.

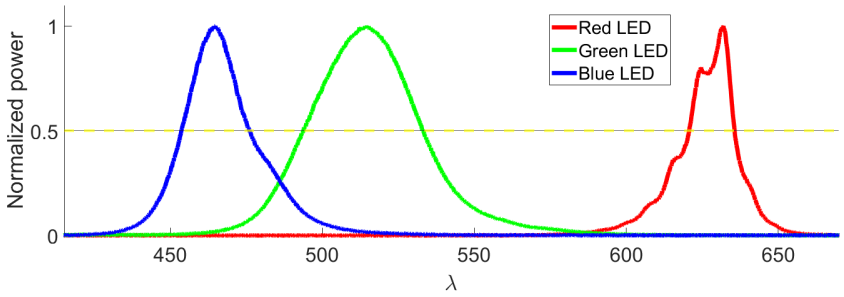

Figure 3.16: Measured LED frequencies. The power is normalized.

The coherence length is inversely proportional to the width of the spectral band. It is therefore different for the 3 coloured diodes. Coherence is lowest for the green LED.

LED matrix configurations It should be noted that most publications use an array of LEDs with a spacing between LEDs ranging from 2.5 mm to 4 mm. In this case, the sample is often positioned at 70-90 mm. Our matrix has a spacing of 6 mm and we position the sample at 245 mm. The total number of LEDs is 32x32. According to our observations, only a maximum of 22 x 22 provide sufficient light on the sample in our configuration.

3.2.2 Optical elements characterisation

Determination of the numerical aperture

The NA value given by the manufacturer of the objective is 0.055. However, when the captured images are examined, it appears that the actual NA of the system is different, Fig. 3.17. Modern bright-field microscopes operate under Kohler illumination using a condenser. This allows the resolution performance of the system to be optimized. In the case of FPM, the lighting is provided by a single LED. It is modelled as a coherent point source producing a plane light wave. In reality, however, a LED produces a cone of light resulting in non-zero

illumination NA. This is particularly remarkable in our configuration, given the large distance between the LED matrix and a specimen. The effective NA of the system should therefore be redefined experimentally. At the same time, to the best of our knowledge, none of the articles on Fourier Ptychography describe the problem of the incorrectly provided NA value.

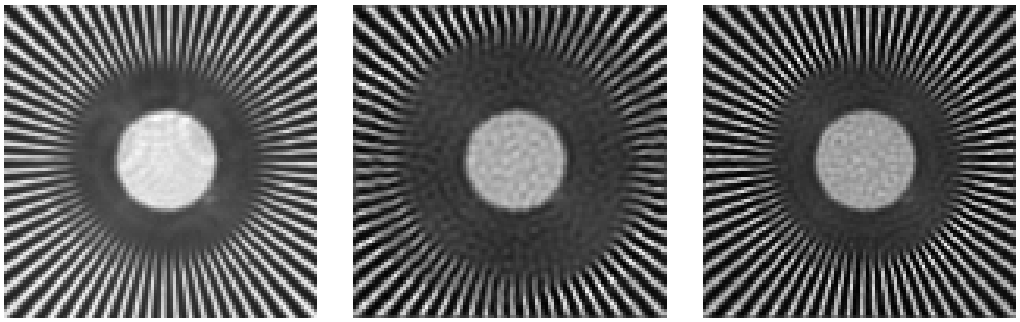

(a) (b) (c)

Figure 3.17: (a) A captured image of a sector star target sample. (b) An image simulated with a manufacturer NA = 0.055. (c) An image simulated with NA = 0.07. The effective NA of the system appears to be higher than that provided by the manufacturer. The size of the region shown is 100 x 100 pixels, which corresponds to 0.32 mm x 0.32 mm at the object plane.

The concepts of NA, maximum acceptable illumination angle θ_{max} and cut-off frequency k_{xmax} are interconnected in Fourier optics :
$k_{xmax} = k_0 \sin\theta_{max} = k_0 \mathrm{NA}$

Therefore, we could determine NA by examining θ_{max} by means of variable angle lighting or by looking at the Fourier spectrum of the captured images.

The first method identifies the angle θ_{max} by observing a transition from a bright field to a dark field. In the final configuration of the system, 12 images are classified as fully illuminated in red light. If a segment of 100x100 pixels is considered, 24 bright field images are obtained. The farthest LED in this series corresponds to an angle $\theta = 3.6\,\mathrm{deg}$, which corresponds to an NA value close to 0.063. For greater accuracy, the radius of the bright field area of $I_{stitched}$ is examined, see Section 3.1.5. It is compared to simulations with different NA value, Fig. 3.18.

We refine the results of the first method by estimating NA numerically during the reconstruction procedure. The value found for most datasets varies between 0.069 and 0.0712. This technique is described in detail in Section 3.5.

The second approach estimates the NA corresponding to each captured image of its Fourier spectrum. A procedure was developed by the members of the TRIO team and will be discussed in Section 3.5.4. Here we present only the results of the analysis for one of the data sets used, Fig. 3.19. We have observed that different LEDs seem to produce different NA values, ranging from 0.065 to 0.075. To our knowledge, this is not mentioned in the literature. The influence of discrepancies in NA values needs to be further analysed and the

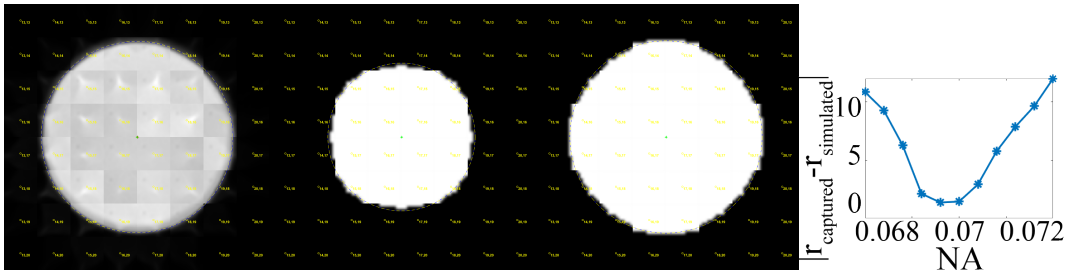

Figure 3.18: (a) An image, $I_{stitched}$, formed by stitching together captured 1200x1200 images segments. (b) $I_{stitched}$, formed by images simulated with a manufacturer NA = 0.055. (C) $I_{stitched}$, formed by images simulated with an NA = 0.07. (d) A comparison of the $r_{captured}$ radius of the bright field area of captured images $I_{stitched}$ with the $r_{captured}$ radius of the simulated bright field area with different NA. The radius of the bright field area of the captured images is closer to the simulations with NA = 0.07.

adapted imaging model needs to be considered. We expect these adjustments to produce promising results in future work.

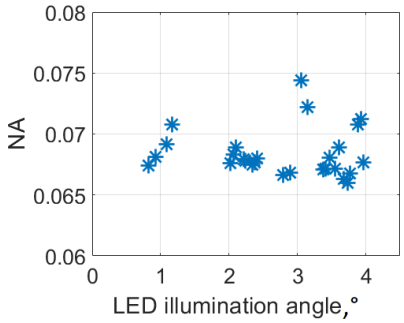

Figure 3.19: Estimation of the NA for bright images as a function of the illumination angle of a LED. The LED angle here is defined as follows $\theta = \frac{180°}{\pi} \arctan \frac{\sqrt{x_{LED}^2+y_{LED}^2}}{h}$, where x_{LED} and y_{LED} are x and y coordinates of the LED element respectively. The estimation method is discussed in Section 3.5.4.

Determination of other parameters

Magnification The magnification factor is calibrated using a microscope micrometer calibration ruler slide, Fig. 3.20. The determined value is 2.03.

Depth of Field We use a 1951 USAF resolution test chart to experimentally determine the depth of field (DOF) of the system. A unit consisting of the objective, the lens, the extension tubes and the camera moves on the rail by manually adjusting the position of a screw. The 420 µm range is covered with

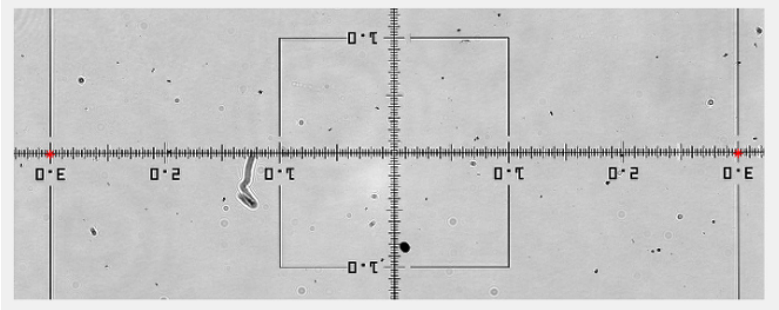

Figure 3.20: Microscope micrometer calibration ruler slide. The separation between 2 indicated points is 6mm.

a 30 µm step. We estimate the contrast for several USAF groups, Fig. 3.21. The resolution of a group (in line pairs / mm) is given by the expression: $r_{USAF} = 2^{\text{group}+(\text{element}-1)/6}$. We define an experimental DOF as the width of the displacement range producing a contrast greater than the maximum contrast value divided by two. As we can see, the value of the DOF depends on the resolution of the USAF group under study, Fig. 3.21 (b). The sampling of the system does not allow to calculate the contrast for elements with a resolution higher than 70 lp/mm. The DOF for the minimum resolvable element is estimated to be about 180 µm.

We then calculate the total DOF theoretically, Eq. (1.11). Considering NA = 0.055 (the manufacturer value), $\lambda = 630$ nm, $m = 2.03$ and taking $e = 6.5$ µm being the pixel pitch of the camera sensor : $Z_{tot} = 266.5$ µm. This value becomes smaller, when NA = 0.07 is supposed : $Z_{tot} = 174.3$ µm. This value is in accordance with the experimentally defined DOF.

In addition, the Tamura Coefficient (TC) criterion and a 146 µm microsphere was used to confirm this value, Fig. 3.22. The TC for the image I is defined as follows [242]:

$$TC(g) = \sqrt{\frac{\sigma(I)}{\text{mean}(I)}}, \tag{3.5}$$

where $\sigma(I)$ is the standard deviation of I, mean(I) is the mean value of I. Like in the previous case, the experiment consists of gradually translating the objective along its axis. Only a quarter of the microsphere is used to calculate the criterion, Fig. 3.22 (c-g). We have estimated the DoF by assessing the width of the resulting curve at its half value. It equals 212 µm, which is close to the value found by the DOF estimate with the USAF target. The fabrication of a slide with the microsphere and its application to quantitative phase imaging will be discussed in Section 4.1.

Such a high DOF makes it possible to obtain sharp images of thick samples. In addition, one of the advantages of the Fourier Ptychography is that the FOV can be further extended numerically by performing a defocus aberration correction.

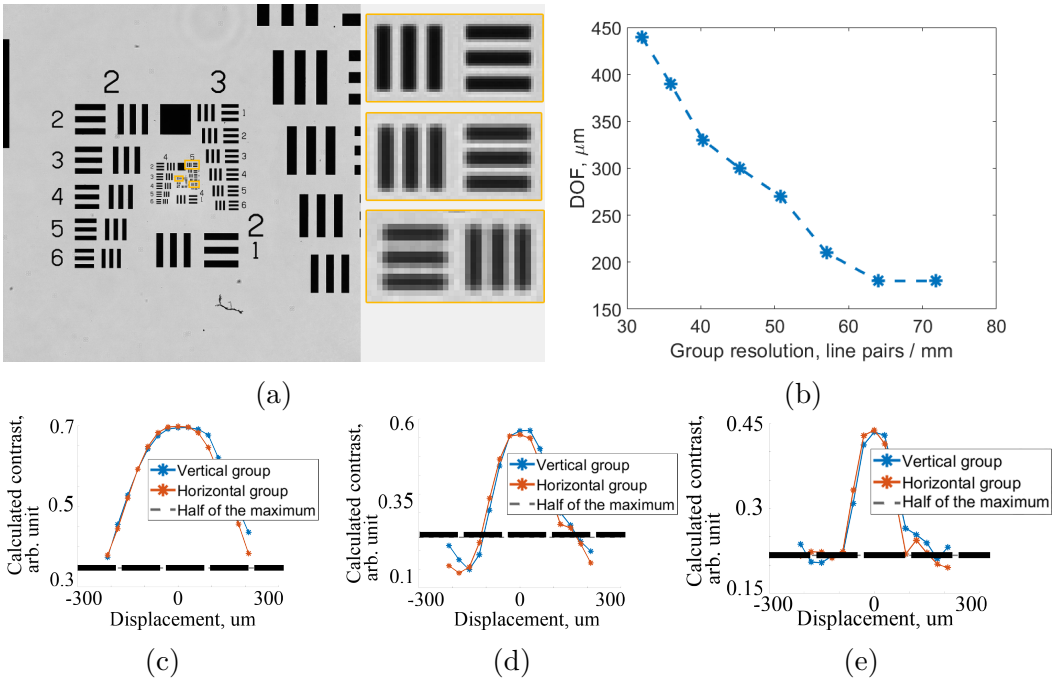

Figure 3.21: DOF estimation using a USAF target. (a) The USAF target, complete FOV and zoom in on the three groups presented below. (b) The width of the displacement range producing a contrast greater than the maximum value divided by two as a function of the resolution of the USAF group studied. (c-e) Contrast curves for (c) the group 5-1, (d) the group 5-5, and (e) the group 6-2. The size of the full FOV image is 2048 x 2048 pixels, which corresponds to 6.6 mm x 6.6 mm at the object plane.

3.2.3 System characterisation

Sampling

An aperture overlap rate [187] is 78% when using red LEDs and the camera PCO.edge, see Section 2.3.4. The maximum illumination angle is about 20°.

The Nyquist criterion is fulfilled for red and green illumination. It is, however, violated for the blue light with a spatial-sampling-ratio of a system $R_{cam} = 0.99 < 1$.

Segment centres calculation

The reconstruction procedure does not directly use the whole FOV images, but breaks them down into smaller segments. The illumination angles must then be calculated for each segment separately.

Theoretically, this should not be a problem because these angles can be calculated in a purely geometric way. The wavevector formula for a segment

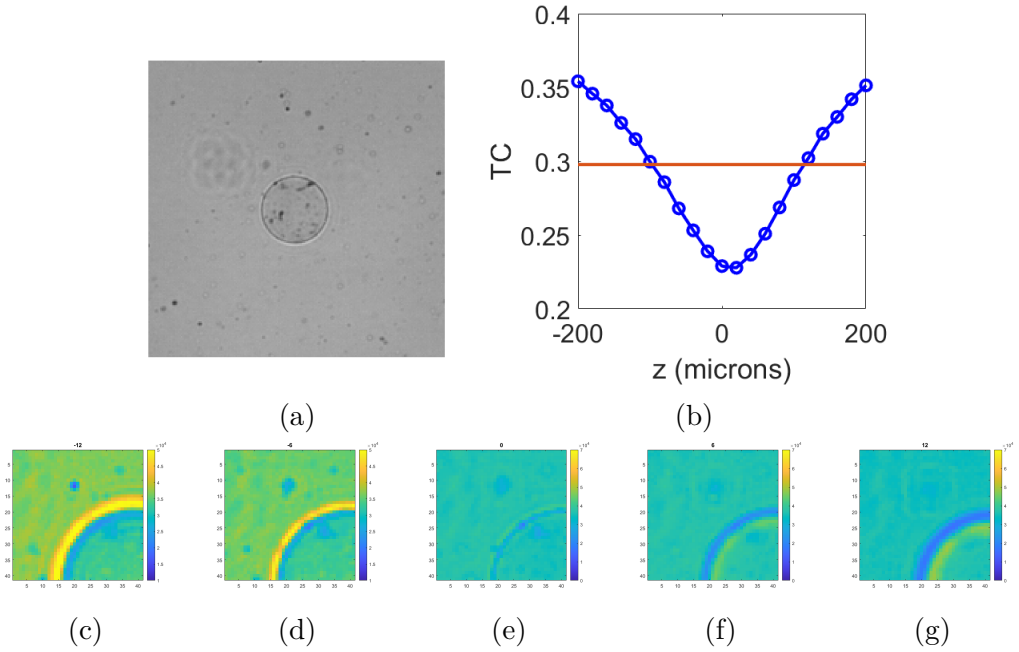

Figure 3.22: DOF estimation using a 146 µm microsphere. (a) A 200 x 200 pixels segment of one of the captured images containing the microsphere. The size is 0.65 mm x 0.65 mm at the object plane. (b) The TC as a function of axial translation. (c-d) Images segments used to calculate the TC (in false color). The axial position are : (c) -240 µm, (d) -120 µm, (e) 0 µm, (f) 120 µm, (g) 240 µm.

centered on a position (x_c, y_c) is given by [186, 244]:

$$\begin{aligned} k_x^l &= \frac{2\pi}{\lambda} \frac{(x_c - x_l)}{\sqrt{(x_c - x_l)^2 + (y_c - y_l)^2 + h^2}} \\ k_y^l &= \frac{2\pi}{\lambda} \frac{(y_c - y_l)}{\sqrt{(x_c - x_l)^2 + (y_c - y_l)^2 + h^2}}, \end{aligned} \tag{3.6}$$

where (x_l, y_l) is a position of the l-th LED in the LED matrix plane. It is calculated as $(x_l, y_l) = (h_{l_x} d, h_{l_y} d)$, where h_{l_x} and h_{l_y} are the led indices in x and y directions respectively counting from the centre of the LED array, d is a spacing between neighbouring LEDs. The position of a segment centre (x_c, y_c) is also given by a straightforward geometric relation :

$$\begin{aligned} x_c &= x_0 - N_x P_p \\ y_c &= y_0 - N_y P_p, \end{aligned} \tag{3.7}$$

where (N_x, N_y) are number of pixels from the segment center to optical axis pixel (x_0, y_0) of the full FOV raw image and P_p is a pixel pitch at the object plane. The ideal optical axis would be at position $(x_0, y_0) = (0, 0)$.

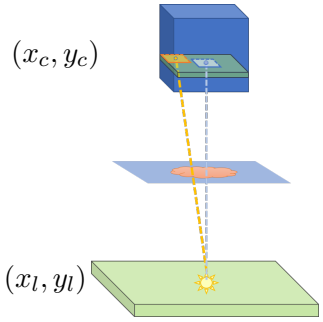

Figure 3.23: The illumination angle corresponding to the same LED is different for an optical axis segment (blue rectangle) than for a corner segment (orange rectangle).

However, when this formula is applied on our data, we observe strong artifacts on the reconstructed phase images for segments far away from the optical axis pixel, Fig. 3.24(a). Indeed, the stripes become denser and denser as the distance from the optical axis increases. We assume that the reason for this is that the center of a segment undergoes a displacement greater than $N_{pixels}L_{pixel}$. This could be due to the deflection of the illumination beams by a sample or optics. We propose therefore to introduce a correcting coefficient k_c accounting for this additional displacement.

$$\begin{aligned} x_c &= x_0 - k_c N_x P_p \\ y_c &= y_0 - k_c N_y P_p. \end{aligned} \tag{3.8}$$

The coefficient is determined by minimizing a difference between the bright field border locations of the measured and simulated images. For most of our data sets, this value is estimated to be close to $k_c = pi/4$. Reconstruction with an applied coefficient has much less stripes on the phase, Fig 3.24(b).

We note that a similar issue has also been encountered in other research. Zhou et al. formulated it as a problem of independent deviation of the central position of each segment [249]. In such a case, two additional parameters (offsets of x_c and y_c) are estimated during reconstruction. However, by examining the reported values of the reconstructed offsets for different segments, we suggest that a correction coefficient k_c might also be a good approximation for their data sets.

While our method works well in practice, it lacks a solid theoretical basis. The exact nature of this phenomenon should be examined in more detail. A possible explanation could have been provided by Pan et al. They also observed distinct stripes on the reconstructed segments in the border regions of the FOV [150]. However, they approach this problem from a completely different perspective. The authors question the imaging model itself by arguing that the spatially invariant approximation on FPM is not appropriate.

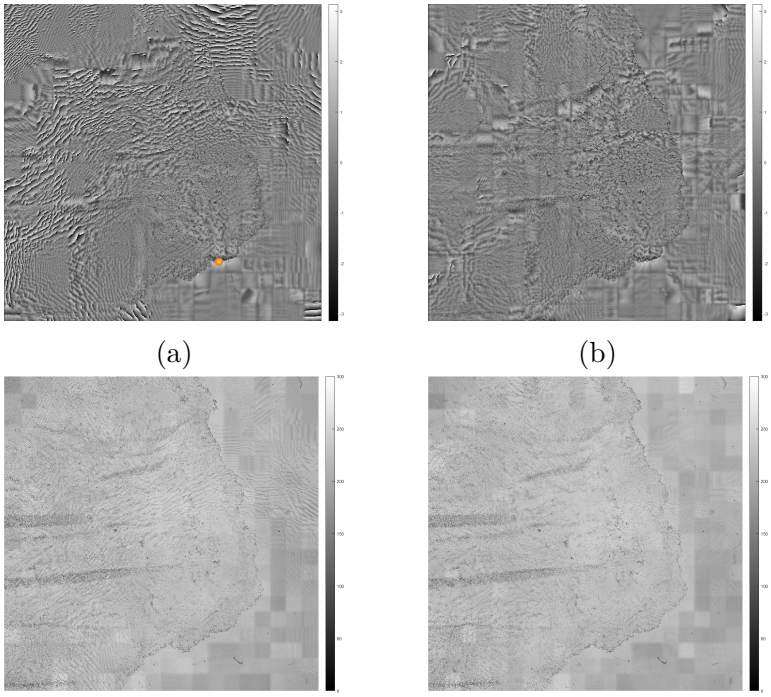

(a) (b)

(c) (d)

Figure 3.24: The results of the reconstruction. A corresponding low-resolution bright field image can be found in Fig. 3.6. The orange dot indicates the optical axis pixel for the data set used. The phase (a) and the amplitude (c) given the standard formula for the segment position, Eq. (3.7). The phase (b) and the amplitude (d) given the applied coefficient, Eq. (3.8).

3.2.4 Camera study

To our knowledge, none of the authors have studied noise statistics for Fourier ptychographic microscopy. This section focuses on characterising the electrical noise of the camera. A number of studies assume the correct type of noise, namely a mixed Poisson-Gaussian noise [203, 240, 241]. However, this assumption is not universal. Most papers presume that the data are corrupted by noise following the Poisson distribution [11, 226], some even consider simple Gaussian noise. This section aims to clarify the issue of electronic (camera) noise, one of the main sources of error in Fourier Ptychography measurements.

There are several reasons for conducting this study. First of all, it is useful for the confirmation of the choice of the cost function used in the optimization procedure. Secondly, it gives us the correct information for the simulations and thus the validation of the methods implemented. Finally, at the time this study was conducted, the final configuration of the FPM system had not yet been decided. Having several CCD cameras and a sCMOS camera, we aimed for the optimal one according to the parameters and the observed noise.

Camera characteristics The Table 3.1 lists the sensor and pixel sizes of the cameras studied as well as their dynamic range (ADC). Ideally, we would like to have the biggest sensor size. The smaller the pixel size, the better the resolution and the higher the system's spatial-sampling ratio (the Nyquist criterion is better met considering the other parameters fixed). At the same time, cameras with a larger pixel size may have a better SNR since the signal is integrated over a larger area. Prosilica GE-1050 was excluded from the analysis for a small FOV. Hitachi HV-F202GV camera is RGB, while others have a monochrome sensor. Since the FPM allows a wave multiplexing strategy (see Section 4.4), these cameras were considered despite their weak FOV.

	Camera	Sensor size, mm^2	Pixel size, μm^2	ADC
1	Prosilica GE-2040	15.10 x 15.10	7.4 x 7.4	12 bit
2	Hitachi HV-F202GV I	7.04 x 5.28	4.4 x 4.4	12 bit
3	Manta G-145B	8.95 x 6.70	6.4 x 6.4	12 bit
4	Prosilica GE-1050	5.63 x 5.63	5.5 x 5.5	12 bit
5	PCO.edge	13.31 x 13.31	6.5 x 6.5	16 bit

Table 3.1: Available camera specifications

First, we review all the types of noise that could be generated by a digital camera. These include :

- Additive Gaussian noise. It arises from disturbances of the actual light signal by noise in the sensor electronics, often related to the temperature of the camera.
- Poisson shot noise. It is a signal-dependent noise due to poor counting of independent photons by a sensor. These variations are often attributed to quantum fluctuations.
- Dark current. This type of noise is due to leakage current, i.e. electrons generated in the sensor independently of the light signal. Captured images are subsequently corrupted by a constant offset which itself follows a Poisson distribution.
- Hot pixels and salt-and-pepper noise. If the sensor is damaged, some of its pixels may no longer follow the linear response curve, producing values much higher than the expected signal level. If the load capacity of a pixel is exceeded, its value can be reset to zero producing salt-and-pepper noise.
- Other. Quantization noise is always present in discrete measurements, but it is not significant for FPM compared to shot noise. Anisotropic or periodic noises may also be observed.

We therefore look for the presence and levels of these noises in order to estimate the significant sources that most influence FPM reconstructions. To begin with, we estimate the dark current image, the presence of hot pixels and the possible anisotropy of the noise. Next, we determine the statistical distribution of the noise.

Dark frame We calculate the dark current image by simply averaging 10^3 of images taken in the absence of light. The result, Fig. 3.25, indicates that all cameras have different average noise levels and different anisotropy profiles. Different integration times were also examined to ensure the consistency of results. The statistical properties of the resulting dark image also indicate that the captured raw images must be processed differently before reconstruction. For example, the dark image of the PCO.edge camera has a variance value of less than 3 and can be approximated by a constant (its mean value 100.4), while the GE2040 (variance value 47) and the Hitachi (variance value 140) cameras require dark image subtraction. Different integration periods were also examined to ensure consistency of findings.

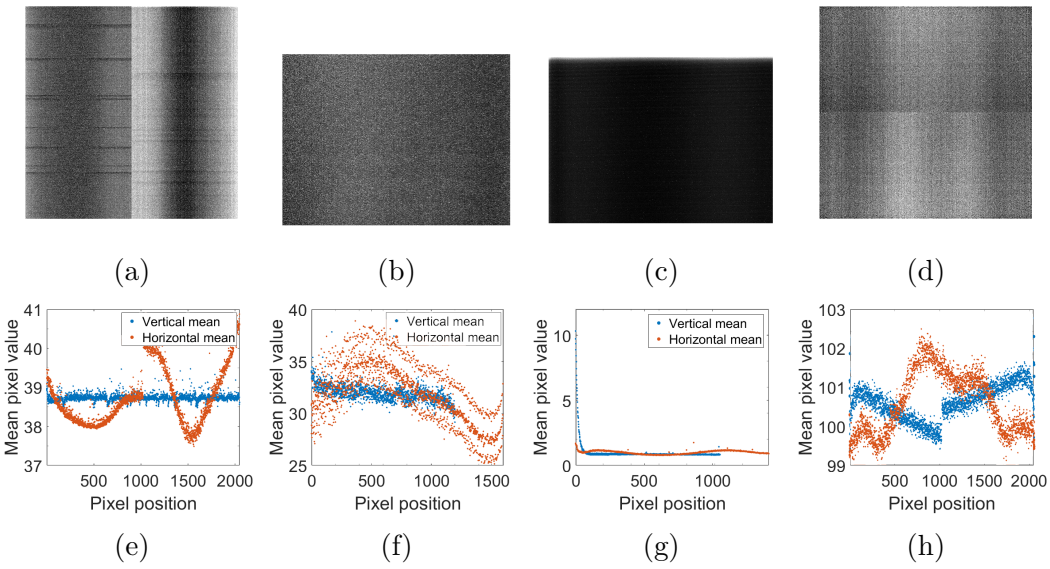

Figure 3.25: Camera's dark frame. Top row - the estimated image, bottom row - mean vertical (blue) and horisontal (orange) profiles of that image. (a) The Prosilica GE2040 camera. Mean dark image value – 38.7, value variance – 47.0. (b) The Hitachi HV-F202GV camera. Mean dark image value – 100.4, value variance – 2.9. (c) The Prosilica G145 camera. Mean dark image value – 1.4, value variance – 1.0. (d) The PCO.edge camera. Mean dark image value – 100.4, value variance – 2.9.

Hot pixels Of all the devices tested, the Prosilica GE2040 had the largest hot pixel problem. These pixels must first be identified and then treated. All

the data in this paragraph will be examined for this camera.

Several methods can be considered to define if a pixel is "hot". One of the simplest definitions is to find the pixels in the dark image that are greater than 10 times its median value. Both the mean intensity and the number of these pixels increase with the integration time, Fig. 3.26. At t = 10s, up to 0.03% of the pixels are classified as "hot". However, this value depends largely on the threshold value of the classification. Another observation is the appearance of a zero value pixel to the right of a hot pixel.

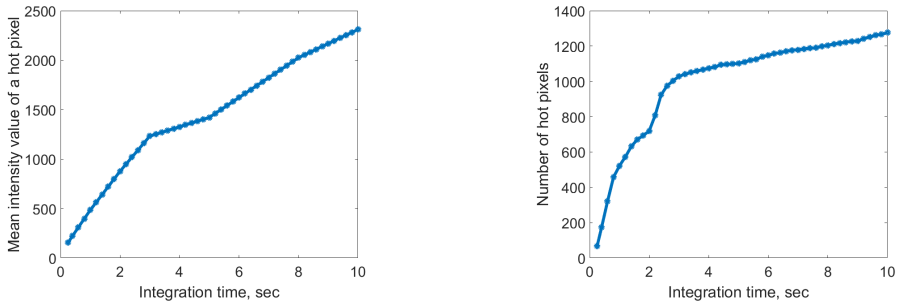

(a) (b)

Figure 3.26: (a) Mean value of the intensity of a hot pixel as a function of the integration time. (b) Number of hot pixels as a function of integration time.

At the same time, a large number of pixels produce values that give higher intensities than the average background noise over a long exposure time. These values are not large enough to be classified as "hot" and too numerous to be interpolated without losing a significant portion of the signal. Given that the camera GE2040 requires integration times of longer than 5s for distant dark-field images, this issue is susceptible to compromise the reconstruction results and has to be treated.

Statistical law of noise In order to determine the noise law, we take 10^3 images of the same scene for each camera. We calculate the variance of the intensities for each pixel $x_{i,j}$ of these $j = 1..100$ images and relate it to the mean value of a pixel $x_{i,j}$. Indeed, one of the properties of the Poisson distribution is the equality of the expected value of the event to its variance. On the other hand, the variance of a given Gaussian distribution is constant with respect to the expected value.

Figure 3.27 shows the result of plotting the variance against a pixel mean for 10^3 simulated images. Each point on the graphs represents a pixel of the image with its mean and variance calculated from 100 noise realizations. The images that produced the first figure (b) are corrupted by Gaussian noise. The second figure (c) represents the images whose pixels follow the Poison distribution, Eq. 2.37.

The 4 following figures (d-g) show the same analysis for the experimental data from the cameras tested. For all cameras, the conclusion is that the noise

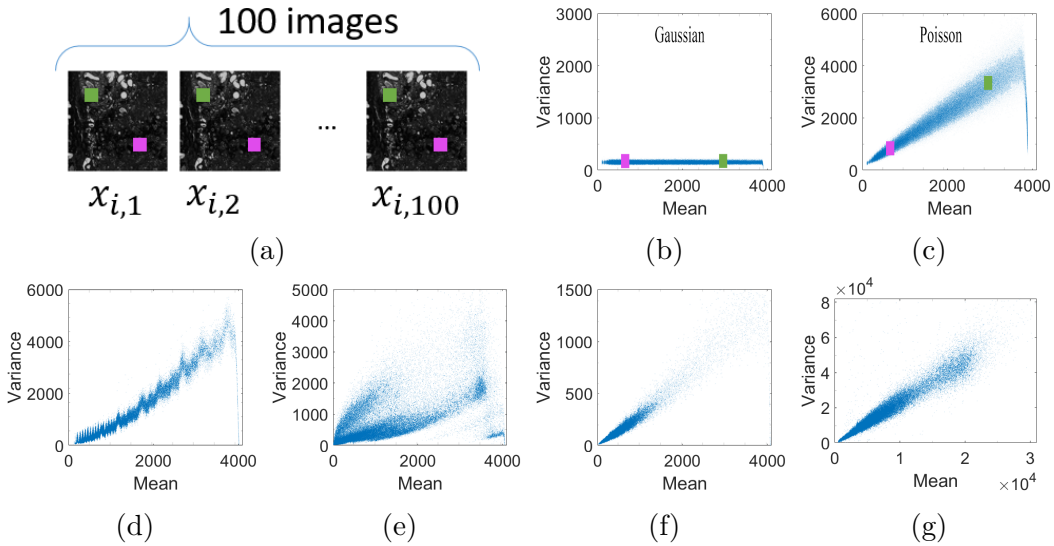

Figure 3.27: Determination of the noise law. (b-g) Scatterplots of pairs (E, σ^2), where each dot is calculated as $E = \text{mean}(x_{i,k})$, $\sigma^2 = \text{var}(x_{i,k})$, where $i = 1...m^2$ is a pixel position, $k = 1...K$ is a noise realisation number. (a) Example of $K = 100$ simulated images used for analysis. The noise is generated for each pixel ($x_{i,k}$) independently. (b) Results for 100 realizations of Gaussian noise. The green and pink squares represent the pair (E, σ^2) for 2 distinct pixels shown in the figure (a). (c) Results for 100 realizations of Poisson noise. The same scene captured with the camera (d) Prosilica GE2040, (e) Hitachi HV-F202GV, (f) Prosilica G145, (g) PCO.edge.

has both Poisson and Gaussian components. A Gaussian noise component is deduced from the fact that the curve corresponding to a Poisson component is elevated, as opposed to a variance baseline at 0. Three out of the four cameras studied produced curves resembling those simulated under the hypothesis of a mixed Poisson-Gaussian noise. That is to say that each pixel could be modelled by the Eq. 2.40. The Hitachi color camera, however, gave unexpected results.

Such an analysis also provides quantitative noise measures. Indeed, when a linear regression is performed, the slope of the line indicates a scale coefficient α of the Poisson distribution and the elevation is a measure of the standard deviation σ^2 of the Gaussian component.

As can be seen, the mean of a pixel is equal to its variance up to a scaling coefficient, which is different for all the cameras studied. This indicates that the current assumption in the FPM of a Poisson noise component with a unit scale [11, 226] is not entirely accurate. As far as we know, this issue has not been addressed in the literature, even when the mixed noise hypothesis is used. However, it is important at least for a correct simulation of noise, when validating methods. Furthermore, this observation needs to be studied in greater detail in order to possibly propose a new cost function. This is particularly relevant when different integration times are used.

These tests were performed under different scenes, different illumination angles, different wavelengths, different exposure times, but also outside the microscope system to make sure that this noise is not related to the optics.

It should be acknowledged that Poisson-Gaussian noise is often used to model the signal errors of CCD and CMOS camera sensors [124]. In addition, the Poisson probability distribution function (PDF) could be approximated by a Gaussian PDF for large numbers. If the dataset contained only bright field images, the Gaussian noise hypothesis might be sufficient. A more accurate noise model is required due to the presence of low-intensity dark field images.

It should also be noted that, following the completion of this study, another work has proposed a method for estimating the standard deviation of the Poisson or Gaussian components for FPM [146]. The study did not attempt to determine the degree of similarity of the actual noise to the mixed Poisson-Gaussian distribution. The noise was regarded as being either purely Poisson or purely Gaussian.

Camera response curve The dynamic range of the GE2048 camera requires different acquisition times depending on the LED used. It is therefore necessary to control the linearity of the response curve of this camera in order to ensure a correct normalization of the intensity images, Fig. 3.28. A camera response curve identifies the relationship between the intensity measured by the camera and the relative radiance of the scene. The Debevec-Malik algorithm, often used in the context of high dynamic range images generation, is used for this analysis [42]. Without going into details, we only mention that several images of the same scene must be taken with different exposure times.

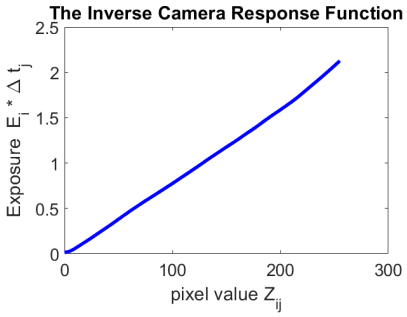

Figure 3.28: GE2048 camera response curve.

Camera choice We first opted for Prosilica GE-2040 which provides the largest FOV. However, we then decided to sacrifice the edge of the FOV to reduce the acquisition time as a result of a higher dynamic range of the PCO.edge camera. The higher noise levels of the GE-2040 compared to the PCO.edge were also taken into account in this decision.

3.3 Quality assessment

The question of evaluating the results of experimental reconstruction is not obvious. In particular because of system uncertainties, noise and the fact that the physical model used is only an approximation. Qualitative observations are therefore still taken into account in the FPM, for example by assessing the morphology of blood cells [143, 226].

Perhaps the most common quantitative metrics is what is known as the "convergence index" (CI) [69, 244]:

$$\mathrm{CI} = \sum_{l} \frac{\mathrm{mean}_{x,y}\left(\sqrt{g_l(x,y)}\right)}{\sum_{x,y}\left|\sqrt{I_l(x,y)} - \sqrt{g_l(x,y)}\right|}, \tag{3.9}$$

where $I_l(x,y)$ are captured images, $l = 1..L$; $g_l(x,y)$ are images generated from the resulting object estimate $O(k_x, k_y)$ according to the Eq. (2.20). CI value is the highest for the "best" result.

We also use the value of the objective functions, indicated in Section 2.4.3, to control the quality of the results. We underline once again that the metric values depend not only on the reconstructed object itself but also on the chosen system parameters intervening in the Eq. (2.20). It is therefore difficult to draw conclusions on the results even if the metric chosen was appropriate.

3.4 Data pre-treatment

Some recent research efforts have been devoted to the pre-processing of FPM data [51, 84, 146, 239].

The mixed Poisson-Gaussian nature of the electrical noise is a non-systematic error that cannot be addressed in the data pre-processing stage. Indeed, it would be unwise to de-noise the raw images, as this could disturb the frequency properties of the signal and lead to the loss of its part. However, the hot pixels and dark frame could and should be eliminated before reconstruction.

3.4.1 Normalization, hot pixels and dark frame

First of all, if different exposure times are used, the images must be re-normalized to match the observation model. As was shown above, the GE2048 camera has a linear response curve. Therefore, we simply multiply the captured images by a normalization coefficient $k_t = t_{max}/t_l$ where t_l is the exposure time used to capture the image $l = 1..L$ and t_{max} is the maximum exposure time used. We note that such normalization calls into question the estimated law of noise. This issue needs to be studied and addressed in further research.

Hot pixels and the dark frame are eliminated by the methods described in Section 3.2.4.

3.4.2 Offsets

While our first attempts only dealt with the issues described above, we then realized that another part of the signal, related to differences in lighting, also had to be suppressed. In fact, there is a constant offset on the captured images. The value of this offset depends on the lighting angle. It is higher for bright field images and lower for remote LEDs. Several authors have also reported this issue [51, 84, 146, 196, 239].

We follow the proposal of Lei Tian et al [196]. The offset is determined for each LED by evaluating an average value of some region of the sample. This region is chosen so that it has uniform intensity in bright field images and no signal in dark field images. The authors proposed to set an empirically defined threshold on the resulting offsets. Negative value resulting after subtraction of offsets are set to 0.

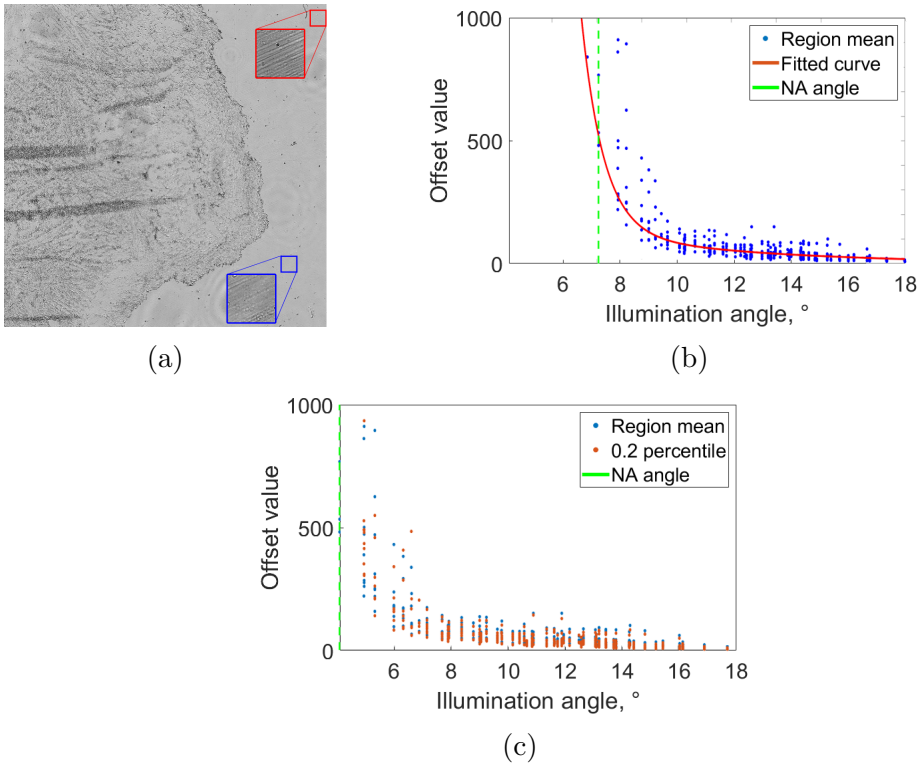

Figure 3.29: Offsets determination. (a) A full FOV image of a histological slide. The coloured squares indicate the homogeneous regions used to calculate offsets. (b) Estimated offset values before thresholding. A blue dot represents a pair (LED angle θ, average intensity over the regions). The red curve is fitted to this data, indicating the dependence of the offset value on the illumination angle. The green line indicates the shift from bright field to dark field images, determined by the system NA. (c) The first $X = 0.2$ percentile traced against the average value over the regions.

Fig. 3.29(a) shows an example of two regions taken to perform the mean

value calculation. Two regions are used instead of one to increase robustness. Fig. 3.29 (b) shows the values obtained as a function of the illumination angle θ. As can be seen, the value of the offset decreases noticeably as the illumination becomes more and more oblique. A vertical line represents the numerical aperture angle.

We choose the threshold constant to be equal to the minimum offset value over a disc of dark-field LEDs around the bright-field circle. This choice is better than an empirical value, but it is also not entirely justified.

Some samples do not exhibit a uniform area large enough to perform the above procedure. The first X percentile can be used in this case instead of the average value over a region, Fig. 3.29(c).

Zhang et al. proposed a slightly different data pre-processing procedure [239]. Instead of subtracting the dark frame image and estimating the residual offsets after, they scaled the dark frame image by a weighted coefficient. This coefficient is, as in our case, defined on the basis of the average value of two uniform sub-regions. The authors also suggested detecting stray light in order to exclude the detected pixels from the updates of the reconstruction procedure.

Noise suppression during reconstruction Lexin Hou et al. followed a different path and proposed to estimate compensations iteratively during the reconstruction process rather than as a data pre-processing step [84]. Offsets are determined by comparing the captured images with those simulated from the current object estimate. Yao Fan et al. also introduced background suppression as part of the reconstruction [51]. They estimate the background noise in the form of an image for each LED rather than a constant offset. These incremental approaches promise to avoid eliminating a useful signal along with the noise. However, they indirectly modify the underlying objective function and are only integrated into projection-type algorithms.

Another way to perform an adaptive background suppression is to include the additive noise directly into the image formation model [14]. In this way, the measurement noise, as well as a relaxation constraint, are treated as optimization variables. Such an approach has the disadvantage of adding $2L$ of additional variables (a noise image and a relaxation image per LED) to the reconstruction procedure.

3.4.3 Results and discussion

Figure 3.30 shows the results of the reconstruction with different pre-processing steps applied. Initially, the reconstruction is performed directly after normalizing the exposure times and removing the hot pixels, (a). The dark frame is then subtracted from the captured images, (b). Finally, the estimated offsets are subtracted and the negative values are subjected to a threshold, (c). When angular-dependent offsets are not processed, we see its influence as a

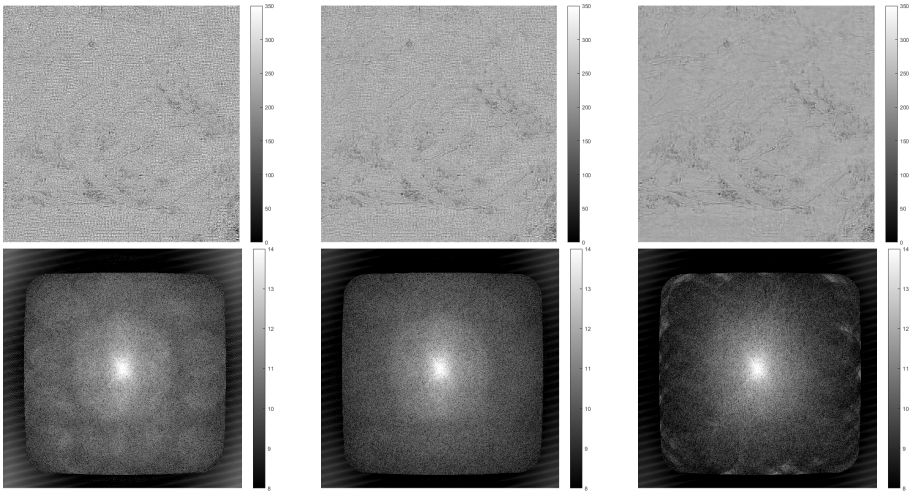

(a) (b) (c)

Figure 3.30: Reconstruction with different pre-processing steps applied. A region of interest from the sample in Fig. 3.6 is used. The size of the raw image region used is 150 x 150 pixels, which corresponds to 0.5 mm x 0.5 mm at the object plane. Top row - amplitude image, bottom row - Fourier spectrum (log of the absolute value). (a) Normalizing the exposure times and removing the hot pixels. (b) The dark frame is then subtracted. (c) The estimated offsets are subtracted and the negative values are subjected to a threshold.

disc in the Fourier spectrum of the reconstructed object (bottom line). This disc disappears when the offsets are subtracted.

While in practice, after testing different options, we find that our data processing method gives satisfactory results, it lacks theoretical foundations and should be examined in greater depth. In addition, other methods available in the literature should be implemented and tested. We also note that another noise-related problem, namely background interferences, should also be studied [83].

3.5 Numerical recovery of system parameters and aberrations

Methods for characterizing system parameters in a data pre-processing step have been described above. However those estimations are still not perfect and deviations can happen in actual experimental setup. In addition, we have not proposed a method to characterize the optical aberration of the constructed microscope. Fortunately, the redundancy of the collected data makes it possible to numerically estimate system parameters as well as aberrations.

3.5.1 Embedded pupil function recovery

Historically, one of the first estimates of this type was the wavefront correction, proposed for the classical projection type algorithm. The method was termed "Embedded pupil function recovery" [143].

The idea can be summarized as follows. Along with the reconstruction of the object $O(k_x, k_y)$ itself, a procedure for retrieving the pupil function $P(k_x, k_y)$ is applied to correct the optical aberrations. This is a currently standard practice for the FPM procedure. The flowchart of the classical projection-based algorithm, Fig. 2.14, therefore contains an additional step, Fig. 3.31. Given the use of the adaptive steps strategy, the update equations for $O(k_x, k_y)$ and $P(k_x, k_y)$ become[1]:

$$O_l^{(t+1)}(k_x, k_y) = O_l^{(t)}(k_x, k_y) + \alpha^{(t)} \frac{P^*(k_x, k_y)}{(|P^*(k_x, k_y)|^2)_{\max}} \nabla O_l^{(t)}(k_x, k_y) \quad (3.10)$$

$$P^{(t+1)}(k_x, k_y) = P^{(t)}(k_x, k_y) + \beta^{(t)} \frac{O_l^{(t)*}(k_x, k_y)}{(|O_l^{(t)*}(k_x, k_y)|^2)_{\max}} \nabla O_l^{(t)}(k_x, k_y) \quad (3.11)$$

where

$$\beta^{(t+1)} = \frac{\alpha^{(t+1)}}{\sqrt{L}} \quad (3.12)$$

is the step size of the pupil update [252].

Similarly, the embedded pupil function recovery can be implemented with gradient-based algorithms. In this case, the gradient is calculated for each cost function over the variable $P(k_x, k_y)$ and the joint optimization is applied. We haven't implemented this feature in our work, since we have chosen to work with the projection-based methods.

[1] The notations used are similar to [186]

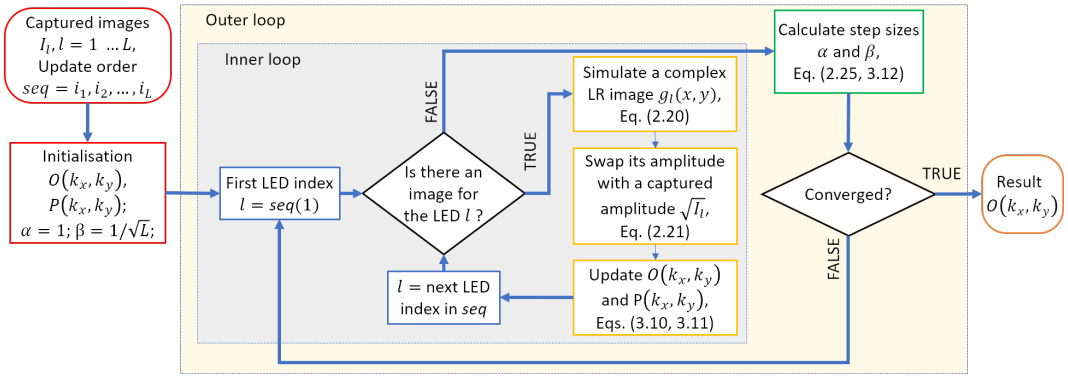

Figure 3.31: A flowchart of the PIE algorithm with embedded pupil function recovery for FPM reconstruction.

3.5.2 Modeling aberrations with Zernike polynomials

Another way to recover the pupil is to model its aberrations using Zernike polynomials. Indeed, the phase component of the pupil function $W(k_x, k_y)$ is supposed to be decomposable into Zernike polynomials $Z(m, n)$ with different coefficients $a_{(m,n)}$ [243] :

$$W(k_x, k_y) = \sum \left(a_{(m,n)} Z(m, n) \right) \tag{3.13}$$

The pupil function in the imaging model can then be rewritten as follows :

$$P(k_x, k_y) = P_c(k_x, k_y) e^{iW(k_x, k_y)} \tag{3.14}$$

where P_c is the circular opening function defined by Eq. (2.10). The Zernike mode coefficients $a_{(m,n)}$ are then treated like any other variable system parameter and their estimation is described in the next section.

According to our observations, the most important optical defect to be corrected is out-of-focus aberration. It is also the aberration which, in our experience, varies the most according to the position of the segment in the field of vision. In addition, the ability to correct the defocus extends the depth of field of the objective lens used. It can be modelled as a second-order Zernike mode $Z(2, 0)$. Fig. 3.32 shows a biological sample reconstructed with and without defocus correction, as well as the defocus coefficient estimation curve. While other work suggests that other Zernike modes may also be quite strong [16, 178], we have not observed this for our system. This may be due to the use of optics with strong aberration corrections.

Pengming Song et al. went further and proposed to estimate Zernike coefficients taking into account the position of the segment in the field of view, instead of estimating them for each segment independently [178]. The dependence of the aberrations on the position can be modelled by introducing the segment coordinate (x, y) into the classical wavefront aberration function

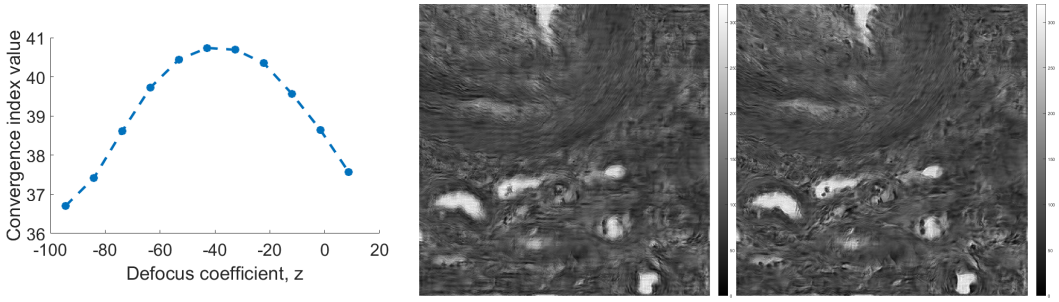

(a) (b) (c)

Figure 3.32: The influence of defocusing aberration. The example is a segment of a stained biological human kidney tissue, the raw images contain 100x100 pixels, which corresponds to 0.36 mm x 0.36 mm at the object plane. The focus distance for the acquisition has been set approximately, without using the technique described in Section 3.1.5. (a) Convergence index values plotted as function of defocus coefficients. The coefficient optimized is $z = -43$. (b) The result of reconstruction without correction of defocusing. Only the amplitude part is shown. (c) Reconstruction using aberrations modeled by $Z(2, 0)$ with the coefficient $z = -43$. The structures are clearly better resolved.

: $W(k_x, k_y, x, y)$. This algorithm has not been implemented in current work, but is likely to be beneficial when strong optical aberrations are expected.

3.5.3 System parameters estimation

This section describes the recovery of uncertain system parameters and Zernike mode coefficients. Several schemes have been proposed in the literature [16, 148, 178, 186, 237, 249]. The methods are mainly based on the idea of comparing simulated data with real data using a metric to be optimized. The most common measure used is the convergence index, Eq. (3.9).

The simplest and most robust scheme is to simply perform the reconstruction under different parameter values and calculate the metric for each result [16]. Fig. 3.33 shows the estimation of several system parameters, including NA, distance between the sample and the LED matrix h, wavelength λ, magnification and optical axis shifts Δx, Δy. The most basic PIE algorithm is used to avoid possible distortion of the evaluation of the results by the aberration and/or adaptive step size recovery strategy. The resulting curves are not convex for some parameters. In addition, it is not obvious that the convergence index is the best metric to optimize. While this measure addresses the ambiguity of phase shift, it does not reflect the correct noise model. A metric based on amplitude or Poisson cost may be more appropriate. An additional difficulty is the interconnection of system parameters. Indeed, if, for example, the distance between the sample and the LED matrix is overestimated, the recovered NA value will be underestimated.

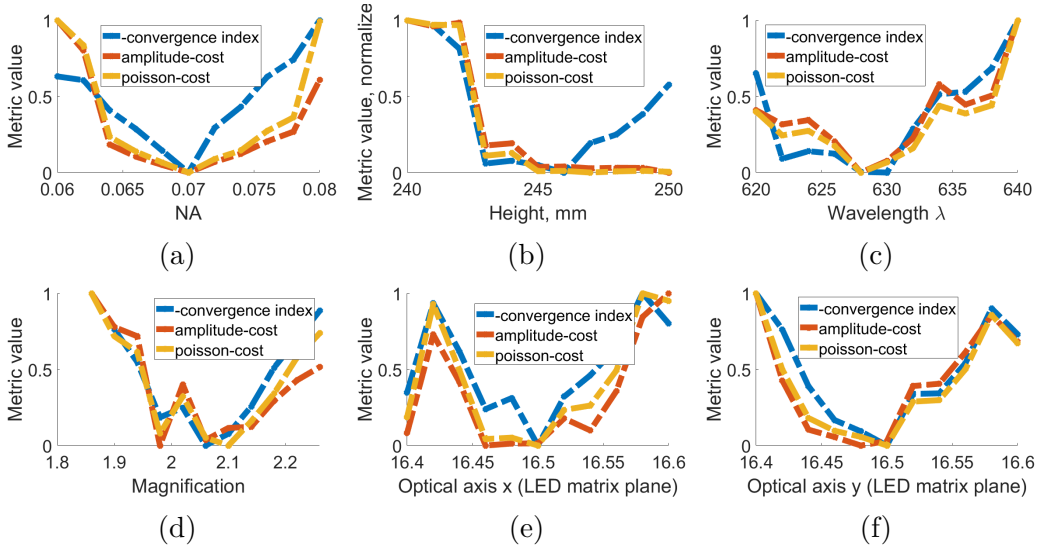

Figure 3.33: Estimation of system parameters. Three curves are drawn here for each parameter: the negative convergence index (blue), the amplitude-based cost function (red) and the Poisson-based cost function (yellow). The parameters considered are : (a) NA, (b) distance between the sample and the LED matrix h, (c) wavelength λ, (d) magnification, (e) optical axis shifts Δx, (f) Δy.

We note that the above method is hardly suitable for real-life applications because the run time of the reconstruction becomes too long. Zichao Bian et al. proposed to use the Generalized Pattern Search algorithm instead of the brute force strategy used in the current work [16]. Another proposal is the simulated annealing algorithm [226, 249].

An alternative approach to reducing uncertainties in the design matrix is to directly estimate the resulting angle (x and y component) of each LED separately. This leads however to an increase in the number of variables. Thus, instead of estimating 6 system parameters for each segment, we would have to estimate $2L$ (hundreds additional variable). An Pan et al. proposed to combine the two methods. The angles are first estimated using a simulated annealing algorithm and the system parameters are then deduced by linear regression [148]. More details on the correction of angular misalignment will be given below.

3.5.4 Angles misalignment correction

The estimation of the parameters presented above is based on the assumption that the individual LEDs have little or no misalignment. The possible angle deviations are supposed to be due to a wrong estimation of any of the 6 global parameters of the system: optical axis shift Δx, Δy, height h, wavelength λ, NA and magnification. However, this may not reflect reality. Mechanical

misalignments in the positioning of the LED elements and optical imperfections can introduce individual angle deviations. In addition, the specimen itself may reflect a beam unevenly in its different parts due to local optical thickness variations or refraction of the internal interfaces [202]. At the same time, even a small deviation in the angle of a single LED can lead to a deterioration in the quality of the reconstruction, Fig. 3.34. This is particularly true for LEDs at the edge of bright field and black field areas, where an incorrect estimation of the angle can lead to misclassification of the captured image.

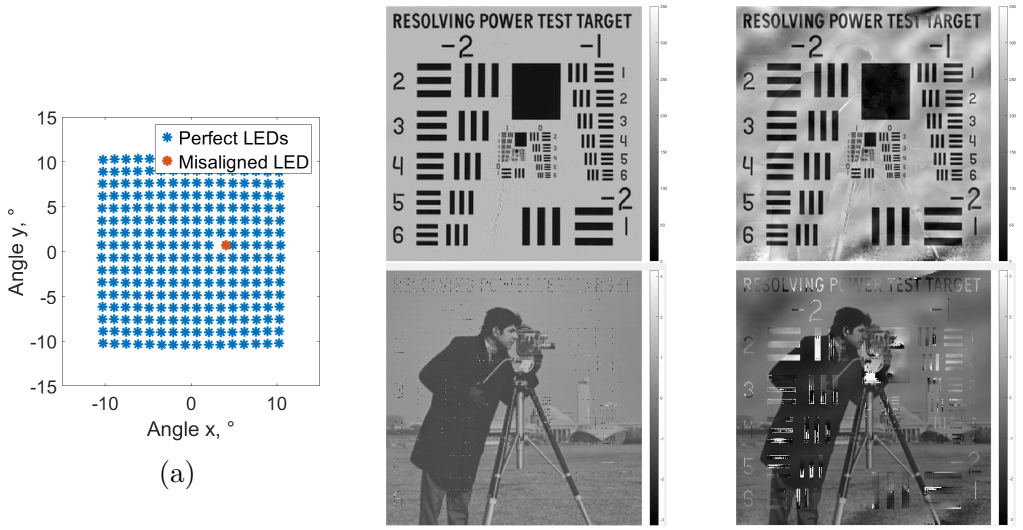

(a) (b) (c)

Figure 3.34: Influence of the angle deviation of a single LED. (a) LEDs angles. The blue dots represent perfectly calibrated angles. The orange point is a misaligned angle, the position error is about 40% in the x-direction. The erroneous LED is located near the bright field boundary and the deviation causes it to be classified as a dark field instead of a bright field. (b,c) The results of the reconstruction from a set of simulated data. (b) The angles are perfect. (c) Only one LED (indicated by the orange dot) is misaligned. The artifacts are particularly visible in the phase image but the amplitude image is also affected because of the leakage between the real and imaginary parts during reconstruction.

Two distinct families of methods address the problem of misalignment of individual angles.

The first group of techniques is based on the optimization of an image quality metric. This is similar to the global system parameters estimation. The convergence index and amplitude cost are the measures most often used for the optimization. The simulated annealing method seeking the best angle correction is often applied at each step (corresponding to each captured image) of a sequential optimization scheme [148, 186, 226]. Another option is to use a derivative of the image quality metric with respect to the angle (or rather

the spectrum shifts components $k_x l$ and $k_y l$). Gradient-based optimization can then be performed [116, 230]. Sining Chen et al. proposed yet another iterative approach, based on a feedback parameter controlling the portion of information used at each step [25]. The misalignments themselves are inferred using a cross-correlation function. All methods in this group, however, are prone to get stuck in the local minima due to the large number of parameters to be optimized.

The second family of methods consists in correcting the angles before the reconstruction stage. Regina Eckert et al. were the first to propose analyzing the spectrum of captured images to estimate the corresponding angle [49, 50]. The algorithm works in a two-step process. The angles are first deduced for bright field LEDs based on the detection of circles in Fourier domain. Indeed, when bright-field LEDs are used to illuminate the sample, the spectra of the captured images feature a pair of discs symmetrical with respect to the frequency origin, Fig. 3.35. The center (kx_l, ky_l) and the radius r_l of the observed discs correspond respectively to the illumination angle of the LED k (or rather its carrier frequency) and the NA. The angles are then iteratively re-estimated for all LEDs using joint optimization of the object and angles. This stage belongs to the first family of angles correction strategies.

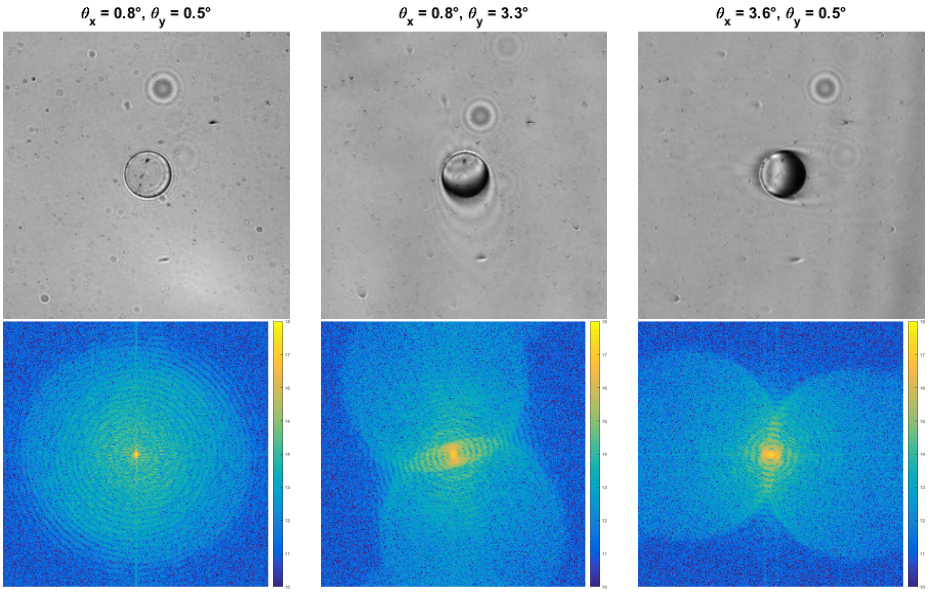

(a) (b) (c)

Figure 3.35: Examples of circular regions in Fourier domain for bright-field angles. The sample is a 150 um microsphere, more information about this sample in the next chapter. Top row - a region of the captured intensity image. Bottom row - its Fourier transform. The size of the region used is 280 x 280 pixels, which corresponds to 0.9 mm x 0.9 mm at the object plane. The illumination angle x and y components are (a) [0.8°, 0.5°]; (b) [3.6°, 0.5°]; (c) [0.8°, 3.3°].

Despite the promising benefits of the Regina Eckert method, we found that it does not work with our data. Indeed, the first step of the algorithm fails to correctly identify Fourier-domain circular regions. This is due to the fact that our circles tend to be noisier and have fuzzy contours with open arcs. This is not the case with the data provided by the team of Regina Eckert and Laura Waller, Fig. 3.36.

A new method with encouraging results is currently being developed by the TRIO team. Like in the case of the algorithm above, our method allows to recovery triplets (kx_l, ky_l, r_l) from spectral images. The Fourier transform of captured images is symmetrical because the images are real. We introduce these symmetries into band limited cost functions which permit to stick to non perfect contours. This also allows for rapid convergence and improved robustness. Fig. 3.37 shows the results of bright-field angles estimation using the method developed. We plan to report on the details of the algorithm in a forthcoming work.

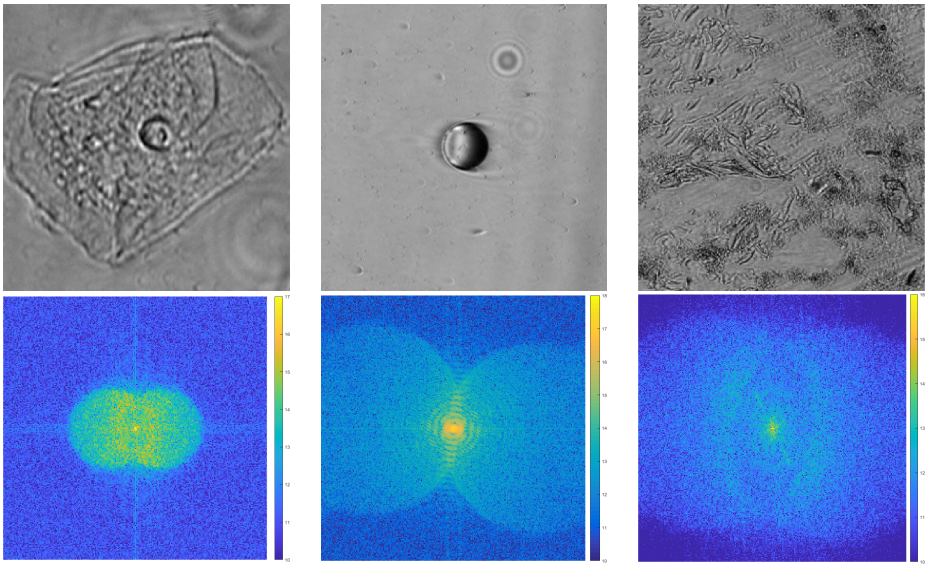

(a) (b) (c)

Figure 3.36: Comparison of spectra for 2 different FPM systems. Top row - an image segment captured in bright field, oblique lighting. Bottom row - its Fourier transform (a logarithm of the amplitude is shown). (a) Histological slide data provided by the Laura Waller team. (b) 150 µm microsphere captured with our system. (b) Mouse breast tissue slide captured with our system.

In conclusion, we underline the importance of angle corrections, especially for border images. We also note once again that individual angle correction can compensate for misalignments in the global system parameters. It has been reported [202] that the benefits are even more pronounced for thick samples and/or 3D reconstruction. Although these methods are not yet fully integrated

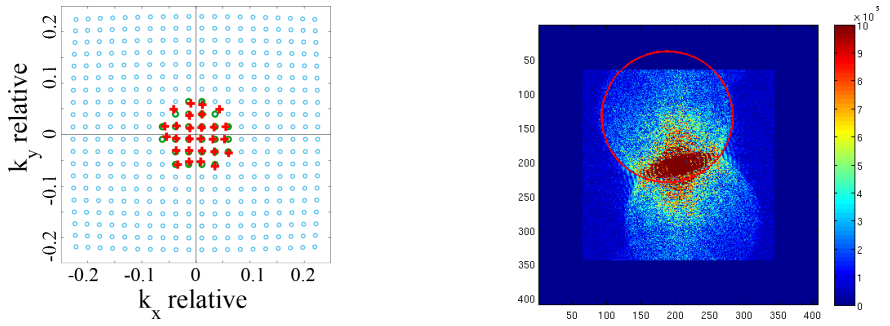

(a) (b)

Figure 3.37: Results of the estimation of bright field angles by the method currently being developed. The sample is a 150 µm microsphere. (a) Plot of estimated angles. The circles are the theoretical values of the angles. The green circles correspond to bright field LEDs. The red crosses indicate the angles estimated from the captured images. (b) A circle fitted on the spectrum of one of the captured images.

into current work, the results of simulations and preliminary study of experimental data suggest that angle correction is an essential element of artifact-free reconstruction.

3.5.5 LEDs intensities

We have already mentioned above (Section 3.2.1) the differences in irradiance of different LEDs. Moreover, different parts of the field of view receive different amounts of light. In addition to this fixed pattern of illumination differences, we also observe random fluctuations on individual acquisitions. This problem has also been reported in the FPM literature [16, 148].

A conventional way of dealing with uncertainties related to the amount of illumination is the introduction of an intensity correction coefficient. The observation model (Eq. 2.12) can be subsequently modified as follows :

$$I_l(x,y) \approx \frac{1}{c_l}|\mathcal{FT}^{-1}\left\{P(k_x,k_y)O(k_x-k_{x_l},k_y-k_{y_l})\right\}|^2 \equiv \frac{1}{c_l}g_l(x,y), \quad l=1,...,L, \tag{3.15}$$

where c_l is the intensity correction factor.

This leads to the modification of the reconstruction cost function. For example, the new amplitude cost (Eq. 2.35) is now stated as (in a non-vectorized form):

$$f_A = \sum_{l=1}^{L}\left\|\sqrt{c_l I_l(x,y)}-\sqrt{g_l(x,y)}\right\|^2, \tag{3.16}$$

The optimal value for the correction factor c_l can be found by minimizing

the cost function with respect to c_l, from which it is derived:

$$c_l = \frac{\sum_{x,y} g_l(x,y)}{\sum_{x,y} I_l(x,y)} \tag{3.17}$$

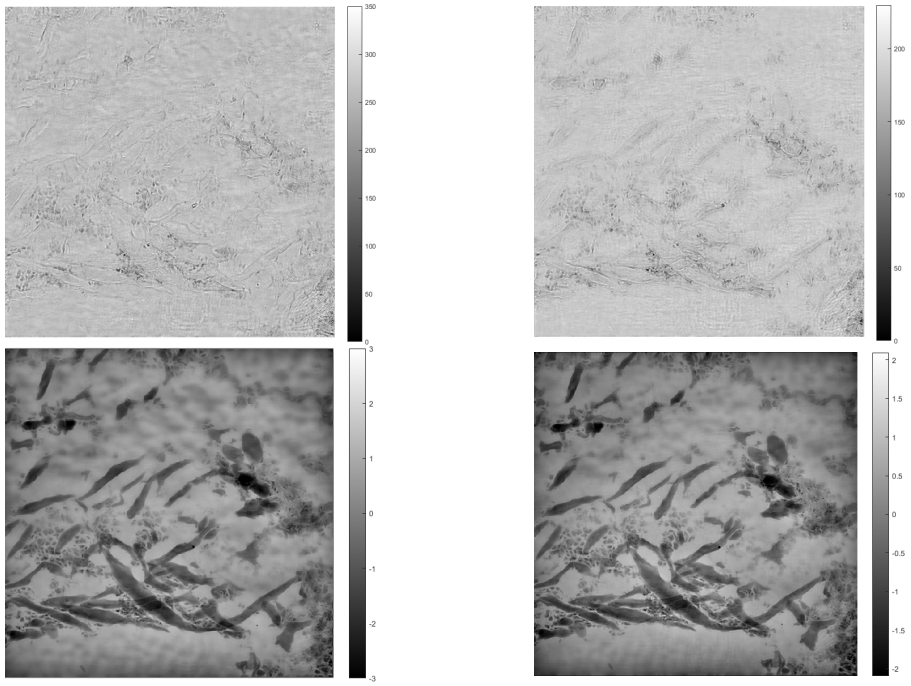

(a) (b)

Figure 3.38: Results of the reconstruction of a region of a biological tissue sample. The same sample as in Fig. 3.6 is shown. The size of the raw image region used is 150 x 150 pixels, which corresponds to 0.54 mm x 0.54 mm at the object plane. Top row - amplitude, bottom row - phase. (a) The PIE algorithm described by a flowchart 3.31 without the intensity correction routine.(b) 4 iterations of the intensity correction routine are performed. Each iteration includes 50 steps of the PIE algorithm. Fewer artifacts are visible.

The classic way to introduce this intensity correction is to update the captured images at the end of each iteration step of the PIE algorithm, starting with the 2nd step [16]: $\tilde{I}_l(x,y) = c_l I_l(x,y)$. We follow a similar procedure, but instead of updating the measurements at each step, we do it every 25 steps after the initial 25 iterations without the intensity correction. This approach is slower because it requires more iterations, but we found it to be more robust. We also found that more than 5 iterations of the intensity correction routine typically result in the loss of high-frequency information and decreased phase contrast for our data. Indeed, coefficients of images corresponding to high lighting angles tend to become quite low. The results of reconstruction with and without intensity correction are shown in the Fig. 3.38.

3.6 Importance of light coherence

The imaging equations imply a coherent single wavelength system. However, as we have seen with LED spectrum measurements, such an approximation may not be adequate in our case. Green LEDs, for example, have a spectral width of 22 nm and can hardly be considered perfectly coherent. Addressing this incoherence could potentially improve the quality of the reconstruction.

We test this hypothesis by performing an incoherent sum on coherent reconstructions within the actual wavelength range. We observe that the image quality metrics are lower despite the visual improvements, see Fig. 3.39. However, the metrics must also be adjusted to reflect the incoherence of LEDs. The technique described above is more an indication of potential improvements in the imaging model than a fully developed algorithm.

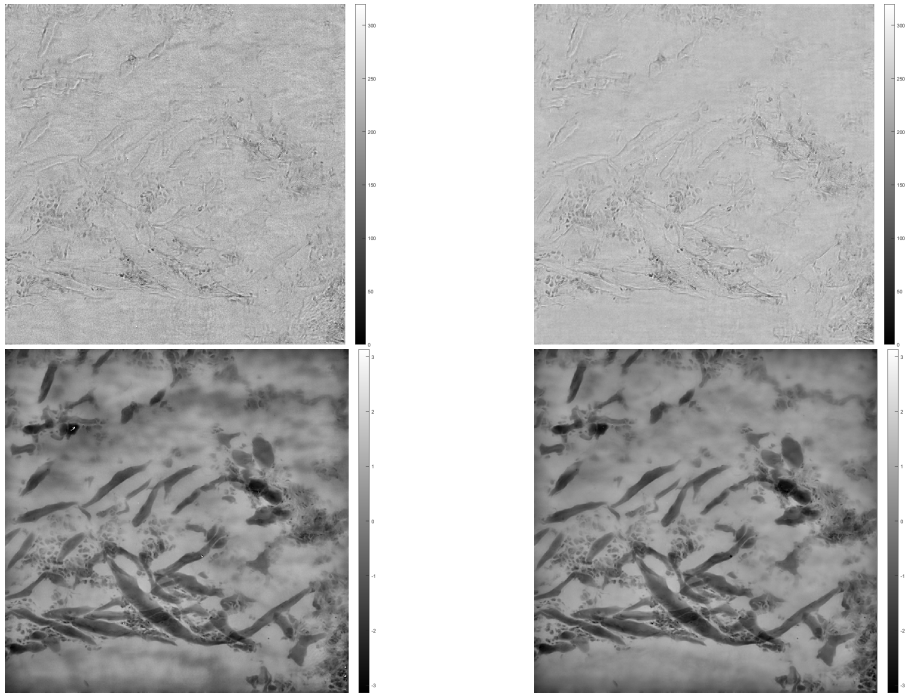

(a) (b)

Figure 3.39: Illustration of the importance of taking into account the non-coherence of light. The same sample as in Fig. 3.38 is shown. The size of the raw image region used is 150 x 150 pixels, which corresponds to 0.54 mm x 0.54 mm at the object plane. Top row - amplitude, bottom row - phase. (a) Single reconstruction. (b) The images are calculated as an incoherent sum over 25 coherent reconstructions in the wavelength range.

Although the problem of LEDs incoherence is rarely mentioned in the majority of the FPM literature, it is still addressed in several research papers. Among the first works in this direction, Siyuan Dong et al. developed a

method called coherent state decomposition [48]. While the reported applications are intended for color-multiplexed FPM imaging, the authors suggest that a similar technique could also be used to solve the incoherence problem for monochrome imaging. Their method is likewise based on the idea of an incoherent summation. Each captured image is regarded as a sum of three target images corresponding to red, blue and green wavelength. We could consider our configuration as a sum of several acquisitions corresponding to close wavelengths within the spectral band, as opposed to a sum of three distant wavelengths. In such a case, the forward imaging model, Eq. (2.12), becomes:

$$I_l(x,y) \approx \sum_{j=1}^{J} |\mathcal{FT}^{-1}\left\{P(k_x,k_y)O(k_x - k_{x_{l,j}}, k_y - k_{y_{l,j}})\right\}|^2, \quad l = 1, ..., L, \tag{3.18}$$

where $(k_{x_{l,j}}, k_{y_{l,j}})$ – the spatial frequency corresponding to the illumination angle of the l-th LED given the wavelengths $\lambda_j \in [\lambda_{min}, \lambda_{max}]$ within its spectral band. Considering the similarity of this method to the one described above and the results obtained, we assume that the implementation of a coherent state decomposition algorithm could considerably improve the quality of our reconstructions. This is one of the subjects of our future research.

Another point of view involves changing the pupil function in the imaging system equations 2.12. Indeed, in a classical FPM, the pupil function is a coherent point spread function (with aberrations). This model can be modified to reflect the partially incoherent nature of LEDs, like it is done in several works [29, 144]. This point is not included in the current work, but it is likely to be beneficial and should therefore be explored in future work.

3.7 Whole field of view reconstruction

3.7.1 Segment size choice

When the image segment is small, it can be approximated by a point receiving light from a LED at a certain angle. However, when the segment is large, this model is no longer valid. At the same time, reconstruction cannot be performed when the number of pixels is insufficient (say 10x10 pixels). The lower limit is therefore defined by the sampling required to meaningfully perform a discrete Fourier transform operation on the captured intensity images. The upper limit is set by the adequacy of the plane light wave approximation which is also related to the coherence length of the LED. Another reason for using small segments is the ability to recover space-dependent lens aberrations and fine-tune local system parameters. Finally, memory requirements are reduced when smaller segments are used and parallel processing can be applied.

We define the exact number experimentally by performing a reconstruction for segments from 50x50 pixels to 300x300 pixels and choosing the best one for

each data set. Nevertheless, a more rigorous procedure for choosing the size of the segments must be proposed and justified in future work.

3.7.2 Segments stitching

Abrupt changes between regions can be easily observed when the reconstructed segments are assembled together, Fig. 3.40 (a). This effect can be mitigated by blending border parts of neighbouring segments. The most commonly used method is alpha blending [190, 198]. Some authors suggest using up to 160 pixels of border overlap between regions (given the segment size of 360 x 360 pixels). However, more details are generally not given.

The method, as we use it, can be described as follows. The border overlap is set to 10 pixels from each segment side. First, we stitch the segments together horizontally and then combine the created lines to reconstruct the complete FOV image. Phase and amplitude images are processed separately to avoid leakage between the two. A linear mask is applied to allow 2 segments to gradually fade into each other, Fig. 3.40 (b). Half of the overlap area is then cut on each side.

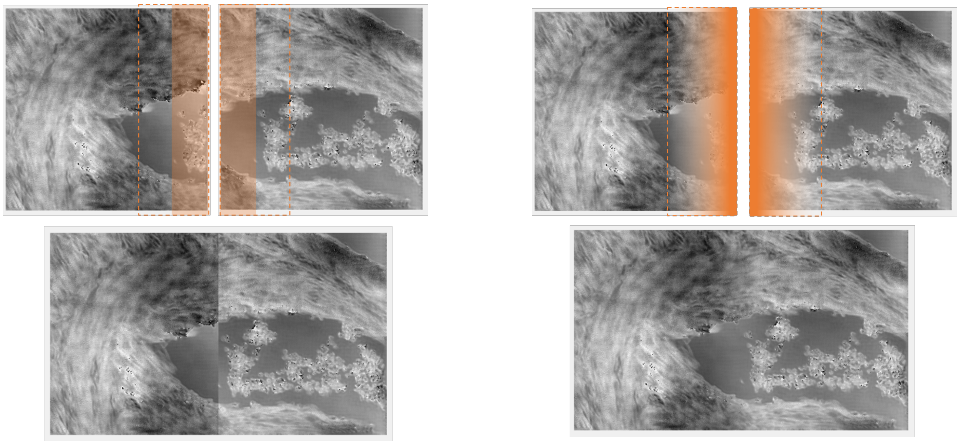

(a) (b)

Figure 3.40: (a) Half of the overlapping portions of the boundary are cut on each side in a binary manner. (b) The linear blending mask is applied.

The final result of the stitching could still appear non-homogeneous. Indeed, one of the reasons is the different overall intensity level of the reconstructed segments due to the iterative nature of the reconstruction algorithms. An improved alpha blending method, combined with the image consistency correction [8], could be applied to resolve this issue. In addition, trivial phase ambiguities, such as constant phase shift, should also be addressed when assembling the phase image.

3.7.3 Phase unwrapping

When the optical phase difference is greater than 2π, phase jumps appear on the reconstruction, Fig. 3.41. A phase unwrapping algorithm removes these jumps and restores the physical continuity of the phase image as well as its real quantitative value. We use Goldstein branch cut [61] algorithm when execution time is limited. Otherwise, quality guided path following phase unwrapping [60] provides more robust results. Both methods are available as open source software [182].

(a) (b)

Figure 3.41: An example of a phase unwrapped by means of a guided path following method. (a) Original phase. (b) Unwrapped image.

It should be noted that some phase jumps may be unrelated to physical changes in optical thickness. Indeed, in areas where amplitudes are close to zero, the recovered phase is not reliable and may appear random on the reconstructed phase image [14].

3.8 More realistic simulations

As we have seen, the perfect imaging model described by the equations (2.12) does not reflect all experimental realities. In order to correctly evaluate the behaviour of different algorithms, these realities must be taken into account when using simulated data sets. Similarly, the reconstruction pipeline should also address experimental issues. Among the most prevalent sources of error are: different types of camera noise, lens and wavefront aberrations, angular positions of the LEDs resulting partly from misalignments of the system parameters, uneven distribution of illumination, fluctuations in illumination brightness and lighting incoherence.

In practice, sample thickness is also a source of difficulties. Indeed, the angular deviations of the different internal slices and the relationships between these slices are not taken into account in the classical FPM. However, these issues are addressed in the 3D version of the technique [78].

3.8.1 Noise generation procedure

Based on the above device characterization, we propose the following procedure to simulate images approximating the data captured with our configuration.

System misalignments are first modelled by disturbing the general parameters (like NA and wavelength), then adding a local displacement to each angle. We note $\tilde{\boldsymbol{A}}_{\boldsymbol{l}}$, $l = 1...L$ a component of a design matrix with misalignments. The intermediate images are then generated as follows $\boldsymbol{y}_l = \left|\left\langle \tilde{\boldsymbol{A}}_{\boldsymbol{l}}, \boldsymbol{O}^* \right\rangle\right|^2$. Scaled Poisson noise is then applied on the simulated images $\boldsymbol{p}_l = \frac{1}{\alpha_l}\text{Pois}\left(\alpha_l \boldsymbol{y}_l\right)$. The scale α_l is defined by the slope of the regression line in the variance-to-mean (σ^2, E) scatter plot and differences in exposure times. This value depends on the camera used. Gaussian noise $\boldsymbol{n}_{\sigma_l}$ is then added. Finally, the images are scaled by random intensity fluctuation coefficients c_l to represent uneven lighting. This results in the simulated images $\boldsymbol{I}_l$, $l = 1, ..., L$ referred to as the set $S3$ in the previous chapter : $\boldsymbol{I}_l = c_l\left(\frac{1}{\alpha_l}\boldsymbol{p}_l + \boldsymbol{n}_{\sigma_l}\right)$.

We note, however, that this noise generation procedure has to be more complete in case a new reconstruction algorithm is proposed. This way, the light incoherence should be modelled using the Eq. (3.18). The deviations of the light rays caused by the interactions of the internal slices of a not infinitely thin sample must also be simulated.

3.8.2 Plausible simulated data sets

One of the complications of simulating a realistic data set is related to the variety of samples that can be studied. Even among purely biological samples, segments with very diverse characteristics can be found, Fig. 3.42. The biggest difference for reconstruction algorithms is whether the sample is described as phase only (transparent) or as amplitude (most of the information is contained in its brightness variations and not in the phase). The latter difference can be particularly important when designing a specific lighting model, as opposed to a sequence of individual LED acquisitions used in the current work [97]. Further, variations in intensity within a region can be strong or rather smooth. The sample can be homogeneous or present a variety of structures. The thickness of the sample also greatly influences the quality of the reconstruction. In addition, syntetic samples and microscope targets have dissimilar spectral properties to those of natural biological tissues. These differences are important not only for reconstruction algorithms, but also for the methods used to recover parameters and angles.

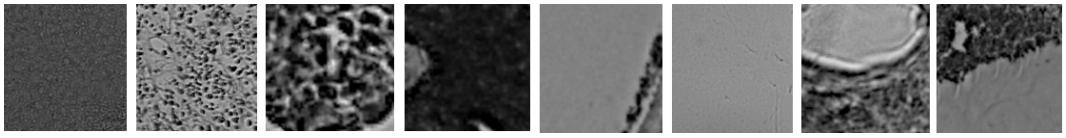

Figure 3.42: Examples of biological sample segments.

3.9 Results and conclusion

The FPM technique promises easy installation and a simple imaging model. One of the difficulties, however, resides in the precise characterization of all the components of the constructed instrument. Moreover, while basic algorithms work well on noise-free simulated data, the experimental realities of our microscope required a few supplementary steps. For this reason, it is important to correctly calibrate the instrument, set up the acquisition phase, pre-process the data, choose a suitable reconstruction procedure and combine the reconstructed segments.

As for the reconstructed procedure, we chose the version of a PIE (Gerchberg-Saxton) algorithm with adaptive step size strategy, defocusing modeling, aberration recovery and intensity correction routine. The global system parameters are optimized for a central segment. The correcting coefficient for segment centres has chosen to be equal to $k_c = pi/4$, however it can be optimized for each acquisition to allow a better accuracy.

Typical run time on a standard desktop PC is approximately 30 seconds for segment reconstruction from 400 low-resolution 100x100 pixel images. We recognise that the speed of the algorithms can be greatly improved, but this was not the focus of the current work.

Figure 3.43 shows the comparison of the results of the basic PIE algorithm without background subtraction with the proposed reconstruction procedure. The same system parameters are used for both reconstructions, except that no correction for the segment centres was used in the first case ($k_c = 1$). The sample in the example is a stained histological slide of mouse breast tissue. The thickness is 6 µm. The Prosilica GE2040 is used. Exposure times ranges from 230 ms to 10 seconds. Under sequential red light illumination ($\lambda = 630$ nm), a total of 400 images have been recorded this way. The estimated NA is 0.071. The segment size is set to 100 x 100 pixels plus 10 pixels on each side of the segment to allow alpha blending stitching.

Additional reconstruction results can be found in the appendix. Examples include biological tissues, the URSAF 1951 and star resolution targets. As can be seen, some artifacts are still present on both amplitude and phase images. We believe that the implementation of some of the features indicated in this chapter will eliminate these imperfections and improve the quality of the reconstruction. During our investigations involving simulations of misaligned noisy images, we found that artifacts caused by different sources often look similar. There is therefore no simple answer to the question of which correction strategy would allow for a perfect reconstruction. However, both the literature review and our experimental research indicates that special efforts need to be made to overcome the effects of partial illumination coherence and to resolve misalignments of individual angles.

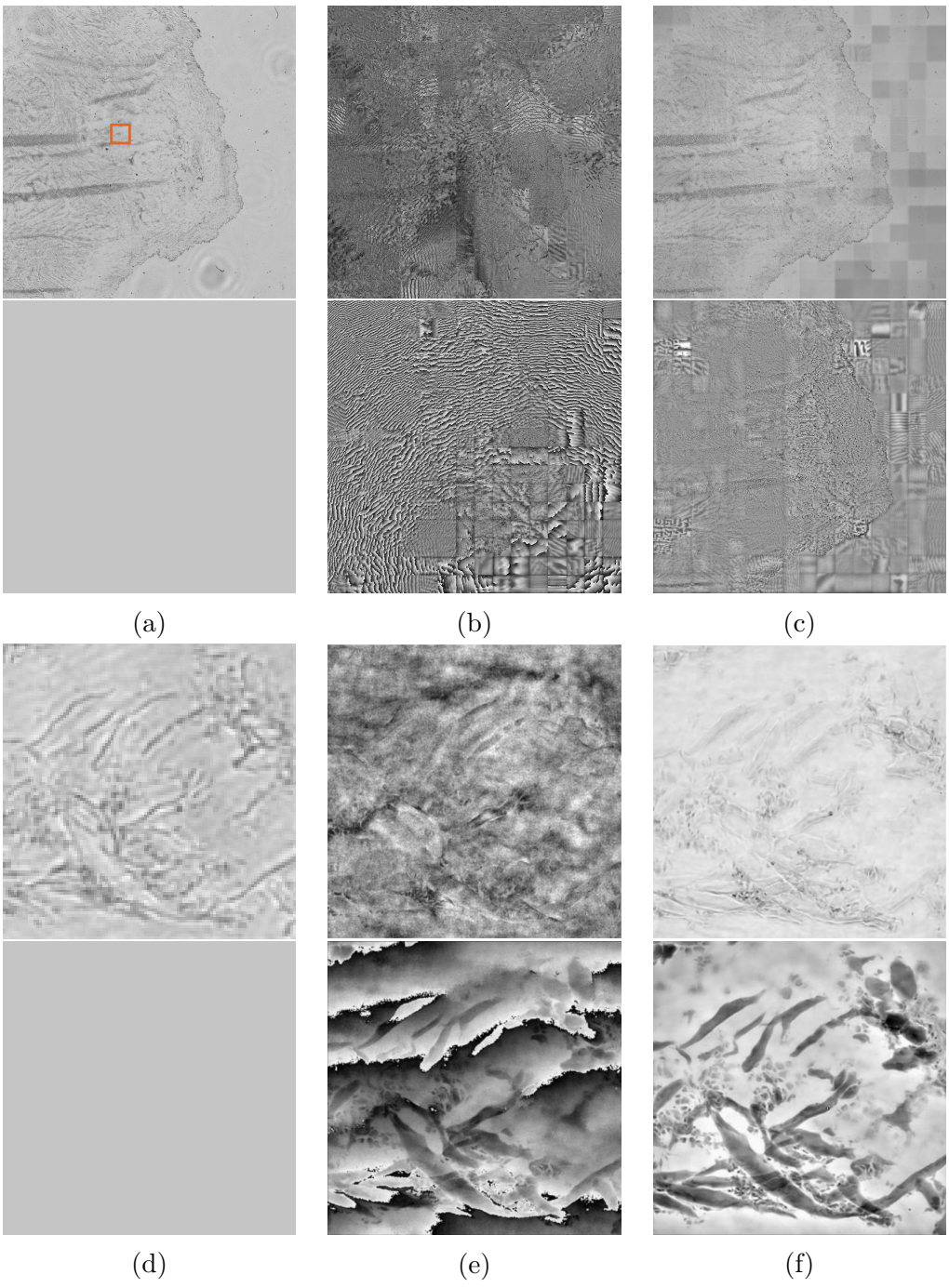

Figure 3.43: Results of the reconstruction. Top row - amplitude, bottom row - phase. (a,d) A low-resolution bright field image. (b,e) Results obtained with the basic PIE algorithm (no segment correcting coefficient k_c). (c,f) Results with the proposed reconstruction procedure. (e,f) The images of a region of interest (zoomed images) are calculated as a sum over 25 reconstructions within the wavelength range. The size of the raw image region used is 120 x 120 pixels, which corresponds to 0.43 mm x 0.43 mm at the object plane.

Chapter 4

Polarized light microscopy and multi-modal imaging

As discussed in previous chapters, FPM can provide more complete information than conventional bright-field microscopy [79]. The constructed microscope provides high-resolution bright-field imaging and quantitative phase contrast.

In order to evaluate the quantitative imaging capabilities of the constructed microscope, we are conducting a comparative study using an object of great optical thickness. The imaging modality chosen for this confrontation is a holographic microscope. The analyzed sample is a soda lime microsphere immersed in Canada balsam.

Furthering the idea of developing a multimodal imaging system, we explore the complementarity and eventual integration of ptychographic Fourier microscopy with polarimetric microscopy. The main motivation for this research is the ability of polarimetric microscopy to access additional physical properties of samples that are not available in conventional optical microscopy or FPM. Indeed, some materials, including some biological tissues, do not react in the same way to light of different polarization states. These materials may exhibit birefringence, dichroism or optical activity. This data can be an important piece of information, for example, for the analysis of biological tissues and for medical diagnosis. In order to obtain the most complete description of the response of a medium to polarized light, we must calculate the Mueller matrix of this medium [131]. For this we use a Mueller microscope built by members of the TRIO team.

This chapter first presents the quantitative phase imaging study conducted. Then, the Mueller matrix microscope is presented, followed by a description of the comparative study. Finally, improvements in FPM and its extensions to other modalities are discussed.

4.1 Quantitative phase imaging

As already mentioned, Fourier ptychography is able to recover quantitative phase images [1]. Retrieving quantitative phase information from a transparent object is an essential and important issue for biological tissue imaging.

In the past decades, a number of quantitative phase imaging (QPI) techniques have been introduced [151]. With the development of computational imaging, QPI with simple optical setups can be achieved and still rapidly expanding. Here, we aim to validate the QPI capability of our Fourier ptychographic microscope by comparing the resulting phase images with the images obtained by a Lensless inline digital holographic microscope. Lensless inline digital holographic microscopy (LI-DHM) is one of the widespread quantitative phase imaging techniques. Both methods have been used in various fields, particularly for imaging biological slides because of their simplicity in use, stability in structure and also large field of view.

Small (several to tenth of microns in diameter) transparent microbeads have frequently been used as standards for QPI calibration and validation purposes. This is partly due to the fact that a spherical phase response (from HeLa cells for example [109]) is commonly observed in biological imaging. However, phase imaging of their large counterparts (beads of hundreds of microns in diameter) using either LI-DHM or FPM has not been reported so far. We are aiming to analyze the phase response of a 146 µm soda lime microsphere. It has been immersed in Canada balsam so as to reduce phase difference and to avoid overexposed diffraction rings. The estimation of the LI-DHM phase was approached using a Gerchberg-Saxton (G-S) type algorithm and an inverse problem-based procedure. Confronting the results confirms the QPI capability for both imaging techniques to assess phase responses from such a large transparent object.

4.1.1 Inline holography introduction

Inline holography was first introduced by D. Gabor in 1948 [57]. Due to the twin image distortion, this technique was neglected for a long time. After 2000, due to the improvement of computational imaging techniques along with the development of digital cameras, retrieval of phase information and reduction of the twin image effect have been made possible [43]. Recently, LI-DHMs have become popular. With samples positioned as close as possible to the camera, the demand for light coherency may be reduced. With magnification nearly equals to 1, a high FOV that embraces the sensor can be obtained [229]. Also, subpixel super resolution techniques have been applied to improve performances [229]. Rigid and compact microscopes have been built with those

[1] Some sentences in this section are taken from our article "Lensless inline digital holography versus Fourier ptychography: phase estimation of a large transparent bead" [110].

on chip LI-DHMs [40]. They are cost effective and at the same time, maintain performances comparable with conventional QPI microscopes [177].

Details of our LI-DHM experimental set-up as well as the imaging model and reconstruction algorithms for the constructed device can be found in the published article "Lensless inline digital holography versus Fourier ptychography: phase estimation of a large transparent bead" [110]. The part of this study concerning the construction of the holographic microscope and its phase recovery was mainly carried out by Hongyu Li [2]. Only a brief overview of the LI-DHM, the results and the comparison with the FPM will be presented in the current manuscript.

To the best of our knowledge, there seems to be no report on a quantitative analysis of QPI capability of LI-DHM and FPM for relatively large transparent objects (more than a hundred of microns). Due to the similarity of the optical setups, it could be valuable to assess the performances of both techniques.

4.1.2 Transparent phase sample

For QPI validation purpose, several objects have been considered as standards: red blood cells [17, 140], laser lines etched on glass [17], commercial phase standards [183], and samples with known refractive index such as optical fibers [89] or polystyrene microbeads [140] immersed in oil.

We chose to fabricate our own standard by isolating a single soda-lime (refractive index $n_{glass} = 1.522$ at 633 nm) microsphere on a slide, immersed in Canada balsam for immobilization. The diameter provided by the manufacturer is 150 µm with a standard deviation-to-mean ratio of 10%. The exact diameter of the sphere is then inferred from images captured with a phase-contrast microscope as shown in Fig. 4.1(b). To set the focus plane at the middle of the sample, we have analyzed the captured images at a vicinity of the microsphere boundary and maximized the sharpness of the observed arc. The estimated diameter is 146 µm. The refractive index of the Canada balsam has been measured separately using a refractometer. Depending on the experiments, variations ranging from 1.523 to 1.533 have been observed in the red band. For that reason, we have chosen to compare phase responses retrieved by each of our instruments. The microsphere and Canada balsam have close refractive index values. This reduces the phase difference so as to avoid overexposed diffraction rings.

The sample's response can be approximated by a complex transmittance for incident waves that are almost plane. The phase distribution $P(r)$ across the sample may be obtained by evaluating the delay undertaken by each directly

[2] Hongyu LI is a PhD student of the TRIO team of ICube laboratory. He is currently working on his thesis about digital holography and surface plasmonic resonance.

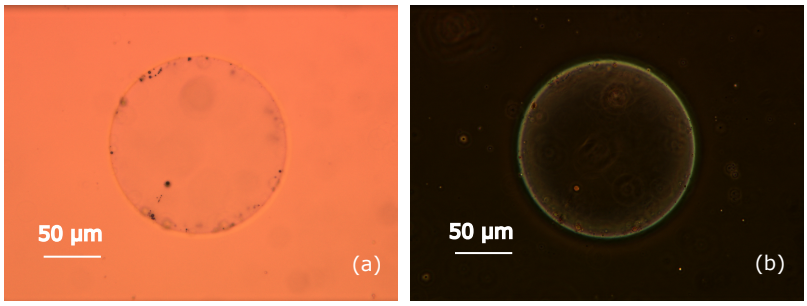

Figure 4.1: Images of microsphere from conventional microscope. Diameter of the sphere is 146 µm. Image under (a) bright-field microscope and (b) phase-contrast microscope.

transmitted ray and can be described by Eq. (4.1):

$$\begin{cases} P(r) = P_{max}\sqrt{1-\left(\frac{r}{R}\right)^2} & \text{, if} \quad r < R \\ P(r) = 0 & \text{, otherwise} \end{cases} \tag{4.1}$$

with $r = \sqrt{(x^2+y^2)}$. R is the radius of the sphere, and P_{max} identifies the maximum phase shift that is produced by the difference of refractive indexes between glass and optical glue.

4.1.3 Lensless inline digital holographic microscope

Image formation and experimental setup The schematic of the LI-DHM built by the TRIO team members is shown in Fig. 4.2(a). The classic Gabor configuration was chosen. The picture of the device can be found in Fig. 4.2(b)

The operating principle can be briefly described as follows. The interference pattern is recorded on a hologram. It is modelled as a mixture of the reference wave $R(x,y)$ and the object wave $O(x,y)$. In cases where phase only (transparent) objects are considered, the object term may be neglected compared with the reference wave. The last ones carry informations to be retrieved. In the LI-DHM configuration where a point-source is used, the waves diffracted by the object are captured in $O(x,y)$. The undiffracted light will serve as the reference $R(x,y)$. Because of the well-known twin effect, a phase image cannot be recovered directly from an inline hologram. As with the FPM, a reconstruction procedure is required.

The full description of the LI-DHM system parameters can be found in the published article [110]. The resulting resolution $2\delta x = \lambda/(NA)$ and depth of field $2\delta z = \lambda/NA^2$ are respectively equal to $2\delta x = 15.4$ µm and $2\delta z = 377$ µm.

Reconstruction Two well-established methods were employed for phase estimation. They are only briefly presented in this section, while details of both are provided in the published article [110].

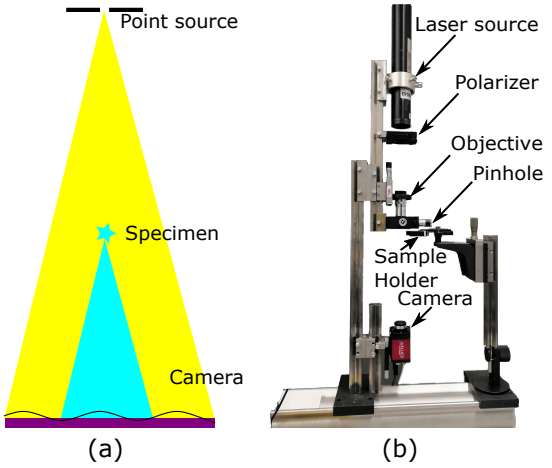

Figure 4.2: Gabor LI-DHM built by members of the TRIO team (a) Schematic diagram (b) Experimental setup.

The first one lies on the commonly used G-S type iterative phase retrieval method [59]. The second one is based on an inverse problem approach [56]. The procedure involving G-S projection includes two steps. To start with, an autofocusing algorithm is applied to get the right focusing position. Once the focus has been estimated, the G-S algorithm is launched and coupled with the so called positive absorption constraint [106]. The latter consists of imposing the limit of 1 to all pixel values that surpass 1 in the two-dimensional (2-D) transmittance that approximates the object. Since the size of the microsphere is known, an object support may be introduced to accelerate the convergence of the algorithm [85].

As for the second investigation, a parameter-based inverse problem algorithm has been used since the regular geometrical shape of the microsphere involves very few variables [56]. It is more robust than the general approach that consists of reconstructing the transmittance distribution directly. It was introduced by Soulez et al. [181] to track the traces of particles and to estimate their size. With the object plane far enough from the camera, the sample may be considered as a phase disk that follows Eq. (4.1). This model can therefore be integrated into the cost function. The optimization is performed using a sequential quadratic programming algorithm.

Phase retrieval results The distance between the object plane and the sensor plane retrieved by the autofocusing method is 17.881 cm. After ensuring such a reliability for the auto-focusing technique, the iterative phase retrieval procedure has been launched. The reconstructed phase distribution is shown in Fig. 4.3 (a). In Fig. 4.3 (b), the maximum phase shift P_{max} is clearly visible. It has been inferred to be about -10.10 rads. These outcomes reflect the QPI performances of the LI-DHM. It is worth mentioning that because of

the restricted support introduced in the object domain (18 pixels larger than the object in radius), the algorithm converges with only 10 iterations.

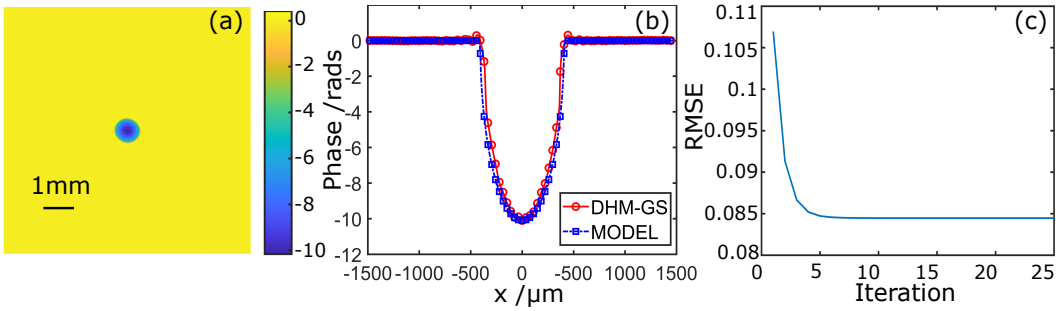

Figure 4.3: Reconstruction of G-S-based iterative phase retrieval algorithm: (a) reconstructed phase distribution. (b) Curve with red circles is a scan through the center of (a). Curve with blue squares is theoretical phase distribution calculated according to Eq. (4.1), with magnified diameter of 816.1 μm (measured diameter 146 μm times magnification factor of 5.59) and maximum phase shift of -10.10 rads. (c) Root-mean-square error (RMSE) as a function of iteration number. Convergence has been attained after 10 iterations.

The focus position and the maximum phase shift have then been used as an initial guess for the optimization process of the inverse problem. The minimum of the cost function has been found to be located at $\vec{p} = (17.878, -9.87)$. It means that the microsphere is 17.878 cm away from the camera, and the maximum phase shift it induces is -9.87 rads. Consistency with the result from the SOG autofocusing technique combined with the G-S phase retrieval method has been maintained.

As shown in Fig. 4.4, the cost function exhibits a minimum at -9.87 rads. However, two other local minimums (-25.88 rads and -18.36 rads) have been found as the maximum phase shift is scanned from -30 to -6, with the object kept at 17.878 cm. For those values of P_{max}, three holograms were simulated for comparison purposes with the captured hologram. The comparison between the simulated diffraction rings and those captured by the camera indicates that the oscillations presented for $P_{max} = -9.87$ are closer to the experimental data. It signifies that such a phase shift would probably be the one sought after.

4.1.4 FPM phase retrieval results and comparison

The FPM configuration used for the study in this section corresponds to the final version of our microscope. Specifically, the camera used is PCO.edge, the position of the specimen holder, as measured by a ruler, gives a length of 245 mm between the object and the LED array, the position of the optical axis is

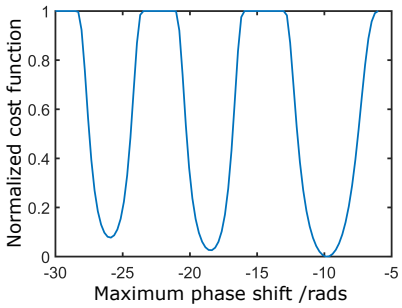

Figure 4.4: Normalized cost function obtained by scanning maximum phase shift while keeping axial position at 17.878 cm.

manually adjusted. For ongoing investigations, 20 x 20 grayscale images are captured using red illumination.

Fig. 4.5 shows phase retrieval results from FPM. The procedure has been executed patch by patch of 280 x 280 pixels each. The object has been enlarged by four times as compared to the original. With the measured magnification of 2.034 for the optical system and the camera's pixel pitch (PP) of 6.5 µm, the PP of a raw image is 3.196 µm. Consequently, the reconstructed image has a PP of 3.196/4 = 799 nm. Those dimensions are taken in the object plane. The diameter of the phase disk is 148.6 µm and the maximum phase shift is -8.3 rads (points with noncontinuous phase variation are neglected).

Phase curves obtained from the three methods (LI-DHM with G-S algorithm, LI-DHM with inverse problem approach, and FPM with G-S algorithm) are shown in Fig. 10. Good consistency between LI-DHM results may be observed. The results from both LI-DHM and FPM exhibit variations that follow Eq. (4.1) with diameter 148 µm (radius R = 74 µm). However, here, FPM appears to underestimate the maximum phase shift by 2 rads. As the sample is optically thick, this result could be produced by an irrelevant approximation of a three-dimensional response by a 2-D function $o(x, y)$. The phase extent P_{max} associated with $o(x, y)$ may be estimated by integrating lightpaths within the object. Based on the axial index profile reported by Horstmeyer et al. [78] [Fig. 4(a) therein], a value lower than the maximum phase extent could be obtained. The introduction of image formation model of Fourier ptychographic tomography would permit to test such a hypothesis. Such a model is not implemented as part of the current work, but will be discussed later in Section 4.4.

Conclusion In this study, optical phase response from a large transparent object has been investigated with LI-DHM and compared to FPM. The sample is a 146-µm glass microsphere. A G-S type phase retrieval algorithm with positive absorption constraint has been used. A parameter-based inverse problem approach has also been applied to the same captured hologram. Reliability of

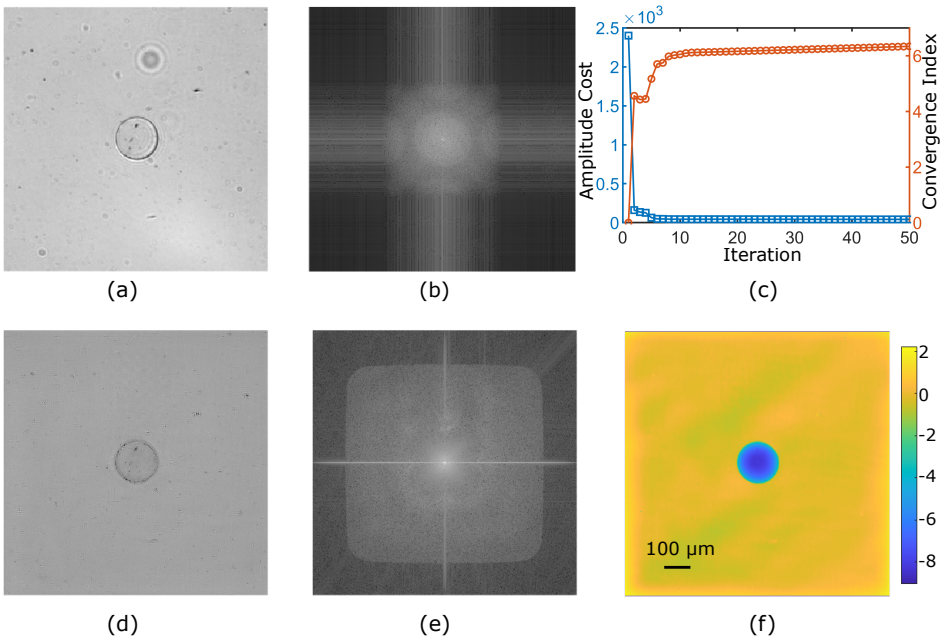

Figure 4.5: Results from FPM. (a) Image captured as the center LED is switched on. (b) Amplitude spectrum of (a). (c) AC (blue squares) and CI (red circles) as functions of iteration number. Convergence is attained when the former is minimized and the latter maximized. (d) Amplitude of reconstructed complex image. (e) Amplitude spectrum of (d) (logarithmic scale). (f) Reconstructed phase.

the G-S recovered phase distribution has been assessed through focusing (object) position and maximum value of the phase shift induced by the sample. Analysis of LI-DHM and FPM maps reveals that both instruments are capable of providing phase distributions that would be expected from a microbead, confirming their QPI capability. FPM seems to provide smaller amplitudes as for the phase extent.

We speculate that such a difference could be due to the approximation of an optically thick sample by an infinitely thin 2D model. It is crucial to introduce the 3D model of Fourier ptychography tomography in our FPM project in order to test this hypothesis. This aspect should therefore be one of the main focuses of the forthcoming research. Another possible source of this difference is the misalignments of the individual LEDs, which confirms the importance of implementing an angular misalignment correction procedure.

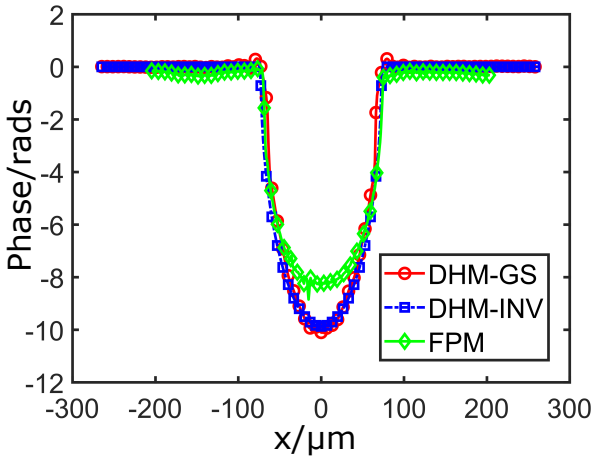

Figure 4.6: Phase curves recovered by LI-DHM and FPM. Curve with red circles is obtained by LI-DHM G-S algorithm. Curve with blue squares is phase distribution simulated according to Eqs 4.1, with diameter estimated from Fig. 4.1 and maximum phase shift provided by LI-DHM inverse problem approach. Curve with green diamonds represents phase retrieved from FPM G-S algorithm.

4.2 Polarized light microscopy

Like FPM, Mueller Matrix Microscopy (MMM) can also access some information about the phase delays experienced by light as it passes through a sample [131]. In this section, we focus on the complementarity between FPM and MMM phase delays and highlight their differences[3]. The experimental validation is focused on a histological slide of mouse mammary tissue.

4.2.1 Basics of polarization of light

As indicated in Chapter 1, light can be described by wave-like vibrations propagating as coupled electric and magnetic fields [205]. These fields are perpendicular to each other. The polarization of light describes the preferential distribution of the orientation of the oscillations of electromagnetic waves. By convention, when we refer to polarization in current work, we refer to the oscillations of the electric field.

Types of polarization Light from common sources such as the sun or an incandescent lamp is a radiation composed of multiple waves with different and random polarization states. These waves form unpolarized light, meaning

[3]Some sentences in this section are taken from our conference paper "Fourier ptychographic microscopy and Mueller matrix microscopy: differences and complementarity" [19].

that the direction of the electric field fluctuates randomly over time. The LEDs we use in our Fourier ptychographic microscope produce a partially coherent unpolarized light.

There are three main types of polarization: linear, elliptical and circular (which is a case of elliptical polarization). In linear polarization, the electric field oscillates in a single direction, see Fig. 4.7. When the orientation of the electric field rotates around the axis of propagation of the wave, it is called circular or elliptical polarization.

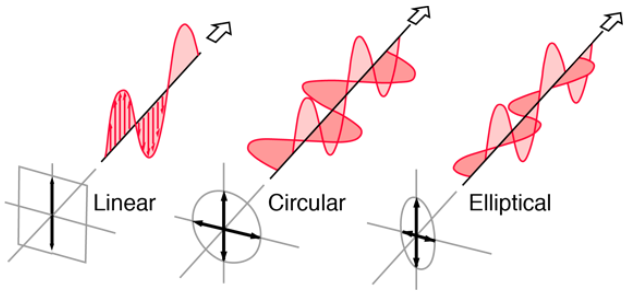

Figure 4.7: Polarization types: linear, circular and elliptical. Reprinted from [58].

Polarizers Polarized light can be obtained by passing unpolarized light through a polarizer. This projects the waves of all polarization states into a single polarization state. The orientation is defined by the axis of the polarizer.

There are several types of polarizers that fall into different categories. They can be divided according to the type of polarization they produce: linear or elliptical (mainly circular). Another possible category concerns the physical phenomena through which they act: birefringence, dichroism or reflection. In the context of this work, unless otherwise specified, when we mention polarizers, we refer to a linear dichroic polarizer.

When unpolarized light passes through an ideal linear polarizer, its intensity is halved. This is the consequence of Malus's law which gives the relation between the intensity of a linearly polarized light beam before and after its passage through a polarizer:

$$I = I_0 \cos^2 \theta, \tag{4.2}$$

where I is the initial intensity of the linearly polarized beam, I_0 is its intensity after passing through the polarizer whose axis is at the angle θ with respect to the initial polarization direction.

Waveplates Polarization of elliptical or circular type can be obtained by using a waveplate. A retarder, or a waveplate, is an element that forces one orthogonal component of the electric field to be retarded relative to another.

It is therefore characterized by two axes, slow and fast, and by the magnitude of the delay produced. The latter quantity is called retardance.

An ideal waveplate does not attenuate or deflect the beam and only produces the delay. A quarter-wave plate causes a 90 deg phase shift between the two components of the polarization state.

Anisotropic media Polarizers and waveplates could be used to reveal the optical anisotropies exhibited in certain samples and other polarization properties. The polarimetric response of a sample can be described by three main properties: birefringence, dichroism and depolarization.

Anisotropic media having different refractive indices as a function of the polarization state are said to be birefringent. These media divide an incident ray into two components that take different paths. They therefore change the state of polarization, for example from circular or linear to elliptical. Among the most common anisotropic materials are crystals and plastics under stress. In the case of biological tissues, it is mainly ordered cell structures that exhibit anisotropy [131]. These include different types of fibrous structures, actin and myosin filaments, starch condensates, collagen and elastin.

The quantity called retardance quantifies the birefringence. It measures the magnitude of the delay that the sample produces between the orthogonal components of the electric field. A birefringent material therefore behaves like a retarder, hence the name retardance.

A material is said to exhibit dichroism when it absorbs light unevenly depending on the polarization state of the light. Dichroism or diattenuation is therefore the ability of the medium to attenuate the intensity of light according to its polarization state. We call linear dichroism the attenuation of linearly polarized light.

Depolarization is the ability of the medium to depolarize the wave passing through it. A polarizer, for example, exhibits dichroism but does not depolarize the beam.

Mueller matrix The polarimetric properties of light and its interactions with the medium can be described by means of the Stokes-Muller formalism. The Stokes vector, or the Stokes parameters, is used to describe the polarization state of the light. It consists of 4 elements: $\vec{S} = (S_0, S_1, S_2, S_3)$. Those parameters can be expressed as a function of the total intensity of the beam ($S_0 = I$), its degree of polarization and parameters related to the shape of the polarization ellipse [184]. Thus, the light arriving at the sample can be described by a Stocks vector $\vec{S}_{in}$. The sample changes its state, the outgoing light is designated by $\vec{S}_{out}$: $\vec{S}_{out} = M\vec{S}_{in}$, see Fig. 4.8.

As for the Mueller matrix M, it allows a complete characterization of the polarimetric properties of the medium, in the absence of non-linear effects [153]. It is a 4x4 real matrix. At least 16 intensity measurements are required to determine a Mueller matrix at each point of a sample.

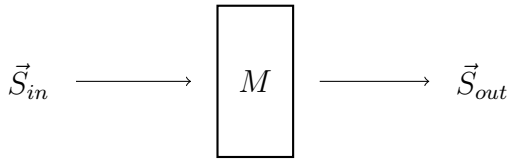

Figure 4.8: Stocks-Mueller formalism.

A Mueller matrix M can be further interpreted physically using a polar decomposition proposed by Lu and Chipman as follows [118]: $M = M_\delta M_R M_D$, where M_δ is a diattenuator, M_R is a retarder and M_D is a depolarizer. In such a context, a sample would be described by a combination of these matrices. Retardance can be calculated from the retarder element of the Mueller matrix M_R [216]. Moreover, linear retardance and circular retardance can also be deduced from M_R.

4.2.2 Applications of polarization microscopy

Polarization microscopy has been used in many areas, including chemistry, geology, materials science and, of course, biology and medicine [131]. First Mueller matrix imaging techniques were developed in the 1990s. Its main principle of operation is based on the interaction of polarized light with the bonds of the ordered molecules in a direction-sensitive manner [131].

In the biomedical context, many different applications of polarimetric imaging have been considered. For example, a reflection polarization microscope is often used to detect abnormalities in hair structure to diagnose trichothiodystrophy [207]. An low-cost polarized transmission microscope, based on a cell phone, has recently been proposed to diagnose malaria [158]. It has also been shown that 3D polarized light imaging is capable of performing structural reconstructions of the entire human brain at the microscopic scale [7].

For the present study, we were particularly interested in the birefringence of biological samples obtained with a Mueller matrix microscope. However, other properties, for example the degree of depolarization, may also be useful in biomedical imaging [208].

4.2.3 Mueller matrix microscope

MMM retrieve the polarization properties of a sample. It does this by a complete measurement of the Mueller matrix. Thus, it has access to the changes in polarimetric state that occur between the incidence of the light beam and its appearance after the passage of the sample. The main operating principle of the polarizing microscope is the interaction of the polarized light with the bonds of ordered molecules in a direction sensitive manner [131].

We used a spectral Mueller matrix microscope built by members of the TRIO team. It produces polarimetric images at several wavelengths. It

should be noted that over the last few years, the TRIO team has worked on three polarimetric imaging projects: Polaris, Dermapol and Mueller microscopy. Polaris is one of the first polarimetric imaging devices developed by the TRIO team to analyze biological samples, especially cancerous tissues [96]. The Dermapol project started in 2017 [208]. Broadly speaking, it is a compacted and improved version of Polaris. It is designed to detect malignancy of suspicious dermatological lesions. The operating principle of the built Mueller matrix microscope is close to that of the Polaris imager. The two main differences are: the scale is microscopic rather than macroscopic; and the illumination mode is transmission rather than reflection.

Presentation and components

The Mueller microscope used is depicted on Fig. 4.9. Its components and the imaging principle can be summarized as follows (in the case of a single pair of generated/analyzed polarization states for a single wavelength).

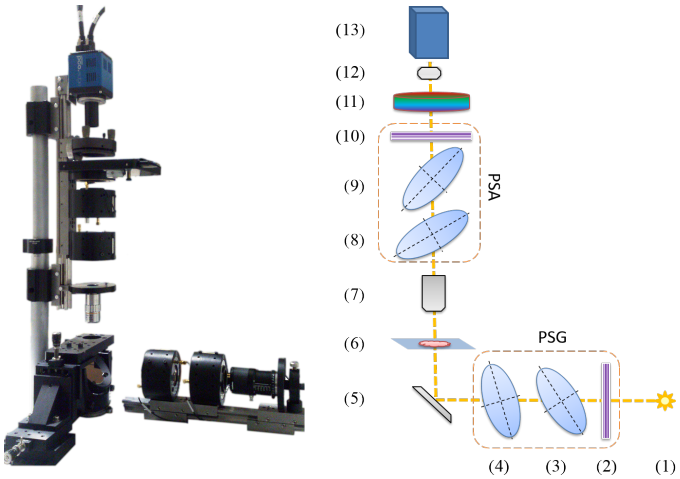

(a) Photograph (b) Scheme (see text)

Figure 4.9: Mueller Matrix Microscope.

A collimated source (1) emits an unpolarized white light. The beam passes through a polarization state generator (PSG) consisting of a linear polarizer (2) and two liquid crystal variable retarders (LCVR) (3,4). By applying the appropriate amount of voltage to these 2 LCVRs, we are able to generate any polarization state on the Poincaré sphere. An infinity corrected 10x Mitutoyo objective (7) is then used to collect the response of the specimen. The light then enters a polarization state analyzer (PSA). It consists, just like the PSG, of two LCVRs (8,9) and a linear polarizer (10). A motorized optical filter wheel (11) selects the appropriate band to study (500 nm, 550 nm, 600 nm, 650 nm, 700 nm). Finally, an achromatic 200 mm lens tube (12) focuses the image onto the monochrome sCMOS camera pco.edge 4.2 (13).

Given a well-chosen distribution of 4 PSA and 4 PSG states on the Poincaré sphere[4], 16 images are sufficient to extract the Mueller matrix M of the sample. Those 16 measurements can be put in the form of a 4x4 matrix I_N (at each point of the sample). The following relationship is consequently established :

$$I_N = AMW, \tag{4.3}$$

where A is a matrix containing 4 incoming Stocks vectors, it describes the states of the light generated by the PSG. The W matrix consists of 4 Stocks vectors equivalent to the PSA states.

Reconstruction and calibration

Theoretically, to obtain the Mueller matrix M of the sample, one can perform a simple inversion and multiplication of the matrices :

$$M = A^{-1} I_N W^{-1}. \tag{4.4}$$

However, two conditions must be satisfied in order to perform this operation.

First, the matrices A and W should be well conditioned. This requirement is ensured by a careful selection of PSG and PSA configurations for each acquisition. Indeed, the optimal conditioning is obtained when the 4 generated states and the 4 analyzed states are both represented as the vertices of a tetrahedron on the Poincaré sphere. This essentially corresponds to the states of polarization that are most different from each other. In order to obtain these states, we mechanically fix the appropriate axes of the LCVRs (45° for elements 3 and 9 of the Fig. 4.9(b), and 22.5° for elements 4 and 8) and apply the required amount of voltage for each acquisition. The procedure used for the determination of voltages for our microscope is similar to that described in Mark Karnokin's thesis on the Polaris instrument [96].

Secondly, the A and W matrices must be known with a high degree of accuracy. The characterization of the instrument must therefore be carried out. A procedure called Eigenvalues Calibration Method (ECM) [38] is applied for this purpose. To this end, 4 known calibration targets are used: the empty space (no sample), a linear polariser with the axis oriented at 0°, a polariser at 90° and a waveplate with the axis at 30°. The matrices A and W are determined from four measurements made on these reference samples. However, the procedure is not straightforward because it is difficult to place the calibration targets perfectly on the sample holder. Fortunately, ECM circumvents this problem by determining not only the polarimetric parameters of the targets, but also their orientations. Details of the algorithm can be found in Mark Karnokin's thesis. Note that in the case of Polaris, a mirror was used as the first calibration target instead of empty space.

[4]The Poincaré sphere, is a graphical representation of the polarization of light, where three Stokes parameters (S_1, S_2, S_3) are plotted in a 3D unitary sphere surface.

The Mueller matrix is then decomposed into dichroism, retardance and depolarization featured by the studied medium.

4.3 Fourier Ptychographic and Mueller Matrix Microscopes: comparison

This section focuses mainly on the investigation of the complementarity between the optical phase and the polarimetric retardance. These physical quantities are retrieved by two constructed devices, namely the Fourier ptychographic microscope and the Mueller matrix microscope. The observations on the histological slides are presented for experimental validation.

As already mentioned, QPI transforms the optical path differences undergone by electromagnetic waves exiting a medium into a reconstructed image of these phase shifts in degrees. This quantity in turn describes the product of the refractive index of the medium and its thickness. This can provide an important piece of information for biomedical analysis [39].

Both QPI and polarimetric imaging techniques have many applications in biomedical tissue analysis; combining the two could yield even richer information. The ability of our ptychographic Fourier microscope to retrieve quantitative phase images has been successfully demonstrated in Section 4.1.

Although reports comparing and even combining QPI techniques with polarimetric methods can be found in the literature, to the best of our knowledge, this work is the first to assess the complementarity of Fourier ptychographic and Mueller matrix microscopes.

In the view of the expected complementarity between quantitative phase and polarimetric information, a number of research efforts have been made to explore the possibility of combining the two. Many of these have focused on a determination of a Jones matrix, which is another polarimetric formalism. Various multimodal devices, mainly relying on holographic microscopy to achieve QPI capabilities, have been proposed [72, 101, 217, 224]. Other relevant instruments include, for example, a device based on a shearing interferometer to measure phase images enriched with birefringence information [4] or a quantitative polarization interference microscope [18].

There are also studies that combine polarimetric imaging with conventional ptychography, a technique closely related [69] to FPM [6, 18, 52, 234]. However, so far, no device has yet been proposed to couple Fourier ptychography with Mueller matrix measurements. In addition, no investigation focuses on the study of birefringent samples by FPM or the potential effects of anisotropy on phase reconstruction. Therefore, it may be worthwhile to present evidence of the complementarity of these two techniques in the context of histological imaging.

We note that while retardance is the focus of the polarization aspect of this study, other properties, such as the degree of depolarization, may also be

useful in biomedical imaging [208]. It should also be noted that other research fields could benefit from the fusion of QPI and polarimetry. For example, one of the current projects in collaboration with the MaCEPV (Materials for electronic and photovoltaic devices) team at the ICube laboratory aims to use constructed microscopes to characterize photovoltaic elements.

4.3.1 Complementarity

In order to demonstrate the complementarity of the two techniques, we use a stained histological slide of mouse breast tissue (6 µm thick). Despite staining with H&E (hematoxylin and eosin), the sample reveals low contrast in visible light. This is the same sample that we used in the previous chapter (Fig. 3.6).

The first configuration of the FPM device is used to produce the images from the current section. In other words, the camera is the Prosilica GE2040 and the optical axis is not mechanically aligned. Under sequential red light illumination, a total of 400 images have been recorded.

The result of the FPM procedure is shown in Fig. 4.10 (b, c). The top row represents the entire FOV, the bottom row shows a selected region of interest (the size of raw image (a) is 120 x 120 pixels). Patches of 100 x 100 pixels were used for independent reconstructions which were then stitched together. The initial pixel size in the sample plane is 3.6 µm. The reconstructed image is four times larger than the raw images so as to include all recovered frequencies. This gives a pixel size of 720 nm in the same plane. The size of the area under observation is 7.4 mm x 7.4 mm.

Fig. 4.10 (d) shows the same area captured with a 40x phase contrast microscope. Both Fourier ptychography and phase contrast modalities produce images with sharp edges; the layering and the thickness of the internal structures are made visible. However, the image obtained by the phase contrast microscope is not quantitative.

Numerous polarimetric parameters can be computed from the Mueller matrix of a specimen. However, we are only interested in phase retardation (birefringence) for the present study.

Fig. 4.11 represents 4 different parameters recovered from the same sample in the red band ($\lambda = 630$ nm for the FPM and $\lambda = 650$ nm for the MMM). The intensity image recovered by the FPM (a) is what can be observed with a monochromatic conventional microscope. The intensity (a) shows low contrast. On the other hand, the structures within the purple and cyan ovals can be easily distinguished from the surroundings for MMM (b, c) and FPM (d) phase images. These structures correspond to collagen and produce equal amounts of linear retardance (b). At the same time, some of these fibres, whose alignment is different, are contrasted by opposite values on the circular retardance image (c), see the purple oval and the cyan oval. The quantitative phase obtained by FPM (d) highlights all the structures present in the specimen. This is manifested by roughly equal values within all ovals.

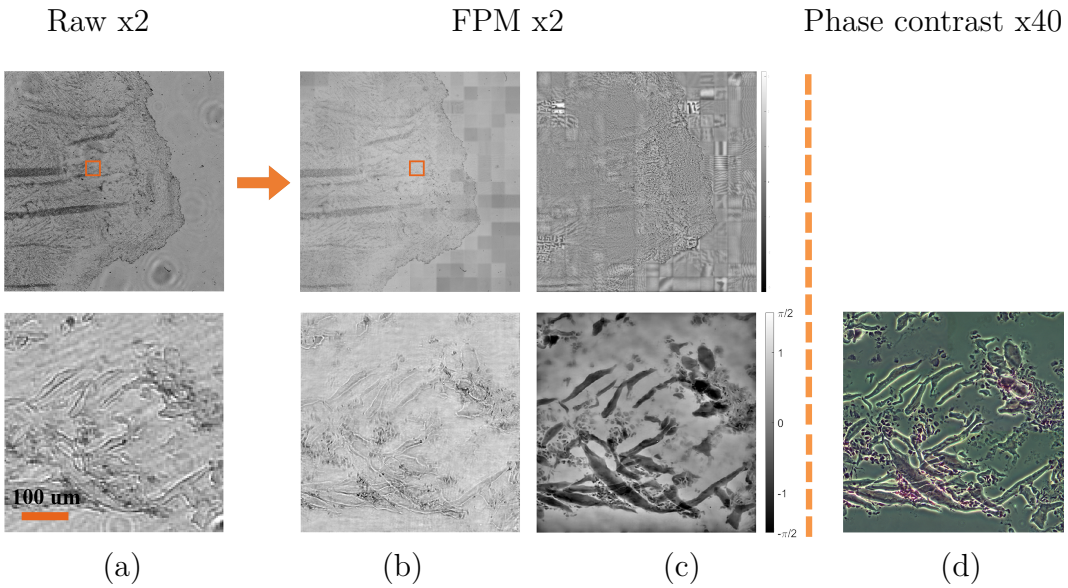

Figure 4.10: FPM reconstruction results. Top row – the entire FOV, bottom row – region of interest of 0.43 mm in the object plane. (a) Raw intensity image corresponding to the central LED. (b) Reconstructed high resolution intensity image. (c) Reconstituted quantitative phase. (d) Image obtained by a 40x phase contrast microscope.

We also note that the images in the Fig. 4.11 have almost equivalent resolution. However, the FOV of the Fourier ptychographic microscope is about 5 times higher than the FOV of the Mueller matrix microscope.

4.3.2 Discussion

We have demonstrated the complementarity of a Fourier ptychographic microscope and a Mueller matrix microscope. A mouse breast tissue slide was used for experimental validation.

We have observed that the FPM phase highlights thicknesses and shapes of the structures. These are the rather geometric properties of the sample. The polarimetric retardance represents the birefringence of the medium. It allows to improve differentiation between different types of tissues. This in turn gives greater access to the cellular composition of the sample. In addition, the circular retardance can also reveal the alignment of tissue fibres.

Visual validation confirmed the contribution of information between the two modalities. A quantitative assessment is planned for future work. In addition, a more in-depth study involving a simpler birefringent sample with perfectly identified properties would also be of great interest.

Our two instruments have been constructed with almost the same spatial resolution. This allows for a meaningful comparative analysis. It has yet to be

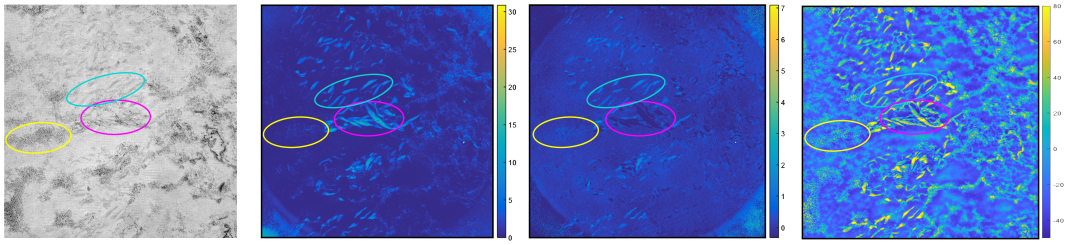

(a) (b) (c) (d)

Figure 4.11: Mouse mammary tissue studied with different modalities. (a) Intensity, $\lambda = 630$ nm; (b) Linear retardance, $\lambda = 650$ nm; (c) Circular retardance, $\lambda = 650$ nm; (d) Quantitative phase, $\lambda = 630$ nm. Scales are in degrees.

demonstrated whether an enrichment of information would still be observed with higher magnification. Furthermore, although the current discussion has focused on a single wavelength, multispectral analysis is feasible with both instruments. The extent of complementarity would be investigated for a wider range of wavelengths.

4.4 Extensions and improvements

Recent advances in FPM have shown the potential not only to improve the quality of reconstruction, but also to extend the classical configuration to other imaging modalities. Due to the limited duration of the current PhD thesis, it was not possible to study all possible improvements. Nevertheless, we discuss here the most promising ones and indicate those that are prioritized for implementation given our configuration.

4.4.1 3D Fourier Ptychography

As indicated in our QPI study with a microsphere, it is important to consider the thickness of the sample in order to obtain a reliable reconstruction. Fortunately, the collected data already contains 3D information about the sample [199]. This information is encoded in the redundancy of the overlapping spectra and can be used to perform 3D Fourier ptychographic tomography.

Several different models and methods have been proposed in the literature to achieve 3D reconstruction. On of the first work in this direction proposed to divide the sample into two slices, which constituted the proof of concept for future work on 3D FPM [113]. As an extension of this idea, a so-called "multi-slice" approach has been proposed [199, 235]. The development of this method came as no surprise, since it is a well-known technique in conventional ptychography [122], the real-space counterpart of the FPM. The main idea is to represent a thick sample as a stack of multiple infinitely thin samples with an empty space between them. The imaging model is then modified to take into account the interaction of light propagation through these slices. The reconstruction algorithm is also modified accordingly.

Another method, called "Fourier ptychographic tomography" uses a 3D model based on the first Born approximation for mainly transparent samples. Unlike a multi-slice approach, such a model also takes into account backscattered light and does not directly specify the number of slices [78]. Recently, Chao Zuo et al. demonstrated an even more sophisticated technique called "Fourier ptychographic diffraction tomography" [253]. Among other features, their imaging model uses a more accurate Rytov approximation.

It is also possible to perform a 3D reconstruction in FPM by modifying the original configuration. The aperture scanning FPM [137] or coupling with light field microscopy [107, 112, 194] can be cited as an example. As part of our project, we suggest that a multi-slice model be implemented first because of its simplicity.

4.4.2 Other modalities

It has been successfully demonstrated that a large number of other imaging modalities can be coupled to FPM. Perhaps the easiest extension to implement

would be the dark field microscopy [200].

As already mentioned, multi-channel colour imaging can also be achieved [91]. In its simplest from, red, green and blue channel can be captured and reconstructed separately, Fig. 4.12. However, information from all three channels can also be captured at the same time and broken down during the reconstruction process [48, 185]. A color correction strategy could improve the quality of the separation [91, 215].

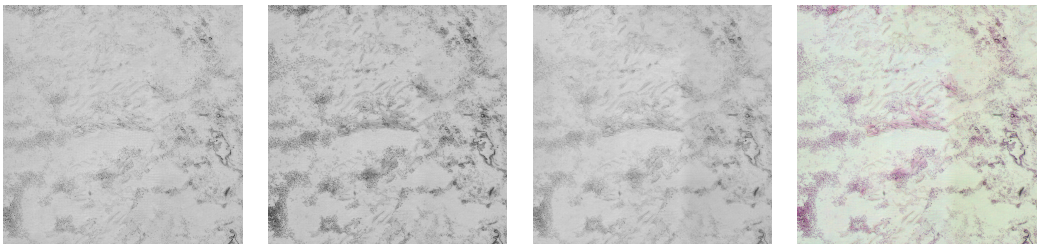

(a) (b) (c) (d)

Figure 4.12: Reconstruction of a region of a mouse breast tissue sample. The same sample is presented in the results of the previous chapter. (a) Red channel. (b) Green channel. (c) Blue channel. (d) Assembled colour image, the weights of the channels are normalized.

The FPM device can be designed to operate in reflective mode (Epi-Illuminated Fourier Ptychography) instead of conventional transmission [144, 145].

It has been shown that FPM can also work with wavelengths of the spectrum outside of visible light. For example, telecommunication wavelengths [3], near-infrared [170] and X-rays [176, 209] imaging have been successfully tested.

Fluorescence imaging, an important modality of biomedical research, can also be incorporated into Fourier ptychography [35, 47]. Fluorescence being an incoherent imaging technique, the original method must therefore be modified accordingly. This is usually done by introducing non-uniform lighting patterns or by coupling with structured illumination microscopy [46, 69].

The principles of Fourier ptychography can also be applied to macroscopic imaging of objects up to 200 meters away [76, 223].

While our research has focused on a small NA objective, FPM can also work with high numerical aperture lenses [141], oil-immersion [190], or no lens at all [254].

4.4.3 Better illumination design

A rectangular LED array is far from being an optimum lighting configuration. Indeed, it is prone to the problem of raster grid artifacts [243] (not exposed in this thesis). More importantly, it does not take into account the non-uniformity of illumination from different angles, outlined in Section 3.2.1. Several lighting configurations have been proposed in the literature to circumvent these problems. Most of them share similar hemisphere geometry

[5, 28, 147, 155, 156, 157]. We have built our own lighting unit that we plan to use for our future work, Fig. 4.13. Among its features, the individual LEDs all point to the center of a sample and the brightness of elements is much higher. In addition, it may be advantageous to use denser sampling for bright field LEDs than for dark field LEDs [68]. This is due to the fact that typical histological samples have most of the signal strength in the low frequencies. According to some reports, a new design of the illuminator can significantly reduce the artifacts encountered.

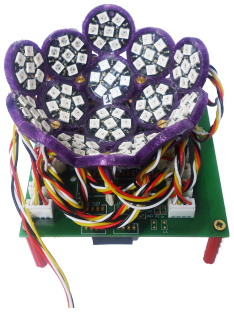

Figure 4.13: A dome-shaped LED array designed by TRIO team members.

4.4.4 Reducing acquisition time

One of the main drawbacks of our FPM device is a long acquisition and processing time. Fortunately, it has been shown that a ptychographic microscope can be configured to allow high-speed, and even real-time imaging [197, 198, 250].

One of the main adjustments proposed to allow for this acceleration concerns illumination changes [198]. Specifically, several LEDs must be lit simultaneously, so that each captured image contains several regions in Fourier space. This approach is referred to as multiplexed illumination [196]. A number of researches have focused on the search for optimal illumination patterns and corresponding reconstruction methods [31, 97, 188, 189, 202]. Likewise, multicolor LEDs could be lit simultaneously to enable a so-called wavelength multiplexing scheme [185, 250].

In addition, it has been shown that the number of acquisitions can be reduced with almost no loss of quality by selective lighting [146] and/or by changing the sampling configuration of the LED array [243]. In fact, only LEDs corresponding to the most informative parts of the spectrum could be used in this case [13, 24, 133, 238, 248].

In any case, it is important to increase the brightness of LEDs and ensure that the camera has a high dynamic range to achieve high-speed imaging.

Another way is to modify more radically the classical configuration, for example by introducing a lens array [108], a multi-aperture paradigm [103] or a diffractive beam splitting [73].

4.4.5 Other improvements

As mentioned in Section 3.2.3, the Nyquist criterion is violated for blue LEDs due to our system configurations. In addition, the analysis of the spectra of the images captured in red and green light also showed a slight aliasing problem, despite theoretical predictions. This problem can be solved by a so-called "upsampled" strategy [187]. The implementation of this approach is supposed to improve the reconstruction quality of our instrument, especially for blue light.

Several reports have shown the increase in reconstruction quality due to the application of high dynamic range (HDR) imaging [13, 243, 244]. In general, the signal-to-noise ratio can be improved by applying HDR techniques. This is particularly pronounced in the case of FPM datasets, where the captured images have a remarkably different dynamic range. As can be seen in Fig. 3.6(c), images featuring a transition zone are not captured in optimal conditions: to avoid overexposing the bright field region, the dark field region must be underexposed. Combining images captured with three different exposure times would solve this problem.

The FPM can be used to image unstained living cells. Since several independent images are captured sequentially, motion correction may be necessary. The compensation procedures have been proposed in the literature and can be implemented with our configuration, if necessary [15, 119].

4.5 Conclusion

In conclusion, we have demonstrated a potential for multi-modal imaging with our constructed Fourier Ptychographic microscope.

In particular, we conducted a study confirming the QPI capabilities of the device, in addition to the super resolution capabilities demonstrated in the previous chapter. At the same time, thanks to the comparison with digital holographic microscopy, we highlighted the need to implement a 3D version of the imaging model. The reconstruction algorithms must be modified accordingly. Given the amount of overlap provided by our configuration and the literature review, no hardware modifications are required to obtain 3D capabilities with our microscope.

Pursuing the idea of multimodal imaging, we used a Mueller matrix microscope built in the team. We conducted a comparative study of the constructed Fourier ptychographic microscope with the polarimetric microscope. The results show the complementarity of the two techniques. Experimental validation is done on biological tissues. The motivation to merge the two modalities being confirmed, this will be one of the next steps in our research. Preliminary studies have been carried out to equip the built FPM device with Stocks polarimetric imaging capabilities. This investigation is briefly presented in the next chapter when the perspectives of the current thesis are discussed. It

constitutes the basis for a major future work of the TRIO team.

Finally, we presented additional possible extensions and improvements of the constructed Fourier ptychographic microscope. Among the first upgrades to be integrated, there should be a transition to a dome-shaped LED array manufactured by TRIO team members. The 3D model and the "upsampled" strategy are of equal importance. This complements the aspects already indicated in the previous chapter and provides guidance for future work.

Chapter 5

Conclusion and Future Work

5.1 General Conclusion

5.1.1 Overview

During this thesis work, we focused on the development of a microscope system offering a large amount of relevant information retrieved at an affordable cost. In particular, we built our version of the Fourier ptychographic microscope, a recent computational imaging technique. We then used another optical modality, the Mueller matrix microscope, in order to highlight the complementary nature of the information obtained by two devices.

This work is the first in the field of computational microscopy carried out in the research groups that hosted me. On the one hand, the IMAGeS team has expertise in inverse problems and image processing, and on the other hand, the TRIO team is skilled in the construction of optical devices and polarimetric imaging. This thesis, being at the intersection of the two fields, opens a new research topic for both teams.

The implementation of the Fourier ptychographic microscope required not only the construction of the instrument from scratch, but also the implementation of the methodological workflow for its calibration, data pre-processing and reconstruction. The Mueller polarimetric matrix microscope, on the other hand, is an almost straightforward extension of the Polaris macroscopic imaging system to the microscopic one. While the author was involved in all stages of the development of the FPM device, the construction of the second microscope was mainly carried out by other members of the TRIO team. As a result, this document places more emphasis on the first system.

A fully functional system has been developed and its capabilities have been demonstrated. Its complementarity with a Mueller matrix microscope was revealed, which validates the interest of their prospective fusion. In addition, although it has not been possible to carry out all the improvements and research we would have liked, we provide clear guidelines for future work. Some of this work has already begun within the teams.

5.1.2 Contributions

The contributions of this thesis concern both the experimental developments related to the deployment of the devices and the developments of different parts of the data processing chain.

The Chapter 1 served as the theoretical basis for this project. Since the author had no background in optics, the completion of the first chapter was important for her understanding of the principles and limitations of light microscopy.

The main operational principle of the FPM technique is then outlined and detailed in Chapter 2. One of the main premises of the method is to solve a so-called "phase problem". In order to obtain a deeper and more intuitive understanding of the topic, a 1d variant of this problem was introduced and analyzed. The imaging model of the FPM is then explained in detail. The same chapter continues by examining the numerical aspects of the problem and the methods for solving it. Thus, popular reconstruction procedures were broken down into different building blocks that could be combined with each other. Many of these elements were implemented and tested. This made it possible to compare the algorithms and to justify an optimal one for the constructed microscope. Specifically, the PIE method (alternating projections) with an adaptive step size strategy was retained.

Chapter 3 describes all the steps performed for the realization of our Fourier ptychographic microscope. We first presented the hardware specifications, the instrument design and its experimental implementation. An important part of this chapter is devoted to various procedures for characterizing and calibrating the instrument. Indeed, in the course of this work, we were able to appreciate how crucial the calibration step is for the proper functioning of computational imaging techniques. Among the procedures proposed are the calibration of the optical axes, the characterization of the LED matrix, the determination of the numerical aperture and the introduction of a correction coefficient for the calculation of segments centers. We also conducted a study on the noise statistics of the available cameras. The results of this survey confirmed the chosen optimization procedure, provided the correct information for methods validation and supported the choice of the optimal camera. Subsequently, several methods to address the experimental realities of our microscope were proposed and validated on real data. As part of these developments, we have implemented data pre-processing methods, an essential step in obtaining clean reconstructed images. Then, aberration correction, a well-documented procedure in FPM, was introduced into the algorithms and the importance of defocus correction for our device was emphasized. We then discussed procedures for correcting angular misalignment, a major source of errors in our configuration. We proposed to evaluate the LEDs angles by carefully estimating the global system parameters. However, as we realized later, a correction of individual angles may also be necessary. Work on a suitable method to solve this problem has started in the team. We have also adopted a method to compensate for the

difference in brightness of individual LEDs. Then, we demonstrated the importance of taking into account the partial coherence of our illumination unit. Afterwards, we provided the methods we have adapted for the final stages of reconstruction, i.e. phase unwrapping and segments stitching techniques. Finally, we completed this chapter by transforming the identified errors into realistic data simulation procedures. This last step is important for the correct validation of the procedures developed for our instrument.

Chapter 4 presents the second device involved, the polarimetric Mueller matrix microscope. It also explains the optical modalities implemented by the devices built during this thesis and presents comparative studies. Indeed, while Chapter 3 demonstrated the super-resolution capability of the Fourier ptychographic microscope, the last chapter evaluates its quantitative imaging modality. For this purpose, we have studied a sample of great optical thickness, which we have manufactured ourselves. Importantly, we compared the results obtained with another optical modality, namely lensless inline digital holographic microscopy. This research led to a publication in a peer-reviewed journal. It also revealed the importance of extending a conventional 2D imaging model to its 3D version. Although this extension was not foreseen at the beginning of this thesis, we speculate that it could be an important step towards obtaining correct quantitative phase values. Finally, the Mueller matrix microscope was installed and its operating principle explained. We then experimentally validated the complementarity of the information extracted by FPM and MMM. From an application point of view, we made sure to show the relevance of this research on biological samples. This part of the work was the subject of an international communication with a published act. In addition, improvements to the FPM and its extension to other modalities are discussed.

Overall, we find that a wide range of aspects have been covered, particularly in the case of FPM. This brought a new research topic to the teams and set directions for future work on the project.

5.1.3 Authors contributions

Several people have contributed to the current work.

Jean Dillinger helped me enormously all along this thesis with the experimental part of it. He designed the scheme of the mechanical elements of the Fourier ptychographic microscope. He also programmed its LabView image acquisition programme. In addition, he was the main contributor to the construction and calibration of the Mueller matrix microscope.

Mark Torzanski was the one who led the manufacturing process for the extension tubes, he also helped me with the irradiance measurements of the LED array. Cemal Draman programmed the LED array and fabricated the dome of LEDs.

Yoshitate Takakura and Hongyu Li led the Lensless digital online holo-

graphic microscope part of this study. Yoshitate Takakura provided additional mechanical elements to reinforce the first version of the FPM device. He also contributed to the mechanical alignment procedure of its optical axis. In addition, he helped me with valuable discussions on the experimental results. He is also working on the spectral analysis procedure for angle estimation mentioned in this study (Fig. 3.37).

Both Jihad Zallat and Christian Heirich, as my scientific advisor, have greatly participated in this study. Their contributions on the general direction of this project were particularly valuable.

5.2 Future Work

This work opens up possibilities for future research at different levels. These include prospects related to the improvement of the FPM device, the development of a new measurement system that would combine Fourier ptychography and polarimetric imaging, as well as opportunities in terms of applications.

Improvements to the FPM device Although our Fourier ptychographic instrument is functional, some artifacts still remain. Getting rid of them should be one of the first short-term objectives of the current project. As indicated throughout this document, there are many procedures that could be implemented to potentially improve the quality of reconstruction. This concerns both hardware and software. Here we summarise the most promising ones according to our assessment.

First of all, the development of the method for estimating individual angles must be continued and applied to the reconstruction. Next, we propose to implement the 3D version of FPM. This is useful not only for the volumetric reconstruction per se, but also to diminish the 2D reconstruction artifacts by correcting multiple scattering effects. We also expect that addressing the effects of partial illumination coherence could produce cleaner results. The development of such a technique and the provision of evidence of its effectiveness would be a valuable research outcome.

As far as hardware improvements are concerned, a new version of the microscope should incorporate the manufactured dome of LEDs. Note that this also includes the development of a routine for at least a rough estimate of the positions of the new LEDs.

In less urgent terms, the reconstruction algorithms can be further improved and completed. Some of the promising avenues are described in Chapter 2. For example, adding a regularisation to the optimization procedure or implementing a sequential version of the global algorithms could be worthwhile. In addition, even if methods based on convex relaxation are not practical because of their run time, it is still desirable to implement one for comparison purposes. Also, as we have shown, the removal of offset background noise is an important step. However, some details of our procedure could still be improved. It

might also be interesting to implement a method of noise suppression during reconstruction in order to compare the resulting offsets. In addition to the points indicated above, it would be interesting, from a research point of view, to examine the issue of calculating segment centres. Indeed, we had to introduce a correction coefficient because of the artifacts observed for segments far from the pixel on the optical axis. At the same time, our method lacks a solid theoretical basis. Revealing the exact nature of this phenomenon could provide valuable publication material.

Fourier ptychographic and polarimetric imaging system We presented evidence of the complementarity of Fourier ptychographic microscopy with polarimetric microscopy. The next major milestone is the investigation of the possibility of coupling these optical modalities into a single device. Bibliographical research has shown that this has never been done.

Such an imaging system deserves in-depth theoretical and experimental research before it can be proposed, even as a prototype. Nevertheless, we present here our first drafts for future work in this direction. We propose to use Stokes imagery to give polarimetric capabilities to our FPM device. As its name suggests, Stokes imaging is capable of recovering a Stokes vector of the light beam exiting the sample. As in the case of Mueller matrix determination, the Stokes vector is recovered from a set of intensity measurements.

Stokes imaging requires the insertion of a polarization state analyser (PSA) between the sample and the observation head. Fortunately, the long working distance of the 2x objective chosen for our FPM instrument allows such an insertion, see Figure 5.1. Unlike the compound PSA used in our Mueller matrix microscope, this prototype uses a simple thin waveplate with controllable orientation of the axis. The light arriving at the sample must be linearly polarised, so a polariser has to be fixed underneath the sample holder platform. The diagram of this configuration is shown in the Figure 5.1(a).

We suggest that the analysis focuses on the same microsphere sample as presented for our QPI study. Indeed, this allows the results to be compared with theoretical calculations of the microsphere response in polarisation. Incidentally, the cleanest possible reconstruction is particularly important for this fusion research. Indeed, this study should ensure that the polarimetric response is unambiguously identified from any possible reconstruction artifacts.

Other perspectives and applications Other instrumental perspectives for this study include the use of higher magnification objectives for both FPM and MMM devices. Consideration should also be given to moving towards a more practical FPM for actual clinical or industrial use. Indeed, as discussed in Chapter 4, both acquisition and reconstruction time can be considerably reduced. The LED multiplexing should be the first strategy to be applied in this respect. As a related project, the FPM can also be used to improve the resolution of another optical modality available in the TRIO team, light field

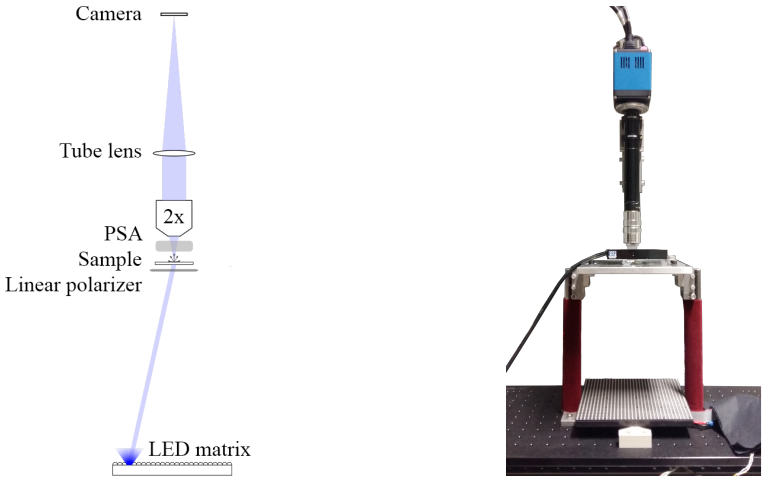

(a) (b)

Figure 5.1: TA preliminary prototype proposed for the fusion of FPM and polarimetric imaging. (a) The imaging diagram. (b) The photo.

microscopy.

Finally, a whole range of applications, from biomedical imaging to materials science, remains to be explored. These may include, for example, tissue identification and labeling and the analysis of reconstructed scenes.

Appendix A

Additional FPM reconstruction results

In the following we include some of the reconstruction results obtained with our FPM device. The samples are :

- Unstained human kidney tissue. Fig. A.1 demonstrates the ability of the microscope to retrieve information from unstained biological samples.
- Stained human kidney tissue. Fig. A.2 demonstrates the ability of the microscope to obtain super-resolution for biological samples where the information is concentrated in the amplitude part, rather than in the phase part.
- Minor staining of mouse kidney tissue. Fig. A.3 demonstrates the contribution of phase information in some samples despite the presence of dye.
- Laser grating. Fig. A.4 confirms the accuracy of the complex image reconstructed by correctly identifying the word "NanOptron" decoded in the Fourier transform of the sample.
- 1951 USAF resolution test chart. Fig. A.5 features a reconstruction of a standard microscope resolution test target.
- Sector Star Target. Fig. A.6 features another common resolution test target.

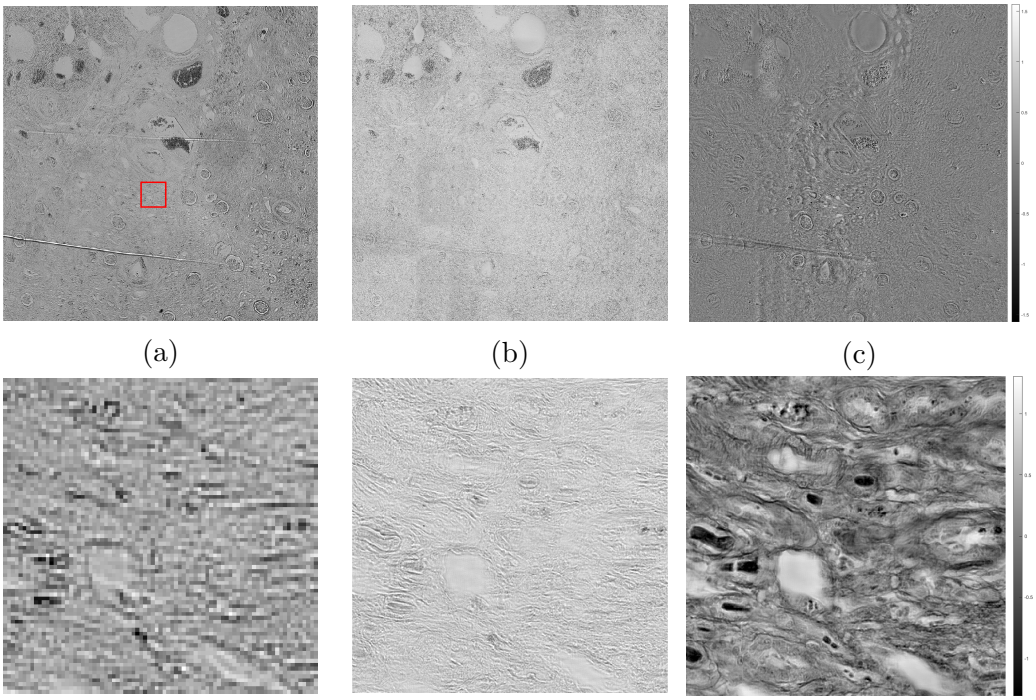

Figure A.1: Human kidney tissue, unstained. Illumination with green light, 20x20 LEDs used. The size of the raw segment is 1020 x 1020 pixels, which corresponds to 3.7 mm x 3.7 mm at the object plane. The magnified region is 80 x 80 pixels, the corresponding reconstructed region is 400 x 400 pixels. (a,d) The amplitude of a low-resolution bright field segment. (b,e) The reconstructed amplitude. (c,f) The reconstructed phase. (d-f) Zoom on the area indicated by the red square in image (a).

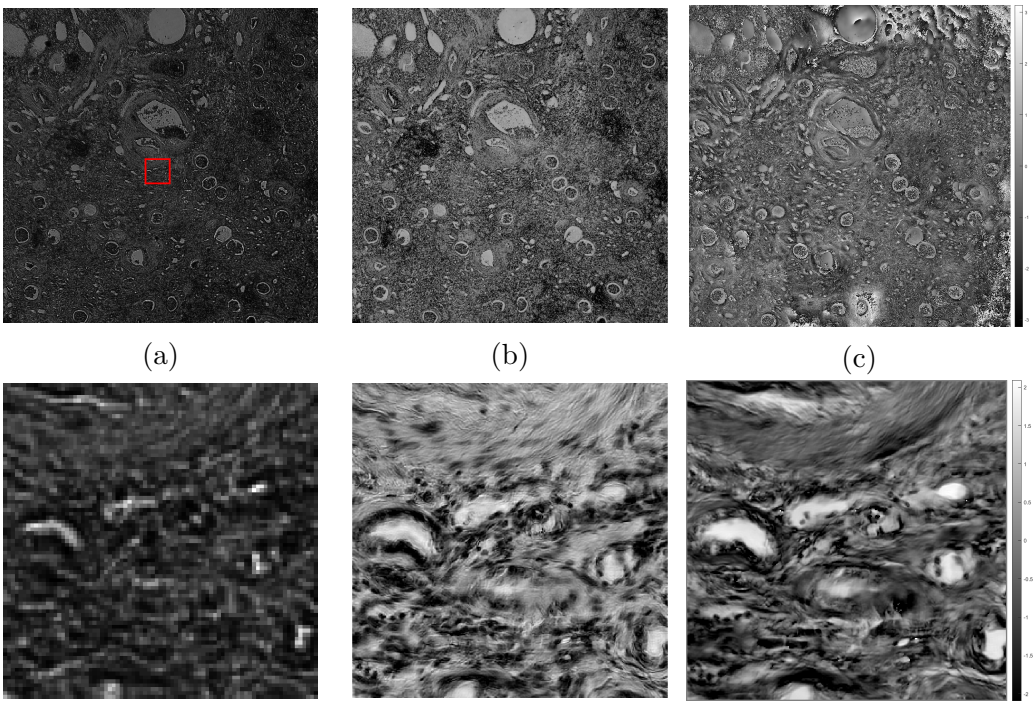

Figure A.2: Human kidney tissue, pink coloring. Illumination with red light, 16x16 LEDs used. The acquisition is performed with the focusing distance adjusted to blue light, which resulted in a high defocusing coefficient value $z = -116$. The size of the raw segment is 1020 x 1020 pixels, which corresponds to 3.7 mm x 3.7 mm at the object plane. The magnified region is 80 x 80 pixels, the corresponding reconstructed region is 280 x 280 pixels. (a,d) The amplitude of a low-resolution bright field segment. (b,e) The reconstructed amplitude. (c,f) The reconstructed phase. (d-f) Zoom on the area indicated by the red square in image (a).

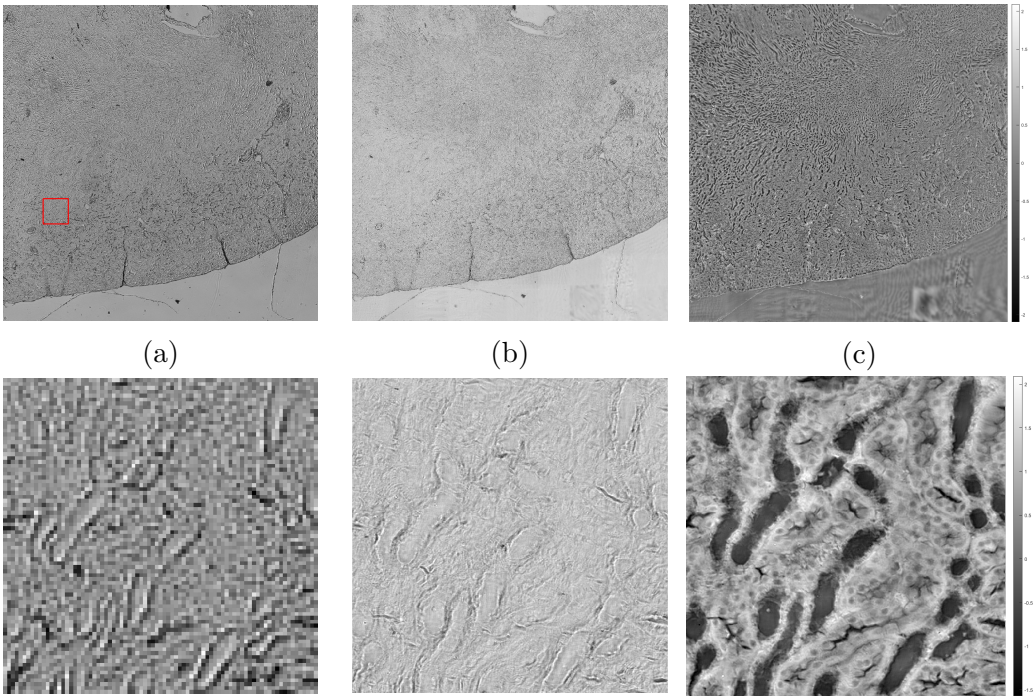

(a) (b) (c)

(d) (e) (f)

Figure A.3: Mouse kidney tissue, 6 µm light yellow coloring. Illumination with green light, 20x20 LEDs used. The size of the raw segment is 1020 x 1020 pixels, which corresponds to 3.7 mm x 3.7 mm at the object plane. The magnified region is 80 x 80 pixels, the corresponding reconstructed region is 400 x 400 pixels. (a,d) The amplitude of a low-resolution bright field segment. (b,e) The reconstructed amplitude. (c,f) The reconstructed phase. (d-f) Zoom on the area indicated by the red square in image (a).

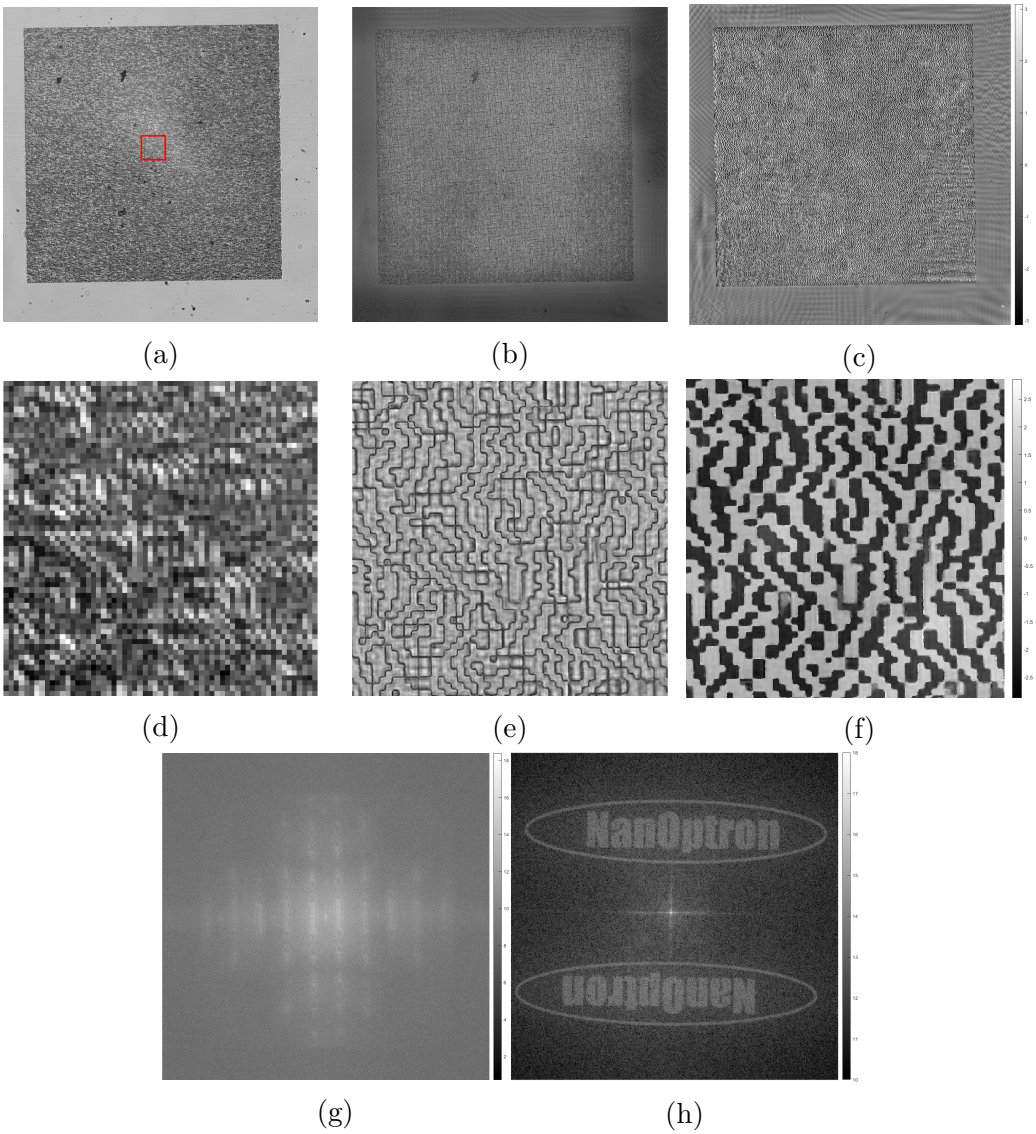

Figure A.4: Laser grating featuring the word "NanOptron" in its diffraction pattern. Illumination with green light. The size of the raw segment is 790 x 790 pixels, which corresponds to 2.5 mm x 2.5 mm at the object plane. The magnified region is 60 x 60 pixels, the corresponding reconstructed region is 300 x 300 pixels. (a,d) The amplitude of a low-resolution bright field segment. (b,e) The reconstructed amplitude. (c,f) The reconstructed phase. (d-f) Zoom on the area indicated by the red square in image (a). (g) Fourier transform of the reconstructed object. (e) Zoom on the central part of the Fourier transform (the image is rotated and flipped). This particular reconstruction is obtained with the quasi-Newtonian algorithm proposed by Laura Waller's team.

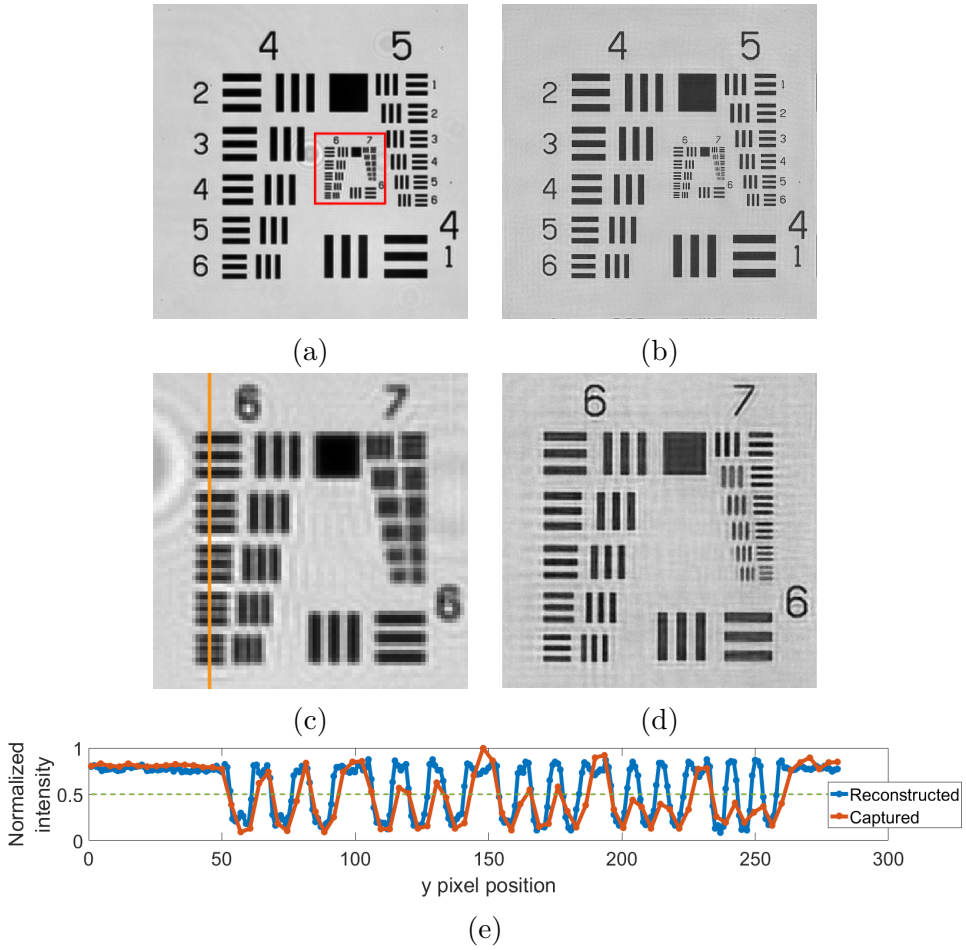

Figure A.5: 1951 USAF resolution test chart. Illumination with red light, 16x16 LEDs used. The size of the raw segment is 360 x 360 pixels, which corresponds to 1.15 mm x 1.15 mm at the object plane. The magnified region is 80 x 80 pixels, the corresponding reconstructed region is 280 x 280 pixels. The reconstruction was performed without the intensity correction routine because it produced artifacts. On the other hand, the spectrum of this sample is very different from that of a typical biological tissue. (a,c) The amplitude of a low-resolution bright field segment. (b,d) The reconstructed amplitude. (c,d) Zoom on the area indicated by the red square in the image (a). (e) Profile traced across the orange line in the image (c). All selected elements of the reconstructed image have the same contrast, while the contrast of the captured image decreases as smaller line pairs are processed.

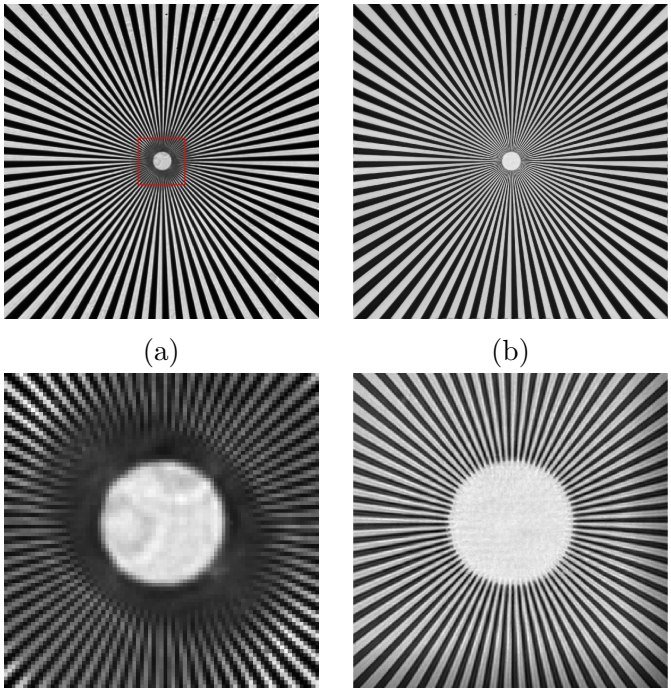

(a) (b)

(c) (d)

Figure A.6: Sector star target. Illumination with red light, 16x16 LEDs used. The size of the raw segment is 540 x 540 pixels, which corresponds to 1.7 mm x 1.7 mm at the object plane. The magnified region is 80 x 80 pixels, the corresponding reconstructed region is 280 x 280 pixels. (a,c) The amplitude of a low-resolution bright field segment. (b,d) The reconstructed amplitude. (c,d) Zoom on the area indicated by the red square in the image (a).

Bibliography

[1] D. S. Acton, J. S. Knight, A. Contos, S. Grimaldi, J. Terry, P. Lightsey, A. Barto, B. League, B. Dean, J. S. Smith, et al. Wavefront sensing and controls for the James Webb Space Telescope. In *Space Telescopes and Instrumentation 2012: Optical, Infrared, and Millimeter Wave*, volume 8442, page 84422H. International Society for Optics and Photonics, 2012.

[2] T. Adali and P. J. Schreier. Optimization and estimation of complex-valued signals: Theory and applications in filtering and blind source separation. *IEEE Signal Processing Magazine*, 31(5):112–128, 2014.

[3] I. Ahmed, M. Alotaibi, S. Skinner-Ramos, D. Dominguez, A. A. Bernussi, and L. G. de Peralta. Fourier ptychographic microscopy at telecommunication wavelengths using a femtosecond laser. *Optics Communications*, 405:363–367, 2017.

[4] S. Aknoun, P. Bon, J. Savatier, B. Wattellier, and S. Monneret. Quantitative retardance imaging of biological samples using quadriwave lateral shearing interferometry. *Optics express*, 23(12):16383–16406, 2015.

[5] M. Alotaibi, S. Skinner-Ramos, A. Alamri, B. Alharbi, M. Alfarraj, and L. G. de Peralta. Illumination-direction multiplexing Fourier ptychographic microscopy using hemispherical digital condensers. *Applied optics*, 56(14):4052–4057, 2017.

[6] N. Anthony, G. Cadenazzi, H. Kirkwood, E. Huwald, K. Nugent, and B. Abbey. A direct approach to in-plane stress separation using photoelastic ptychography. *Scientific reports*, 6:30541, 2016.

[7] M. Axer, K. Amunts, D. Grässel, C. Palm, J. Dammers, H. Axer, U. Pietrzyk, and K. Zilles. A novel approach to the human connectome: ultra-high resolution mapping of fiber tracts in the brain. *Neuroimage*, 54(2):1091–1101, 2011.

[8] J. Bao, J. Fan, X. Hu, J. Wang, and L. Wang. An effective consistency correction and blending method for camera-array-based microscopy imaging. In *2017 International Conference on Systems, Signals and Image Processing (IWSSIP)*, pages 1–5. IEEE, 2017.

[9] M. Bass and V. N. Mahajan. *Handbook of Optics, ; Volume I: Geometrical and Physical Optics, Polarized Light, Components and Instruments.* McGraw-Hill, 2010.

[10] M. Bertalmío. *Denoising of photographic images and video: fundamentals, open challenges and new trends*. Springer, 2018.

[11] L. Bian, J. Suo, J. Chung, X. Ou, C. Yang, F. Chen, and Q. Dai. Fourier ptychographic reconstruction using Poisson maximum likelihood and truncated Wirtinger gradient. *Scientific reports*, 6, 2016.

[12] L. Bian, J. Suo, Q. Dai, and F. Chen. Fourier ptychography for high space-bandwidth product microscopy. *Advanced Optical Technologies*, 6(6):449–457, 2017.

[13] L. Bian, J. Suo, G. Situ, G. Zheng, F. Chen, and Q. Dai. Content adaptive illumination for Fourier ptychography. *Optics letters*, 39(23):6648–6651, 2014.

[14] L. Bian, J. Suo, G. Zheng, K. Guo, F. Chen, and Q. Dai. Fourier ptychographic reconstruction using Wirtinger flow optimization. *Optics express*, 23(4):4856–4866, 2015.

[15] L. Bian, G. Zheng, K. Guo, J. Suo, C. Yang, F. Chen, and Q. Dai. Motion-corrected Fourier ptychography. *Biomedical optics express*, 7(11):4543–4553, 2016.

[16] Z. Bian, S. Dong, and G. Zheng. Adaptive system correction for robust Fourier ptychographic imaging. *Optics express*, 21(26):32400–32410, 2013.

[17] W. Bishara, U. Sikora, O. Mudanyali, T.-W. Su, O. Yaglidere, S. Luckhart, and A. Ozcan. Holographic pixel super-resolution in portable lensless on-chip microscopy using a fiber-optic array. *Lab on a Chip*, 11(7):1276–1279, 2011.

[18] P. Bouchal, L. Štrbková, Z. Dostál, R. Chmelík, and Z. Bouchal. Geometric-phase microscopy for quantitative phase imaging of isotropic, birefringent and space-variant polarization samples. *Scientific reports*, 9(1):1–11, 2019.

[19] A. Bozhok, J. Dellinger, Y. Takakura, J. Zallat, and C. Heinrich. Fourier ptychographic microscopy and Mueller matrix microscopy: differences and complementarity. In *Unconventional Optical Imaging II*, volume 11351, page 1135122. International Society for Optics and Photonics, 2020.

[20] O. Bunk, M. Dierolf, S. Kynde, I. Johnson, O. Marti, and F. Pfeiffer. Influence of the overlap parameter on the convergence of the ptychographical iterative engine. *Ultramicroscopy*, 108(5):481–487, 2008.

[21] E. J. Candes, Y. C. Eldar, T. Strohmer, and V. Voroninski. Phase retrieval via matrix completion. *SIAM review*, 57(2):225–251, 2015.

[22] E. J. Candes, X. Li, and M. Soltanolkotabi. Phase retrieval via Wirtinger flow: Theory and algorithms. *IEEE Transactions on Information Theory*, 61(4):1985–2007, 2015.

[23] F. Charrière, A. Marian, F. Montfort, J. Kuehn, T. Colomb, E. Cuche, P. Marquet, and C. Depeursinge. Cell refractive index tomography by digital holographic microscopy. *Optics letters*, 31(2):178–180, 2006.

[24] S. Chen, T. Xu, J. Zhang, B. Huang, and X. Wang. Optimized fast spectral sampling for adaptive Fourier ptychographic microscopy. In *Ninth International Conference on Digital Image Processing (ICDIP 2017)*, volume 10420, page 104201P. International Society for Optics and Photonics, 2017.

[25] S. Chen, T. Xu, J. Zhang, X. Wang, and Y. Zhang. Random Positional Deviations Correction for Each LED via ePIE in Fourier Ptychographic Microscopy. *IEEE Access*, 6:33399–33409, 2018.

[26] S. Chen, T. Xu, J. Zhang, X. Wang, and Y. Zhang. Optimized Denoising Method for Fourier Ptychographic Microscopy Based on Wirtinger Flow. *IEEE Photonics Journal*, 11(1):1–14, 2019.

[27] X. Chen, H. Cheng, Y. Wen, H. Wu, and Y. Wang. Reconstruction method based on the Hilbert fractal curve recovery sequence in a Fourier ptychography microscope. *Applied optics*, 58(3):517–527, 2019.

[28] X. Chen, J. Wu, C. Ma, and Q. Dai. Advanced Illumination Pattern in Fourier Ptychographic Microscopy. In *Mathematics in Imaging*, pages JT3A–41. Optical Society of America, 2016.

[29] X. Chen, Y. Zhu, M. Sun, D. Li, Q. Mu, and L. Xuan. Apodized coherent transfer function constraint for partially coherent Fourier ptychographic microscopy. *Optics express*, 27(10):14099–14111, 2019.

[30] Y. Chen and E. Candes. Solving random quadratic systems of equations is nearly as easy as solving linear systems. In *Advances in Neural Information Processing Systems*, pages 739–747, 2015.

[31] Y. F. Cheng, M. Strachan, Z. Weiss, M. Deb, D. Carone, and V. Ganapati. Illumination pattern design with deep learning for single-shot Fourier ptychographic microscopy. *Optics express*, 27(2):644–656, 2019.

[32] S. Chowdhury, A.-H. Dhalla, and J. Izatt. Structured oblique illumination microscopy for enhanced resolution imaging of non-fluorescent, coherently scattering samples. *Biomedical optics express*, 3(8):1841–1854, 2012.

[33] S. Chowdhury and J. Izatt. Structured illumination quantitative phase microscopy for enhanced resolution amplitude and phase imaging. *Biomedical optics express*, 4(10):1795–1805, 2013.

[34] J. Chung, R. W. Horstmeyer, and C. Yang. Fourier ptychographic retinal imaging methods and systems, June 12 2018. US Patent 9,993,149.

[35] J. Chung, J. Kim, X. Ou, R. Horstmeyer, and C. Yang. Wide field-of-view fluorescence image deconvolution with aberration-estimation from Fourier ptychography. *Biomedical optics express*, 7(2):352–368, 2016.

[36] J. Chung, X. Ou, R. P. Kulkarni, and C. Yang. Counting white blood cells from a blood smear using Fourier ptychographic microscopy. *PloS one*, 10(7):e0133489, 2015.

[37] J. Chung and C. Yang. SYSTEMS AND METHODS FOR CODED-APERTURE-BASED CORRECTION OF ABERRATION OBTAINED FROM FOURIER PTYCHOGRAPHY, Dec. 26 2019. US Patent App. 16/552,948.

[38] E. Compain, S. Poirier, and B. Drevillon. General and self-consistent method for the calibration of polarization modulators, polarimeters, and Mueller-matrix ellipsometers. *Applied optics*, 38(16):3490–3502, 1999.

[39] C. L. Curl, C. J. Bellair, P. J. Harris, B. E. Allman, A. Roberts, K. A. Nugent, and L. M. Delbridge. Quantitative phase microscopy: a new tool for investigating the structure and function of unstained live cells. *Clinical and experimental pharmacology and physiology*, 31(12):896–901, 2004.

[40] M. U. Daloglu et al. Low-cost and portable UV holographic microscope for high-contrast protein crystal imaging. *APL Photonics*, 4(3):030804, 2019.

[41] M. W. Davidson. Nikon MicroscopyU (Review Articles). `https://www.microscopyu.com/microscopy-basics/` Nikon MicroscopyU Website, 2020. Accessed: 2020-02-18.

[42] P. E. Debevec and J. Malik. Recovering high dynamic range radiance maps from photographs. In *ACM SIGGRAPH 2008 classes*, pages 1–10. Association for Computing Machinery, 2008.

[43] L. Denis et al. Twin-image noise reduction by phase retrieval in in-line digital holography. In M. Papadakis, A. F. Laine, and M. A. Unser, editors, *Wavelets XI*, volume 5914 of *Proc. SPIE*, pages 148 – 161, 2005.

[44] T. Dimitrova and A. Weis. The wave-particle duality of light: A demonstration experiment. *American Journal of Physics*, 76(2):137–142, 2008.

[45] S. Dong, Z. Bian, R. Shiradkar, and G. Zheng. Sparsely sampled Fourier ptychography. *Optics express*, 22(5):5455–5464, 2014.

[46] S. Dong, P. Nanda, K. Guo, J. Liao, and G. Zheng. Incoherent Fourier ptychographic photography using structured light. *Photonics Research*, 3(1):19–23, 2015.

[47] S. Dong, P. Nanda, R. Shiradkar, K. Guo, and G. Zheng. High-resolution fluorescence imaging via pattern-illuminated Fourier ptychography. *Optics express*, 22(17):20856–20870, 2014.

[48] S. Dong, R. Shiradkar, P. Nanda, and G. Zheng. Spectral multiplexing and coherent-state decomposition in Fourier ptychographic imaging. *Biomedical optics express*, 5(6):1757–1767, 2014.

[49] R. Eckert, Z. F. Phillips, and L. Waller. Efficient illumination angle self-calibration in Fourier ptychography. *Applied optics*, 57(19):5434–5442, 2018.

[50] R. Eckert, L. Tian, and L. Waller. Algorithmic self-calibration of illumination angles in Fourier ptychographic microscopy. In *Computational Optical Sensing and Imaging*, pages CT2D–3. Optical Society of America, 2016.

[51] Y. Fan, J. Sun, Q. Chen, M. Wang, and C. Zuo. Adaptive denoising method for Fourier ptychographic microscopy. *Optics Communications*, 404:23–31, 2017.

[52] P. Ferrand, M. Allain, and V. Chamard. Ptychography in anisotropic media. *Optics letters*, 40(22):5144–5147, 2015.

[53] C. Fienup and J. Dainty. Phase retrieval and image reconstruction for astronomy. *Image recovery: theory and application*, 231:275, 1987.

[54] J. R. Fienup. Phase retrieval algorithms: a comparison. *Applied optics*, 21(15):2758–2769, 1982.

[55] J. R. Fienup, J. C. Marron, T. J. Schulz, and J. H. Seldin. Hubble Space Telescope characterized by using phase-retrieval algorithms. *Applied optics*, 32(10):1747–1767, 1993.

[56] C. Fournier et al. Inverse problem approaches for digital hologram reconstruction. In B. Javidi and J.-Y. Son, editors, *Three-Dimensional Imaging, Visualization, and Display 2011*, volume 8043 of *Proc. SPIE*, pages 234 – 247, 2011.

[57] D. Gabor. A New Microscopic Principle. *Nature*, 161:777–778, 1948.

[58] A. Garg, R. Sharma, and V. Dhingra. Polarization studies in a computer based laboratory. *Latin-American Journal of Physics Education*, 5(1):17, 2011.

[59] R. W. Gerchberg. A practical algorithm for the determination of phase from image and diffraction plane pictures. *Optik*, 35:237–246, 1972.

[60] D. C. Ghiglia and M. D. Pritt. Two-dimensional phase unwrapping: theory, algorithms, and software. *Wiely-Interscience, first ed.(April 1998)*, 1998.

[61] R. M. Goldstein, H. A. Zebker, and C. L. Werner. Satellite radar interferometry: Two-dimensional phase unwrapping. *Radio science*, 23(4):713–720, 1988.

[62] J. W. Goodman. *Introduction to Fourier optics*. Roberts and Company Publishers, 2005.

[63] P. C. Goodwin. A primer on the fundamental principles of light microscopy: optimizing magnification, resolution, and contrast. *Molecular reproduction and development*, 82(7-8):502–507, 2015.

[64] D. J. Griffiths. Introduction to electrodynamics, 2005.

[65] C. Guo, S. Liu, and J. T. Sheridan. Iterative phase retrieval algorithms. I: optimization. *Applied optics*, 54(15):4698–4708, 2015.

[66] C. Guo, C. Wei, J. Tan, K. Chen, S. Liu, Q. Wu, and Z. Liu. A review of iterative phase retrieval for measurement and encryption. *Optics and Lasers in Engineering*, 89:2–12, 2017.

[67] K. Guo, Z. Bian, S. Dong, P. Nanda, Y. M. Wang, and G. Zheng. Microscopy illumination engineering using a low-cost liquid crystal display. *Biomedical optics express*, 6(2):574–579, 2015.

[68] K. Guo, S. Dong, P. Nanda, and G. Zheng. Optimization of sampling pattern and the design of Fourier ptychographic illuminator. *Optics express*, 23(5):6171–6180, 2015.

[69] K. Guo, S. Dong, and G. Zheng. Fourier ptychography for brightfield, phase, darkfield, reflective, multi-slice, and fluorescence imaging. *IEEE Journal of Selected Topics in Quantum Electronics*, 22(4):77–88, 2016.

[70] M. G. Gustafsson. Surpassing the lateral resolution limit by a factor of two using structured illumination microscopy. *Journal of microscopy*, 198(2):82–87, 2000.

[71] H. Häberlin. *Photovoltaics: system design and practice*. John Wiley & Sons, 2012.

[72] L. Han, Z.-J. Cheng, Y. Yang, B.-Y. Wang, Q.-Y. Yue, and C.-S. Guo. Double-channel angular-multiplexing polarization holography with common-path and off-axis configuration. *Optics express*, 25(18):21877–21886, 2017.

[73] X. He, C. Liu, and J. Zhu. Single-shot Fourier ptychography based on diffractive beam splitting. *Optics letters*, 43(2):214–217, 2018.

[74] S. W. Hell and J. Wichmann. Breaking the diffraction resolution limit by stimulated emission: stimulated-emission-depletion fluorescence microscopy. *Optics letters*, 19(11):780–782, 1994.

[75] S. T. Hess, T. P. Girirajan, and M. D. Mason. Ultra-high resolution imaging by fluorescence photoactivation localization microscopy. *Biophysical journal*, 91(11):4258–4272, 2006.

[76] J. Holloway, Y. Wu, M. K. Sharma, O. Cossairt, and A. Veeraraghavan. SAVI: Synthetic apertures for long-range, subdiffraction-limited visible imaging using Fourier ptychography. *Science advances*, 3(4):e1602564, 2017.

[77] R. Horstmeyer, R. Y. Chen, X. Ou, B. Ames, J. A. Tropp, and C. Yang. Solving ptychography with a convex relaxation. *New journal of physics*, 17(5):053044, 2015.

[78] R. Horstmeyer, J. Chung, X. Ou, G. Zheng, and C. Yang. Diffraction tomography with Fourier ptychography. *Optica*, 3(8):827–835, 2016.

[79] R. Horstmeyer, X. Ou, G. Zheng, P. Willems, and C. Yang. Digital pathology with Fourier ptychography. *Computerized Medical Imaging and Graphics*, 42:38–43, 2015.

[80] R. Horstmeyer and C. Yang. A phase space model of Fourier ptychographic microscopy. *Optics express*, 22(1):338–358, 2014.

[81] R. Horstmeyer, G. Zheng, X. Ou, and C. Yang. Aperture scanning fourier ptychographic imaging, Aug. 23 2016. US Patent 9,426,455.

[82] R. W. Horstmeyer, Y. Chen, J. A. Tropp, and C. Yang. Ptychography imaging systems and methods with convex relaxation, Nov. 19 2015. US Patent App. 14/710,947.

[83] L. Hou, H. Wang, M. Sticker, L. Stoppe, J. Wang, and M. Xu. Adaptive background interference removal for Fourier ptychographic microscopy. *Applied optics*, 57(7):1575–1580, 2018.

[84] L. Hou, H. Wang, J. Wang, and M. Xu. Background-noise Reduction for Fourier Ptychographic Microscopy Based on an Improved Thresholding Method. *Current Optics and Photonics*, 2(2):165–171, 2018.

[85] J. Hu, Q. Li, and Y. Zhou. Support-domain constrained phase retrieval algorithms in terahertz in-line digital holography reconstruction of a non-isolated amplitude object. *Appl. Opt.*, 55(2):379–386, 2016.

[86] Y. Huang, A. C. Chan, A. Pan, and C. Yang. Memory-efficient, Global Phase-retrieval of Fourier Ptychography with Alternating Direction Method. In *Computational Optical Sensing and Imaging*, pages CTu4C–2. Optical Society of America, 2019.

[87] K. Jaganathan, Y. C. Eldar, and B. Hassibi. Phase retrieval: An overview of recent developments. *arXiv preprint arXiv:1510.07713*, 2015.

[88] K. Jaganathan, Y. C. Eldar, and B. Hassibi. STFT phase retrieval: Uniqueness guarantees and recovery algorithms. *IEEE Journal of selected topics in signal processing*, 10(4):770–781, 2016.

[89] M. H. Jericho et al. Quantitative phase and refractive index measurements with point-source digital in-line holographic microscopy. *Appl. Opt.*, 51(10):1503–1515, 2012.

[90] S. Jiang, K. Guo, J. Liao, and G. Zheng. Solving Fourier ptychographic imaging problems via neural network modeling and TensorFlow. *Biomedical optics express*, 9(7):3306–3319, 2018.

[91] W. Jiang, Y. Zhang, and Q. Dai. Multi-channel super-resolution with Fourier ptychographic microscopy. In *Optoelectronic Imaging and Multimedia Technology III*, volume 9273, page 927336. International Society for Optics and Photonics, 2014.

[92] W. Jiang, Y. Zhang, and Q. Dai. Parameterized reconstruction based Fourier Ptychography. In *2016 IEEE International Conference on Multimedia and Expo (ICME)*, pages 1–6. IEEE, 2016.

[93] X. Jiang, S. Rajan, and X. Liu. Wirtinger Flow Method With Optimal Stepsize for Phase Retrieval. *IEEE Signal Processing Letters*, 23(11):1627–1631, 2016.

[94] P. Kancharla and S. S. Channappayya. A weighted optimization for Fourier Ptychographic Microscopy. In *2019 National Conference on Communications (NCC)*, pages 1–4. IEEE, 2019.

[95] A. Kappeler, S. Ghosh, J. Holloway, O. Cossairt, and A. Katsaggelos. PtychNet: CNN based Fourier ptychography. In *2017 IEEE International Conference on Image Processing (ICIP)*, pages 1712–1716. IEEE, 2017.

[96] M. Karnoukian. *Imagerie spectro-polarimétrique: système, algorithmes et biopsie optique*. PhD thesis, Université de Strasbourg, 2017.

[97] M. Kellman, E. Bostan, M. Chen, and L. Waller. Data-Driven Design for Fourier Ptychographic Microscopy. In *2019 IEEE International Conference on Computational Photography (ICCP)*, pages 1–8. IEEE, 2019.

[98] J. Kim, B. M. Henley, C. H. Kim, H. A. Lester, and C. Yang. Incubator embedded cell culture imaging system (EmSight) based on Fourier ptychographic microscopy. *Biomedical optics express*, 7(8):3097–3110, 2016.

[99] J. Kim and C. Yang. Multi-well fourier ptychographic and fluorescence imaging, July 28 2016. US Patent App. 15/007,159.

[100] J. Kim and C. Yang. Array level Fourier ptychographic imaging, Nov. 28 2017. US Patent 9,829,695.

[101] Y. Kim, J. Jeong, J. Jang, M. W. Kim, and Y. Park. Polarization holographic microscopy for extracting spatio-temporally resolved Jones matrix. *Optics Express*, 20(9):9948–9955, 2012.

[102] R. Kolte and A. Özgür. Phase retrieval via incremental truncated Wirtinger flow. *arXiv preprint arXiv:1606.03196*, 2016.

[103] P. C. Konda, J. M. Taylor, and A. R. Harvey. Scheimpflug multi-aperture Fourier ptychography: coherent computational microscope with gigapixels/s data acquisition rates using 3D printed components. In *High-Speed Biomedical Imaging and Spectroscopy: Toward Big Data Instrumentation and Management II*, volume 10076, page 100760R. International Society for Optics and Photonics, 2017.

[104] A. Konijnenberg, W. Coene, and H. Urbach. Study of cost functionals for ptychographic phase retrieval to improve the robustness against noise, and a proposal for another noise-robust ptychographic phase retrieval scheme. *arXiv preprint arXiv:1703.10892*, 2017.

[105] A. Konijnenberg, W. Coene, and H. Urbach. Model-independent noise-robust extension of ptychography. *Optics express*, 26(5):5857–5874, 2018.

[106] T. Latychevskaia and H.-W. Fink. Solution to the Twin Image Problem in Holography. *Phys. Rev. Lett.*, 98(23):233901, 2007.

[107] B. Lee, J.-Y. Hong, J. Cho, Y. Jeong, and B. Lee. One-Shot Light Field Fourier Ptychographic Microscopy for Complex Imaging. In *Applied Industrial Optics: Spectroscopy, Imaging and Metrology*, pages JT3A–54. Optical Society of America, 2016.

[108] B. Lee, J.-y. Hong, D. Yoo, J. Cho, Y. Jeong, S. Moon, and B. Lee. Single-shot phase retrieval via Fourier ptychographic microscopy. *Optica*, 5(8):976–983, 2018.

[109] K. Lee, K. Kim, J. Jung, J. Heo, S. Cho, S. Lee, G. Chang, Y. Jo, H. Park, and Y. Park. Quantitative phase imaging techniques for the study of cell pathophysiology: from principles to applications. *Sensors*, 13(4):4170–4191, 2013.

[110] H. Li, A. Bozhok, Y. Takakura, J. Dellinger, P. Twardowski, and J. Zallat. Lensless inline digital holography versus Fourier ptychography: phase estimation of a large transparent bead. *Optical Engineering*, 59(8):083104, 2020.

[111] J. Li and T. Zhou. On Gradient Descent Algorithm for Generalized Phase Retrieval Problem. *arXiv preprint arXiv:1607.01121*, 2016.

[112] M. Li, Y. Li, L. Zhong, R. Wen, C. Kuang, and H. Li. Light field Fourier ptychographic microscopy. In *Third International Conference on Photonics and Optical Engineering*, volume 11052, page 110521K. International Society for Optics and Photonics, 2019.

[113] P. Li, D. J. Batey, T. B. Edo, and J. M. Rodenburg. Separation of three-dimensional scattering effects in tilt-series Fourier ptychography. *Ultramicroscopy*, 158:1–7, 2015.

[114] Z. Li, D. Wen, Z. Song, G. Liu, W. Zhang, and X. Wei. Sub-Diffraction Visible Imaging Using Macroscopic Fourier Ptychography and Regularization by Denoising. *Sensors*, 18(9):3154, 2018.

[115] J. Liu, Y. Li, W. Wang, J. Tan, and C. Liu. Accelerated and high-quality Fourier ptychographic method using a double truncated Wirtinger criteria. *Optics express*, 26(20):26556–26565, 2018.

[116] J. Liu, Y. Li, W. Wang, H. Zhang, Y. Wang, J. Tan, and C. Liu. Stable and robust frequency domain position compensation strategy for Fourier ptychographic microscopy. *Optics Express*, 25(23):28053–28067, 2017.

[117] Q. Liu, C. Kuang, Y. Fang, P. Xiu, Y. Li, R. Wen, and X. Liu. Effect of spatial spectrum overlap on Fourier ptychographic microscopy. *Journal of Innovative Optical Health Sciences*, 10(02):1641004, 2017.

[118] S.-Y. Lu and R. A. Chipman. Interpretation of Mueller matrices based on polar decomposition. *JOSA A*, 13(5):1106–1113, 1996.

[119] C. Ma, Z. Liu, L. Tian, Q. Dai, and L. Waller. Motion deblurring with temporally coded illumination in an LED array microscope. *Optics letters*, 40(10):2281–2284, 2015.

[120] X. Ma, Z. Zhang, M. Yao, J. Peng, and J. Zhong. Spatially-incoherent annular illumination microscopy for bright-field optical sectioning. *Ultramicroscopy*, 195:74–84, 2018.

[121] A. Maiden, D. Johnson, and P. Li. Further improvements to the ptychographical iterative engine. *Optica*, 4(7):736–745, 2017.

[122] A. M. Maiden, M. J. Humphry, and J. Rodenburg. Ptychographic transmission microscopy in three dimensions using a multi-slice approach. *JOSA A*, 29(8):1606–1614, 2012.

[123] A. M. Maiden and J. M. Rodenburg. An improved ptychographical phase retrieval algorithm for diffractive imaging. *Ultramicroscopy*, 109(10):1256–1262, 2009.

[124] M. Makitalo and A. Foi. Optimal inversion of the generalized Anscombe transformation for Poisson-Gaussian noise. *IEEE transactions on image processing*, 22(1):91–103, 2013.

[125] C. A. Metzler, A. Maleki, and R. G. Baraniuk. BM3D-PRGAMP: Compressive phase retrieval based on BM3D denoising. In *2016 IEEE International Conference on Image Processing (ICIP)*, pages 2504–2508. IEEE, 2016.

[126] J. Miao, P. Charalambous, J. Kirz, and D. Sayre. Extending the methodology of X-ray crystallography to allow imaging of micrometre-sized noncrystalline specimens. *Nature*, 400(6742):342, 1999.

[127] J. Miao, T. Ishikawa, I. K. Robinson, and M. M. Murnane. Beyond crystallography: Diffractive imaging using coherent x-ray light sources. *Science*, 348(6234):530–535, 2015.

[128] V. Micó, J. Zheng, J. Garcia, Z. Zalevsky, and P. Gao. Resolution enhancement in quantitative phase microscopy. *Advances in Optics and Photonics*, 11(1):135–214, 2019.

[129] J. Minion, M. Pai, A. Ramsay, D. Menzies, and C. Greenaway. Comparison of LED and conventional fluorescence microscopy for detection of acid fast bacilli in a low-incidence setting. *PLoS One*, 6(7), 2011.

[130] I. Muniraj, C. Guo, R. Malallah, D. Cassidy, L. Zhao, J. P. Ryle, J. J. Healy, and J. T. Sheridan. A fast converging and error reducing phase retrieval algorithm for Fourier Ptychographic microscopy. In *Digital Holography and Three-Dimensional Imaging*, pages W1A–4. Optical Society of America, 2017.

[131] D. B. Murphy. *Fundamentals of light microscopy and electronic imaging.* John Wiley & Sons, 2002.

[132] M. A. Neifeld. Information, resolution, and space–bandwidth product. *Optics letters*, 23(18):1477–1479, 1998.

[133] T. Nguyen, Y. Xue, Y. Li, L. Tian, and G. Nehmetallah. Deep learning approach for Fourier ptychography microscopy. *Optics express*, 26(20):26470–26484, 2018.

[134] M. Odstrčil, A. Menzel, and M. Guizar-Sicairos. Iterative least-squares solver for generalized maximum-likelihood ptychography. *Optics express*, 26(3):3108–3123, 2018.

[135] E. Optics. Edmund Optics (Imaging Resource Guide). `https://www.edmundoptics.com/knowledge-center/industry-expertise/imaging-optics/imaging-resource-guide/` Edmund Optics Website, 2020. Accessed: 2020-01-30.

[136] E. Optics. Edmund Optics Products. `https://www.edmundoptics.com/c/infinity-corrected-objectives/629/#/` Edmund Optics Website, 2020. Accessed: 2020-01-30.

[137] X. Ou, J. Chung, R. Horstmeyer, and C. Yang. Aperture scanning Fourier ptychographic microscopy. *Biomedical optics express*, 7(8):3140–3150, 2016.

[138] X. Ou, J. Chung, R. Horstmeyer, G. Zheng, and C. Yang. Embedded pupil function recovery for fourier ptychographic imaging devices, Mar. 29 2018. US Patent App. 15/820,295.

[139] X. Ou, J. Chung, and C. Yang. Laser-based fourier ptychographic imaging systems and methods, Nov. 24 2016. US Patent App. 15/160,941.

[140] X. Ou, R. Horstmeyer, C. Yang, and G. Zheng. Quantitative phase imaging via Fourier ptychographic microscopy. *Optics letters*, 38(22):4845–4848, 2013.

[141] X. Ou, R. Horstmeyer, G. Zheng, and C. Yang. High numerical aperture Fourier ptychography: principle, implementation and characterization. *Optics express*, 23(3):3472–3491, 2015.

[142] X. Ou, R. Horstmeyer, G. Zheng, and C. Yang. Variable-illumination fourier ptychographic imaging devices, systems, and methods, Nov. 15 2016. US Patent 9,497,379.

[143] X. Ou, G. Zheng, and C. Yang. Embedded pupil function recovery for Fourier ptychographic microscopy. *Optics express*, 22(5):4960–4972, 2014.

[144] S. Pacheco, B. Salahieh, T. Milster, J. J. Rodriguez, and R. Liang. Transfer function analysis in epi-illumination Fourier ptychography. *Optics letters*, 40(22):5343–5346, 2015.

[145] S. Pacheco, G. Zheng, and R. Liang. Reflective Fourier ptychography. *Journal of biomedical optics*, 21(2):026010, 2016.

[146] A. Pan, Y. Zhang, M. Li, M. Zhou, J. Min, M. Lei, and B. Yao. SNR-based adaptive acquisition method for fast Fourier ptychographic microscopy. *arXiv preprint arXiv:1709.07747*, 2017.

[147] A. Pan, Y. Zhang, K. Wen, M. Zhou, J. Min, M. Lei, and B. Yao. Subwavelength resolution Fourier ptychography with hemispherical digital condensers. *Optics express*, 26(18):23119–23131, 2018.

[148] A. Pan, Y. Zhang, T. Zhao, Z. Wang, D. Dan, M. Lei, and B. Yao. System calibration method for Fourier ptychographic microscopy. *Journal of biomedical optics*, 22(9):096005, 2017.

[149] A. Pan, C. Zuo, Y. Xie, M. Lei, and B. Yao. Vignetting effect in Fourier ptychographic microscopy. *Optics and Lasers in Engineering*, 120:40–48, 2019.

[150] A. Pan, C. Zuo, Y. Xie, Y. Zhang, M. Lei, and B. Yao. Vignetting effect in Fourier ptychographic microscopy. *arXiv preprint arXiv:1710.06717*, 2017.

[151] Y. Park, C. Depeursinge, and G. Popescu. Quantitative phase imaging in biomedicine. *Nature Photonics*, 12(10):578–589, 2018.

[152] S. Perrin and P. Montgomery. Fourier optics: basic concepts. *arXiv preprint arXiv:1802.07161*, 2018.

[153] J. L. Pezzaniti and R. A. Chipman. Mueller matrix imaging polarimetry. *Optical engineering*, 34(6):1558–1569, 1995.

[154] M. A. Pfeifer, G. J. Williams, I. A. Vartanyants, R. Harder, and I. K. Robinson. Three-dimensional mapping of a deformation field inside a nanocrystal. *Nature*, 442(7098):63, 2006.

[155] Z. F. Phillips, M. V. D'Ambrosio, L. Tian, J. J. Rulison, H. S. Patel, N. Sadras, A. V. Gande, N. A. Switz, D. A. Fletcher, and L. Waller. Multi-contrast imaging and digital refocusing on a mobile microscope with a domed led array. *PloS one*, 10(5):e0124938, 2015.

[156] Z. F. Phillips, R. Eckert, and L. Waller. Quasi-dome: A self-calibrated high-NA LED illuminator for Fourier ptychography. In *Imaging Systems and Applications*, pages IW4E–5. Optical Society of America, 2017.

[157] Z. F. Phillips, G. Gunjala, P. Varma, J. Zhong, and L. Waller. Design of a Domed LED Illuminator for High-Angle Computational Illumination. In *Imaging Systems and Applications*, pages ITh1A–2. Optical Society of America, 2015.

[158] C. W. Pirnstill and G. L. Coté. Malaria diagnosis using a mobile phone polarized microscope. *Scientific reports*, 5:13368, 2015.

[159] W. H. Press, S. A. Teukolsky, W. T. Vetterling, and B. P. Flannery. *Numerical recipes in C*, volume 2. Cambridge Univ Press, 1982.

[160] B. Products. Biocompare Products (Microscope Slide Scanners). `https://www.biocompare.com/Bio-Imaging-Microscopy/`Biocompare Website, Microscope Slide Scanner, 2020. Accessed: 2020-01-30.

[161] Z. Products. Zeiss Products. `https://www.micro-shop.zeiss.com/en/us/shop/objectives/` Zeiss Website, 2020. Accessed: 2020-01-30.

[162] J. Qian, C. Yang, A. Schirotzek, F. Maia, and S. Marchesini. Efficient algorithms for ptychographic phase retrieval. *Inverse Problems and Applications, Contemp. Math*, 615:261–280, 2014.

[163] T. Qiu, P. Babu, and D. P. Palomar. PRIME: Phase retrieval via majorization-minimization. *IEEE Transactions on Signal Processing*, 64(19):5174–5186, 2016.

[164] D. Ren, E. Bostan, L.-H. Yeh, and L. Waller. Total-variation regularized Fourier ptychographic microscopy with multiplexed coded illumination. In *Mathematics in Imaging*, pages MM3C–5. Optical Society of America, 2017.

[165] L. Repetto, E. Piano, and C. Pontiggia. Lensless digital holographic microscope with light-emitting diode illumination. *Optics letters*, 29(10):1132–1134, 2004.

[166] Y. Rivenson, T. Liu, Z. Wei, Y. Zhang, K. de Haan, and A. Ozcan. PhaseStain: the digital staining of label-free quantitative phase microscopy images using deep learning. *Light: Science & Applications*, 8(1):23, 2019.

[167] J. M. Rodenburg. Ptychography and related diffractive imaging methods. *Advances in imaging and electron physics*, 150:87–184, 2008.

[168] J. M. Rodenburg and H. M. Faulkner. A phase retrieval algorithm for shifting illumination. *Applied physics letters*, 85(20):4795–4797, 2004.

[169] D. Sayre. X-ray crystallography: The past and present of the phase problem. *Structural Chemistry*, 13(1):81–96, 2002.

[170] S. Sen, I. Ahmed, B. Aljubran, A. A. Bernussi, and L. G. de Peralta. Fourier ptychographic microscopy using an infrared-emitting hemispherical digital condenser. *Applied optics*, 55(23):6421–6427, 2016.

[171] S. Sen, D. B. Desai, M. H. Alsubaie, M. V. Zhelyeznyakov, L. Molina, H. S. Sarraf, A. A. Bernussi, and L. G. de Peralta. Imaging photonic crystals using Fourier plane imaging and Fourier ptychographic microscopy techniques implemented with a computer controlled hemispherical digital condenser. *Optics Communications*, 383:500–507, 2017.

[172] N. T. Shaked. Quantitative phase microscopy of biological samples using a portable interferometer. *Optics letters*, 37(11):2016–2018, 2012.

[173] N. T. Shaked, Z. Zalevsky, and L. L. Satterwhite. *Biomedical optical phase microscopy and nanoscopy*. Academic Press, 2012.

[174] F. Shamshad, F. Abbas, and A. Ahmed. Deep ptych: Subsampled fourier ptychography using generative priors. In *ICASSP 2019-2019 IEEE International Conference on Acoustics, Speech and Signal Processing (ICASSP)*, pages 7720–7724. IEEE, 2019.

[175] Y. Shechtman, Y. C. Eldar, O. Cohen, H. N. Chapman, J. Miao, and M. Segev. Phase retrieval with application to optical imaging: a contemporary overview. *IEEE signal processing magazine*, 32(3):87–109, 2015.

[176] H. Simons, H. Poulsen, J. Guigay, and C. Detlefs. X-ray Fourier ptychographic microscopy. *arXiv preprint arXiv:1609.07513*, 2016.

[177] A. C. Sobieranski et al. Portable lensless wide-field microscopy imaging platform based on digital inline holography and multi-frame pixel superresolution. *Light Sci. Appl*, 4(10):e346, 2015.

[178] P. Song, S. Jiang, H. Zhang, X. Huang, Y. Zhang, and G. Zheng. Full-field Fourier ptychography (FFP): Spatially varying pupil modeling and its application for rapid field-dependent aberration metrology. *APL Photonics*, 4(5):050802, 2019.

[179] P. Song, W. Jiang, Y. Zhang, and Q. Dai. Fourier ptychographic reconstruction using weighted replacement in the fourier domain. In *2016 IEEE International Conference on Image Processing (ICIP)*, pages 3171–3175. IEEE, 2016.

[180] L. Sorber, M. V. Barel, and L. D. Lathauwer. Unconstrained optimization of real functions in complex variables. *SIAM Journal on Optimization*, 22(3):879–898, 2012.

[181] F. Soulez et al. Inverse-problem approach for particle digital holography: accurate location based on local optimization. *JOSA A*, 24(4):1164–1171, 2007.

[182] B. Spottiswoode. 2D phase unwrapping algorithms. `https://fr.mathworks.com/matlabcentral/fileexchange/22504-2d-phase-unwrapping-algorithms` MATLAB Central File Exchange, 2020. Accessed: 2020-09-09.

[183] M. Stockmar et al. Near-field ptychography: phase retrieval for inline holography using a structured illumination. *Sci. Rep.*, 3:1927, 2013.

[184] G. G. Stokes. On the composition and resolution of streams of polarized light from different sources. *TCaPS*, 9:399, 1851.

[185] J. Sun, Q. Chen, J. Zhang, Y. Fan, and C. Zuo. Single-shot quantitative phase microscopy based on color-multiplexed Fourier ptychography. *Optics letters*, 43(14):3365–3368, 2018.

[186] J. Sun, Q. Chen, Y. Zhang, and C. Zuo. Efficient positional misalignment correction method for Fourier ptychographic microscopy. *Biomedical optics express*, 7(4):1336–1350, 2016.

[187] J. Sun, Q. Chen, Y. Zhang, and C. Zuo. Sampling criteria for Fourier ptychographic microscopy in object space and frequency space. *Optics Express*, 24(14):15765–15781, 2016.

[188] J. Sun, Q. Chen, Y. Zhang, C. Zuo, S. Feng, Y. Hu, and J. Zhang. Optimized multiplexing super resolution imaging based on a Fourier ptychographic microscope. In *AOPC 2015: Advanced Display Technology; and Micro/Nano Optical Imaging Technologies and Applications*, volume 9672, page 967219. International Society for Optics and Photonics, 2015.

[189] J. Sun, Y. Zhang, C. Zuo, Q. Chen, S. Feng, Y. Hu, and J. Zhang. Coded multi-angular illumination for Fourier ptychography based on Hadamard codes. In *International Conference on Optical and Photonic Engineering (icOPEN 2015)*, volume 9524, page 95242C. International Society for Optics and Photonics, 2015.

[190] J. Sun, C. Zuo, L. Zhang, and Q. Chen. Resolution-enhanced Fourier ptychographic microscopy based on high-numerical-aperture illuminations. *Scientific reports*, 7(1):1187, 2017.

[191] M. Sun, X. Chen, Y. Zhu, D. Li, Q. Mu, and L. Xuan. Neural network model combined with pupil recovery for Fourier ptychographic microscopy. *Optics Express*, 27(17):24161–24174, 2019.

[192] Y. Sun, S. Xu, Y. Li, L. Tian, B. Wohlberg, and U. S. Kamilov. Regularized Fourier ptychography using an online plug-and-play algorithm. In *ICASSP 2019-2019 IEEE International Conference on Acoustics, Speech and Signal Processing (ICASSP)*, pages 7665–7669. IEEE, 2019.

[193] T. Tahara, X. Quan, R. Otani, Y. Takaki, and O. Matoba. Digital holography and its multidimensional imaging applications: a review. *Microscopy*, 67(2):55–67, 2018.

[194] Y. Tani, S. Usuki, and K. T. Miura. Improving spatial resolution of the light field microscope with Fourier ptychography. In *Unconventional and Indirect Imaging, Image Reconstruction, and Wavefront Sensing 2017*, volume 10410, page 1041009. International Society for Optics and Photonics, 2017.

[195] Thorlabs. Thorlabs Products. `https://www.thorlabs.com/newgrouppage9.cfm?objectgroup_id=10186/` Thorlabs Website, 2020. Accessed: 2020-01-30.

[196] L. Tian, X. Li, K. Ramchandran, and L. Waller. Multiplexed coded illumination for Fourier Ptychography with an LED array microscope. *Biomedical optics express*, 5(7):2376–2389, 2014.

[197] L. Tian, Z. Liu, L.-H. Yeh, M. Chen, and L. Waller. Real-time in vitro Fourier ptychographic microscopy for high resolution wide field of view phase imaging. *arXiv preprint arXiv:1506.04274*, 2015.

[198] L. Tian, Z. Liu, L.-H. Yeh, M. Chen, J. Zhong, and L. Waller. Computational illumination for high-speed in vitro Fourier ptychographic microscopy. *Optica*, 2(10):904–911, 2015.

[199] L. Tian and L. Waller. 3D intensity and phase imaging from light field measurements in an LED array microscope. *optica*, 2(2):104–111, 2015.

[200] L. Tian and L. Waller. Quantitative differential phase contrast imaging in an LED array microscope. *Optics express*, 23(9):11394–11403, 2015.

[201] L. Tian, J. Wang, and L. Waller. 3D differential phase-contrast microscopy with computational illumination using an LED array. *Optics letters*, 39(5):1326–1329, 2014.

[202] L. Tian, L.-h. Yeh, R. Eckert, and L. Waller. Computational microscopy: illumination coding and nonlinear optimization enables gigapixel 3D phase imaging. In *2017 IEEE International Conference on Acoustics, Speech and Signal Processing (ICASSP)*, pages 6225–6229. IEEE, 2017.

[203] X. Tian. Fourier ptychographic reconstruction using mixed Gaussian–Poisson likelihood with total variation regularisation. *Electronics Letters*, 2019.

[204] D. Tolhurst, Y. Tadmor, and T. Chao. Amplitude spectra of natural images. *Ophthalmic and Physiological Optics*, 12(2):229–232, 1992.

[205] H. G. Tompkins. *A user's guide to ellipsometry*. Courier Corporation, 2006.

[206] A. Tripathi, I. McNulty, and O. G. Shpyrko. Ptychographic overlap constraint errors and the limits of their numerical recovery using conjugate gradient descent methods. *Optics Express*, 22(2):1452–1466, 2014.

[207] D. Utsumi, M. Yasuda, H. Amano, Y. Suga, M. Seishima, and K. Takahashi. Hair abnormality in Netherton syndrome observed under polarized light microscopy. *Journal of the American Academy of Dermatology*, 2020.

[208] B. Varin, J. Rehbinder, J. Dellinger, C. Heinrich, J. Schmidt, C. Spenlé, D. Bagnard, and J. Zallat. Tumor growth monitoring using polarized light. In *European Conference on Biomedical Optics*, page 11075_27. Optical Society of America, 2019.

[209] K. Wakonig, A. Diaz, A. Bonnin, M. Stampanoni, A. Bergamaschi, J. Ihli, M. Guizar-Sicairos, and A. Menzel. X-ray Fourier ptychography. *Science advances*, 5(2):eaav0282, 2019.

[210] G. Wang, G. B. Giannakis, and J. Chen. Scalable solvers of random quadratic equations via stochastic truncated amplitude flow. *IEEE Transactions on Signal Processing*, 65(8):1961–1974, 2017.

[211] G. Wang, G. B. Giannakis, and Y. C. Eldar. Solving systems of random quadratic equations via truncated amplitude flow. *IEEE Transactions on Information Theory*, 64(2):773–794, 2017.

[212] G. Wang, G. B. Giannakis, Y. Saad, and J. Chen. Phase retrieval via reweighted amplitude flow. *IEEE Transactions on Signal Processing*, 66(11):2818–2833, 2018.

[213] H. Wang, L. Rong, D. Wang, X. Zhang, C. Zhai, S. Panezai, Y. Wang, and J. Zhao. Influences of overlap index on Fourier ptychography imaging. In *2017 International Conference on Optical Instruments and*

Technology: Optoelectronic Imaging/Spectroscopy and Signal Processing Technology, volume 10620, page 106201N. International Society for Optics and Photonics, 2018.

[214] H. Wang, W. Yue, Q. Song, J. Liu, and G. Situ. A hybrid Gerchberg–Saxton-like algorithm for DOE and CGH calculation. *Optics and Lasers in Engineering*, 89:109–115, 2017.

[215] M. Wang, Y. Zhang, Q. Chen, J. Sun, Y. Fan, and C. Zuo. A color-corrected strategy for information multiplexed Fourier ptychographic imaging. *Optics Communications*, 405:406–411, 2017.

[216] W. Wang, L. G. Lim, S. Srivastava, J. S. B. Yan, A. Shabbir, and Q. Liu. Roles of linear and circular polarization properties and effect of wavelength choice on differentiation between ex vivo normal and cancerous gastric samples. *Journal of biomedical optics*, 19(4):046020, 2014.

[217] Z. Wang, L. J. Millet, M. U. Gillette, and G. Popescu. Jones phase microscopy of transparent and anisotropic samples. *Optics letters*, 33(11):1270–1272, 2008.

[218] X. Wei and H. P. Urbach. The CRLB and Maximum likelihood in ptychography with Poisson noise. *arXiv preprint arXiv:2003.05475*, 2020.

[219] Z. Wei, W. Chen, C.-W. Qiu, and X. Chen. Conjugate gradient method for phase retrieval based on the Wirtinger derivative. *JOSA A*, 34(5):708–712, 2017.

[220] A. J. Williams, J. Chung, X. Ou, G. Zheng, S. Rawal, Z. Ao, R. Datar, C. Yang, and R. J. Cote. Fourier ptychographic microscopy for filtration-based circulating tumor cell enumeration and analysis. *Journal of biomedical optics*, 19(6):066007, 2014.

[221] G. Williams, M. Pfeifer, I. Vartanyants, and I. Robinson. Effectiveness of iterative algorithms in recovering phase in the presence of noise. *Acta Crystallographica Section A: Foundations of Crystallography*, 63(1):36–42, 2007.

[222] R. Xu, M. Soltanolkotabi, J. P. Haldar, W. Unglaub, J. Zusman, A. F. Levi, and R. M. Leahy. Accelerated Wirtinger flow: A fast algorithm for ptychography. *arXiv preprint arXiv:1806.05546*, 2018.

[223] M. Yang, X. Fan, H. Zhao, C. Li, and M. Xiang. Research on influences of atmospheric turbulence on long-distance Fourier pthchographic imaging. In *Digital Optical Technologies 2019*, volume 11062, page 110620Q. International Society for Optics and Photonics, 2019.

[224] T. D. Yang, K. Park, Y. G. Kang, K. J. Lee, B.-M. Kim, and Y. Choi. Single-shot digital holographic microscopy for quantifying a spatially-resolved Jones matrix of biological specimens. *Optics express*, 24(25):29302–29311, 2016.

[225] L.-H. Yeh. Analysis and comparison of Fourier Ptychographic phase retrieval algorithms. *Technical Report No. UCB/EECS-2016-86*, 2016.

[226] L.-H. Yeh, J. Dong, J. Zhong, L. Tian, M. Chen, G. Tang, M. Soltanolkotabi, and L. Waller. Experimental robustness of Fourier ptychography phase retrieval algorithms. *Optics express*, 23(26):33214–33240, 2015.

[227] Z. Yuan and H. Wang. Phase retrieval via reweighted Wirtinger flow. *Applied optics*, 56(9):2418–2427, 2017.

[228] H. Zhang, Y. Chi, and Y. Liang. Provable non-convex phase retrieval with outliers: Median truncated wirtinger flow. *arXiv preprint arXiv:1603.03805*, 2016.

[229] J. Zhang et al. Adaptive pixel-super-resolved lensfree in-line digital holography for wide-field on-chip microscopy. *Sci. Rep.*, 7(1):1–15, 2017.

[230] J. Zhang, X. Tao, P. Sun, and Z. Zheng. A positional misalignment correction method for Fourier ptychographic microscopy based on the quasi-Newton method with a global optimization module. *Optics Communications*, 2019.

[231] J. Zhang, T. Xu, J. Liu, S. Chen, and X. Wang. Precise brightfield localization alignment for Fourier ptychographic microscopy. *IEEE Photonics Journal*, 10(1):1–13, 2017.

[232] J. Zhang, T. Xu, Z. Shen, Y. Qiao, and Y. Zhang. Fourier ptychographic microscopy reconstruction with multiscale deep residual network. *Optics express*, 27(6):8612–8625, 2019.

[233] J. Zhang, T. Xu, X. Wang, S. Chen, and G. Ni. Fast gradational reconstruction for Fourier ptychographic microscopy. *Chinese Optics Letters*, 15(11):111702, 2017.

[234] X. Zhang, B. Cheng, C. Liu, W. Shen, and J. Zhu. Quantitative birefringence distribution measurement using mixed-state ptychography. *Optics express*, 25(25):30851–30861, 2017.

[235] Y. Zhang, Z. Cui, X. Ji, H. Wang, and Q. Dai. 3D Fourier ptychographic microscopy based on the Beam propagation method and time-reversal scheme. *IEEE Access*, 2019.

[236] Y. Zhang, Z. Cui, J. Zhang, P. Song, and Q. Dai. Group-based sparse representation for Fourier ptychography microscopy. *Optics Communications*, 404:55–61, 2017.

[237] Y. Zhang, W. Jiang, and Q. Dai. Nonlinear optimization approach for Fourier ptychographic microscopy. *Optics Express*, 23(26):33822–33835, 2015.

[238] Y. Zhang, W. Jiang, L. Tian, L. Waller, and Q. Dai. Self-learning based Fourier ptychographic microscopy. *Optics express*, 23(14):18471–18486, 2015.

[239] Y. Zhang, A. Pan, M. Lei, and B. Yao. Data preprocessing methods for robust Fourier ptychographic microscopy. *Optical Engineering*, 56(12):123107, 2017.

[240] Y. Zhang, P. Song, and Q. Dai. Fourier ptychographic microscopy using a generalized Anscombe transform approximation of the mixed Poisson-Gaussian likelihood. *Optics Express*, 25(1):168–179, 2017.

[241] Y. Zhang, P. Song, J. Zhang, and Q. Dai. Fourier ptychographic microscopy with sparse representation. *Scientific reports*, 7(1):8664, 2017.

[242] Y. Zhang, H. Wang, Y. Wu, M. Tamamitsu, and A. Ozcan. Edge sparsity criterion for robust holographic autofocusing. *Optics Letters*, 42(19):3824–3827, 2017.

[243] G. Zheng. *Fourier Ptychographic Imaging*. 2053-2571. Morgan & Claypool Publishers, 2016.

[244] G. Zheng, R. Horstmeyer, and C. Yang. Wide-field, high-resolution Fourier ptychographic microscopy. *Nature photonics*, 7(9):739–745, 2013.

[245] G. Zheng, C. Yang, and R. Horstmeyer. Fourier ptychographic x-ray imaging systems, devices, and methods, Feb. 13 2018. US Patent 9,892,812.

[246] G. Zheng, C. Yang, and R. Horstmeyer. Fourier ptychographic imaging systems, devices, and methods, June 9 2020. US Patent 10,679,763.

[247] J. Zhong, L. Tian, P. Varma, and L. Waller. Nonlinear optimization algorithm for partially coherent phase retrieval and source recovery. *IEEE Transactions on Computational Imaging*, 2(3):310–322, 2016.

[248] A. Zhou, N. Chen, H. Wang, and G. Situ. Analysis of Fourier ptychographic microscopy with half of the captured images. *Journal of Optics*, 20(9):095701, 2018.

[249] A. Zhou, W. Wang, N. Chen, E. Y. Lam, B. Lee, and G. Situ. Fast and robust misalignment correction of Fourier ptychographic microscopy for full field of view reconstruction. *Optics express*, 26(18):23661–23674, 2018.

[250] Y. Zhou, J. Wu, Z. Bian, J. Suo, G. Zheng, and Q. Dai. Fourier ptychographic microscopy using wavelength multiplexing. *Journal of biomedical optics*, 22(6):066006, 2017.

[251] C. Zuo. Quantitative phase imaging camera with a weak diffuser. *Frontiers in Physics*, 7:77, 2019.

[252] C. Zuo, J. Sun, and Q. Chen. Adaptive step-size strategy for noise-robust Fourier ptychographic microscopy. *Optics Express*, 24(18):20724–20744, 2016.

[253] C. Zuo, J. Sun, J. Li, A. Asundi, and Q. Chen. Wide-field high-resolution 3d microscopy with Fourier ptychographic diffraction tomography. *Optics and Lasers in Engineering*, 128:106003, 2020.

[254] C. Zuo, J. Sun, J. Zhang, Y. Hu, and Q. Chen. Lensless phase microscopy and diffraction tomography with multi-angle and multi-wavelength illuminations using a LED matrix. *Optics express*, 23(11):14314–14328, 2015.

Résumé étendu

Introduction et objectifs

Un principe fondamental de la microscopie optique est la mesure des interactions entre la lumière et un échantillon d'intérêt. Cependant, certaines informations sur ces interactions ne sont pas accessibles en raison des limites imposées à la fois par les lois de la physique et par les capacités actuelles des instruments. Un système de microscopie offrant un bon compromis entre le coût de fabrication et la quantité d'informations recueillies serait d'un grand intérêt. Le but de cette thèse est de proposer un tel instrument de mesure et de développer des méthodes de traitement de données correspondantes. Le domaine d'application choisi est la biologie et la médecine, afin d'améliorer l'analyse des tissus biologiques.

Pour atteindre ce but, le premier objectif est de réaliser un microscope à haute résolution et de développer des méthodes de reconstitution de scènes d'intérêt. Dans le cadre de cette thèse, nous avons choisi la Microscopie Ptychographique de Fourier (MPF) pour obtenir une image ayant à la fois un large champ de vue et une haute résolution spatiale. Cette technique appartient à un groupe de méthodes de l'imagerie numérique et, comme son nom l'indique, repose essentiellement sur le traitement numérique. Le deuxième objectif est de confronter le microscope construit avec une autre modalité d'imagerie, la microscopie polarimétrique de Mueller. Cette étape vise à donner une vision complète de l'interaction de la lumière avec l'échantillon en complétant les informations de phase et d'intensité (issues de la Ptychographie) avec les informations de polarisation.

Contexte

Ce travail de recherche a été réalisé au sein du Laboratoire des sciences de l'ingénieur, de l'informatique et de l'imagerie ICube (UMR 7357). Le projet s'inscrit dans le cadre d'une collaboration entre deux équipes - IMAGeS et TRIO. Ce travail est le premier dans le domaine de la microscopie numérique pour les deux équipes. Les contributions de cette thèse concernent à la fois les développements expérimentaux liés à la mise en œuvre des dispositifs et les développements des différentes parties de la chaîne de traitement des données.

Nous nous sommes particulièrement concentrés sur la réalisation du microscope ptychographique de Fourier et sur les méthodes de traitement correspondantes. En deuxième lieu, nous avons utilisé un microscope de Mueller pour accéder aux propriétés polarimétriques des échantillons. Nous nous sommes notamment intéressés à la complémentarité des informations extraites par ces deux modalités optiques construites.

Organisation du mémoire

La thèse contient 5 chapitres.

La première partie de la thèse a pour objectif de poser les bases et les limites de la microscopie optique afin de mettre en évidence la contribution de la ptychographie de Fourier. Dans le deuxième chapitre, nous expliquons en détail le fonctionnement de la MPF et son modèle physique. Nous poursuivons en examinant les aspects numériques du problème et les différentes méthodes de reconstruction. Le troisième chapitre présente le dispositif expérimental qui met en œuvre la MPF. Nous proposons ensuite des méthodes pour sa caractérisation et son étalonnage. Le quatrième chapitre présente une étude portant sur l'imagerie en phase quantitative. Ensuite, le microscope à matrice de Mueller est présenté, suivi d'une description de l'étude comparative. Enfin, nous tirons des conclusions et présentons les perspectives du travail accompli.

Chapitre 1 – Microscopie optique

Les principes de fonctionnement et les composants d'un microscope optique sont d'abord résumés, après une introduction aux méthodes d'imagerie optique et aux propriétés de la lumière. Cette discussion conduit à présenter les méthodes capables de dépasser les limites de l'imagerie conventionnelle.

L'optique est une branche de la physique qui étudie la lumière et ses interactions avec la matière. Dans le cadre de ce travail, nous nous concentrons principalement sur l'optique géométrique et l'optique d'onde. Parmi les attributs fondamentaux de la lumière auxquels nous nous référons dans ce travail figurent la direction de la propagation, l'amplitude, la phase, la fréquence et la polarisation. La lumière peut interagir avec la matière de différentes manières. Nous nous appuierons principalement sur la réfraction, la transmission, la réflexion, l'absorbance et la diffraction pour décrire le fonctionnement des systèmes construits. Ces notions sont donc exposées dans le premier chapitre.

Ensuite, les instruments optiques rencontrés au cours des travaux réalisés sont présentés. Les principaux composants d'un microscope optique sont également détaillés. Les microscopes utilisés dans ce travail sont des microscopes à transmission. Un microscope optique classique est un microscope à champ clair. Cela signifie que la lumière visible est utilisée pour éclairer l'échantillon.

Seuls les angles d'éclairage dans la plage de l'ouverture numérique sont acceptés par l'optique. L'image est ensuite formée en contrastant la quantité de lumière transmise/atténuée par l'échantillon à différentes positions spatiales. Le manuscrit poursuit en décrivant les caractéristiques et les limites de ce type de microscopie. En effet, la performance d'un microscope à champ clair n'est pas évaluée par un seul paramètre, mais plutôt comme une combinaison de plusieurs caractéristiques importantes. Celles-ci sont indiquées.

Ensuite, la nature des limites physiques de la microscopie classique est examinée. Dans le même temps, de nombreuses méthodes ont été proposées par les chercheurs pour remédier à certaines de ces limites une par une ou pour trouver les meilleurs compromis. L'état de l'art de ces méthodes est exposé. Les variations matérielles qui permettent de faire évoluer la configuration classique sont présentées en premier lieu. Ensuite, les avantages de l'imagerie numérique sont examinés.

Les techniques d'imagerie numérique cherchent à surmonter les limites physiques de l'imagerie traditionnelle par le traitement numérique des données. Nous sommes particulièrement intéressés par l'amélioration de la résolution et de la récupération de la phase. Les techniques permettant de résoudre chacun de ces problèmes sont présentées. La méthode de ptychographie de Fourier choisie pour les travaux actuels cible les deux problèmes en même temps.

Chapitre 2 – Problème de la phase et la ptychographie de Fourier

Nous présentons ensuite en détail l'une des principales limites de la microscopie optique qui est la perte d'informations sur la phase. Nous expliquons comment la ptychographie de Fourier permet d'estimer la phase. Cette technique a été initialement proposée en 2013 et a depuis fait l'objet de nombreux développements théoriques et expérimentaux.

Sa mise en œuvre instrumentale ne suppose qu'une modification matérielle d'un microscope classique. Il s'agit du remplacement de l'éclairage standard par une matrice de diodes électroluminescentes (DELs). Cela permet d'utiliser un éclairage à angle variable. Un autre avantage majeur d'un tel microscope est le faible coût de la solution. Nous montrons également comment cette technique surmonte partiellement un compromis entre un large champ de vue et une haute résolution spatiale.

Récupération de phase

Nous donnons d'abord un bref aperçu des techniques de récupération de phase en imagerie optique et dans d'autres domaines. Nous décrivons également la Ptychographie conventionnelle, précurseur de la méthode de la Ptychographie de Fourier.

Dans le contexte de l'imagerie optique, la phase quantitative établit un lien direct entre l'image reconstruite et le retard de l'onde électromagnétique de sortie. Cette quantité décrit à son tour le produit de l'indice de réfraction du matériau et de son épaisseur. Les techniques d'imagerie de phase quantitative appliquent, dans la plupart des cas, des approches algorithmiques.

Il existe de nombreuses techniques différentes pour la récupération de phase à l'aide de l'imagerie numérique. Certaines de ces méthodes reposent sur l'enregistrement de l'intensité des figures d'interférence. D'autres méthodes enregistrent directement des images conventionnelles d'intensité dans le domaine spatial. La ptychographie de Fourier, utilisée dans cette thèse, est l'une de ces dernières.

Microscopie ptychographique de Fourier

Pour expliquer le modèle de la ptychographie de Fourier plus en profondeur, nous simplifions le problème direct de la formation des images 2D à sa version 1D. La dérivation de ce modèle est décrite en détail dans le manuscrit. Elle peut être résumée comme suit. Afin de manipuler facilement la phase et l'amplitude de l'onde comme une seule valeur, des nombres complexes sont utilisés. Tout signal peut être représenté dans son domaine fréquentiel en calculant sa transformée de Fourier. En pratique, nous travaillons avec des signaux discrets et appliquons une transformée de Fourier discrète[1]. Nous expliquons ensuite comment le signal passe à travers le filtrage passe-bas, ce qui entraîne une perte de résolution. Nous montrons que ce n'est pas le signal filtré qui est mesuré en imagerie, mais son intensité, qui est le carré de l'amplitude. Cette perte d'informations de phase rend impossible l'accès au spectre par une simple transformation de Fourier.

La fréquence de coupure du filtre, ou de manière équivalente la largeur de la bande spectrale, définit la résolution finale du système. La largeur de la bande spectrale est intrinsèque au système de mesure utilisé et, dans de nombreux cas, impossible à élargir sans compromettre les autres caractéristiques du système. Cependant, nous pouvons accéder indirectement à ces hautes fréquences en décalant la composante de fréquence zéro du spectre ou, de manière équivalente, en décalant la bande spectrale. Il découle des propriétés de la transformée de Fourier que le décalage de fréquence peut être effectué en multipliant le signal dans le domaine spatial par une exponentielle complexe. Ce principe de capture de signaux d'intensité correspondant à différents décalages de fréquence est à la base de l'idée de la Ptychographie de Fourier.

Il est ensuite décrit comment mettre en œuvre un analogue 2D du problème direct en utilisant l'optique. Pour cela, le concept d'optique de Fourier est d'abord étudié, ce qui est nécessaire pour comprendre les propriétés de la transformée de Fourier optique. Puis, le processus d'acquisition d'images pour

[1] Aucune équation n'est donnée dans le présent document. Celles-ci se trouvent dans la version complète du manuscrit.

la ptychographie de Fourier est décrit. En bref, une matrice des DELs est utilisée pour couvrir une grande partie du spectre en faisant varier les angles d'éclairage. Pour chaque élément DEL, et donc pour chaque angle d'éclairage, l'image à faible résolution est capturée par la caméra. Un échantillon imagé doit être fin.

Nous continuons en énumérant les hypothèses, les approximations et les limites de la procédure donnée ci-dessus. Nous énumérons également les principales différences entre la ptychographie conventionnelle et la ptychographie de Fourier.

Aspects numériques

Après avoir étudié et approfondi le problème direct, nous présentons le problème inverse. La procédure de reconstruction d'images en MPF est un problème non linéaire et non convexe dans lequel les données consistent en plusieurs mesures de l'intensité du signal complexe inconnu. Il n'y a donc, en général, aucune garantie d'atteindre un minimum global. En outre, les données ont une large gamme dynamique due à la présence d'images en fond noir et en fond clair et sont corrompues par le bruit et les aberrations. De plus, des désalignements et des approximations du modèle d'observation sont inévitables dans des situations expérimentales réelles. Pour rendre le problème encore plus complexe, les mesures et les images reconstituées sont de grande taille. Bien que le problème soit résolu pour plusieurs petits segments plutôt que pour des images à plein champ de vision, la taille des variables reste élevée même après cette division.

Nous formulons d'abord le problème inverse comme une procédure d'optimisation. Nous recherchons un tel objet qui minimiserait la norme de la différence entre les images capturées et celles qui auraient été produites compte tenu de la matrice de conception. La matrice de conception représente le modèle direct, c'est-à-dire le processus de formation des images.

On vise à récupérer le signal original de manière unique. Nous analysons donc la question de la stabilité et de l'unicité de ce problème. Les exigences relatives à l'échantillonnage sont également discutées. Tout d'abord, il y a le risque du repliement de spectre. Deuxièmement, le degré de chevauchement dans le domaine des fréquences influence la qualité de l'image reconstruite.

De nombreux algorithmes de récupération de phase ont été proposés pour résoudre ce problème non convexe. Celles-ci comprennent diverses familles d'algorithmes d'optimisation, allant des méthodes basées sur la projection aux approches d'apprentissage profond. Par ailleurs, ces méthodes peuvent être différenciées par le choix de la fonction de coût, la stratégie de troncature du gradient, le calcul de la taille du pas, la procédure d'initialisation, l'utilisation d'un ensemble de données complet par rapport à une seule image par itération, les contraintes de régularisation, etc.

La solution initiale du problème de la Ptychographie de Fourier est un al-

gorithme de projections alternées. C'est une approche séquentielle basée sur le "moteur itératif ptychographique" (parfois appelé Gerchberg-Saxton). Des modifications aux projections alternées originales ont été proposées depuis lors. Un autre algorithme séquentiel largement utilisé est la méthode de Newton. Le terme "séquentiel" fait référence au mode de fonctionnement de l'algorithme, où une étape de mise à jour est effectuée pour chaque image, une à la fois. Par opposition aux algorithmes "globaux" où une mise à jour utilise l'ensemble complet des images pour chaque itération. De nombreux algorithmes sont globaux et décrits comme un problème d'optimisation avec une certaine fonction de coût. En 2015, une solution au problème de récupération des phases basée sur le calcul de Wirtinger et appelée flux de Wirtinger a été proposée puis adaptée au cadre de la MPF. Divers autres algorithmes basés sur un gradient ont également été proposés. Un autre groupe de solveurs sont des méthodes basées sur la convexité. Elles promettent d'atteindre le minimum global au détriment de la reformulation du problème dans des dimensions supérieures. Dans la pratique, cependant, la solution est calculée à l'aide d'une méthode non convexe. Les méthodes basées sur les réseaux de neurones sont également de plus en plus utilisées ces dernières années. Enfin, il est important de noter que la Ptychographie de Fourier est étroitement liée à la Ptychographie conventionnelle. Les nombreux développements algorithmiques en cours dans la Ptychographie conventionnelle peuvent souvent être directement appliqués à son homologue de Fourier. Les méthodes du problème plus général de la récupération de phase peuvent également être adaptées pour le cadre de la MPF. En outre, en théorie, tout algorithme d'optimisation pour un problème non convexe pourrait potentiellement convenir. La recherche dans ce domaine est en cours et de nouvelles procédures sont constamment proposées.

Les résultats de l'analyse bibliographique ont permis de déduire différentes briques qui, en combinaison, constituent des algorithmes existants (dans la plupart des cas). Les principales composantes qui caractérisent les méthodes sont les suivantes : algorithme du moteur d'optimisation, approche incrémentale versus globale, stratégie de sélection de la taille de pas, méthode d'initialisation, hypothèses sous-jacentes du modèle de bruit, régularisation de gradient par troncature, présence de terme de régularisation dans la fonction de coût, traitement des aberrations optiques et autres erreurs. Bien qu'il ne soit pas envisageable de mettre en œuvre toutes les méthodes possibles dans une seule étude doctorale, nous déployons certaines des approches les plus importantes de notre point de vue. Cela nous a permis de comparer différentes approches et de choisir un algorithme optimal pour le dispositif construit.

Il n'existe pas de réponse unique, claire et évidente quant à l'algorithme ou l'aspect d'un algorithme qui constitue le meilleur choix dans toutes les conditions et contraintes possibles. Pour la présente thèse, la décision a été prise d'utiliser une méthode de projections alternées avec une stratégie de taille de pas adaptative. Plusieurs raisons ont contribué à ce choix. Premièrement, il s'agit d'une des méthodes les plus robustes. Elle permet de reconstituer de

manière cohérente et avec des résultats satisfaisants la plupart des ensembles de données que nous avons testés, y compris les ensembles expérimentaux. Deuxièmement, c'est la plus rapide des méthodes que nous avons mises en œuvre, avec une convergence rapide et de faibles besoins en mémoire. Étant donné le nombre de pixels à traiter et à reconstruire, cela devient un avantage significatif. Troisièmement, des algorithmes de projections alternées sont largement utilisés dans la recherche sur la MPF. Quatrièmement, elle minimise implicitement une fonction de coût de type amplitude, ce qui s'avère être un bon choix pour les données corrompues par le bruit de Poisson. Enfin, le cadre des algorithmes de projections permet une grande flexibilité et une interprétation plus intuitive des résultats des itérations.Il est facile d'intégrer les modifications et de tester leurs effets directement à chaque étape de mise à jour de l'algorithme. D'autre part, les méthodes globales sont plus sensibles à l'initialisation et peuvent se retrouver bloquées dans les minima globaux. Comme l'ensemble des données est traité à chaque itération, il nécessite plus de calculs qu'une méthode itérative. En outre, la plupart des algorithmes, autres que la méthode des projections, nécessitent un réglage fin des paramètres. De plus, le nombre d'options à prendre en compte dans ces algorithmes, telles que la fonction de coût, la troncature du gradient, la taille du pas de mise à jour, rend difficile la justification de tous ces choix.

Chapitre 3 – Réalisation du microscope ptychographique de Fourier

Cette partie du mémoire traite des développements expérimentaux de l'appareil ptychographique. Cela implique la conception et l'assemblage de l'instrument, ainsi que sa caractérisation et la recherche de méthodes pour aborder les problèmes de désalignement et de bruit.

Introduction de l'instrument

Nous donnons d'abord les spécifications et les restrictions retenues pour la conception de l'appareil. Sur la base de ces contraintes et de l'expérience de l'équipe TRIO dans le développement de dispositifs optiques, il a été décidé de construire le microscope à partir de zéro plutôt que d'acheter et de modifier un microscope existant. En conséquence, les étapes de conception suivantes ont été mises en œuvre : le schéma du système a été proposé, l'équipement a été commandé et les pièces mécaniques ont été fabriquées, le dispositif a été assemblé, étalonné et caractérisé.

Nous présentons d'abord les composants de l'appareil construit. Suivant la proposition de la configuration classique de la MPF, les composants du système comprennent : une matrice des DELs, un objectif de microscope, un tube d'extension, une caméra, ainsi que des pièces mécaniques pour tenir

un échantillon et des composants optiques. À cette fin, le schéma des pièces mécaniques a été conçu dans le logiciel SolidWorks par les membres de l'équipe TRIO. Nous décrivons également la fabrication du tube d'extension. La caméra et la matrice de DELs sont contrôlées par un programme d'acquisition d'images écrit en LabVIEW par les membres de l'équipe TRIO.

Nous présentons ensuite les étalonnages de pré-acquisition et la procédure d'acquisition. En microscopie, il est essentiel de régler correctement la distance focale. Le système peut introduire des flous, des aberrations et d'autres erreurs lorsque l'échantillon est de-focalisé. Ceci est particulièrement important dans le contexte de l'imagerie numérique. On décrit alors un moyen de contrôler la mise au point avant les acquisitions. En outre, notre système présente, par construction, un certain degré d'instabilité par rapport à l'axe optique. Par axe optique, nous entendons ici une ligne passant par le centre de la matrice de DELs et perpendiculaire à celui-ci. Nous proposons donc une méthode qui permet d'estimer le pixel de l'axe optique. Nous l'utilisons pour aligner mécaniquement l'axe optique en inclinant physiquement le rail de support de la caméra. Mais aussi pour estimer les angles des DELs avant la procédure de récupération de phase.

Caractérisation du dispositif

Ensuite, nous détaillons autres étalonnages effectués. Certaines de ces méthodes sont inspirées par la littérature, d'autres sont nos contributions. Le système construit se compose de trois éléments principaux : l'unité d'éclairage, la partie optique et la caméra numérique. Chacun de ces composants doit être soigneusement caractérisé afin d'obtenir le modèle d'imagerie correct et de réduire l'influence des erreurs.

Les erreurs dans tout système expérimental peuvent être divisées en erreurs systématiques et aléatoires non systématiques. Dans la MPF, les différences d'irradiation des DELs, les aberrations optiques et le bruit du courant d'obscurité peuvent être classées comme systématiques. Les fluctuations de la luminosité des DELs et du bruit de la caméra, à l'exception du courant d'obscurité et des pixels chauds, sont des erreurs non systématiques. Les désalignements angulaires peuvent être classés comme systématiques et non systématiques. En effet, une partie des déviations est due à des imperfections mécaniques du système construit et à une erreur d'estimation des paramètres, et une autre partie est due à des déviations causées par un échantillon. Le même raisonnement peut être appliqué aux dés-alignements de l'ouverture numérique (ON) attachés à chaque DEL. D'une part, l'ON dépend de l'éclairage et de l'optique, et d'autre part, un échantillon épais peut également influencer les variations d'ouverture. Certaines de ces erreurs peuvent probablement être réduites en modifiant et en ajustant mécaniquement l'instrument, mais cela augmenterait le coût de la fabrication.

On propose donc, d'abord, des méthodes de caractérisation de la matrice

des DELs. La géométrie de la matrice des DELs utilisée est un simple rectangle. Par conséquent, la quantité de lumière arrivant à l'échantillon depuis une DEL distante est différente de celle arrivant d'une DEL proche de l'axe optique. Nous avons mesuré la tension relative de chaque DEL et simulé l'irradiance relative en nous basant sur la géométrie de la matrice des DELs. Ces valeurs sont utilisées pour déterminer les coefficients de correction pour les intensités des images capturées. Ensuite, un spectromètre portable a été utilisé pour mesurer la fréquence centrale et évaluer la cohérence des DELs. Nous avons constaté que les chiffres mesurés sont différents de la spécification donnée par le fabricant de la matrice des DELs.

Ensuite, des méthodes de caractérisation des éléments optiques sont mises en œuvre. Il s'agit notamment de la redéfinition expérimentalement du ON effectif. Nous estimons également le grossissement et la profondeur de champ du système.

Un autre aspect important de la caractérisation du système est le calcul des centres de segments. En effet, la procédure de reconstruction n'utilise pas directement les images du champ de vision entier, mais les décompose en segments plus petits. Les angles d'éclairage doivent ensuite être calculés pour chaque segment séparément. Théoriquement, cela ne devrait pas poser de problème car ces angles peuvent être calculés de manière purement géométrique. Cependant, lorsque les formules classiques sont appliquées à nos données, nous observons de forts artefacts sur les images de phase reconstruites pour les segments éloignés du pixel de l'axe optique. Nous proposons donc d'introduire un coefficient de correction tenant compte de la déviation observée.

Nous avons également étudié la question du bruit électronique, l'une des principales sources de bruit dans les mesures de la MPF. À notre connaissance, aucune étude sur les statistiques de bruit pour la microscopie ptychographique de Fourier n'a été proposée dans la littérature. Un certain nombre d'études supposent le type de bruit correct, à savoir un bruit mixte Poisson-Gaussien. Cependant, cette hypothèse n'est pas universelle. La plupart des articles supposent que les données sont corrompues par le bruit suivant la distribution de Poisson, certains considèrent même un simple bruit gaussien. Toutefois, il est important de connaître ces statistiques afin de valider le choix de la fonction de coût utilisée dans la procédure d'optimisation. Mais aussi pour proposer la production correcte de simulations de données pour la validation des méthodes. Nous clarifions ainsi cette question.

Pré-traitement des données

Nous soulignons également l'importance d'une autre problématique, à savoir le pré-traitement des images capturées.

Tout d'abord, si des temps d'exposition différents sont utilisés, les images doivent être re-normalisées pour correspondre au modèle d'observation. Ensuite, les pixels chauds et le bruit de fond pourraient et devraient être éliminés

avant la reconstruction.

Si nos premières tentatives n'ont porté que sur les problèmes décrits ci-dessus, nous avons ensuite réalisé qu'une autre partie du signal, liée aux différences d'éclairage, devait également être supprimée. En effet, on observe un décalage constant sur les images capturées. La valeur de ce décalage dépend de l'angle d'éclairage. Il est plus élevé pour les images en champ clair et plus faible pour les DELs distantes. Nous mettons donc en œuvre une méthode pour l'élimination de ces offsets angulairement variables.

Récupération des paramètres et des aberrations

La partie précédente du chapitre 3 portait sur les méthodes de caractérisation des paramètres du système lors d'une étape de prétraitement des données. Toutefois, ces estimations ne sont pas encore parfaites et des écarts peuvent se produire dans le cadre d'une installation expérimentale réelle. En outre, nous n'avons pas proposé de méthode pour caractériser l'aberration optique du microscope construit. Heureusement, la redondance des données collectées permet d'estimer numériquement les paramètres du système ainsi que les aberrations.

Historiquement, l'une des premières estimations de ce type a été la correction du front d'onde, proposée pour l'algorithme classique de type projection. Cette méthode était appelée "récupération intégrée de la fonction de la pupille". Une autre façon de récupérer la pupille est de modéliser ses aberrations à l'aide de polynômes de Zernike. Nous expliquons ces deux méthodes et les mettons en œuvre.

Ensuite, nous abordons la récupération des paramètres incertains du système et des coefficients des polynômes de Zernike. Les méthodes sont principalement basées sur l'idée de comparer des données simulées avec des données réelles en utilisant une métrique à optimiser. Nous discutons aussi des déviations angulaires individuelles. Ces dernières peuvent être introduites par des dés-alignements mécaniques dans le positionnement des DELs et des imperfections optiques.

Nous discutons également de la compensation des fluctuations de la luminosité des DELs. En dernier lieu, nous montrons comment la prise en compte de l'incohérence de la lumière pourrait améliorer la qualité de la reconstruction.

Sur la base de la caractérisation du dispositif ci-dessus, nous proposons une procédure pour simuler des images approchant les données capturées avec notre microscope. Les dés-alignements du système sont d'abord modélisés en perturbant les paramètres globaux (comme l'ON et la longueur d'onde), puis en ajoutant un décalage local à chaque angle. Le bruit de Poisson est appliqué sur les images simulées. Le bruit gaussien est ensuite ajouté. Enfin, les images sont mises à l'échelle par des coefficients de fluctuation d'intensité aléatoire représentant un éclairage inégal.

Résultats

La technique de la MPF promet une fabrication facile et un modèle d'imagerie simple. L'une des difficultés réside toutefois dans la caractérisation précise de tous les composants de l'instrument construit. De plus, si les algorithmes de base fonctionnent bien sur des données simulées sans bruit, les réalités expérimentales de notre microscope ont nécessité quelques étapes supplémentaires. Pour cette raison, il est important de étalonner correctement l'instrument, de régler la phase d'acquisition, de prétraiter les données, de choisir une procédure de reconstruction appropriée et de combiner les segments reconstruits.

En ce qui concerne la procédure de reconstruction, nous avons choisi un algorithme de projections alternées (moteur itératif ptychographique). La version de base est enrichie d'une stratégie de taille de pas adaptative, d'une modélisation de défocalisation, d'une méthode de récupération d'aberration et d'une routine de correction d'intensité. Les paramètres globaux du système sont optimisés pour un segment central. Un facteur de correction est également appliqué pour le calcul des centres de segments.

Enfin, nous comparons l'algorithme de projections alternées de base sans soustraction de bruit avec la procédure de reconstruction proposée. L'échantillon utilisé dans l'exemple est une lame histologique colorée de tissu mammaire de souris. L'épaisseur est de 6 µm. Les résultats montrent clairement que la version enrichie proposée est supérieure en termes de qualité de la reconstruction.

Chapitre 4 – Microscopie en lumière polarisée et imagerie multimodale

Comme nous l'avons montré, la MPF peut fournir des informations plus complètes que la microscopie classique en champ clair. Le microscope construit fournit une imagerie en champ clair à haute résolution et un contraste de phase quantitatif. Afin d'évaluer les capacités d'imagerie quantitative du microscope construit, nous menons une étude comparative en utilisant un objet de grande épaisseur optique. La modalité d'imagerie choisie pour cette confrontation est un microscope holographique. L'échantillon analysé est une microsphère de chaux sodée immergée dans du baume du Canada. Cette étude a fait l'objet d'un article publié.

Poursuivant l'idée de développer un système d'imagerie multimodal, nous explorons la complémentarité et l'intégration éventuelle de la microscopie de Fourier ptychographique avec la microscopie polarimétrique. La principale motivation de cette recherche est la capacité de la microscopie polarimétrique à accéder à des propriétés physiques qui ne sont pas disponibles en MPF. En effet, certains matériaux, y compris certains tissus biologiques, ne réagissent pas de la même manière à la lumière de différents états de polarisation. Ces matériaux peuvent présenter une biréfringence, un dichroïsme ou une activité optique. Ces données peuvent constituer une information importante, par

exemple, pour l'analyse des tissus biologiques et pour le diagnostic médical. Afin d'obtenir la description la plus complète de la réponse d'un milieu à la lumière polarisée, nous devons calculer la matrice de Mueller de ce milieu. Pour cela, nous utilisons un microscope Mueller construit par les membres de l'équipe TRIO.

Ce chapitre présente d'abord l'étude d'imagerie de phase quantitative. Ensuite, le microscope à matrice de Mueller est présenté, suivi d'une description de l'étude comparative. Enfin, les améliorations de la MPF et ses extensions à d'autres modalités sont discutées.

Imagerie de phase quantitative

La récupération d'informations quantitatives sur la phase d'un objet transparent est une question essentielle et importante pour l'imagerie des tissus biologiques.

Au cours des dernières décennies, un certain nombre de techniques d'imagerie de phase quantitative (IPQ) ont été introduites. Ici, nous visons à valider la capacité de l'IPQ de notre microscope ptychographique de Fourier. Pour cela, on compare les images de phase de la MPF avec les images obtenues par un microscope holographique numérique sans lentilles (Lensless inline digital holographic microscopy or LI-DHM en anglais). LI-DHM est l'une des techniques d'imagerie quantitative de phase les plus répandues. Les deux méthodes ont été utilisées dans divers domaines, notamment pour l'imagerie des lames biologiques, en raison de leur simplicité d'utilisation, de leur stabilité de construction et aussi de leur grand champ de vision.

De petites micro-billes transparentes (de plusieurs dizaines de microns de diamètre) ont souvent été utilisées comme référence pour l'étalonnage et la validation de l'IPQ. Cela est dû en partie au fait qu'une réponse de phase sphérique (provenant des cellules HeLa par exemple) est couramment observée en imagerie biologique. Cependant, l'imagerie de phase de leurs homologues de grande taille (perles de centaines de microns de diamètre) utilisant soit LI-DHM soit la MPF n'a pas été signalée jusqu'à présent. Nous cherchons à analyser la réponse de phase d'une microsphère de chaux sodée de 146 µm. Elle a été immergée dans du baume du Canada afin de réduire la différence de phase et d'éviter les anneaux de diffraction surexposés. L'estimation de la phase par LI-DHM a été abordée en utilisant un algorithme de type Gerchberg-Saxton et une procédure basée sur un problème inverse.

L'analyse des images reconstruites par LI-DHM et la MPF révèle que les deux instruments sont capables de fournir les distributions de phase que l'on attendrait d'une micro-bille, confirmant ainsi leur capacité de l'IPQ. La FPM semble fournir des amplitudes de l'étendue de la phase plus faibles que LI-DHM. Nous spéculons qu'une telle différence pourrait être due à l'approximation d'un échantillon optiquement épais par un modèle 2D infiniment mince.

Microscopie en lumière polarisée

Nous abordons d'abord brièvement la théorie de l'imagerie polarimétrique. La lumière peut être décrite par des vibrations de type ondulatoire se propageant sous forme de champs électriques et magnétiques couplés. Ces champs sont perpendiculaires les uns aux autres. La polarisation de la lumière décrit la distribution préférentielle de l'orientation des oscillations des ondes électromagnétiques. Nous décrivons brièvement d'autres notions de base nécessaires pour comprendre le fonctionnement du microscope polarimétrique. Il s'agit notamment des définitions des types de polarisation, des polariseurs, des plaques d'onde, des milieux anisotropes et de la matrice de Mueller.

Nous présentons ensuite le microscope de Mueller utilisé et décrivons son principe de fonctionnement. Le microscope de Mueller permet de récupérer les propriétés de polarisation d'un échantillon. Il le fait par une mesure de la matrice de Mueller. La matrice de Mueller est ensuite décomposée en dichroïsme, retard et dépolarisation du milieu étudié. Nous ne nous focalisons pas sur le développement du microscope de Mueller, car c'est une technologie que l'équipe maîtrise déjà. L'accent est plutôt mis sur la complémentarité entre les deux systèmes conçus et sur l'intérêt éventuel de les combiner.

Microscopes ptychographique de Fourier et de polarisation : comparaison

Les techniques d'imagerie polarimétrique et la MPF ont toutes deux de nombreuses applications dans l'analyse des tissus biomédicaux ; la combinaison des deux pourrait donner des informations encore plus riches. Nous étudions la complémentarité entre les retards de phase observés avec le MPF (la phase optique) et la microscopie de Mueller (le retardance). Nous mettons en évidence leurs différences. Des observations sur des lames histologiques sont présentées pour une validation expérimentale. Cette partie de travail a fait l'objet d'une communication internationale avec un acte publié.

Bien que des études comparant et même combinant les techniques de l'IPQ avec les méthodes polarimétriques puissent être trouvées dans la littérature, à notre connaissance, ce travail est le premier à évaluer la complémentarité des microscopes ptychographiques de Fourier et à matrice de Mueller.

Afin de démontrer la complémentarité des deux techniques, nous utilisons une lame histologique colorée de tissu mammaire de souris (6 µm d'épaisseur). Malgré la coloration par H&E (hématoxyline et éosine), l'échantillon révèle un faible contraste en lumière visible. C'est le même échantillon que nous avons utilisé dans le chapitre précédent.

Nous avons observé que la phase de la MPF met en évidence les épaisseurs et les formes des structures. Ce sont les propriétés plutôt géométriques de l'échantillon. Le retard polarimétrique représente la biréfringence du milieu. Il permet d'améliorer la différenciation entre les différents types de tissus. Cela donne à son tour un meilleur accès à la composition cellulaire de l'échantillon.

En outre, le retard circulaire peut également révéler l'alignement des fibres tissulaires. La validation visuelle a confirmé l'apport d'informations entre les deux modalités. Nos deux instruments ont été construits avec presque la même résolution spatiale. Cela permet une analyse comparative significative.

La motivation de fusionner les deux modalités étant confirmée, ce sera l'une des prochaines étapes de notre recherche. Des études préliminaires ont été menées pour équiper l'appareil FPM construit de capacités d'imagerie polarimétrique de Stokes.

Extensions et améliorations

Les progrès récents en matière de la MPF ont montré qu'il était possible non seulement d'améliorer la qualité de la reconstruction, mais aussi d'étendre la configuration classique à d'autres modalités d'imagerie. En raison de la durée limitée de la thèse de doctorat actuelle, il n'a pas été possible d'étudier toutes les améliorations possibles. Néanmoins, dans la dernière partie du manuscrit, nous discutons des améliorations les plus prometteuses et indiquons celles qui sont prioritaires pour la mise en œuvre compte tenu de notre configuration. Nous discutons, entre autres, de la ptychographie de Fourier 3D, du couplage avec d'autres modalités, d'une meilleure architecture d'éclairage et des techniques permettant de réduire le temps d'acquisition.

Chapitre 5 – Conclusions

Au cours de ce travail de thèse, nous nous sommes concentrés sur le développement d'un système de microscope offrant une grande quantité d'informations pertinentes récupérées à un coût abordable. En particulier, nous avons construit notre version du microscope ptychographique de Fourier, une technique d'imagerie numérique récente.

Nous avons ensuite utilisé une autre modalité optique, le microscope à matrice de Mueller, afin de mettre en évidence la nature complémentaire des informations obtenues par deux appareils.

La mise en œuvre du microscope ptychographique de Fourier a nécessité non seulement la construction de l'instrument à partir de zéro, mais aussi la mise en place du flux de travail méthodologique pour son étalonnage, le prétraitement des données et la reconstruction. Alors que l'auteur a participé à toutes les étapes du développement du dispositif de la MPF, la construction du microscope polarimétrique à matrice de Mueller a été principalement réalisée par d'autres membres de l'équipe TRIO. Par conséquent, ce document met davantage l'accent sur le premier système.

Du point de vue de l'application, nous nous sommes assurés de montrer la pertinence de ces recherches sur les échantillons biologiques. En outre, nous présentons en annexe les résultats des reconstructions obtenues sur différents types d'échantillons.

Un système pleinement fonctionnel a été mis au point et ses capacités ont été démontrées. Sa complémentarité avec un microscope à polarisation a été mise en évidence, ce qui valide l'intérêt de leur fusion prospective. De plus, bien qu'il n'ait pas été possible de réaliser toutes les améliorations et recherches que nous aurions souhaitées, nous fournissons des lignes directrices claires pour les travaux futurs. Une partie de ce travail a déjà commencé au sein des équipes.

Anastasia BOZHOK

Microscopies ptychographique de Fourier et de polarisation : modèles, méthodes, comparaison

Résumé

Un système de microscopie offrant un bon compromis entre le coût de fabrication et la quantité d'informations recueillies est d'un grand intérêt pour un domaine de l'imagerie biomédicale. Le but de cette thèse est de proposer un tel instrument de mesure et de développer des méthodes de traitement de données correspondantes.

Pour atteindre ce but, nous avons d'abord réalisé un microscope ptychographique de Fourier. Cette technique repose essentiellement sur le traitement numérique. L'un de ses principaux avantages est la capacité d'obtenir une image ayant à la fois un large champ de vue et une haute résolution spatiale.

Ensuite, nous avons confronté le microscope construit avec un microscope polarimétrique de Mueller. Cette étape a permis de compléter les informations de phase et d'intensité (issues de la ptychographie) avec les informations de polarisation.

Mots-clés : Ptychographie de Fourier, Microscopie polarimétrique, Phase Quantitative

Résumé en anglais

A microscopy system offering a good compromise between the manufacturing cost and the amount of information retrieved is of great interest for a field of biomedical imaging. The aim of this thesis is to propose such a measuring instrument and to develop corresponding data processing methods.

To reach this goal, we first realized a Fourier ptychographic microscope. This technique relies mainly on digital processing. One of its main advantages is the ability to obtain an image with both a wide field of view and high spatial resolution.

Next, we compared the microscope built with a polarimetric Mueller matrix microscope. This step allowed us to complete the phase and intensity information (obtained by the ptychography) with the polarisation information.

Keywords: Fourier Ptychography, Polarimetric Microscopy, Quantitative Phase